2018

THz Sources Based on Er-Doped GaAs Driven at Telecom-Fiber Wavelengths

Andrea Mingardi
Wright State University

THz SOURCES BASED ON ER-DOPED GAAS DRIVEN AT TELECOM-FIBER WAVELENGTHS

A dissertation in partial fulfillment of the
requirements for the degree of
Doctor of Philosophy

by

ANDREA MINGARDI

B.S., Università degli Studi di Parma, 2012

M.S., Università degli Studi di Parma, 2015

2018

Wright State University

WRIGHT STATE UNIVERSITY

GRADUATE SCHOOL

12/05/2018

I HEREBY RECOMMEND THAT THE DISSERTATION PREPARED UNDER MY SUPERVISION BY Andrea Mingardi ENTITLED THz Sources Based on Er-Doped GaAs Driven at Telecom-Fiber Wavelengths BE ACCEPTED IN PARTIAL FULFILLMENT OF THE REQUIREMENTS FOR THE DEGREE OF Doctor of Philosophy.

_____
Elliott R. Brown, Ph.D.
Dissertation Director

_____
Mary E. Fendley, Ph.D.
Interim Director, Ph.D. in Engineering

Committee on Final Examination:

_____
Barry Milligan, Ph.D.
Interim Dean of the Graduate School

_____
Marian K. Kazimierczuk, Ph.D.

_____
Pradeep Misra, Ph.D.

_____
Jason A. Deibel, Ph.D.

_____
Weidong Zhang, Ph.D.

_____
John R. Middendorf, Ph.D.

ABSTRACT

Mingardi, Andrea. Ph.D., Engineering Ph.D. program, Wright State University, 2018.
THz Sources Based on Er-Doped GaAs Driven at Telecom-Fiber Wavelengths

This dissertation entails the investigation of ultrafast photoconductive (PC) THz sources driven by fiber and semiconductor lasers around λ= 1550-nm to utilize commercial fiber-optic telecom technology. The preferred approach is to use GaAs with a high concentration of erbium, which has performed well when driven with laser sources at both 800 nm wavelength, through intrinsic photoconductivity, and 1550 nm, through extrinsic photoconductivity. Studies in the early 1990s showed that the Er doping level has a solubility limit of $\sim 7 \times 10^{17}$ cm^{-3} at 580 °C, above which erbium is incorporated into GaAs as ErAs nanoparticles which promote resonant absorption around λ= 1550-nm. This research is focused on improving the GaAs:Er extrinsic-photoconductive device performances by engineering the material and improving the design of THz antennas. Antennas with different dimensions have been fabricated and tested, and substrates with different doping levels and epi-layer thicknesses have been studied and characterized to improve absorption of the 1550 nm radiation, increase the dark resistivity and get more THz radiation. The antennas were then fabricated with a planar-processing technique, packaged, and tested as 1550-nm driven PC THz sources.

These are the first THz devices fabricated in the history of Wright State University and have already set a record in terms of power generated by THz photoconductive devices driven at 1550-nm.

Table of Contents

List of Figures

List of Tables

Acknowledgements

As is the case for every Ph.D. student, I have many people who I would like to thank for their contributions to my research. Whether their help was in the lab or through other forms of support, without every single one of them I would have not been able to make it to end of this journey.

First and foremost, I would like to thank my advisor Prof. Elliott Brown. He believed in me when I first arrived at Wright State University and offered me the incredible opportunity to pursue a Ph.D. under his guide. The discussions with him on THz devices and the physics behind them have been incredibly useful and enlightening. In addition, he has shown incredible patience with my writing skills and though me a lot on how to improve them.

Next, I would like to thank the members of my committee. Prof. Marian Kazimierczuk and Prof. Pradeep Misra, for providing insights and useful comments that improved the outcome of my dissertation. Prof. Jason Deibel, for sharing his knowledge on fiber optics and THz characterization. Dr. John Middendorf, for sharing his knowledge on these devices. Dr. Weidong Zhang, for his immense help. He helped me improving my device characterization's skills, he taught about various techniques and he helped with some of the device characterization.

In addition, Dr. Matthieu Martin for teaching me the basis of the fabrication process. Dr. Tyler Growden for helping me improving my fabrication's skills and teaching me multi-level lithography processes. Dr. Ari Feldman and Dr. Richard

Mirin from the National Institute of Standards and Technology for growing all of our samples.

I would also like to thank all of the present and past student members of Prof. Brown's group who shared with me life in the lab: Shahanur Alam, Amal Mirando and Katurah Hansen.

Most of this research was performed under the sponsorship of a Multi-University-Research-Initiative (MURI), "Devices and Architectures for THz Electronics (DATE)"- managed by Dr. Paul Maki, Office of Naval Research, prime contract number N00014-11-1-0721, with extension N00014-16-1-2686. The latter part of the research was supported by the National Science Foundation (Dr. Dimitris Pavlidis) under Grant#1711738.

Finally, I would like to thank my wife Grace for the immense support she has given me through all these years, in both the good and bad times that come on the path of a Ph.D. carrier. To my family, my parents Francesco and Ombretta, my brother Matteo and his girlfriend Mary and my grandma Maria Angela who greatly supported this decision of mine and always provided me moral support. To my new family of in-laws, my parents-in-law Aldo and Patricia, who accepted me as part of their family from the beginning, my brothers-in-law Matteo, Max and Luca with his wife Katie and their children Kennedy and William.

It is thanks to all of these people that I have been able to successfully complete this chapter of my life.

Preface

This thesis extends and develops previous pioneering work on ErAs:GaAs PC devices conducted at Wright State University. The research was conducted on a material with unknown nanoparticle properties and insufficient THz performance to be used in systems applications [1]-[3]. The objective of this work was to fabricate superior devices capable of higher THz power generation and higher efficiency, gain a better physical understanding of the material and devices, and discover new phenomena on this unique nano-composite material. Four different approaches were run in parallel in order to pursue these goals: thorough characterization to better understand the material, improvement of the fabrication process, better understanding of the electromagnetic of the antenna, and thorough testing of the devices.

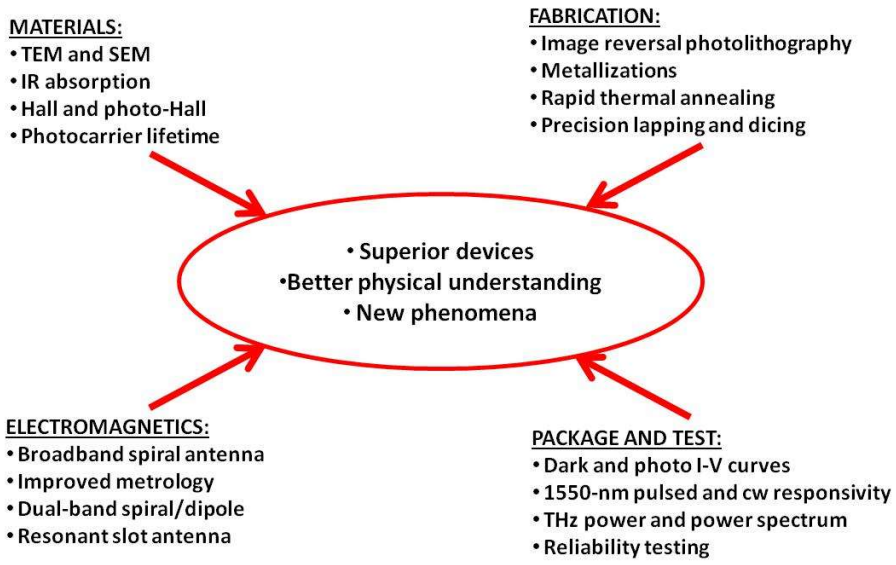

Fig. 0.1 Research plan for this work.

Chapter 1 of this dissertation will open with the definition and description of the THz region of the electromagnetic spectrum and the kind of applications that it can support. Next, an explanation of the two types of THz sources (photoconductive switch and photoconductive mixer) that are being used in THz application will be given. Then, the reasons behind the choice of the driving wavelength and an overview of the state-of-the-art materials used at such wavelength will be discussed.

Chapter 2 will discuss an overview of the different photoconductivity mechanisms and present the history of the material chosen for these devices will be presented.

Chapter 3 will detail the results of the material characterization used for this work, both optical and with regard of the quality of the crystalline structure.

Chapter 4 will introduce the devices tested for this thesis and examine the process of fabrication of the devices as well as their packaging.

Chapter 5 comprises all the results from experiments done to characterize the devices fabricated on the best two samples (ASP174 and ASP194). Tests for responsivity at 1550 nm with pulsed sources as well as tests for total THz power are presented. A new type of infrared filter is here discussed and characterized.

Chapter 6 will continue with the characterization of such devices with the presentation of the power spectra.

Chapter 7 will present and characterize the dual band (THz and microwave) antenna. A study of the effect of the metallization on the performances of the antenna is discussed.

Chapter 8 will present the results obtained from all the samples in order to optimize the material for device application.

Chapter 9 will focus on both the characterization of the devices under continuous-wave laser excitation and their use as photomixers.

Chapter 10 will conclude this work with the first recorded preliminary study on the failure mechanisms for photoconductive switches.

CHAPTER 1
THz region and THz sources.

1.1 The THz Spectrum and Applications

The THz spectrum has been defined as the spectral region from 300 GHz to 10 THz, bordered on the lower end by the microwave region and on the upper end by the far-infrared. On the lower end of the spectrum, research has tried to progress the development of a coherent millimeter wave source that could achieve higher frequencies, but with limited success due to the speed limitations of the devices (i. e. carrier mobility of the semiconductor). For example, 300 GHz represents a challenging barrier to surpass [4]. In the infrared region, coherent radiation is generated using photon emission from lasers. However, due to a change of spontaneous emission physics, low atmospheric transmission (i.e. water absorption) and the fact that the energy of THz photons (4.1 meV at 1 THz) is less than the thermal energy (around 25.6 meV) at room temperature, the lowest frequency for solid-state lasers is approximately 10 THz [5]. These two limits define the boundaries for the THz region (Fig. 1.1).

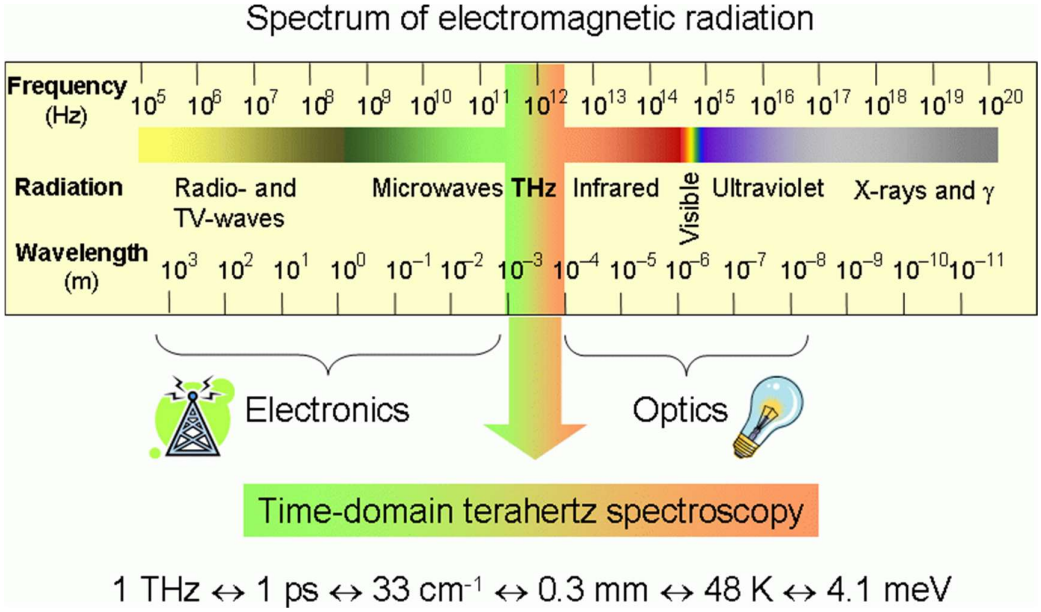

Fig. 1.1 Spectrum of electromagnetic radiation [6].

Despite the problems associated with THz generation, THz radiation is of particular interest due to several advantages. Wavelengths in this region are short enough to provide sub-millimeter spatial resolution in imaging [7], and can penetrate fabrics and plastics, making this spectral region useful for imaging many, otherwise concealed, objects [8]. In addition, many materials have spectral "fingerprints" in the THz region in the form of unique spectral absorption features [9], thus enabling direct detection. Due to high water-vapor absorption (Fig. 1.2), THz waves do not propagate very far in the atmosphere, and for this reason, they cannot penetrate the human body like microwaves can. Nevertheless, this apparent limitation makes THz waves extremely sensitive to hydration, which when combined with the fact that THz photons are non-ionizing, makes these waves ideal for certain biomedical imaging application [10]-[13].

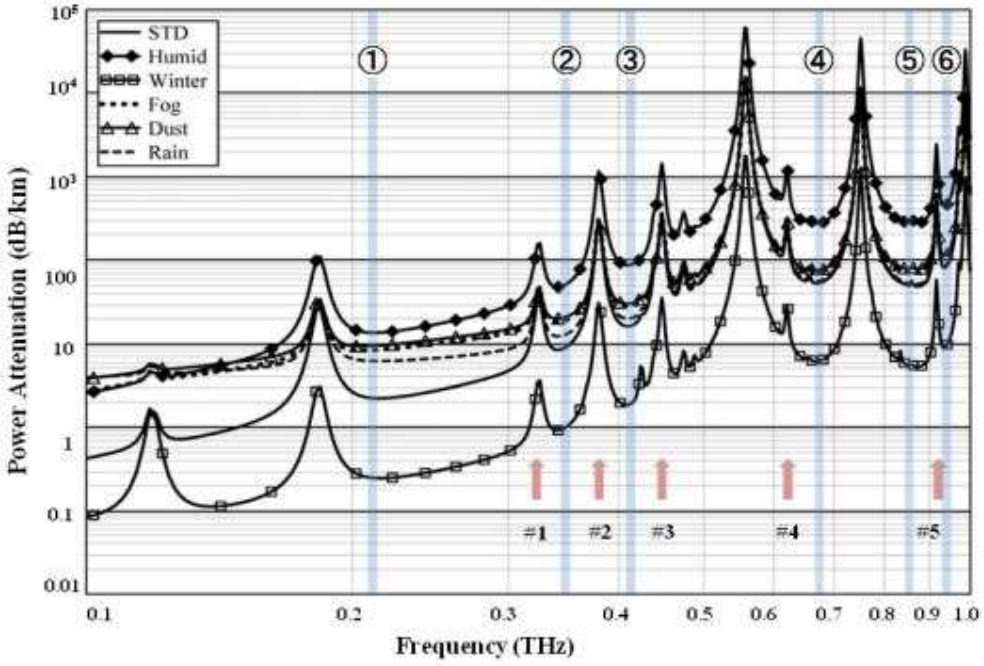

Fig. 1.2 Atmospheric attenuation at sea level for different conditions of temperature, relative humidity (RH), fog, dust and rain. (STD: 20 °C, RH 44%), (Humid: 35 °C, RH 90%), (Winter: -10 °C, RH 30%), (Fog, Dust, and Rain: 20 °C, RH 44%). Six water windows (circled numbers) and 5 weak water lines (broad arrows) are marked for comparison with the THz-TDS measurements. [14].

More specific examples of the applications enabled by the properties of THz photons include: medical imaging of the cornea, burns, and cancer [15]-[18], DNA sequences sensing and THz exposure effects on lymphocytes [19]-[23], material spectroscopy of organic and inorganic materials [24]-[27] especially to identify illicit drugs by identifying spectral signatures [9], [28]-[30], security [8], [31]-[36], high-resolution radars [37]-[39], broadband high data-rate indoor communication systems [40], [41], and communications systems in general [42]-[44].

1.2 Photoconductive THz source - principles of operation

Photoconductive (PC) sources are critically important for THz power generation. For this reason, they will be discussed in more details in this paragraph. The two primary types of PC THz sources are: the photoconductive switch and the

photoconductive mixer (photomixer). PC switches [Fig. 1.3 a)] or Auston switches [45], are pulsed, broadband optoelectronic THz sources [46], [47]. They are mostly used for time-domain spectroscopy (TDS) due to their high bandwidth and the speed at which data can be collected (few seconds). They are also useful in imaging applications because they produce more total THz power compared to photomixers [13], [48]. Photomixers [Fig. 1.3 b)], on the other hand, are tunable, single frequency, continuous-wave (CW) THz sources [49] that are commonly used in frequency-domain spectroscopy applications, where spectral transmittance or reflectance data is recorded as the frequency is swept.

Since this work relates strongly to the PC switches and photomixers, a more in-depth explanation of their principles of operation is provided in the following section.

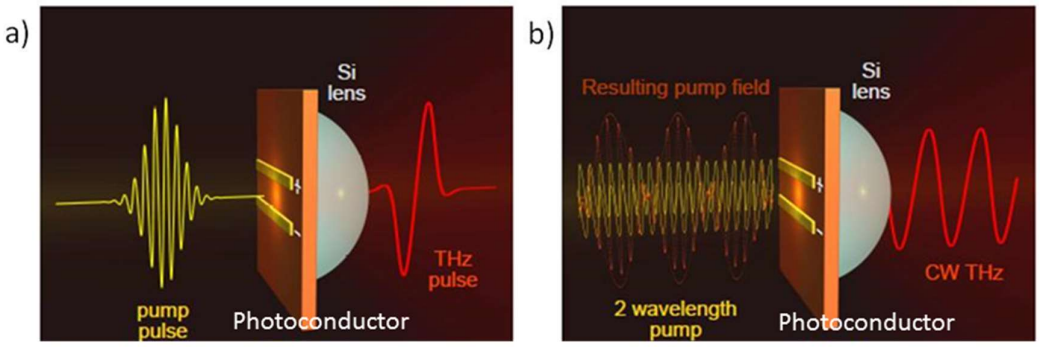

Fig. 1.3 Schematic view of a setup used to generate a) pulsed THz radiation by photoconductive antenna, b) CW THz radiation by photoconductive antenna [50].

1.2.1 Photoconductive switch

The PC switch (Fig. 1.3 a)) consists of a DC biased antenna patterned on a photoconductive substrate. The electrodes are biased by an external voltage, and the gap between them is excited with an ultrashort pulse laser. The excitation generates a large density of photocarriers. The resulting photocurrent lasts only for a short period leading to the generation of a THz pulse [46], [51]-[54], whose duration and spectrum

are determined by the carrier's lifetime in the semiconductor (following the generic equation for bandwidth $\omega=1/\tau$). The concept of generation of pulsed THz radiation from a photoconductive antenna (PCA) is illustrated in Figure 1.3 a).

The development of a photoconductive material is very important for high power THz PC switches. An ideal photoconductive candidate needs to have the following four properties: (1) short photocarrier lifetime (in picoseconds or less), (2) high photocarrier mobility (in the order of 10^3 $cm^2/V\text{-}s$), (3) high breakdown electric field E_B (in the order of hundreds of kV/cm), and (4) high dark resistivity (in the order of 10^3 Ω-cm). These properties ensure a photoconductor that is poorly conductive in its "dark" state and conductive in its "on" state, that can withstand high laser power levels, and can rapidly switch between the "on" and "off" states.

(1) To a shorter pulse in the time-domain corresponds a larger bandwidth in the frequency-domain. Hence, having picosecond, or sub-picosecond, photocarrier lifetime is beneficial because it broadens the bandwidth of THz emission ($\omega=1/\tau$).

(2) The carrier mobility affects the "on" state of the device. When illuminated by laser pulses, photocarriers are created by electron-hole pair generation. The photoconductivity of the semiconductor is proportional to the generated electron and hole densities:

$$\sigma = -en_e\mu_e + en_p\mu_p \tag{1.1}$$

where e is the electron charge, n_e and n_p are the concentrations of electrons and holes, μ_e and μ_p are their mobilities, respectively. The change in the photoconductivity results in a pulsed photo-induced photocurrent when biased by the DC electric field in the gap.

Hence, higher mobility leads to higher conductivity, leading to a larger current in the "on" state.

(3) Having a high breakdown field is beneficial to the "on" state of the device. The photocurrent density is described as:

$$J(t) = N(t) e \mu_e E_B \tag{1.2}$$

where N is density of the photocarriers, e is the electron charge, and E_B is the bias electric field. Since photocurrent is time dependent, it generates an electromagnetic pulse with an electric field that follows the following equation [50]:

$$E_{THz} = \frac{1}{4\pi\varepsilon_0} \frac{A}{c^2 z} \frac{\delta J(t)}{\delta t} = \frac{Ae}{4\pi\varepsilon_0 c^2 z} \frac{\delta N(t)}{\delta t} \mu_e E_B \tag{1.3}$$

where A is the area of the illuminated gap, ε_0 is the vacuum permittivity, c is the speed in vacuum, and z is the distance between the field point and the THz source. A high breakdown field allows for higher bias to which the E_{THz} is linearly dependent.

However, a high bias may result in dielectric breakdown in the epilayer. This breakdown can be one of two types: impact ionization breakdown and thermal-runaway breakdown. The impact ionization breakdown happens when the bias field exceeds E_B, which is an abrupt mechanism. The thermal-runaway breakdown is caused by heating of the epilayer by the photocurrent flow. This mechanism is a slow process that can take from seconds to minutes and sets a tradeoff between the laser intensity and the maximum bias voltage.

(4) The dark resistivity affects the "dark" state of the device. A high dark resistivity increases the off-resistance of the device, thus reducing the dark-current (also referred as leakage current). The benefits of the dark-current's reduction are twofold: for one, it

reduces the Joule heating that could lead to a thermally induced breakdown; in addition, due to a larger difference between the pulse current in the "on" state and the "leakage" current in the "off" state, the reduction of the dark-current will increase the THz optical field due to the dependence of the latter on the photo-current (Eqn. 1.3).

1.2.2 Photoconductive mixer

The process for photomixers is optical heterodyne generation in the semiconductor active region of the device. The optical sources that drive the photomixers are two continuous laser beams with a frequency difference lying in the THz region. The principle of operation for CW THz generation in photomixers is shown in Fig. 1.3 b). The number of generated photocarriers is governed by:

$$\frac{\delta n(t)}{\delta t} = \frac{\eta I_{pump}(t)}{h\nu} - \frac{n}{\tau_{eff}} \tag{1.4}$$

where η is the external quantum efficiency, I_{pump} (t) is the pump intensity, τ_{eff} is the photocarrier recombination time, and hν is the photon energy. Note I_{pump} (t) is proportional to the square of the optical field $|E_{pump}(t)|^2$. This square law is essential for the photomixing.

In this case, there are two laser beams, with optical field E_1 and E_2 and corresponding frequencies ω_1 and ω_2, respectively. I_{pump} (t) can be described as:

$$I_{pump}(t) = (1/2)c\varepsilon_0(E_1+E_2)^2$$

with c the speed of light and ε_0 the permittivity of free space. This equation can be rewritten as [54]:

$$I_{pump}(t) = I_1 + I_2 + 2\sqrt{mI_1I_2}\left[\cos 2\pi(\omega_1-\omega_2) + \cos 2\pi(\omega_1+\omega_2)\right] \tag{1.6}$$

where m is the mixing efficiency, $I_1 = (1/2)\, c\varepsilon_0(E_1)^2$ and $I_2 = (1/2)c\varepsilon_0(E_2)^2$.

If the bias field is kept constant, the photocurrent can be rewritten as [55]:

$$I(t) = I_D + \frac{I_A}{\sqrt{1+\omega^2\tau_{eff}^2}}\sin(\omega t + \phi) \tag{1.7}$$

where $\omega = 2\pi(\omega_1-\omega_2)$ is the THz frequency, and $\varphi=\tan^{-1}(1/\omega\tau)$ is the phase delay due to the carriers' lifetime. $I_D = E_B\mu_e\tau_{eff}(I_1 + I_2)$ is the DC photocurrent and $I_A = 2E_B\mu_e\tau_{eff}\sqrt{I_1I_2}$ is the amplitude of the AC current, responsible for the generation of the CW THz signal. From (1.7):

$$E_{THz}(t) \propto \frac{\delta J(t)}{\delta t} = \frac{\omega I_A}{\sqrt{1+\omega^2\tau_{eff}^2}}\cos(\omega t + \phi) \tag{1.8}$$

Hence, for both photoconductive switches and mixers, it is necessary to have a material with high photocarrier mobility, high critical breakdown field E_B and high dark resistivity. In addition, a short photocarrier lifetime (in the picosecond or sub-picosecond range) is very important for both PC switches and photomixers as it sets an upper bound on the bandwidth over which the devices can radiate.

1.3 Driving wavelengths

Two wavelengths, 780 nm and 1550 nm, are commonly used for driving PC devices based on GaAs and InGaAs, respectively. The reason can be found in the history of telecommunication and optical fibers. In 1970, the first single-mode fiber with attenuation at 633-nanometer below 20 dB/km was created [56]. In the following years the first-generation multi-mode systems working at 850 nm based on AlGaAs laser could transmit light several kilometers without a repeater. A second generation based on InGaAsP lasers emitting at 1300 nm proved to have a lower attenuation of 0.4 dB/km

and it was later found that the minimum attenuation of glass fibers was below 0.2 dB/km at the 1550 nm wavelength (Fig. 1.4).

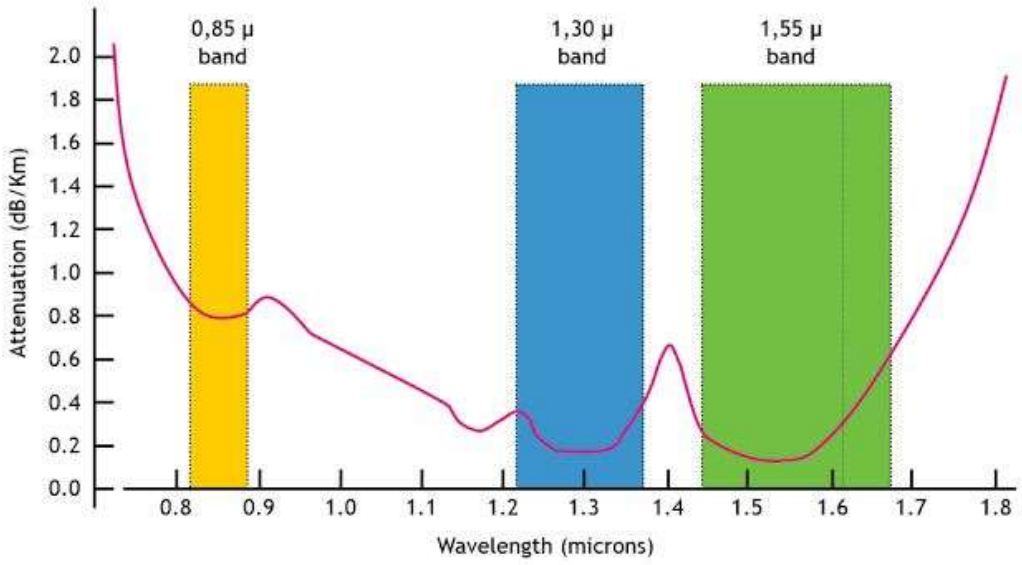

Fig. 1.4 Optical fiber absorption vs wavelength [57].

The next significant milestones were the fabrication of InGaAsP laser with distributed Bragg reflector, which moved the emission wavelength up to 1550 nm, as well as the development of the erbium-doped fiber amplifier (EDFA). In 1986, it was shown that an optical fiber with erbium added to its core could amplify light at a wavelength around 1550 nm, enabling the amplification of the weak signals transmitted in fiber-optic communication systems.

1550-nm became then wavelength of choice for the fiber-telecommunication industry. For this reason, lasers and other components working at this wavelength are typically less expensive compared to those working at shorter wavelengths [58]. It is also easier to manipulate such beams due to the wide variety of components, both active and passive. This choice was also supported by the fact that, due to the core size of 9-µm in diameter for 1550-nm fibers compared to that of 6-µm for 780-nm fiber [59], a

given amount of power has around twice the intensity (P/area) in 780-nm fiber compared to 1550-nm ones. This higher intensity excites Brillouin scattering and other possible nonlinear processes much more readily in 780-nm fiber [60]. With this problem being even more important with pulsed lasers, where the peak power is higher compared to cw lasers. Furthermore, the number of photons per second is $(P \cdot \lambda)/(h \cdot c)$, where P is the average optical power, λ is the radiation wavelength, h is the Plank constant and c is the speed of light in vacuum. Based on this, 1550-nm provides approximately twice the photon flux of 780-nm for a given average optical power. Finally, the 1550-nm wavelength suffers of smaller dispersion into fiber when compared to that of 780-nm [61].

For all of these reasons, the 1550 nm wavelength was chosen for the research of this thesis.

1.4 Materials

1.4.1 Photoconductors at 1550 nm

As previously mentioned, 1550 nm compatible devices benefit from the huge variety and low cost of telecom components. For example, with photomixers, a wavelength difference of 8 nm is required in order to obtain a difference frequency of 1 THz. A simple CW system can consist of two distributed feedback (DFB) laser diodes that are commercially available with a tuning range of about 4.5 nm, making a frequency range of about 1.2 THz possible. For a larger tuning range, one of the DFB diodes can be replaced with an external grating tuned source. If more power is required, erbium-doped fiber amplifiers (EDFAs) can be used. All of these systems are often fiber-based (with polarization maintaining fibers), allowing simple handling and very little alignment effort (Fig. 1.5).

In contrast to the well-established 800 nm photomixers based upon GaAs, devices for 1550 nm operation based upon InGaAs suffer inherently by the roughly 2 times lower band gap than GaAs has. InGaAs has a bandgap of approximately 0.74 eV compared to the one of GaAs of around 1.42 eV. Because of this difference in the bandgaps, the breakdown field, E_B, of InGaAs is lower than that of GaAs. From semiconductor physics, the breakdown field tends to vary with band-gap energy super-linearly following the relationships $E_B\,[\mathrm{V/cm}] = 1.73 \times 10^5\,(U_G\,[e\mathit{V}])^{2.5}$ for direct bandgap material with low doping, and $E_B\,[\mathrm{V/cm}] = 2.38 \times 10^5\,(U_G\,[e\mathit{V}])^2$ for indirect bandgap materials [62]. Thus, E_B is around 4.8 x 10^5 V/cm for GaAs (U_G =1.42 eV) and around 1.3 x 10^5 V/cm for $In_{0.53}Ga_{0.47}As$ (U_G = 0.74 eV).

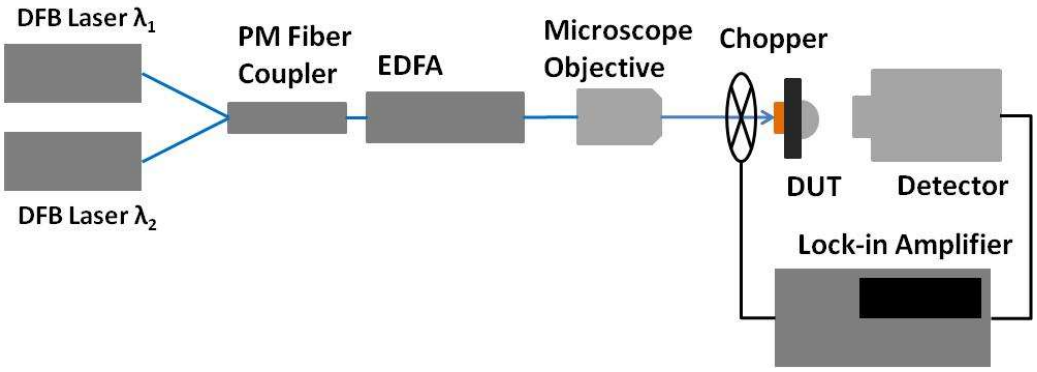

Fig. 1.5 Block diagram of a photomixing setup.

1.4.2 Device parameters

Two aspects need to be addressed in order to develop a good THz photoconductive device: the photoconductive material and the antenna design. Since the antennas were not the main focus of this work, they will not be further discussed. In this section the photoconductive material will be addressed. As previously stated, the material must present: (1) a short photo-carrier lifetime, (2) high carrier mobility, (3) high breakdown field, and (4) high dark resistance. In order to obtain (1), (3) and (4), a viable approach

is to destroy or damage the semiconductor lattice via ion implantation [63]-[64], which creates fast recombination states in the middle of the bandgap. This method, however, usually reduces the mobility (2). The low mobility does not allow transport at the saturation velocity, resulting in low photocurrents and low THz powers.

1.4.2.1 LTG InAlAs:InGaAs Devices

A photoconductor suitable for the operation at the 1.5 μm wavelength is a low temperature grown (LTG) InGaAs/InAlAs multilayer structure that is doped with beryllium [65]. When grown at temperatures below 200°C, the excess arsenic is incorporated as point defects on the Ga lattice sites (antisite defect, AsGa), forming deep donor levels in the material that lie above the middle of the bandgap close to the conduction band edge. The LTG technique helps reduce the lifetime when compared to standard temperature growth (STG) technique [66]. This is attributed to the electrons' capture by ionized arsenic antisites ($AsGa^{+}$). However, the shift of the Fermi level toward the conduction band leads to a highly conductive n-type material at room temperature. To increase the resistivity of the material, the InGaAs-layers are sandwiched between InAlAs-layers barriers (with wider bandgap making them transparent for the incident optical signal) which trap the residual carriers. Doping with beryllium further increases the resistivity.

This photoconductor was used for the first fully fiber-coupled 1550-nm pulsed THz-system by Sartorius et al. [67]. A problem with the material is the low mobility due to the high defect concentration in the material. This leads to many elastic and inelastic scattering events of the carriers with the defect sites. Another improvement can be made by growing the material while keeping the substrate temperature in the range T_S=300–500°C. By doing this it is possible to obtain InAlAs/InGaAs photoconductors with low

defect density and high mobility in InGaAs layers adjacent to InAlAs layers with high defect densities for efficient carrier trapping. With this material, THz powers up to 64 μW can be obtained [68].

1.4.2.2 Ion-Implanted Photoconductors

Another option for PC materials is InGaAs with deep traps generated by ion implantation. Ions with energies in the range of keV to MeV create defect states by kicking out atoms from the crystalline matrix or pushing atoms into interstitials. This results in reducing carrier mobility and the lifetime. The optimum dose depends strongly on the implanted ions (weight) and implantation energy. Annealing is usually required to partially restore the lattice.

Photoconductive switches with THz power of 50 μW using this kind of photoconductor were demonstrated [63]. Furthermore, the dielectric breakdown value can increase by a factor of four when compared to non-implanted samples of InGaAs [64].

1.4.2.3 Extrinsic Photoconductivity at 1550 nm of ErAs:GaAs

A promising alternative to InGaAs-based devices is to use GaAs with 1550 nm drive lasers and utilize sub-band-gap photon absorption mechanisms via the high concentration of nanoparticles-related impurity levels. As is explained in the following chapter, high erbium doping concentration generates a precipitate of ErAs nanoparticles. These ErAs nanoparticles create many energy levels near the mid-gap of GaAs allowing extrinsic 1550 nm absorption [69]. ErAs:GaAs also provides superior mobility due to the excellent lattice matching between ErAs sub-lattice and the GaAs sub-lattice. In addition, this material will benefit from the breakdown voltage of GaAs,

as high as 500 kV/cm (compared to the 200 kV/cm for $In_{0.53}Ga_{0.47}As$) [70], [71]. THz power of about 100 μW was initially demonstrated by Middendorf et al. [1].

1.5 Summary

The material chosen for this work is ErAs:GaAs and the drive wavelength is 1550 nm. The material has already been proven to possess the necessary characteristics for being a THz source. Having the advantages of a large bandgap and the ability to use the 1550-nm radiation as the driving wavelength. Using this material, efforts were aimed at pursuing more efficient, high power devices by optimizing the material characteristics (erbium concentration and thickness of the doped epitaxial layer) and antenna designs. In addition, robust and comprehensive THz characterization and power measurement methods were developed.

CHAPTER 2
The Material

2.1 Photoconductivity

The phenomenon of changing the conductivity of a material via photon absorption is called photoconductivity. When a photon with energy greater than the material bandgap is absorbed, photocarriers (electrons) are generated and the conductivity of the material increases due to its linear dependence on the carrier concentration.

In pure, undoped semiconductors, a photon with enough energy can excite an electron from the valence band to the conduction band, producing an electron-hole pair (Fig. 2.1). This process takes the name of intrinsic photoconductivity. In order for this process to happen, the photon needs to have hν greater than E_g, where E_g is the bandgap energy of the photoconductor. Light with a shorter wavelength (greater quantum energy than the bandgap) is strongly absorbed, while light with a longer wavelength is transmitted. Fig. 2.2 shows the absorption coefficients of the most common semiconductors.

In the case of extrinsic semiconductors (Fig. 2.3), the photo-carriers can be produced by either electron-hole pair generation or by photo-ionizing defect levels, where the necessary energy to ionize the defects is less than E_g. For a p-type extrinsic semiconductor, the impurity atoms create energy levels near the valence band-edge, making it possible for photons with a much lower energy of E_g to excite electrons from the valence band to an acceptor impurity level. In contrast, in an n-type

semiconductor the energy levels associated with the defects are close to the conduction band. In this case, a photon with energy lower than E_g can excite an electron from a donor level to the conduction band.

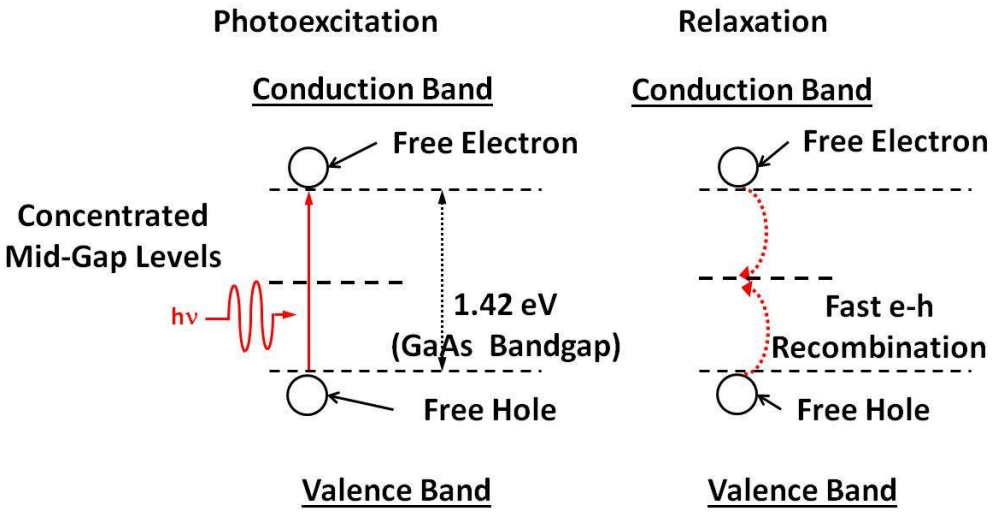

Fig. 2.1 Photo-excitation and relaxation mechanisms for intrinsic GaAs.

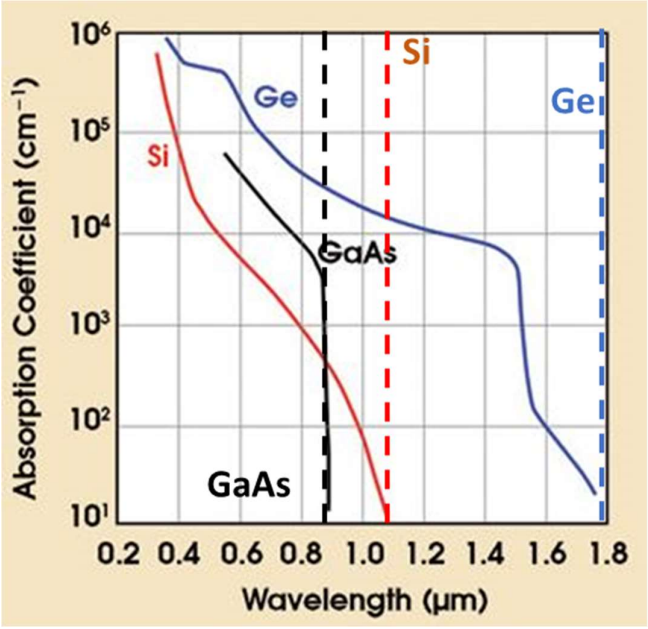

Fig. 2.2 Absorption spectra for different semiconductor materials [72].

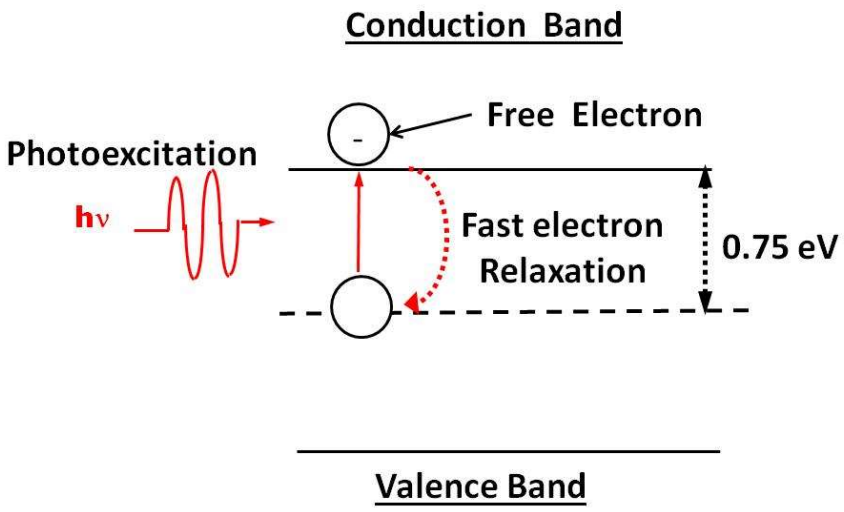

Fig. 2.3 Photo-excitation and relaxation mechanisms for extrinsic GaAs.

2.2 History of ErAs:GaAs

The material used as the photoconductor for the devices in this research was gallium arsenide heavily doped with erbium. This material was first grown by Molecular Beam Epitaxy (MBE) in 1987 with doping concentrations up to $2x10^{19}$ cm^{-3} [73]. Shortly after, a study of the growth and characterization of this material was conducted [74], [75]. In this study, a multilayered GaAs sample was grown while incorporating erbium, with the erbium cell's temperature being varied from 950°C (the layer closest to the substrate) down to 780°C (the layer closest to the surface). Table 2.1 lists the doping concentrations. It was clear that the erbium cell's temperature had an impact on changing the concentration of the erbium into GaAs. Moreover, when imaging the different layers with a Transmission Electron Microscope (TEM), the three most heavily erbium doped layers (close to surface) were revealed to be inhomogeneous and contained a high density of small nanoparticles (Fig. 2.4), of which the concentration increased with the erbium doping level.

A second a sample was grown in order to study the effect of the substrate temperature while keeping the erbium cell's temperature constant. Table 2.2 lists the erbium doping concentrations.

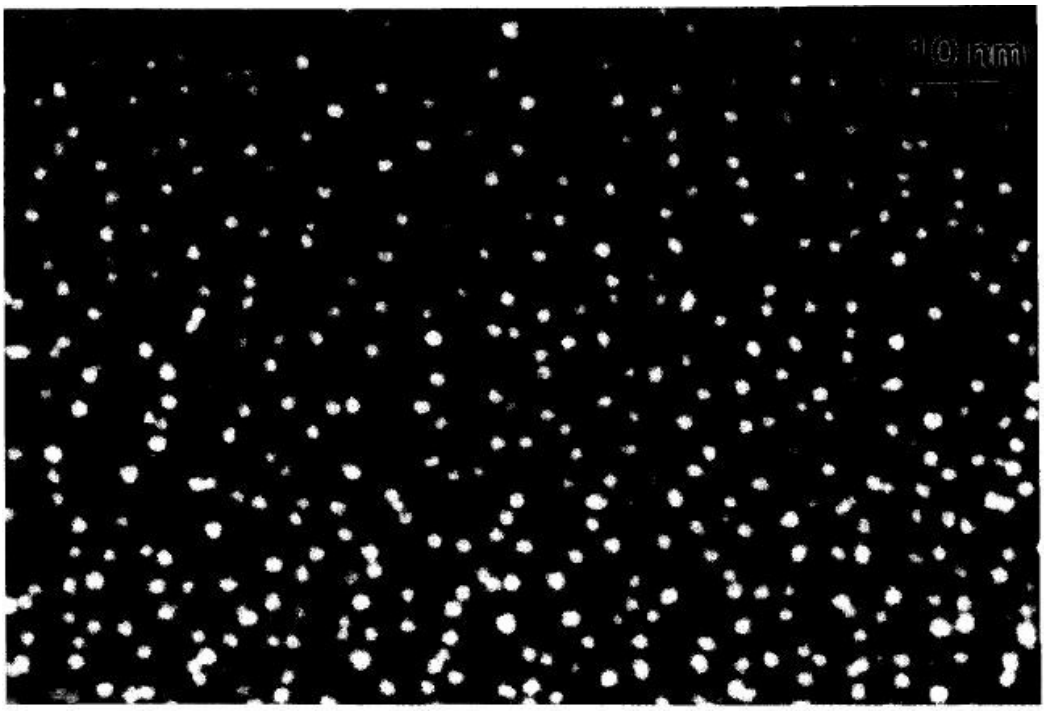

Fig. 2.4 Dark-field (002) beam image of the highest erbium-doped layer in the first sample. The precipitates are clearly visible under these conditions [74].

A direct relationship between of the diameter of these spherical particles and the substrate temperature was found, meaning that as the temperature increased so did the diameter. These results are shown in Table 2.2. The same test was done on the first sample with results listed in Table 2.1. In this case, while the diameter remained fairly constant, the concentration of the precipitate increased with the increasing erbium flux, as shown in Fig. 2.5.

Table 2.1 Variation in particle size with substrate temperature, T_{sub}, fixed and different erbium flux of the erbium-doped layers of the first sample [74].

Erbium concentration (cm^{-3})	T_{sub} during growth (°C)	Growth plus "anneal" time (min)	Precipitate diameter (Å)
2.0×10^{20}	580	270-300	17
4.3×10^{19}	580	210-240	16
2.1×10^{19}	580	150-180	16
3.2×10^{18}	580	90-120	14
1.2×10^{18}	580	30-60	14

Table 2.2 Variation in particle size with substrate temperature, T_{sub}, of the erbium-doped layers of the second sample [74].

Erbium concentration (cm^{-3})	T_{sub} during growth (°C)	Growth plus "anneal" time (min)	Precipitate diameter (Å)
3.6×10^{19}	540	330	11
3.6×10^{19}	560	270	14
3.6×10^{19}	580	210	16
3.6×10^{19}	600	150	21
3.6×10^{19}	620	60	65

A doping concentration of 7×10^{17} cm^{-3} was found to be critical. Above this concentration, the erbium did not incorporate as a substitutional defect, but generated ErAs nanoparticles. The surface morphology was then found to be quickly deteriorating above an erbium concentration of around10^{18} cm^{-3} [74]. In 1993, the dependence of the free-carrier lifetime on the erbium doping concentration in GaAs:Er was studied [76], with the lifetime decreasing smoothly as the doping increases. A carrier lifetime of

approximately 1 ps was obtained with an erbium doping of 5 x 10^{19} cm^{-3} as shown in Fig. 2.6.

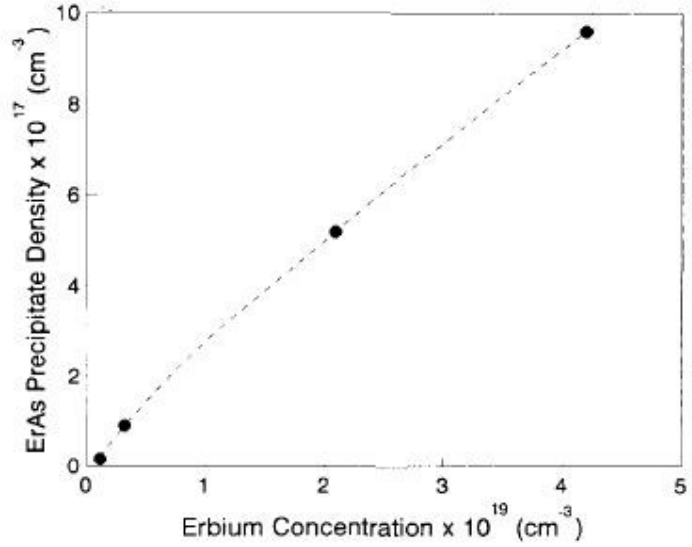

Fig. 2.5 A plot of precipitate density against total erbium concentration [74].

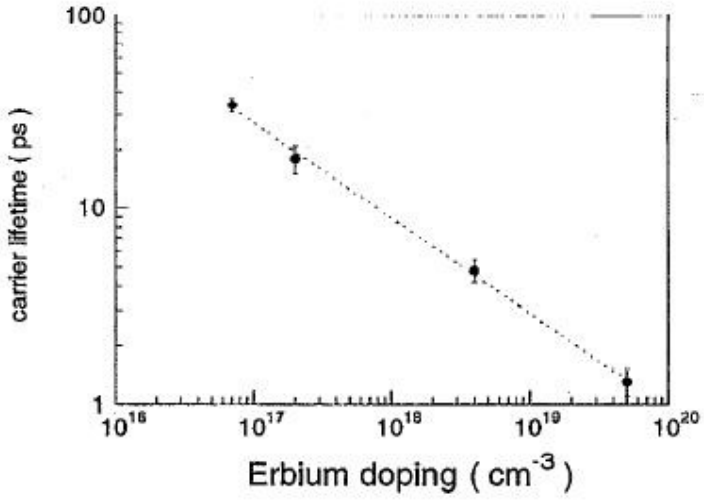

Fig. 2.6 Dependence of the carrier lifetime on the erbium-doping concentration in the MBE grown GaAs:Er epilayers [76].

All these studies lead to the conclusion that higher growth temperature leads to larger nanoparticles, and that higher ErAs concentration results in a higher density of the nanoparticles. Moreover, the growing conditions were found to cause the ErAs

nanoparticles to be arranged in layers with super-lattice of period L which affected the carrier lifetime as shown in Fig. 2.7.

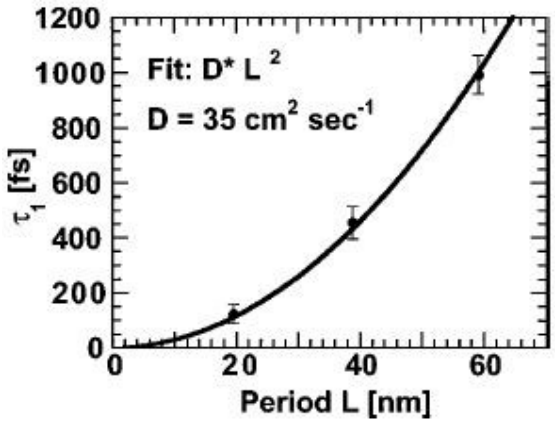

Fig. 2.7 The time constant τ_1 of the transient decay as a function of the super-lattice period L.

It was not until the early 2000s that this material was first tested as a THz PC source. In 2004, a photomixer device was fabricated on ErAs:GaAs [70] with a maximum peak power of approximately 12 μW at 88 GHz and generating 1 μW at 1 THz. Then in 2006, the first photoconductive switch on ErAs: GaAs was demonstrated [77], with an average power of 44 μW. These devices were driven by 780-nm laser sources, not 1550-nm, using the intrinsic photoconductivity process. The first device based on the extrinsic photoconductivity of ErAs:GaAs driven at 1550 nm wavelength was a photoconductive switch antenna that was reported in 2012 [1] with an average output power of 105 μW and an optical-to-THz power efficiency of 0.075%, compared to 75 mW and 0.375% optical-to-THz power efficiency for iron-doped InGaAs [78]. The first ErAs:GaAs photomixer driven at 1550 nm was demonstrated only in 2015 [2] with THz power of 40 nW at 150 GHz.

2.3 Summary

The material of interest, erbium doped gallium arsenide, has been proven to have the necessary characteristics to be used for THz generation. The ErAs nanoparticles can be engineered in order to vary their sizes and density by adjusting the doping density and the growth temperature. However, no study has been done on how the different doping and different nanoparticles size and density affect the THz emission performance of devices based upon this material.

CHAPTER 3
Material characterization

The ErAs:GaAs was grown at the National Institute of Standards and Technologies (NIST), Boulder, CO by Dr. Richard Mirin, Dr. Ari Feldman and Dr. T. Harvey. For each sample, the epitaxial layer was grown on a 3-inch semi-insulating GaAs substrate by Molecular Beam Epitaxy (MBE). The growths were performed at 600°C, with simultaneous deposition of Gallium, Arsenide and Erbium atoms. The GaAs growth rate was about 0.65 mono-layers per second with the Erbium flux being previously calibrated using secondary ion mass spectroscopy (SIMS) on a separate sample.

In 2011, a model for the extrinsic photoconductivity of these materials was theorized by Kawasaki et al. [79] and it is shown in Fig. 3.1. The model represents the ErAs nanoparticle with energy levels determined by quantum confinement of ErAs free electrons within the GaAs barriers [69], [79]. There are only two bound states on each nanoparticle, one corresponding to the Γ-point cell-periodic wave-function in ErAs, and the other to the X point wave-function [69]. The energy levels in Fig. 3.1 depend on both the extent to which the Fermi level in the ErAs pins at the mid-gap level of the GaAs [79] as well as on the size of the nanoparticles (Fig. 3.2). Most importantly, the model shows that a Γ-point bound electron can readily make a bound-to-continuum transition to the Γ-valley of the surrounding GaAs when excited

by a 1550-nm photon. Once excited to the GaAs Γ-valley, the photoconductance is made strong by the high mobility (>1000 cm^2/V-s) of electrons there.

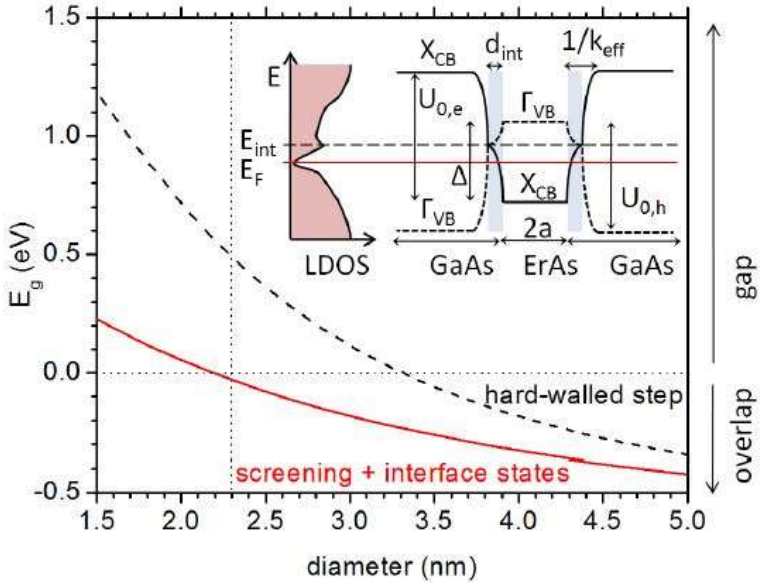

Fig. 3.1 Calculated energy gap versus ErAs particle diameter. Insert shows schematic of the modified confinement potential model [79].

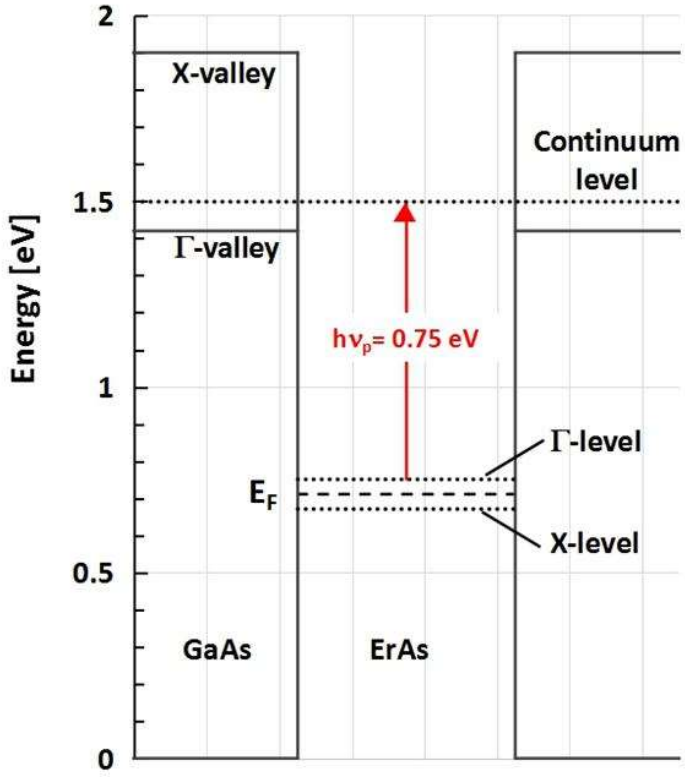

Fig. 3.2 Energy-level model for crystalline ErAs nanoparticles embedded in GaAs [80].

Following this model, the erbium concentration and the epilayer thickness were chosen as a variable parameter in order to optimize the material and increase its 1550-nm absorption and THz generation. The erbium concentration has been varied from 2.2 x 10^{20} cm^{-3} to 8.8 x 10^{20} cm^{-3} while the epilayer thickness was varied between 1 μm and 2 μm. Table 3.1 lists the samples under test.

Table 3.1 List of the substrates used in this work. Details of Erbium doping and epilayer thickness.

	Er doping [cm^{-3}]	Thickness [nm]
ASP174	4.4 x 10^{20}	1.00
ASP180	8.8 x 10^{20}	1.00
ASP194	8.8 x 10^{20}	2.00
ASP280	4.4 x 10^{20}	1.00
ASP294	8.8 x 10^{20}	1.00
ASP328	8.8 x 10^{20}	2.00
ASP365	2.2 x 10^{20}	2.00
ASP372	4.4 x 10^{20}	2.00

All the materials have been tested optically and electrically with microscopy, IR absorption, and Hall characterization. The results are presented in the following section.

3.1 Transmission Electron Microscopy and Scanning Electron Microscopy

The first characterization of the ErAs:GaAs epitaxial layers was done by cross-sectional TEM in order to identify the nanoparticles when the erbium doping density is high. However, because this technique is expensive, only a few samples were imaged.

The dark-field TEM images of ASP174 and ASP180 in the (110) plane are shown in Fig. 3.3 (a) and (b), respectively. ASP174 displays light-tone disks consistent with the fact that Er is much heavier than Ga as well as with the presence of the spherical ErAs nanoparticles. In ASP180, the disks are significantly larger but much less

concentrated. Histograms were then generated for both samples using an object-recognition software [81] and are shown in Fig. 3.3. For ASP174 there is a prevalence of nanoparticles in the 1.0 - 1.5 nm diameter range; while for ASP180, the nanoparticles are mostly in the 2.2 - 2.7 nm diameter range. The most likely diameter is 1.2 nm for ASP174 and 2.5 nm for ASP180, respectively. The nanoparticle densities were then estimated to be 2.2 x 10^{19} cm^{-3} and 4.8 x 10^{18} cm^{-3}, respectively [82]. Both diameters are consistent with those of Ref. [69] where a typical nanoparticle diameter of ≈2.0 nm was obtained for a 600 °C growth and 3.3% ErAs fraction.

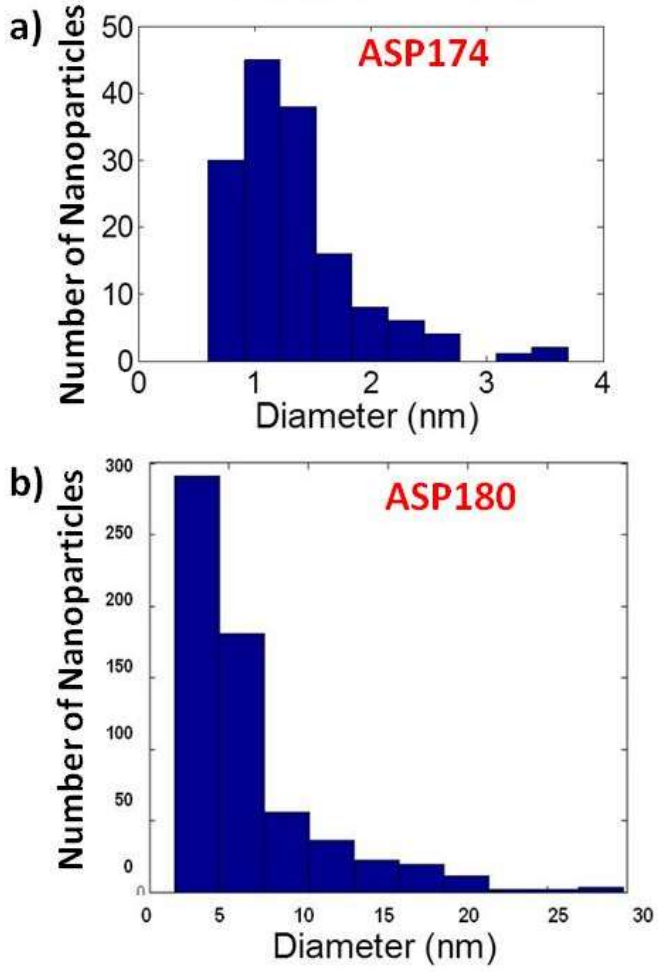

Fig. 3.3 Histograms of the diameter of the nanoparticles for a) ASP174 and b) ASP180.

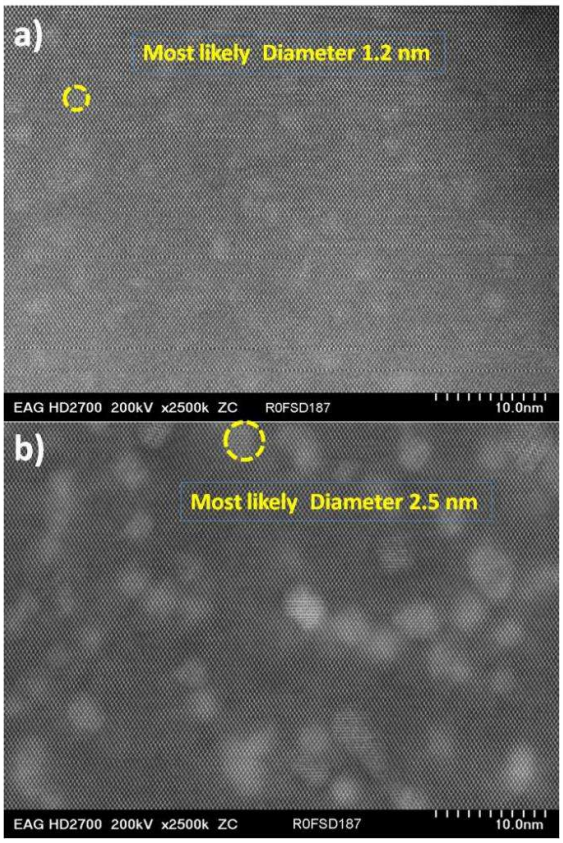

Fig. 3.4 Dark-field cross-sectional TEM for ASP174 (a) and ASP180 (b) in the (100) plane of the GaAs.

The model shown in Fig. 3.1-2 was then applied to the nanoparticles size of obtained by cross-sectional TEM. A gap of 0.86 eV and 0.75 eV between the mid-bandgap and the conduction band of the GaAs was obtained for ASP174 and ASP180, respectively.

A key insight that can also be drawn from these TEM images is the near absence of defects other than the ErAs nanoparticles. This can be attributed to the good lattice matching between the ErAs and the GaAs sub-lattices. ErAs and GaAs have in fact lattice constants within 1.5% of each other. As a result, Er atoms will almost exclusively arrange as homogenous substitution defects while causing very little strain in the crystal lattice.

A tabletop Phenom Pro SEM [83] was also used to check for surface degradation. The SEM allows for the resolution of features down to the micron scale level when imaging non-electrically conducting materials, which is the case for the ErAs:GaAs

samples. Both ASP174 and ASP180 display uniform, smooth epi-layer surfaces, and for this reason they are not displayed here. In contrast ASP280, a replica of ASP174, shows some degree of surface roughness on the epi-layer surface (Fig. 3.5). The most recent samples, ASP328 ASP365 and ASP372, show an even greater, more severe and structured surface roughness, as exhibited in Fig. 3.6, Fig. 3.7 and Fig. 3.8 respectively.

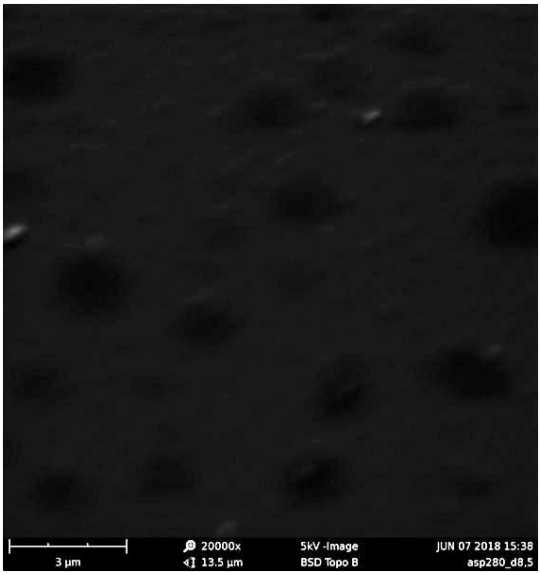

Fig. 3.5 SEM image of the surface of ASP280.

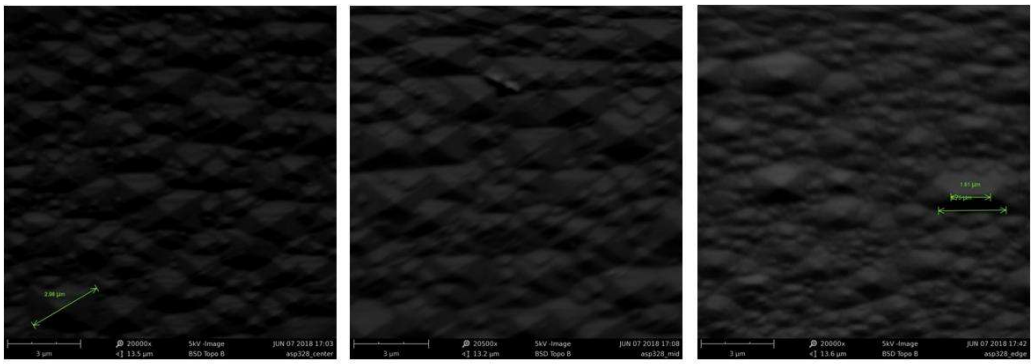

Fig. 3.6 SEM images of the surface of ASP328.

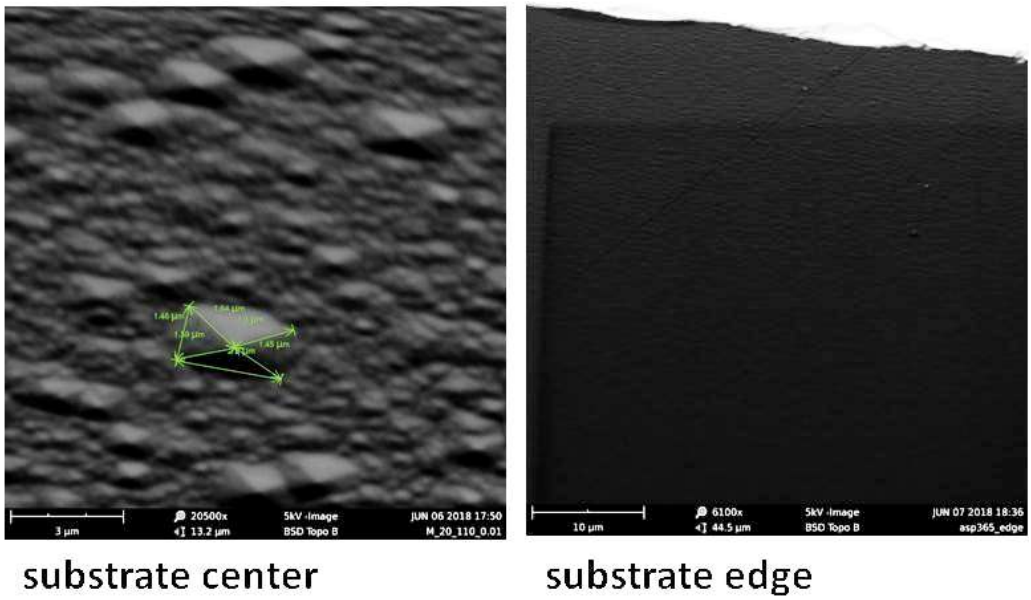

Fig. 3.7 SEM images of the surface of ASP365.

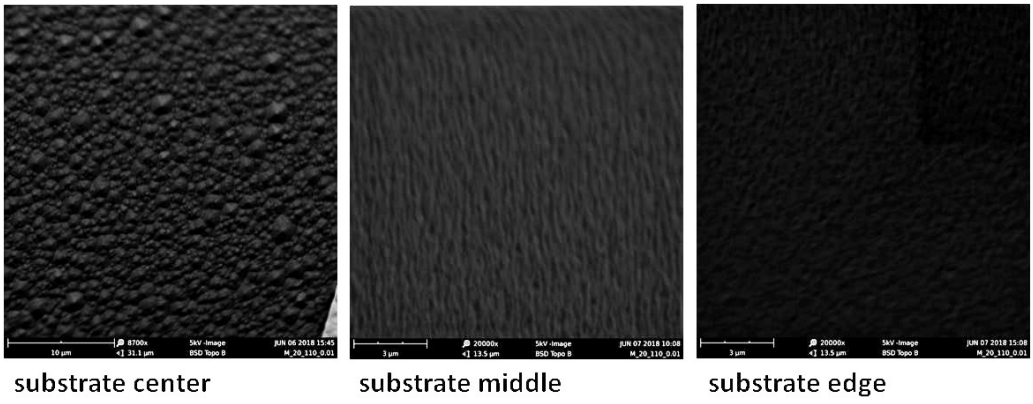

Fig. 3.8 SEM images of the surface of ASP378.

Rigorous studies of the material composition and the crystalline structure have not been carried out. It is possible, however, to speculate that the change in the surface morphology could have been caused by a bad calibration of the growth parameters. In support of this theory, it was found that during the growths of the samples ASP328, ASP365 and ASP372, the As cell was depleted, leading to poor growth conditions of the GaAs matrix in these epi-layers [84].

3.2 Infrared (IR) Measurements

The samples were then characterized for IR absorption spectrum T(λ). For these measurements, two different spectrometers were used. The first is a fiber-coupled grating spectrometer with a step-limited resolution of 1.25 nm and best performance from 900 to 1600 nm. The source was a deuterium lamp, while the detector was a DWARF-Star [85], a NIR high-performance InGaAs detector array (Fig. 3.9 a) shows the schematic and b) the setup). The second spectrometer was a free-space-coupled grating spectrometer having step-limited resolution of 10 nm with best performances from 1400 to 4900 nm. The setup of the monochromator (shown in Fig. 3.10 b)) consists of a silicon carbide filament broad-band source (mimicking black-body radiation), a Cornerstone™ 260 1/4 m VIS-NIR monochromator [86] and a cross-calibrated LiTaO3 pyroelectric detector. All the spectra were normalized to the transmittance of a SI GaAs substrate, identical to those used for the epitaxial growths, and polished on both sides.

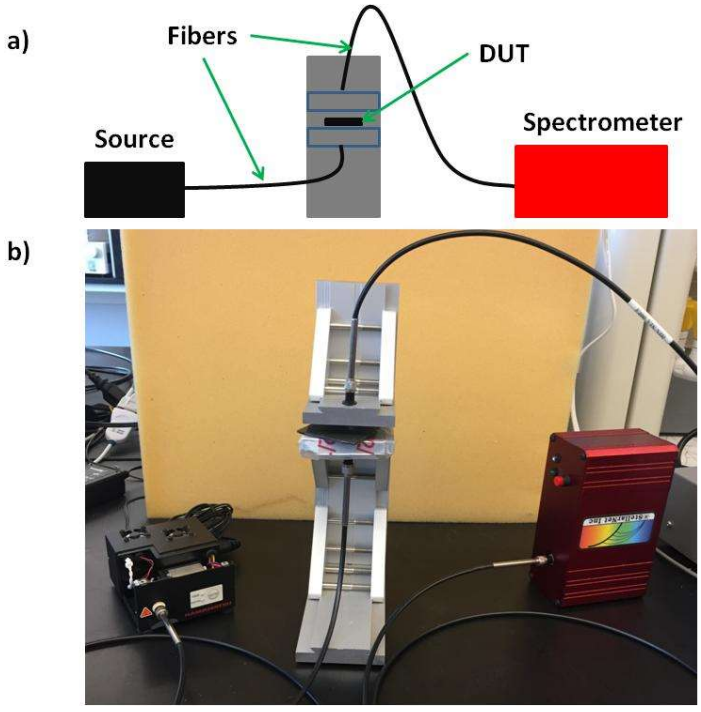

Fig. 3.9 a) schematic configuration of the setup, b) picture of the setup.

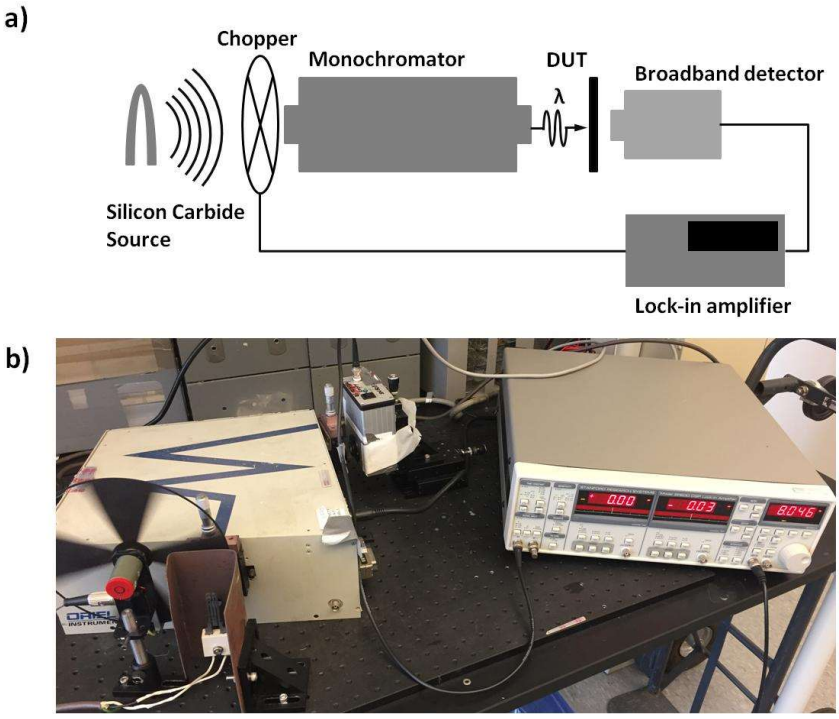

Fig. 3.10 a) schematic of the setup, b) image of the setup.

For each spectrum, two measurements were conducted: background (Si-GaAs) and sample. From the ratio of the sample to the background spectra T(λ), the attenuation coefficient and absorbance spectra were calculated. The governing equation is Beer's law:

$$\alpha(\lambda) = \frac{-\ln\left[T(\lambda)\right]}{t}, \quad A = -\ln\left[T(\lambda)\right] \tag{3.1}$$

where t is the thickness of the epitaxial layer. For all the samples, an area roughly half-way between the center and edge of the 3-inch wafer was selected in order to avoid the regions where the concentration of the doping was intrinsically low (edge of the wafer) or high (center of the wafer).

Fig. 3.11 shows the absorption spectrum of a GaAs sample with a concentration of erbium of 3.0 x 10^{18} cm^{-3} and an epitaxial layer 1.25 μm thick, ASP032. Although the erbium concentration for this material is above the solubility limit of 7 x 10^{17} cm^{-3} [74],

it does not show any absorption around the wavelength of interest, 1550 nm. With the only effect being the generation of a broad absorption tail near the band-edge. Based on this fact, it is clear that erbium doping by itself does not contribute to any resonant 1550 nm absorption, and instead it just generates a broad absorption tail. For the erbium to cause strong absorption around the 1550 nm, it needs to be incorporated as an array of ErAs nanoparticles with proper sizes in order to provide energy levels around the middle of the bandgap of GaAs. Due to these levels, less photon energy is needed to excite a carrier from these levels to the conduction band when compared to cross-gap photoconductivity, making ErAs:GaAs a material suitable for the 1550-nm optical excitation through extrinsic photoconductivity.

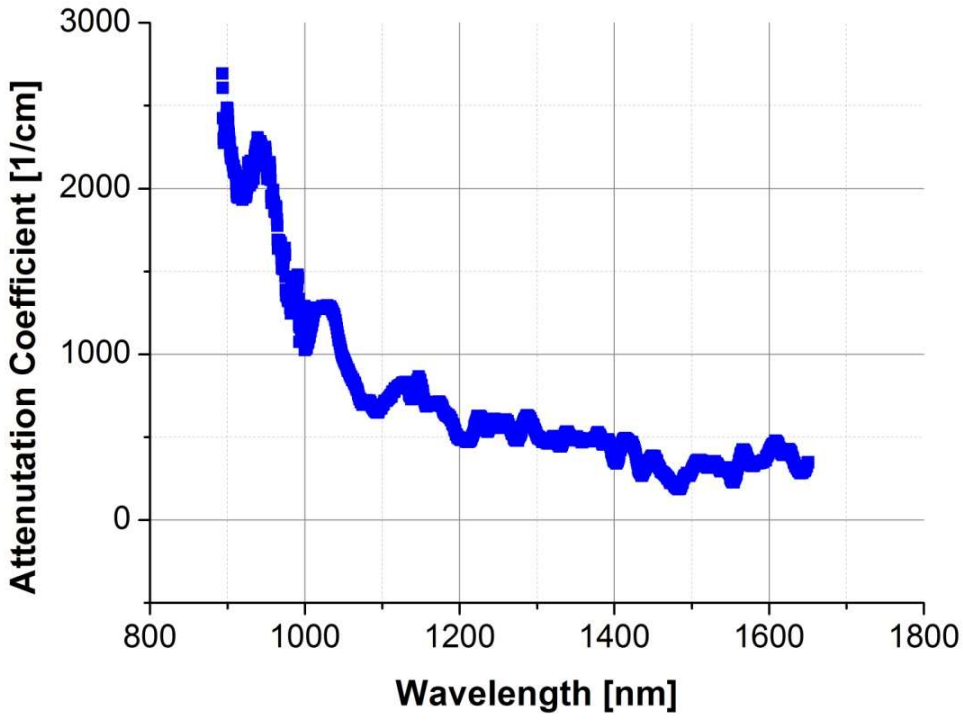

Fig. 3.11 Attenuation spectrum of ASP032, 1.25 µm thick epilayer doped at $3.0x10^{18}$ cm^{-3} grown on Semi Insulated GaAs.

Fig. 3.12 shows the spectra of ASP174 and ASP180 with erbium doping concentration of 4.4 x 10^{20} cm^{-3} and 8.8 x 10^{20} cm^{-3}, respectively, both with a 1 μm epitaxial layer thickness. Resonant absorptions occur centered around 1620 nm and 1560 nm respectively, with absorption coefficients as high as 7750 cm^{-1} and 9800 cm^{-1} [87], respectively. These values are comparable to 850-nm cross-gap absorption for GaAs (approximately 15-20000 cm^{-1}). This is in accordance to the prediction of the model of Fig. 3.1, which places the mid-bandgap energy levels of ASP180 closer to the conduction band when compared to those of ASP174. A subsequent experiment was carried out in order to make sure that the IR attenuations were in fact absorption spectra. For this reason, responsivity measurements as a function of the driving wavelength were carried out. The high responsivity shown in Fig. 3.13 proves the strong absorption of these materials.

Fig. 3.14 shows the absorption spectra for ASP280 and ASP294, replicas of ASP174 and ASP280 respectively. The peaks for these two substrates are at 1480 nm, with an absorption coefficient of 7600 cm^{-1}, and at 1570 nm, with an absorption coefficient of 8600 cm^{-1}, respectively. From both Fig. 3.12 and Fig. 3.14, it can be deduced that a higher erbium concentration in the epi-layer increases the resonant absorption of the material around 1550 nm. It is thus possible to grow materials with high doping concentration and strong absorption, without generating “unwanted” defects, as shown in the previous paragraph on TEM imaging.

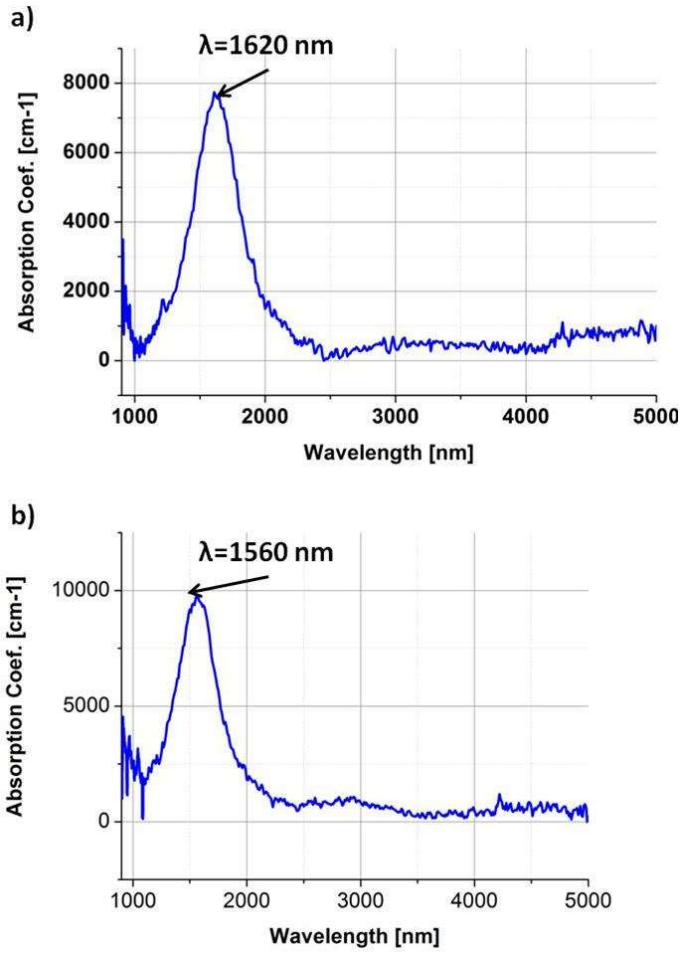

Fig. 3.12 Infrared absorption spectra of a 1 µm epitaxial layer of GaAs doped with a concentration of Erbium of: a) $4.4x10^{20}$ cm^{-3} for ASP174 and b) $8.8x10^{20}$ cm^{-3} for ASP180.

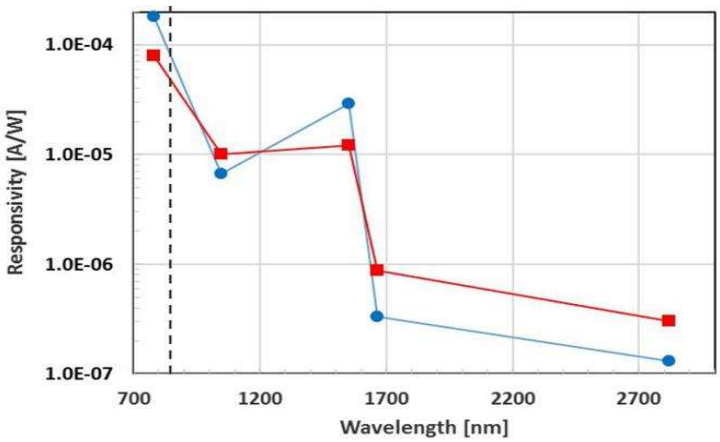

Fig. 3.13 Responsivity vs wavelength for ASP174 (dotted blue) and ASP180 (squared red).

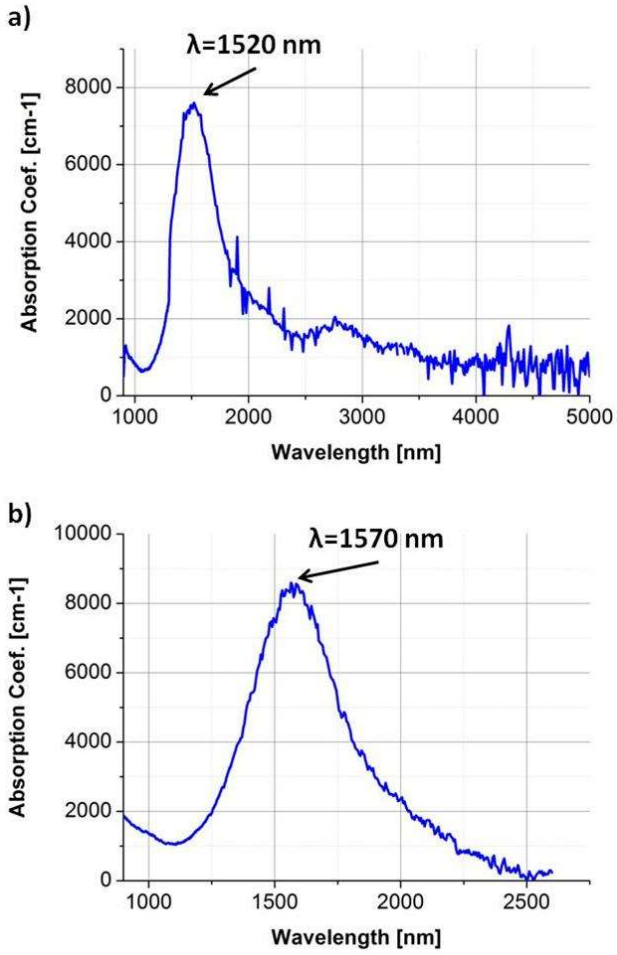

Fig. 3.14 Infrared attenuation spectra of a 1 µm epitaxial layer of GaAs doped with a concentration of Erbium of: a) 4.4x10^{20} cm^{-3} for ASP280 and b) 8.8x10^{20} cm^{-3} for ASP294.

After varying to the doping concentration and while keeping the epi-layer constant (1 µm), an attempt to increase the absorbance at 1550 nm was made by increasing the thickness of the epitaxial layer from 1 µm to 2 µm. Fig. 3.15 shows a comparison between ASP180 and ASP194, both with an erbium doping of 8.8 x 10^{20} cm^{-3}, but with an epi-layer thickness of 1 µm and 2 µm respectively.

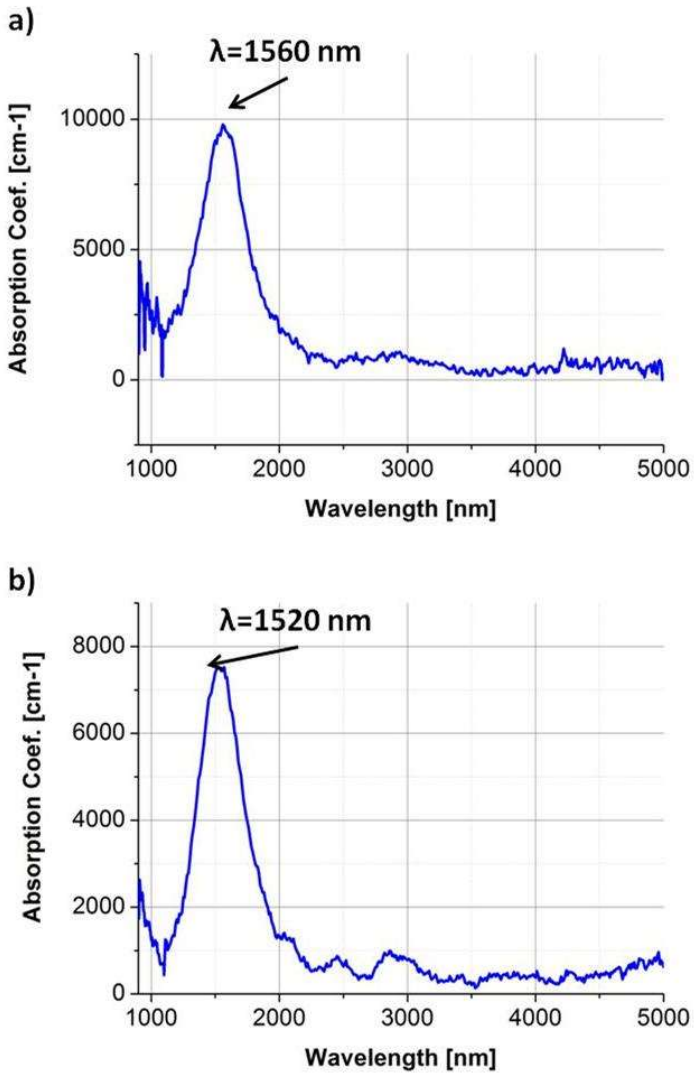

Fig. 3.15 Infrared attenuation spectra of GaAs doped with a concentration of Erbium of 8.8x10^{20} cm^{-3} and an epitaxial layer of: a) 1 µm for ASP180 and b) 2 µm for ASP194.

The increase in the thickness leads to a slight reduction of the absorption coefficient peak, from 9800 cm^{-1} to 7500 cm^{-1}, a 23.5% decrease. Further, the dependence of the doping was studied with the growth of samples ASP328 (a replica of ASP194), ASP365 and ASP372, with corresponding erbium doping concentrations of 8.8 x 10^{20} cm^{-3}, 2.2 x 10^{20} cm^{-3} and 4.4 x 10^{20} cm^{-3}, respectively, all with a 2 µm epitaxial layer thickness. These materials displayed absorption resonances with peak values of 3500 cm^{-1}, 2450 cm^{-1} and 2900 cm^{-1}, respectively (Fig. 3.16). The reason of the low absorption is still unclear. Additionally, these peak values occurred at wavelengths of 2070, 1690 and

1680 nm, much longer than the desired 1550. In comparison to the previous samples, it is also interesting to note the shift of peak absorption. For example, in ASP328 the peak shifted to around 2070 nm, compared to that at 1570 nm of ASP194, despite the fact that both samples had the same Er doping density. The likely reason could be the different shape of the ErAs nanoparticles which is something that has already been reported [88] where oblate-ellipsoid nanoparticles (compared to spherical nanoparticles of ASP194) generated an absorption peak around 2.5 μm.

The outcome from these IR attenuation measurements is that a higher Er doping, well above the solubility limit of erbium into GaAs, can result in an excellent resonance absorption coefficient near 1550 nm. This is due to the proper sizes of ErAs nanoparticles that create energy levels in the middle of the GaAs bandgap [74], [79]. However, the growth conditions can shift the resonant peak to >2.0 μm. Table 3.2 summarizes the results of the IR transmission measurements.

Table 3.2 List of the IR transmission measurements of the different samples.

	Peak attenuation wavelength [nm]	**Peak attenuation [cm^{-1}]**	**Erbium doping concentration [cm^{-3}]**
ASP174	1450	6000	4.4×10^{20}
ASP180	1660	9700	8.8×10^{20}
ASP194	1590	7500	8.8×10^{20}
ASP280	1520	5700	4.4×10^{20}
ASP294	1530	8000	8.8×10^{20}
ASP328	2070	3500	8.8×10^{20}
ASP365	1700	1850	2.2×10^{20}
ASP372	1660	2200	4.4×10^{20}

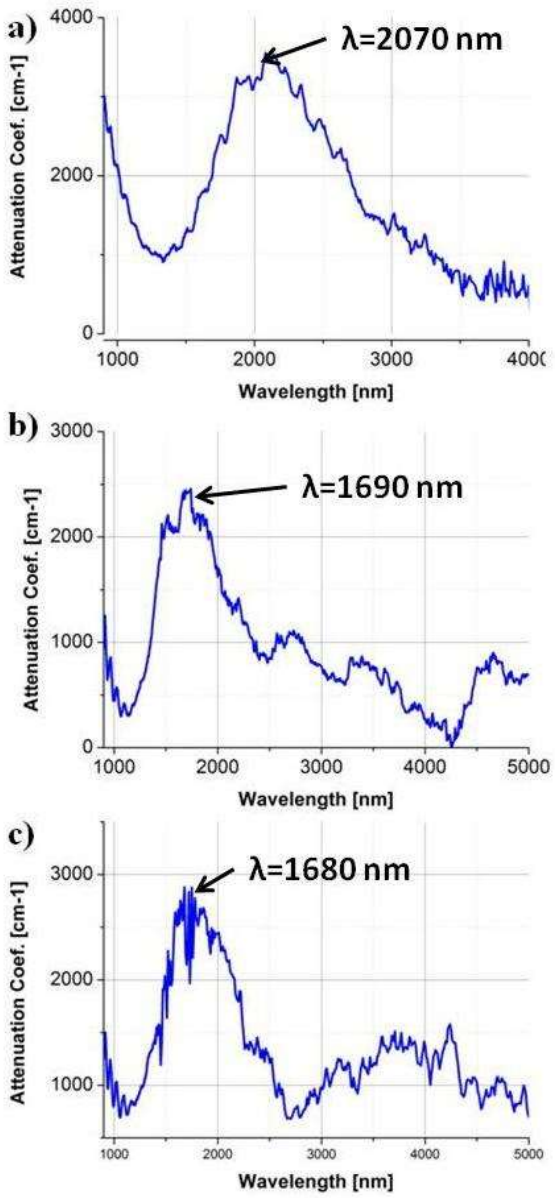

Fig. 3.16 Infrared attenuation spectra of a 2 µm epitaxial layer of GaAs doped with a concentration of Erbium of: a) $8.8x10^{20}$ cm^{-3} for ASP328, b) $2.2x10^{20}$ cm^{-3} for ASP365 and c) $4.4x10^{20}$ cm^{-3} for ASP372.

3.3 Hall measurements

The next experiment that was carried out was the ambient Hall and 1550-nm photo-Hall measurements on van der Pauw structures [89]. Each sample had four small ohmic contacts (AuGe) alloyed at 465 °C for 30 seconds and located on opposite corners of a 5 x 5 mm square chip. The opposite contacts were connected pair-wise to a Keithley

6514 electrometer-grade solid-state source meter. The light source for the photo-Hall was a ThorLabs LPSC-1550-FC 1550-nm diode laser with an on-axis intensity of approximately 2.5 mW/cm^2, high enough to create reliable photo-modulated Hall voltages. Due to the difficulties in obtaining reliable Hall measurements on such high-resistivity samples, only two materials were tested to obtain qualitative information regarding carriers' mobilities and concentrations. In order to obtain more reliable data, three separate van-der-Pauw structures were fabricated on ASP174 and ASP180.

Both the Hall and photo-Hall voltages for all structures, including the one for the control sample with a doping of 3 x 10^{18} cm^{-3}, clearly displayed an n-type polarity, meaning that both the "dark" free carriers and the photocarriers are electrons. The Hall measurements also yield two other important metrics for device performance: the free-carrier concentration and the free-carrier Hall mobility. These are listed in Table 3.3 where the values for ASP174 and ASP180 are averages over three structures (+/- standard deviation). Both the dark- (1.96 x 10^3 cm^2/V-s) and photo-mobility (4.85 x 10^3 cm^2/V-s) of the control sample are comparable to what one would expect for any GaAs sample with free-carrier density of about 3 x 10^{18} cm^{-3} (i. e., 2 x 10^3 cm^2/V-s) [90]. It can be noted that for the control sample the photo-mobility is larger than the dark-mobility, yet the reason is unknown. Interestingly the corresponding mobilities of ASP174 (4.42 x 10^3 and 2.57 x 10^3 cm^2/V-s) remain surprisingly high given the large Er doping concentration of 4 x 10^{20} cm^{-3}. Then for ASP180, where the Er doping is increased another factor of two, both the dark- and photo-Hall mobility drop significantly to values of 2.3 x 10^3 and 0.65 x 10^3 cm^2/V·s, respectively.

Table 3.3 also lists the Hall-derived dark electron density, n. Here it can be seen the trend from n = 9.4 x 10^{10} cm^{-3} for the control sample (ASP032) to 0.7 x 10^{10} cm^{-3} for ASP174, and then a big jump to 53 x 10^{10} cm^{-3} in ASP180. Assuming the transport is

dominated by conduction-band electrons, this can be converted to a bulk Fermi level using the well-known expression

$$n = N_C e^{\left[\frac{(U_C - U_F)}{k_B T}\right]} \tag{3.2}$$

where N_c is the conduction-band effective density-of-states (4.7 x 10^{17} cm^{-3}) in GaAs, and U_C is the conduction band reference energy. As displayed in Table 3.3, the Fermi level between the control sample and ASP174 is decreasing relative to the GaAs conduction-band edge as the Er doping concentration is increased. However, it then increases dramatically between ASP174 and ASP180. Apparently, the effect of the ErAs nanoparticles on ASP174 is to pull the Fermi level down toward the middle of the GaAs bandgap, which is generally accepted for metallic nanoparticles in GaAs, such as As precipitates in low-temperature-grown GaAs. The surprise here is the strong increase in dark free electron concentration with Er, which counters the decrease in Hall mobility such that the dark resistivity $(ne\mu)^{-1}$ of ASP180 is just ≈3x lower than that of ASP174. Interestingly, the 1.2-2.5 nm range spanned by the two samples overlaps the 2.3 nm typical-particle samples studied by XSTM experiments [79].

Table 3.3 Summary of dark- and photo-Hall data on samples ASP174 and ASP180.

Sample	Control	ASP174	ASP180
Er Doping [x10^{18} cm^{-3}]	2.8	440	880
Epilayer Thickness [μm]	1.25	1	1
Most Likely Nanoparticle Diam [nm]	NA	1.2	2.5
Nanoparticle Concentration [cm^{-3}]	NA	2.2x10^{19}	4.8x10^{18}
Distance Between Nanoparticle [nm]	NA	2.4	3.4
Dark and Photocarrier Hall Polarity	n	n	N
Dark Bulk Resistivity [x10^{4} Ohm-cm]	3.41	19.5 ± 1.15	6.8 ± 3.3
Dark Free Carrier Density [x10^{10} cm^{-3}]	9.4	0.74 ± 0.13	53 ± 29
Fermi Energy for U_C=0 [eV]	-0.40	-0.46	-0.35
Dark Hall Mobility [x10^{3} cm^2/V*s]	1.96	4.42 ± 0.57	2.35 ± 1.8
Photo Hall Mobility [x10^{3} cm^2/Vs]	4.85	2.57 ± 0.53	0.65 ± 0.38

3.4 Pump-probe measurements

Pump probe photo-transmission was used to study ultrafast electronic dynamics. In this technique, an ultrashort 1550-nm laser pulse is split into two portions; a stronger beam (pump) is used to excite the sample, generating a non-equilibrium state, and a weaker beam (probe) is used to monitor the pump-induced changes in the optical transmission of the sample. The free carrier concentration (and its variation) inside the material are expected to create a variation of the material optical absorption coefficient [91]. This implies that a variation of transmittance can be detected and observed when sub-band-gap radiation excites the material. The generation of the excess free carriers is done by illuminating the sample with a 1550-nm laser pulse, whose photons energy is high enough to excite carriers from the mid bandgap levels to conduction band. By measuring the changes in the transmission as a function of time delay between the arrival of pump and probe pulses, it is possible to collect information about the relaxation of free electrons states in the sample.

Fig. 3.17 shows the block diagram of the pump probe setup used.

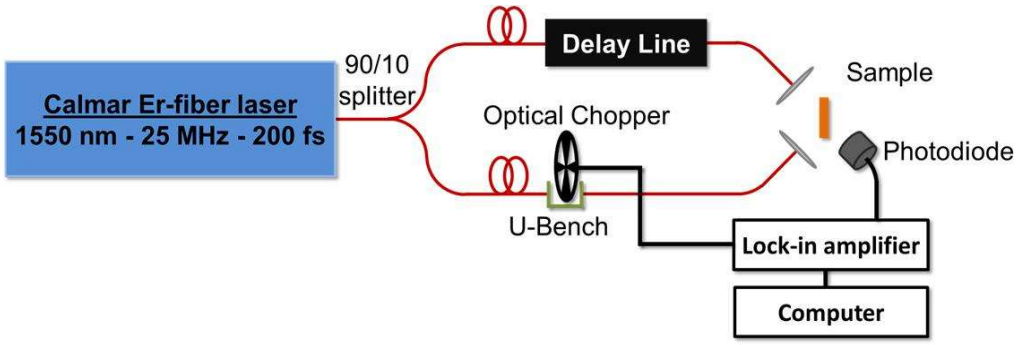

Fig. 3.17 Pump-probe setup, block diagram.

A Calmar Er-fiber 1550 nm laser pulsed source with a 200 fs pulse-width and 25 MHz repetition rate frequency was used to generate both the pump and probe beams. The arrival time of the probe beam was delayed using a delay line. A SM05PD5A - mounted

InGaAs photodiode, capable of detection in the range of 800-1700 nm was used as detector. The results obtained on ASP174 and ASP180 are shown in Fig. 3.18 [92].

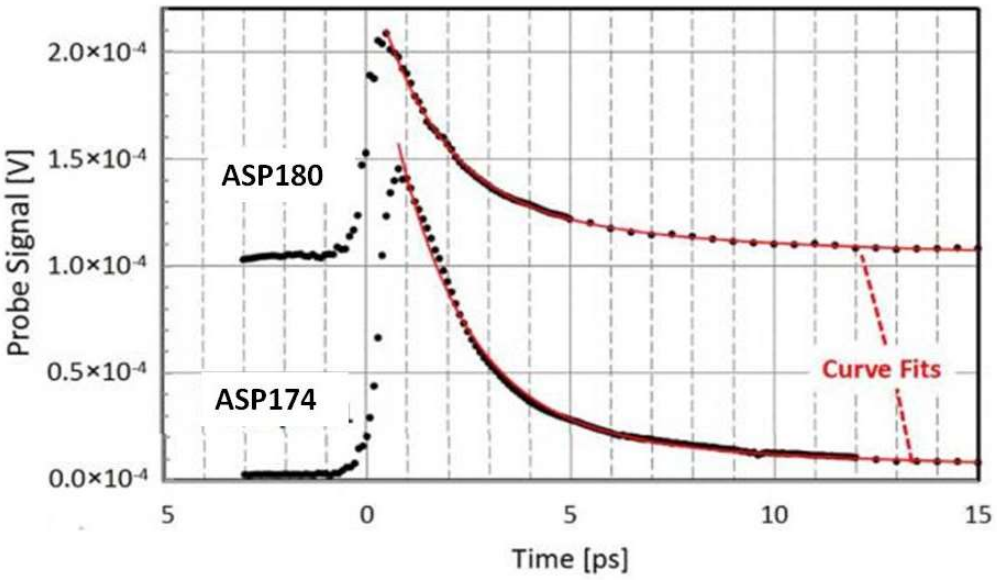

Fig. 3.18 Lifetime measurements done on ASP174 (Sample #1) and ASP180 (Sample #2) [92].

The measured data of both samples displays a positive-going signature, which was expected for ultrafast photoconductivity. The curve is well fit with a double exponential:

$$Y(t) = Ae^{\left(-t/\tau_1\right)} + Be^{\left(-t/\tau_2\right)} \tag{3.3}$$

For ASP174, τ_1 = 1.7 ps, τ_2 = 10.5 ps, A = 2.1 x 10^{-4} V, and B = 2.1 x 10^{-5} V. For ASP180, τ_1 = 1.6 ps, τ_1 = 7.3 ps, A = 1.1 x 10^{-4} V, and B = 2.5 x 10^{-5} V [87]. In both cases, A $\gg$ B so the fast exponential term dominates, which bodes well for terahertz performance. These results are in accordance with the plot of Fig. 2.6 and are suggesting (based on Fig. 2.7) a super-lattice period >60 nm. The control sample (ASP032) was also tested for ultrafast photo-transmission but did not show any significant effect.

3.5 Summary

It is possible to grow very high-quality GaAs:Er material, with very few defects, despite the very high concentration of erbium and formation of ErAs nanoparticles. These materials also proved to have very desirable electrical properties like high electron mobility and high dark bulk resistivity, as proven by Hall measurements. By adjusting the doping concentration and the thickness of the epitaxial layer, the 1550-nm absorption was improved. Pump-probe measurements also proved the lifetime of these samples to be in the picosecond range, which is favorable for THz generation. Table 3.4 shows the comparison between ErAs:GaAs and InGaAs.

Table 3.4 Comparison between ErAs:GaAs and InGaAs.

	ErAs:GaAs	**InGaAs**
1550-nm absorption [cm^{-1}]	10000	15000
Dark resistivity [x 10^3 Ω-cm]	100	1
Carrier mobility [x 10^3 $cm^2/V{\cdot}s$]	3	1.5
Bandgap [eV]	1.42	0.75
Lifetime [ps]	1.6	0.2-0.3

Table 3.4 proves that ErAs:GaAs has comparable absorption to InGaAs, higher dark resistivity, higher mobility and larger bandgap. However, ErAs:GaAs displays a longer lifetime of the photo-carrier which would impact the bandwidth of the devices fabricated on this material. Based on our characterization, a problem of ErAs:GaAs seems to be the repeatability of the growth conditions when doping with high levels ($>10^{20}$ cm^{-3}) of erbium. A more in-depth study of the materials may help clarify this problem and lead to repeatable material growths.

CHAPTER 4
Fabrication and packaging

In parallel with the characterization of the materials, the optimization of the process of fabrication and packaging of the devices was investigated. In particular, different contact-metal stacks have been tested in order to improve THz performance.

4.1 Metallization, lift-off, and rapid thermal annealing

For the metallization stack, gold was chosen to be used for its good conductivity and for its low reaction with the GaAs substrate. In addition, an AuGe layer was used due to its deep diffusion into GaAs. Finally, Ti and Ni were considered in order to improve the adhesion of the metallization to the substrate. Resulting in a multilayer structure, used to accommodate the need of both a good ohmic contacts and a smooth surface after rapid thermal annealing. For this reason, a lift-off process was sought. since the patterning could not have been achieved through dry or wet etching.

The metallization stack was composed of 300 Å of nickel, 400 Å of germanium gold, 300 Å of nickel and 3200 Å of gold. A Denton thermal evaporator DV-502a was used to evaporate the metal, under a vacuum of 10^{-6} Torr or lower. The metal on top of the photoresist (Fig. 4.2) was then removed through a lift-off process, which was carried out as follows. First, for one half hour the patterned substrate is placed upside down on supports in a beaker filled with 1-inch of heated acetone (65 °C) to promote the dissolution of the resist. Next, to complete the lift-off process, the substrate was placed in a different beaker with heated acetone (65 °C), which was then place into an

ultrasonic bath to remove the “stiffer” flakes of metal. The choice for the metallization was driven by the need for both good adhesion and uniformity in the surface morphology as well as a low contact resistance after rapid thermal annealing. The RTA treatment is a necessary step needed in order to both reduce the contact resistance between the metal and the substrate and obtain ohmic contacts.

For GaAs based devices, the most widely used contact stacks for photoconductive THz antennas are Ni/AuGe/Ni/Au [93], [94] and Ti/Au [95]. In this research, the following metallic stacks have been studied: Ti-Au, Ti-AuGe-Au and Ni-AuGe-Ni-Au. Ti/Au contacts are usually preferred for their thermal stability, as titanium has a higher melting temperature (1725 °C) than gold (1063 °C) and germanium (959 °C). On n-doped GaAs, both stacks (Ti based and Ni based) form Schottky contacts prior to annealing. The annealing actively reduces the Schottky barrier. This likely relates to the fact that during the annealing the two stacks interact with the substrate, creating intermediate layers of TiAs and NiAs(Ge), respectively [96], [97]. In contrast to the Ti/Au contact, the AuGe based contacts show a lower contact resistance. This is due to a heating above the eutectic temperature of the AuGe alloy (360 °C) which causes high diffusion depth (200 nm) of Ge into the bulk of the n-doped semiconductor [98]. Another result is the formation of an n+ layer sufficiently heavily doped to produce a linear current-voltage characteristic. The motivation behind the choice of nickel was the improvement of the surface morphology of the contact [99], the contact adherence to the surface and the electrical properties to the contact [100], [101]. This stack, when subject to rapid thermal annealing, undergoes the following transitions [102]:

- At 240 °C, the germanium starts to diffuse out of the AuGe layer and moves towards the two Ni layers either side of the Au.
- At 280 °C, Ge has diffused completely into the Ni layers.

- At 300 °C, GaAs starts dissociating with Ga and As begins diffusing out through the Au layer towards the surface of the contact.
- At 335 °C, Ni from the top layer has diffused in towards the Ni at the GaAs interface associating with As, while Au has diffused through to the GaAs interface associating with the Ga in the form of Au-Ga alloy.
- At 350 °C, Au-Ga is present at the sample surface.

Fig. 4.1 shows the surface morphology of the three stacks after rapid thermal annealing at 465 °C for 30 seconds.

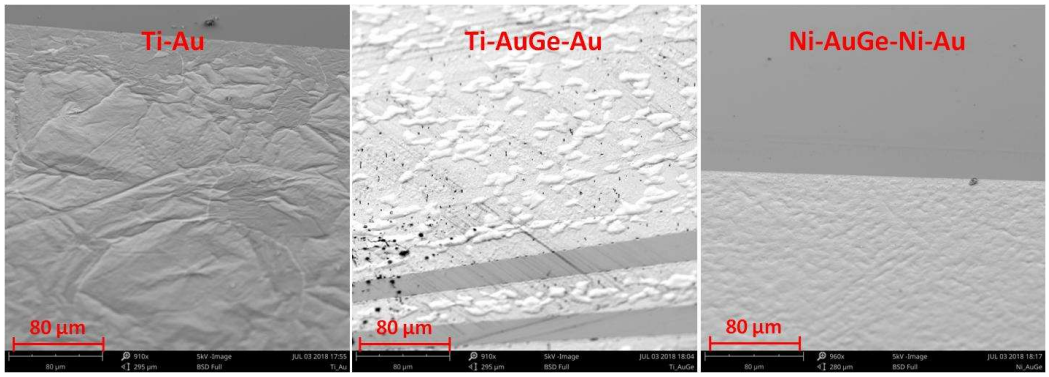

Fig. 4.1 Surface morphology of the three different stacks after rapid thermal annealing at 465°C for 30 seconds.

As it can be seen, while the two Ti-stacks led to a very rough (almost granular) and non-uniform surface, the stack with nickel was smoother and more uniform.

The thicknesses of the metal layers are listed in table 4.1.

Table 4.1 List of thicknesses of the metal layers for the Nickel and Titanium stacks.

	Ti stack #1	Ti stack #2	Ni stack
	Thickness [Å]	Thickness [Å]	Thickness[Å]
Ti	90	90	
Ni			296
AuGe		350	350
Ni			294
Au	3360	3360	3360
Total	3450	3800	4300

The thin film resistivities of the two stacks Ti-AuGe-Au and Ni-AuGe-Ni-Au were then measured using a four-point probe setup as shown in Fig. 4.2.

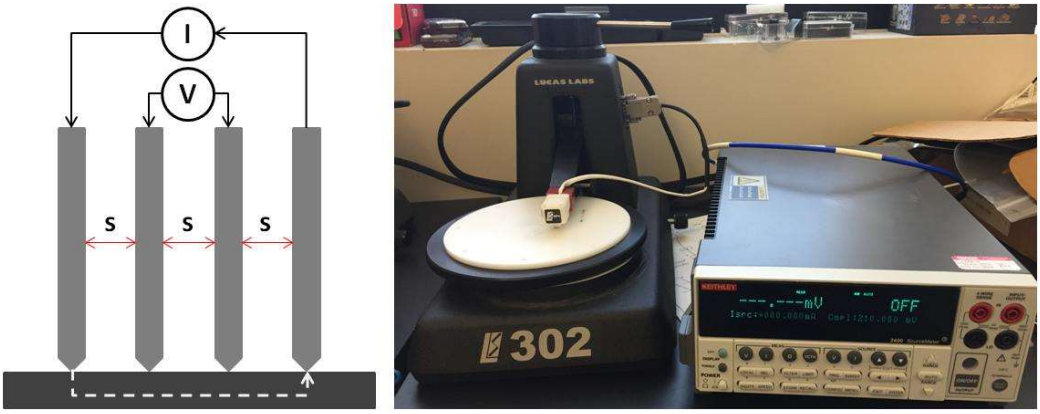

Fig. 4.2 Four-point probe diagram on the left, setup picture on the right.

The resistivity is given by [103]:

$$\rho = \frac{\pi t}{\ln(2)} \frac{V}{I} \tag{4.1}$$

where t is the thickness of the stack, V is the voltage measured between the two inner probes and I is the current flowing between the two outer probes.

A rapid thermal annealing (RTA) step was then performed to improve the contact adhesion and obtain ohmic contacts which, as it will be shown, represent a trade-off between having good ohmic contact and lower metal conductivity. This was achieved by means of contact alloying the stacks containing AuGe layers. During this process, it is important to remove the oxygen from the chamber, as it could react with the metals as well as the exposed GaAs substrate, causing oxidation. For this reason, the chamber was first purged and brought to a pressure of less than 1 Torr. Then an inert gas, in this case nitrogen, is set to flow in the chamber to prevent oxidation. A two-ramp recipe was then implemented in order to rapidly heat the substrate to the annealing temperature (typically below 465 °C) with a minimal temperature overshoot and highest thermal stability.

The measured resistivities of the stacks, both before and after rapid thermal annealing are plotted in Fig. 4.3.

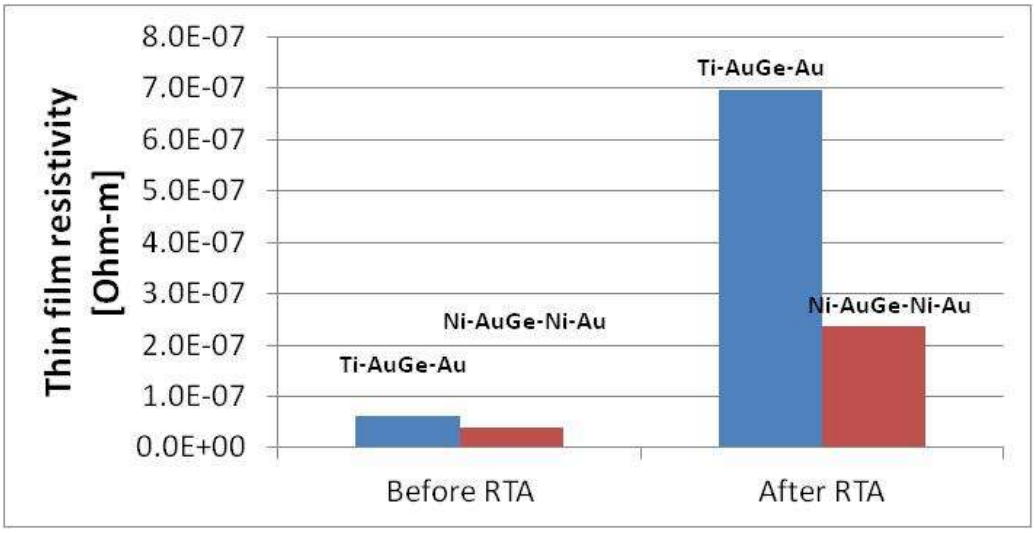

Fig. 4.3 Thin film resistivities of the Ti and Ni stacks, before and after RTA at 465°C for 30 sec.

Before the RTA the Ti and Ni stack displayed thin film resistivities of approximately 6 x 10^{-6} Ω·cm and 4 x 10^{-6} Ω·cm, respectively (for comparison, the bulk resistivity of pure gold is 2.44 x 10^{-6} Ω·cm). After the annealing, these values increase to approximately 7 x 10^{-5} Ω·cm and 2.4 x 10^{-5} Ω·cm respectively, with an increase of almost 12 times for the Ti stack and 6 times for the Ni stack. For this reason, the Ni stack was further studied.

Since the whole sample used for the first test (Table 4.1) was annealed, a second sample with the nickel metal stack was evaporated, with thicknesses listed in Table 4.2, in order to perform this study.

Table 4.2 List of the thicknesses of the metal layers in the Nickel stack.

	Ni stack
	Thickness[Å]
Ni	284
AuGe	305
Ni	284
Au	3327
Total	4200

The surface morphology and the film resistivity of the second Ni-AuGe stack were then studied by varying the temperature and the annealing time. The following temperatures were used: 370 °C, 380 °C, 390 °C, 400 °C, 410 °C and 420 °C. The annealing duration was set to either 20 or 30 seconds. In order to minimize the variation between each test, a single substrate was deposited with the Ni-AuGe stack and then cleaved into twelve smaller pieces. The RTA of each sample was then performed in consecutive runs.

Prior to any annealing, the resistivities of the twelve pieces were measured and Fig. 4.4 shows the results.

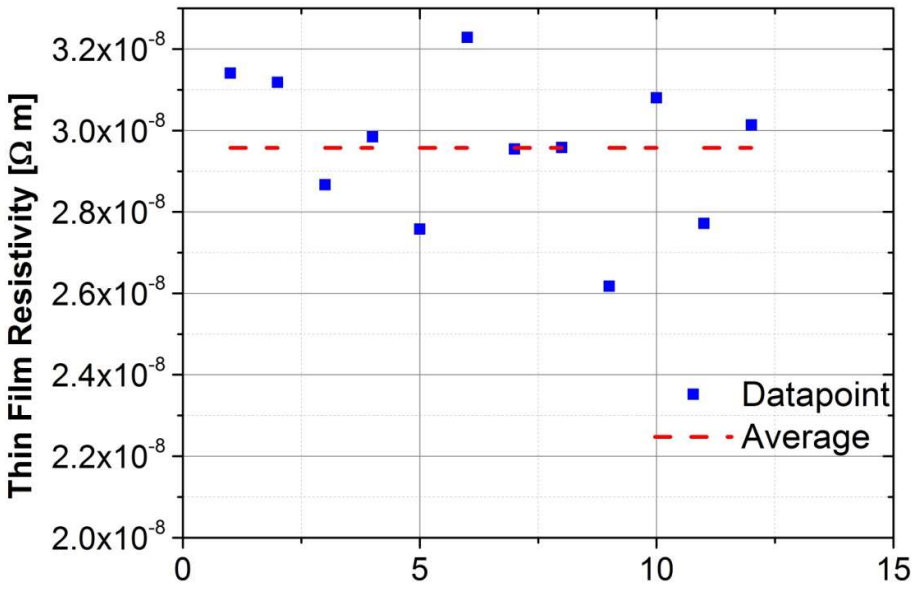

Fig. 4.4 Thin film resistivities of the twelve SI-GaAs pieces with the Ni-AuGe stack.

The thin film resistivity values averaged to 2.96 x 10^{-6} Ω·cm, a value that does not differ much from the value for pure gold (2.44 x 10-6 Ω·cm). In the first experiment, six of the substrates were annealed for 20 seconds at the different temperatures, then the resistivities were measured again (the results are plotted in Fig. 4.5). The surfaces were subsequently examined for degradation of the metallization using the SEM (Fig. 4.6).

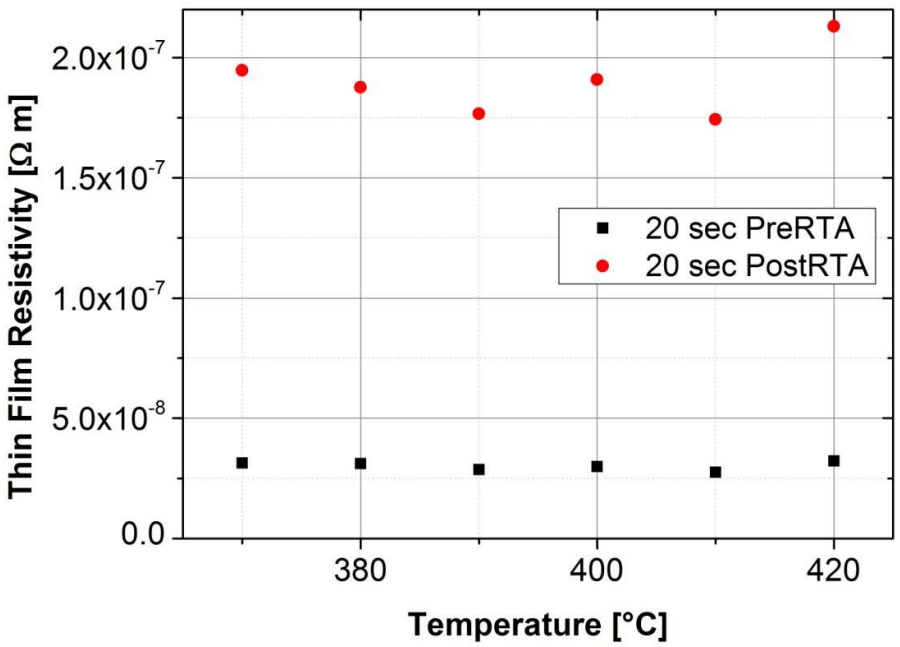

Fig. 4.5 Measured values of the thin film resistivity before and after RTA for 20 sec vs annealing temperature. Dataset on top, plotted results on bottom.

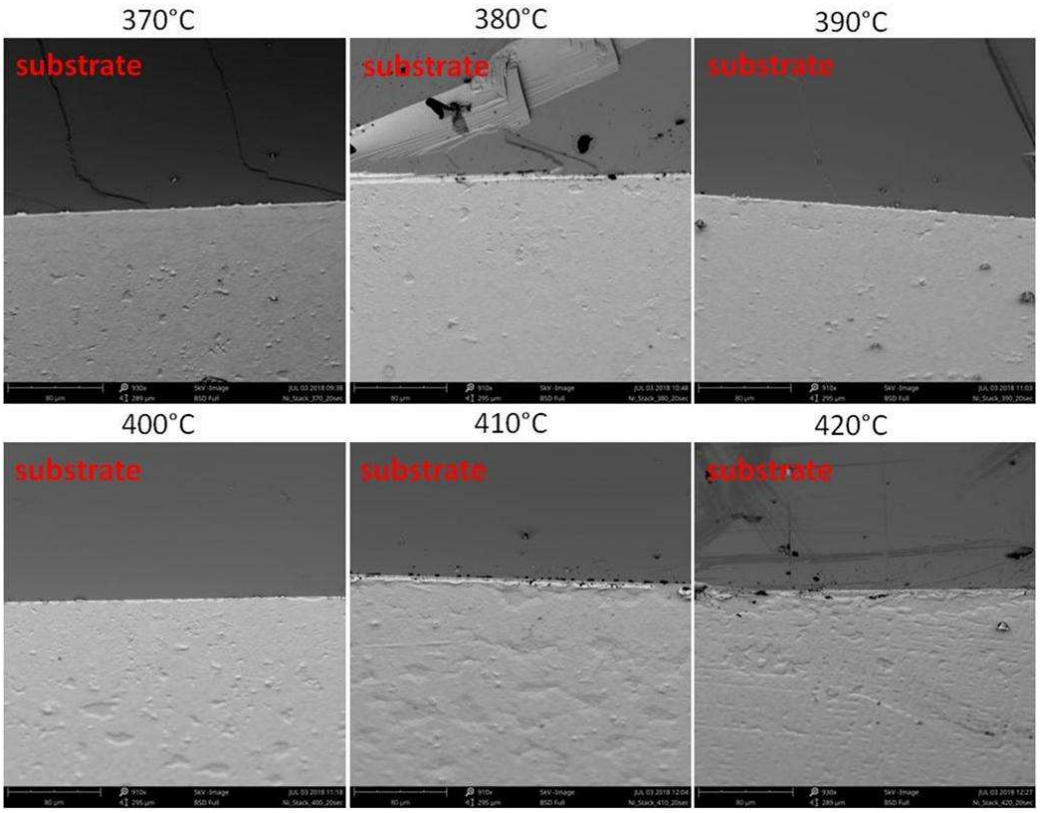

Fig. 4.6 SEM images of the metal surface of the Ni-AuGe stack when annealed for 20 seconds.

In Fig. 4.5, it can be seen how the thin film resistivity increased independently from the annealing temperature, to a value of around 1.9 x 10^{-5} Ω·cm. The lowest value for resistivity was recorded for the annealing temperatures of 390 °C and 410 °C. Fig. 4.6 shows that there is no major difference on the surface morphology after the annealing at different temperatures. The same experiment was carried out at the same annealing temperatures but for 30 seconds. The results are shown in Fig. 4.7.

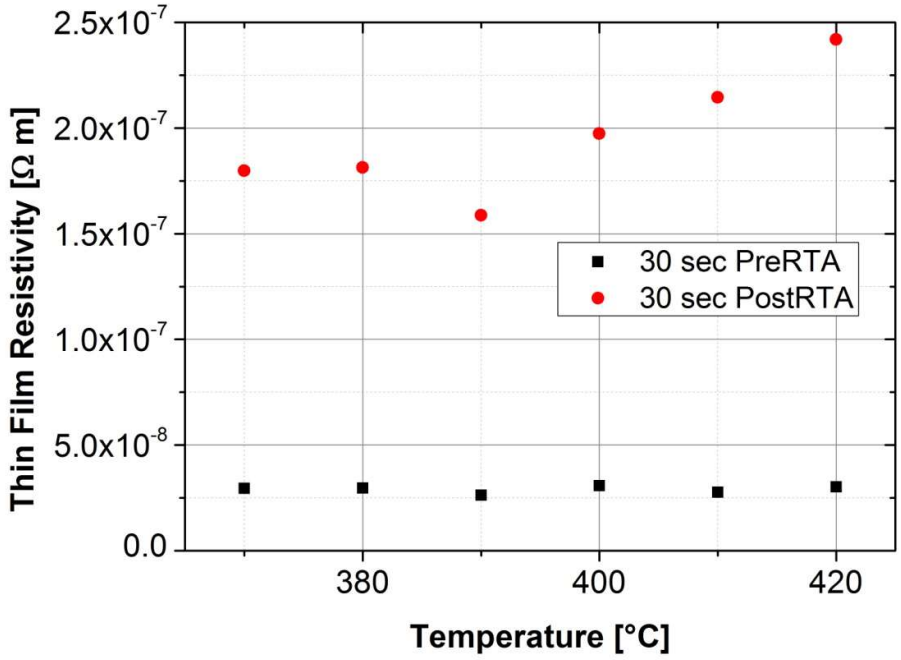

Fig. 4.7 Measured values of the thin film resistivity before and after RTA for 30 sec vs annealing temperature. Dataset on top, plotted results on bottom.

From Fig. 4.7 it can be seen how the thin film resistivity increases to an average value of around 1.95 x 10^{-6} Ω·cm, slightly higher than for the 20-second annealing. The lowest value of 1.58 x 10^{-5} Ω·cm was obtained at the annealing temperature of 390 °C. The highest value of 2.42 x 10^{-5} Ω·cm was obtained at a temperature of 420 °C. As for the case of 20 seconds annealing, no significant difference in the surface morphology of the metallization can be noticed, as shown in Fig. 4.8.

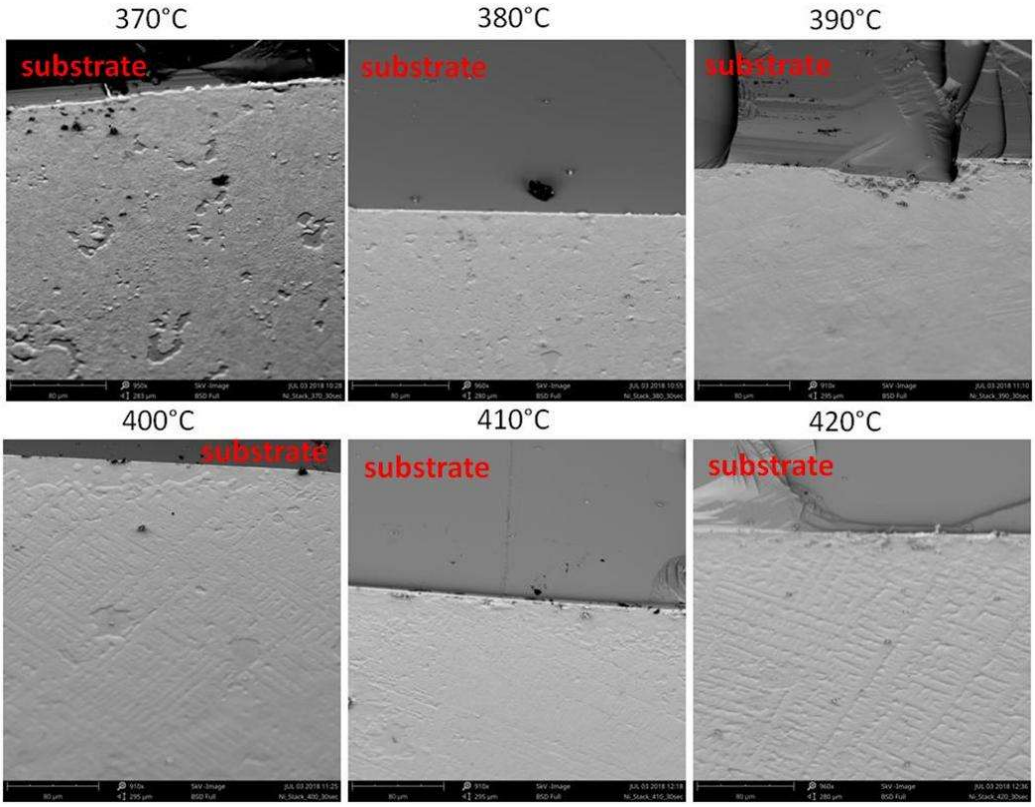

Fig. 4.8 SEM images of the metal surface of the Ni-AuGe stack when annealed for 30 seconds.

Fig. 4.9 shows the final comparison between the thin film resistivities at different temperatures and different annealing durations. At lower annealing temperatures (up to 400 °C) the resulting thin film resistivity was independent of the time of the annealing. In contrast, the substrates annealed for 30 seconds at 410 °C and 420 °C displayed a higher resistivity compared to the substrates annealed for only 20 seconds. The reason, however, is unclear.

From the results obtained, the best annealing recipe was the one that anneals the substrate to 390 °C for 20 seconds.

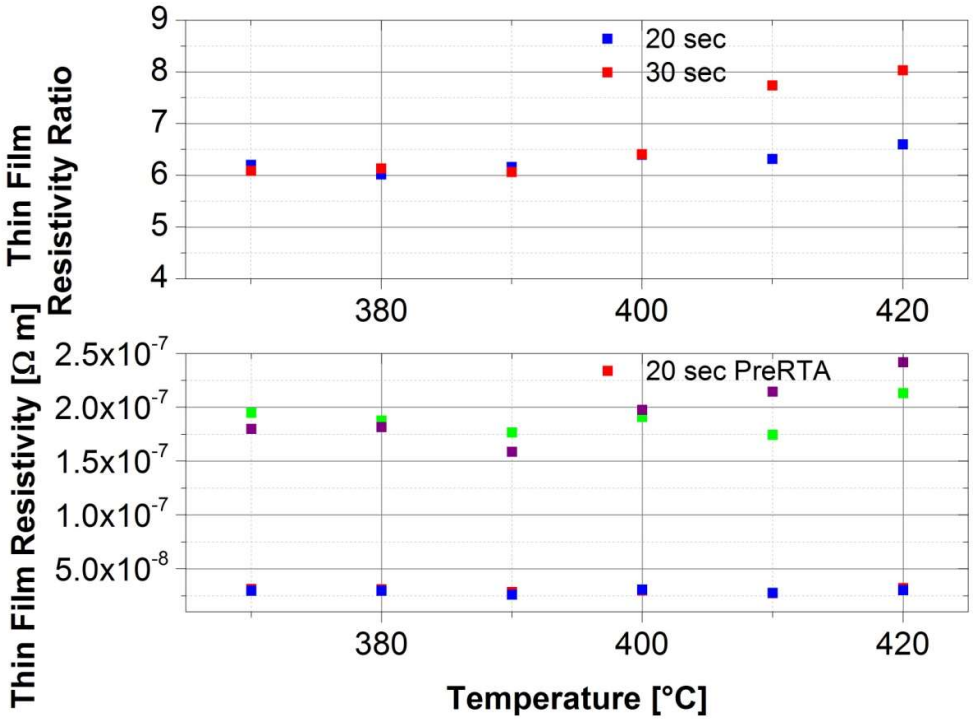

Fig. 4.9 Comparison of the thin film resistivities before and after RTA to the top, and of the after RTA over before RTA ratio of the thin film resistivities to the bottom.

In all of the cases studied, the resistivity of the metallization increased independently from which metal stack was used or the temperature and time chosen for the RTA. The increase in the resistivities is due to the combination of two factors: the thicknesses of the metal layers and the roughness of the surface after the thermal treatment. First Fuchs [104] and then Barker et al. [105] discussed in detail the relation between the resistivity of metal films, their thickness, and the mean free path of the carriers in such films. Fig. 4.10 plots on the y-axis the ratio between the bulk silver conductivity, σ_0, to the thin film conductivity of silver, σ, and on the x-axis the ratio of the film thickness (a) to the mean free path length (l). Assuming the curve in Fig. 4.10 is universal, the film thickness needs to be close to 10 times the mean free path in order to have a ratio close to 1 (i. e. the mean free paths are 5.87 nm for nickel and 37.7 nm for gold). Fuchs explained that this due to the surface scattering which, in thin films, is predominant. In addition, if the surface is not smooth but is rather rough as shown in Fig. 4.1, the surface

scattering becomes even more severe. Over-imposed to Fig. 4.10 are shown two datapoint obtained from samples studied for this research.

For this reason, thick metal films should be deposited in order to have a satisfactory metallization. The rule-of-thumb is to deposit metallic layers 10 times thicker than the mean free path in the metal. In the case of the Ni/AuGe/Ni/Au stack, thicknesses of ≈59 nm, ≈380 nm, ≈59 nm, and ≈380 nm, respectively, should be targeted. This would therefore lead to a total thickness for the stack of 878 nm, which could be achieved using different photoresists or via electro plating. Unfortunately, such thicknesses were not used in this research for practical reasons.

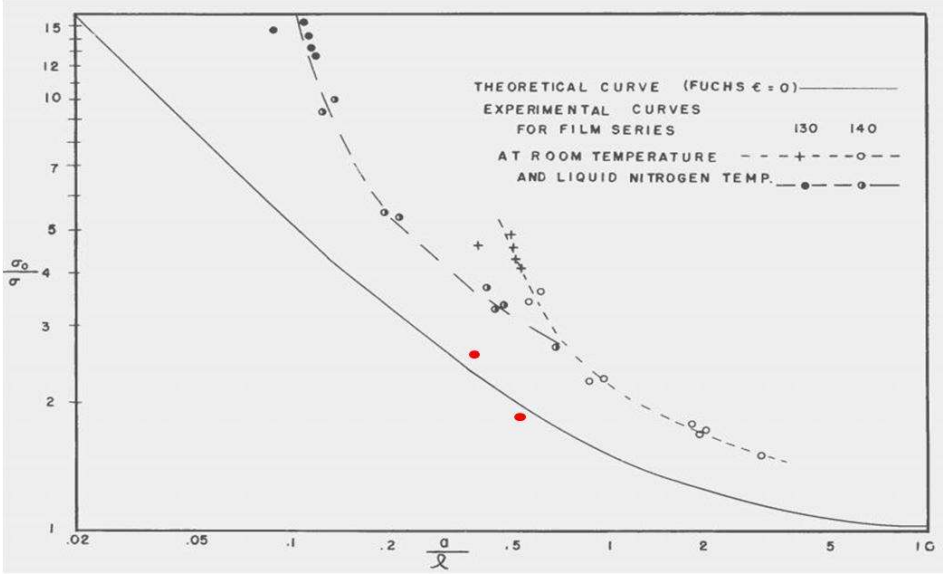

Fig. 4.10 Resistivity 1/σ of thin films divided by resistivity 1/σ0 of the bulk metal. Both ordinates and abscissa are plotted logarithmically, t is the thickness of the film and a is the mean free path [105]. The two red dots are datapoint obtained from samples used during this research.

4.2 THz Optics and packaging

After the lift-off is done, the devices need to be prepared for packaging. The first step is dicing the substrate into 3 x 3 mm chips using a DISCO DAD 2H/6T diamond-blade saw. In order to reduce the chipping of the substrate, different feeding speeds and blades have been tested on SI GaAs. After thorough testing, a feeding speed of 0.5

mm/s and the blade ZH05-SD4800-N1-50 were chosen. An image of the single device die is shown in Fig. 4.11.

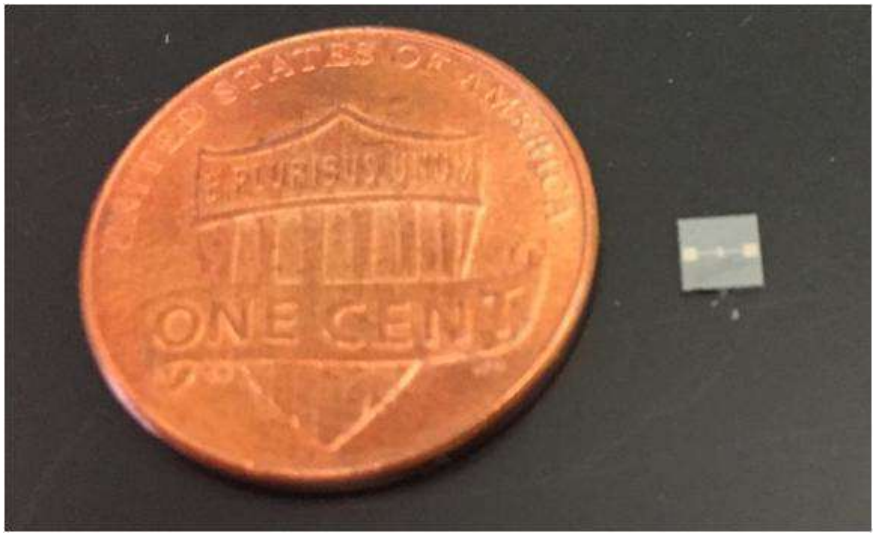

Fig. 4.11 Single chip device next to a penny for scale.

An important issue of these devices is how to couple the THz radiation efficiently into free space. The problem lies in the dielectric constant of the GaAs, $\varepsilon_r \approx 12.96$ at 1 THz [XX]. The high ε_r, paired with the fact that the substrate can be considered a slab, creates a reflection:

$$R = \left(\frac{n_{GaAs}-1}{n_{GaAs}+1}\right)^2 \approx \left(\frac{3.6-1}{3.6+1}\right)^2 \approx 0.32 \tag{4.1}$$

where $n_{GaAs}=3.6$ is the refractive index at 1 THz [106]. A critical angle for the GaAs-air internal reflection is ≈16° from normal, calculated from Snell's law:

$$n_{GaAs}\sin(\theta_{crit}) = n_{air}\sin(90°) \tag{4.2}$$

$$\sin(\theta_{crit}) = \frac{n_{air}}{n_{GaAs}} \tag{4.3}$$

$$\theta_{crit} = \sin^{-1}\frac{n_{air}}{n_{GaAs}} \tag{4.4}$$

where n_{air} is 1 and n_{GaAs} is 3.37.

To avoid total internal reflection, a back-side hemispheric lens made out of high resistivity float zone (HRFZ) silicon with a dielectric constant of 11.62 was used. This solution was pioneered by D. Rutledge's group at Caltech in the 1980s [107]. If the antenna is located at the center of curvature of the lens and the lens is thick enough that the spherical surface is in the far field of the antenna, the radiation rays reach the surface at normal incidence. The drawback of this technique is that it yields a highly diverging beam. To negate this issue, the antenna design places the planar antenna chip behind the lens by approximately the distance r/n_{lens} with r being the radius of curvature of the silicon lens. This success of this method is due to a combination of "hyperhemispherical" lens design with the thickness of the GaAs substrate [107]. Fig. 4.12 shows a cross-section at "ray-view" of a photoconductive antenna (PCA) coupled to a hyperhemispherical lens where the angle α depends on the setback of the antenna.

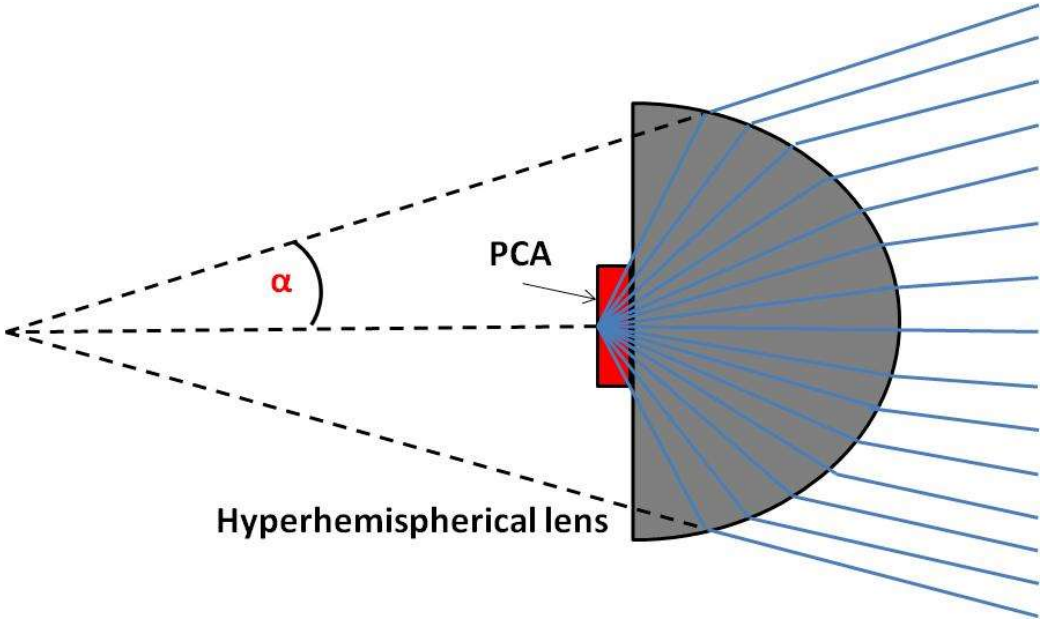

Fig. 4.12 Cross-section of the ray-view of a PCA coupled with a hyperhemispherical lens.

In order to bias the device and handle the lens-coupled antenna, the package shown in Fig. 4.13 was assembled.

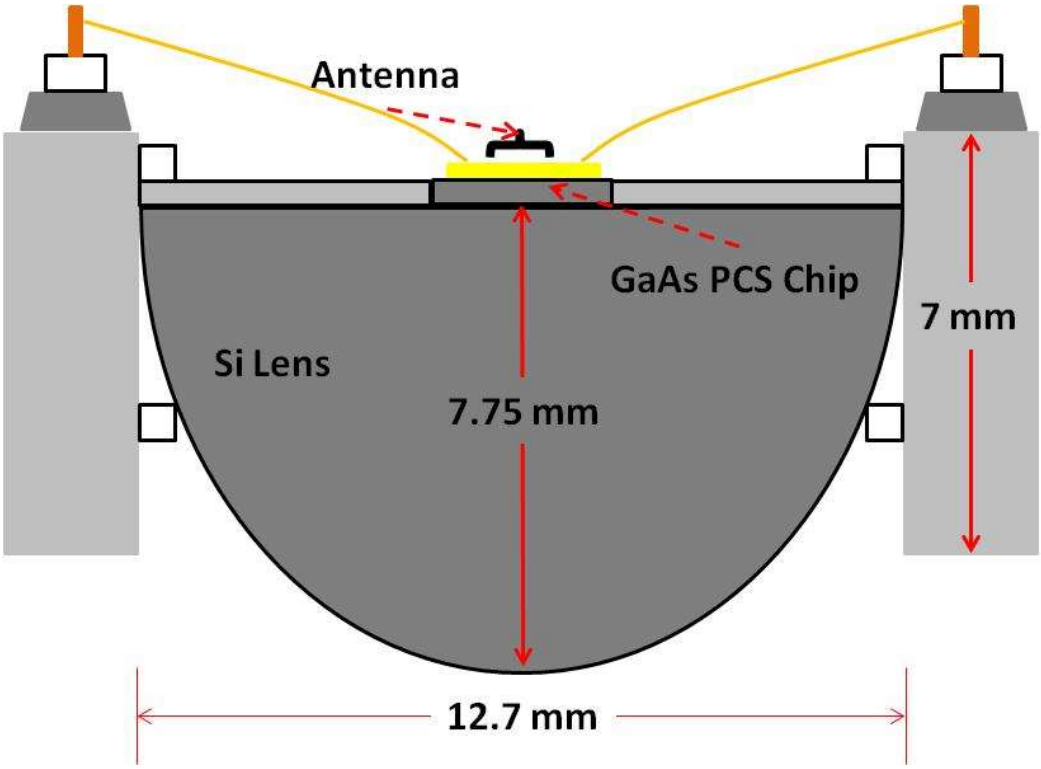

Fig. 4.13 Cross-section view of the packaged lens-coupled antenna.

4.3 Antennae

The antenna chosen for emission tests was an important design consideration, as it affects the output power and dictates the radiation bandwidth. In this work, three antennae have been tested: the first and most important one being a 4-turn square spiral antenna (Fig. 4.14 (a)), a design chosen for its ability to generate large output power and circularly polarized radiation [108]. The second design is a slot antenna (Fig. 4.14 (b)), chosen to operate more efficiently over a narrower band than the square spiral. The third is an Archimedean log spiral antenna (Fig. 4.14 (c)).

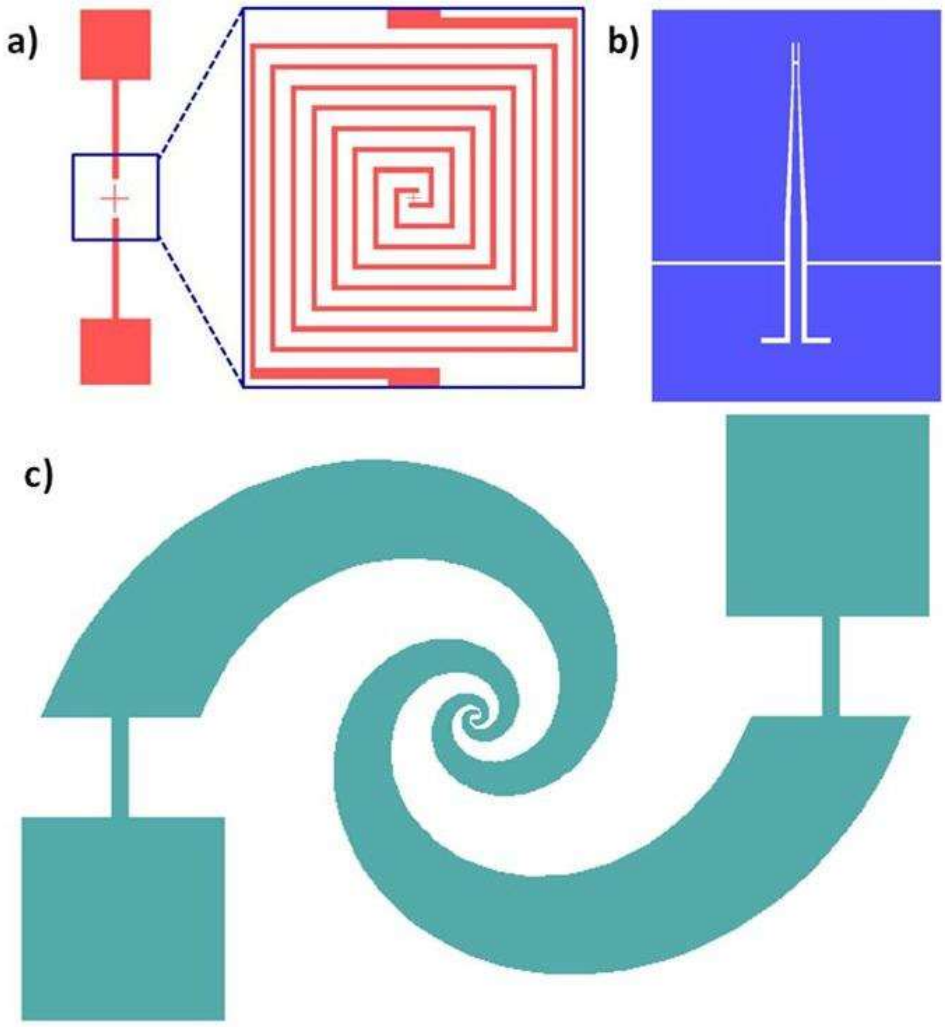

Fig. 4.14 (a) 4-turn square-spiral antenna, (b) slot antenna, and (c) Archimedean log spiral.

The antennae shown in Fig. 4.14 (a) and (c) are examples of self-complementary antenna (antenna where the metal area and the open area are congruent). The self-complimentary, log spiral-based designs are known to provide a beam pattern that is frequency independent. In log spiral antenna designs most radiation propagates perpendicular to the plane of the antenna. The high dielectric constant of GaAs ($\varepsilon_r \approx 13$) traps most of the THz radiation into the GaAs (when coupled with the HRFZ lens) instead of radiating in air. In addition, spiral antennas have a design that allows for a nearly independent frequency radiation resistance, $R_{A,}$ in contrast with dipole antennas. According to Babinet's principle, the R_A of this antenna is:

$$R_A \approx \frac{60\pi}{\sqrt{\varepsilon_{eff}}} \tag{4.7}$$

where ε_{eff} is the effective permittivity of the semiconductor substrate ($\varepsilon_{eff} = (1+\varepsilon_r)/2$) [109]. On the other hand, self-complementary square-spiral antennae, due to their dipole-like nature, provide values for R_A that fluctuate between ≈ 100 and 250 Ω. This is an advantage when compared to the more frequently used self-complementary logarithmic antenna. Additionally, the device in Fig. 4.14 (a) has the key characteristic that each straight section of the square spiral acts as a dipole, leading to a sequence of dipoles designed to radiate at progressively longer wavelengths. The square spiral design is also advantageous because dipole antennas have a greater R_A than the logarithmic self-complementary spiral antennas. By having different size dipoles to form this antenna, the R_A can be kept high across the THz spectrum. Additionally, high directivity of nearly 30 dB has been reported for this type of antenna when coupled with a hyperhemispherical lens [110].

4.3.1 Four turns square-spiral antenna dimensions

Figure 4.18 shows the details of two versions (designs A and B) of the 4-turns square spiral antenna used throughout this dissertation work.

The active region of the antenna is a 9 x 9 μm area, depicted with green stripes in Fig. 4.15. From the center, following a counter-clockwise rotation, the spiral antenna gets formed by adding dipoles, increasing their lengths of 18 μm at every 90° turn. At the end of the fourth turn, bias lines (300 μm long for design A and 731 μm for design B) terminate in large pads (300 x 300 μm for design A and 500 x 500 μm for design B) for wire bonding. The two designs will be discussed further in the following chapter.

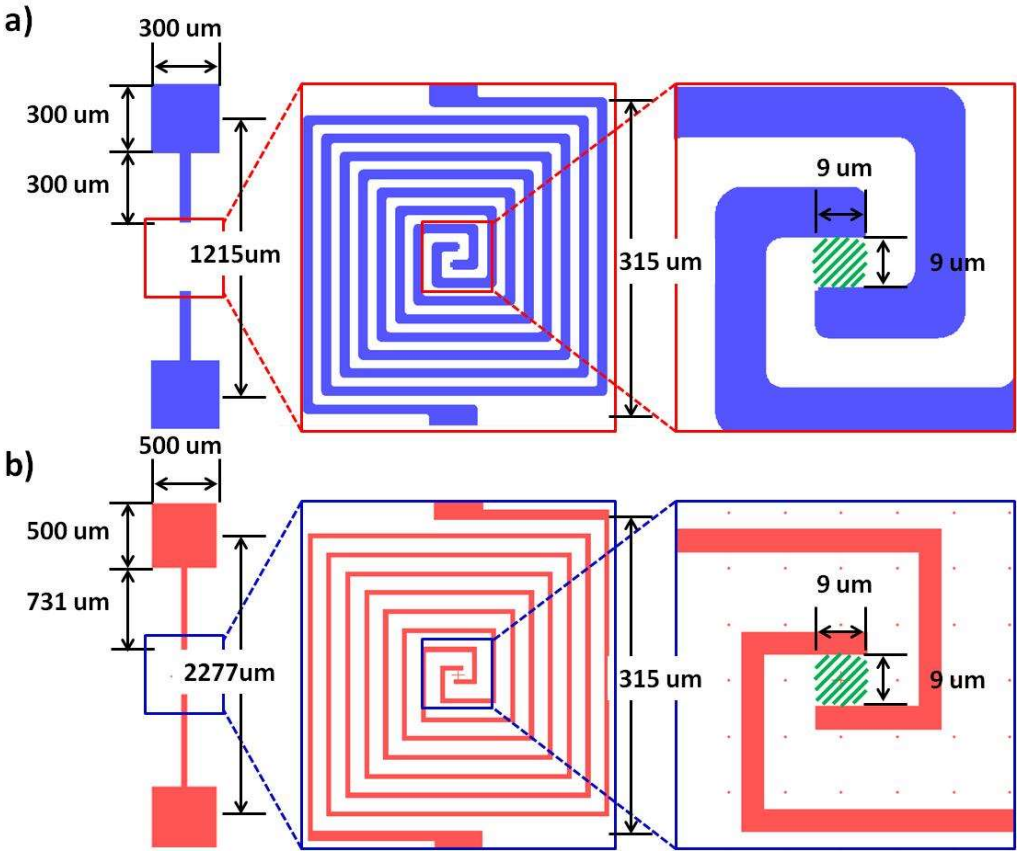

Fig. 4.15 Details of the dimension of the 4-turn self-complementary square-spiral antenna: a) design A and b) design B.

4.3.2 Slot antenna dimensions

Fig. 4.16 shows the slot antenna used for this work.

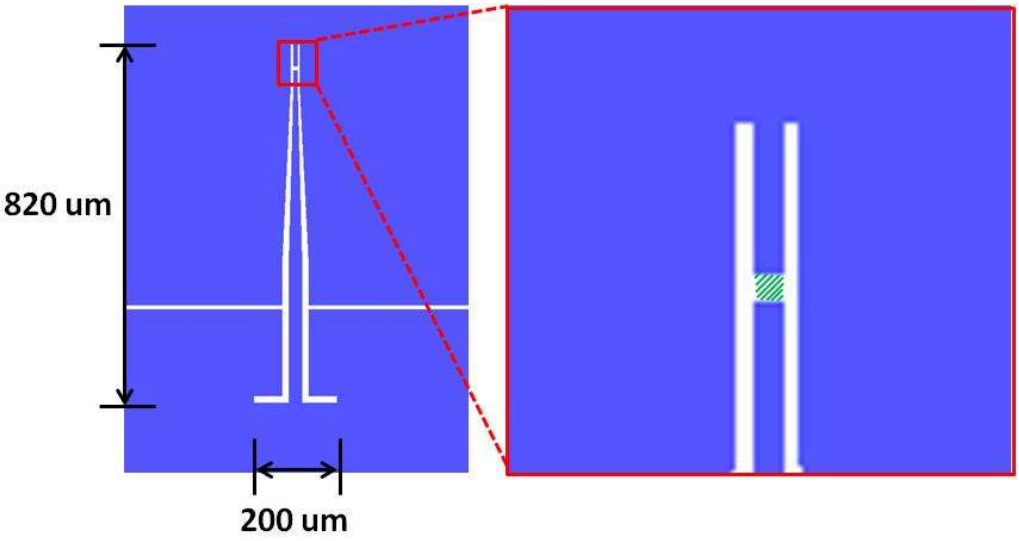

Fig. 4.16 Design and dimensions of the slot antenna.

The slot length of 200 μm was designed to have a full-wave resonant frequency at 567 GHz, following the formula:

$$f_0 = \frac{c / \sqrt{\frac{1+\varepsilon_r}{2}}}{\lambda_{full}} \tag{4.8}$$

where c is the speed of light (3 x 10^{10} cm/s), ε_r is the relative permittivity of the substrate (13 in the case of the GaAs) and λ_{full} is the full physical wavelength in cm. The half-wave resonant frequency is estimated to be roughly 283 GHz.

4.3.3 Archimedean log spiral

Another antenna that was implemented was the well-known Archimedean log spiral antenna [111]. A micro-photograph of the device is shown in Fig. 4.17 with the detail of the 9 x 9 μm active region in the red square inset.

Fig. 4.17 Detail of the active region for the Archimedean log spiral antenna.

4.4 Summary

A satisfactory process was designed to fabricate THz PCA devices with high yield and reliability. The process brought a high yield (>95%) of devices, with very little dimensional mismatch between the fabricated antenna and the design of the mask. Several different types of possible metallization were studied. The one composed of a stack of Ni/AuGe/Ni/Au was found to be the best one, yielding ohmic contacts after RTA and keeping a lower arm resistance when compared to the widely used TiAu. The RTA process was also studied in order to improve the surface uniformity of the metal layer as well as keep a low overall resistance. The packaging of the antennae and the antennae themselves were presented. The following chapter will start the presentation of the results obtained on the testing of the devices fabricated on the two best samples.

CHAPTER 5
PCA Characterization: responsivity and THz power

The fabricated devices were tested and characterized as THz sources. The measurements include: dark-current, photo-current generation, responsivity under optical excitation at 1550 nm (pulsed and CW), and THz power generation. The devices were operated under safe operating conditions, meaning under a combination of optical excitation and bias voltage such that the individual device was far from breakdown and able to operate without degradation of the performance for several days. These operating conditions varied between each device. Based on both electrical and optical characterization, absorption at 1550-nm and dark-current at 50 V (shown in Table 5.1), ASP174 and ASP194 were found to be the two best materials. For this reason, this chapter will cover the results obtained on these two samples, having the material characteristics listed in Table 5.2, will be presented.

Table 5.1 Results on optical and electrical tests on the different samples.

	Peak absorption [cm^-1]	Dark-current [μA]
ASP174	6300	25
ASP180	9150	-
ASP194	7450	1.3
ASP280	5450	23.2
ASP294	8000	80
ASP328	1430	-
ASP365	1420	0.5
ASP372	1600	0.25

Table 5.2 List of samples tested.

	ASP174	ASP194
Erbium Concentration [cm^{-3}]	4.4×10^{20}	8.8×10^{20}
Epilayer Thickness [μm]	1	2

5.1 Photoconductive switch

5.1.1 Dark I-V current

As discussed in Chapter 2, the characteristic of "dark" current was first measured without optical illumination. The experimental setup consisted of a source-meter, namely a Keithley 2400, and two tungsten probes mounted on separate 3-axis micro-positioners. By measurement of the IV curve, the quality of the devices could be determined before packaging. Dark-current measurements can also provide some information about the transport of the device under test. The Kethley 2400 was connected by a laptop computer via a GPIB-USB cable, enabling automatic scans. All the devices have been tested in the same way.

First are shown the results on the PCS having design A (Fig. 4.18 a). To review, design A consists of a 4-turn self-complementary square-spiral antenna, consisting of 9 μm separation between the arms, and a 9 x 9 μm area for the active region. A microphotograph of the fabricated device is shown in Fig. 5.1.

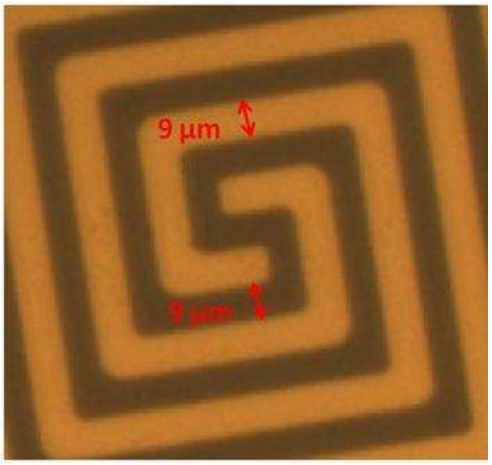

Fig. 5.1 Photoconductive switch design A, square spiral antenna.

Fig. 5.2 shows the dark-currents for the two samples.

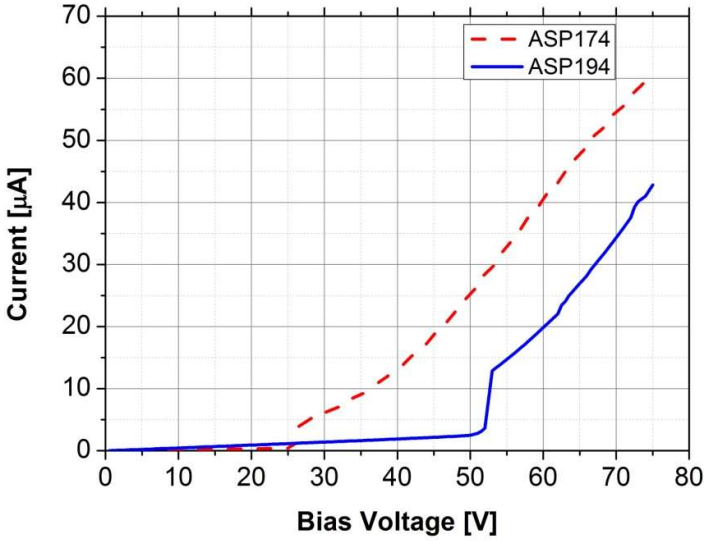

Fig. 5.2 Dark-currents of design A PCS fabricated on ASP174 and ASP194.

The first insight is an abrupt discontinuity in the current when the voltage (or electric field) reaches certain critical values. These voltages were different for the two materials. The theoretical explanation of this phenomenon is beyond the scope of this thesis and hence only the raw data will be shown. More information regarding this matter can be found in Ref. [112] where a qualitative model is proposed, suggesting that the density-of-states at the Fermi level is a strong function of bias voltage,

temperature and magnetic field and can be switched from a “null” Coulomb gap to a “sharp” Kondo resonance peak.

As shown in Fig. 5.2, the device fabricated on ASP194 had a larger dark-current before the discontinuity, compared to that of ASP174. However, after the discontinuity, the ASP194 device displayed a much lower dark-current, which is a desired characteristic for PCS devices.

Nonetheless, the dark-currents from ASP174 and ASP194 were still large. The main reason is the gap dimension between the arms of the 4-turn square-spiral antenna. As shown in Fig. 5.1, from the inner active region of the spiral throughout the spiral’s four turns, the spacing between the arms is 9 μm. With this dimension, the conduction happens evenly in every turn of the spiral, but because of the small spacing, both the electric field and the dark-current are high.

In design B, this problem is alleviated by increasing the spacing between the arms of the spiral. As shown in Fig 5.3, the ratio of the gap to metallization width of design A (9 μm gap and 9 μm metallization) was increased to 3.5 (14 μm gap and 4 μm metallization) with design B.

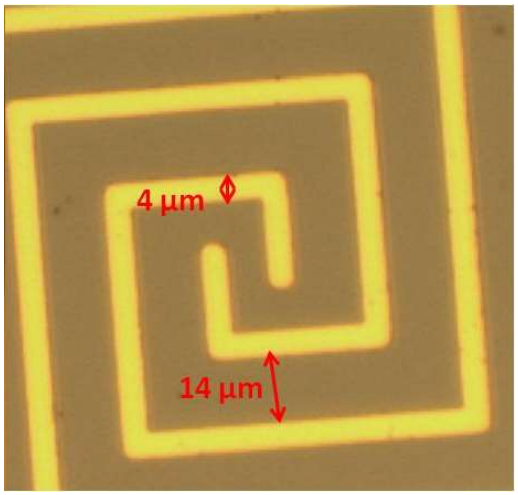

Fig. 5.3 Photoconductive switch design B.

Fig. 5.4 shows the comparison of the dark-current measurements for the two antenna designs based on the same substrate material, ASP194, with a doping density of 8.8 x 10^{20} cm^{-3} and a 2 µm thick epitaxial layer.

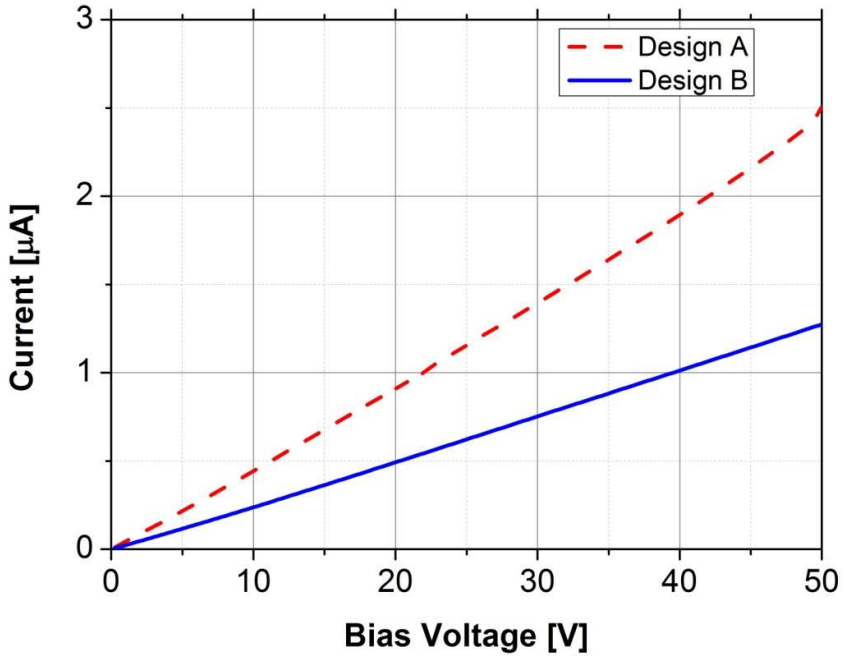

Fig. 5.4 Dark-current comparison between design A (in red) and design B (in blue).

Fig. 5.4 clearly shows that design B lowers the leakage current. In particular, at a bias voltage of 50 V, the current drops from 1.27 µA to 0.56 µA. As a result of this improvement, the device with design B was biased up to a voltage of 145 V, reaching a maximum dark-current of 260 µA. The result is shown in Fig. 5.5.

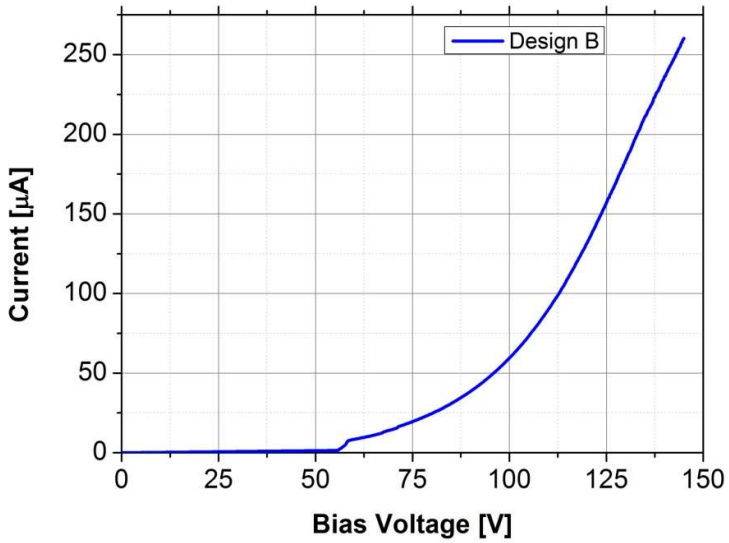

Fig. 5.5 Dark-current for the device fabricated with design B on ASP194, higher bias voltage.

In conclusion, the introduction of design B with 14 μm spacing and 4 μm metallization widths reduced the dark-current. A possible, future improvement would come by implementing a new type of antenna like the log spiral antenna design (a comparison will follow later in this chapter) or even a square-log spiral antenna.

5.1.2 Photo I-V curve under 1550-nm pulsed laser excitation

Following the dark-current, an important metric of the devices is the photocurrent generated under the optical excitation of the 1550 nm pulsed laser, and the related responsivities. Fig. 5.6 shows the setup for characterizing photocurrent.

The setup consisted of the following: a Menlo T-Light 1550 nm mode-lock laser with 90 fs pulse width and 100 MHz repetition rate capable of generating an average optical power of 87 mW coupled to free space; a 10x achromatic standard microscope objective (NA = 0.25, EFL = 15.2 mm) with a focus spot size of 10 μm that matches the driving-gap region of the antenna; a packaged device; a Keithley 2400 source meter; and a laptop computer to control the source meter and collect the data.

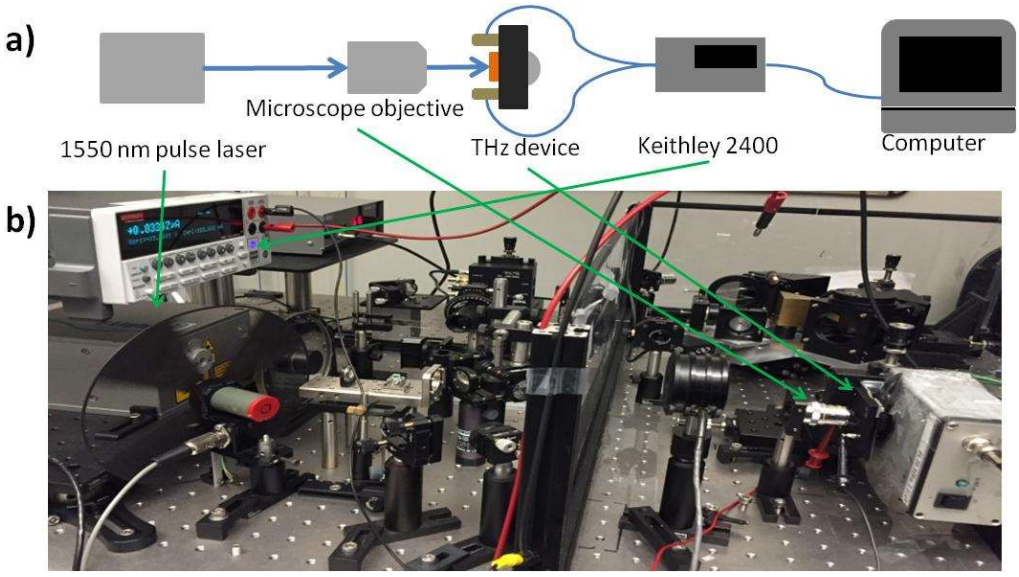

Fig. 5.6 a) Block diagram of the photocurrent setup and b) picture of the setup.

The packaged device was mounted on a 3-axis stage and placed in the beam path after the microscope objective. The device was aligned with the laser beam and the procedure was carried out when the device was under a low bias voltage of 20 V in order to reduce the risk of thermal or electrical failure. To ensure that the laser beam was incident on the active region of the antenna, the photocurrent was monitored either with the sourcemeter itself in DC mode or with an oscilloscope together with a 100 Hz mechanic chopping of the laser beam. To align the device on the z-axis (the beam axis), it was only necessary to adjust the z-axis stage and look for a maximum in the photocurrent. Considering that the metallic arms of the antenna are opaque to the 1550 nm laser, the beam alignment on the x-y plane perpendicular to the beam axis can be determined by counting the number of peaks generated when the laser illuminates the gaps between of the arms (Fig. 4.18). On the axis parallel to the bias pad arms, the total number of peaks is 17, while there are 15 along the perpendicular one. By switching back and forth between the alignment on the z-axis and the x-y plane, and by making sure the maximum signal at the 9th peak on the axis parallel to the bias lines and at the

8th one on the perpendicular axis, the active region became aligned to the laser beam. Additionally, for the devices fabricated with the design B, the active region is the only area of the device with a 9 µm gap, while the spacing between the arms is 14 µm. Thus, at a fixed bias, the central "peak" always had the highest photocurrent in the x-y plane, making the alignment process much easier than that of design A.

Unless otherwise stated, all of the photocurrent tests have been carried out with a laser output power of 84 mW, with an actual power reaching the device of approximately 64 mW due to the attenuation of the achromatic microscope objective. As per the dark-current measurements, the photocurrent and responsivity results for the design A antenna devices will be presented first. The results for the design B will follow, and finally a comparison of the two.

The devices fabricated on ASP174 and ASP194 with design A were tested up to 75 V. Fig. 5.7 shows the resulting measurements.

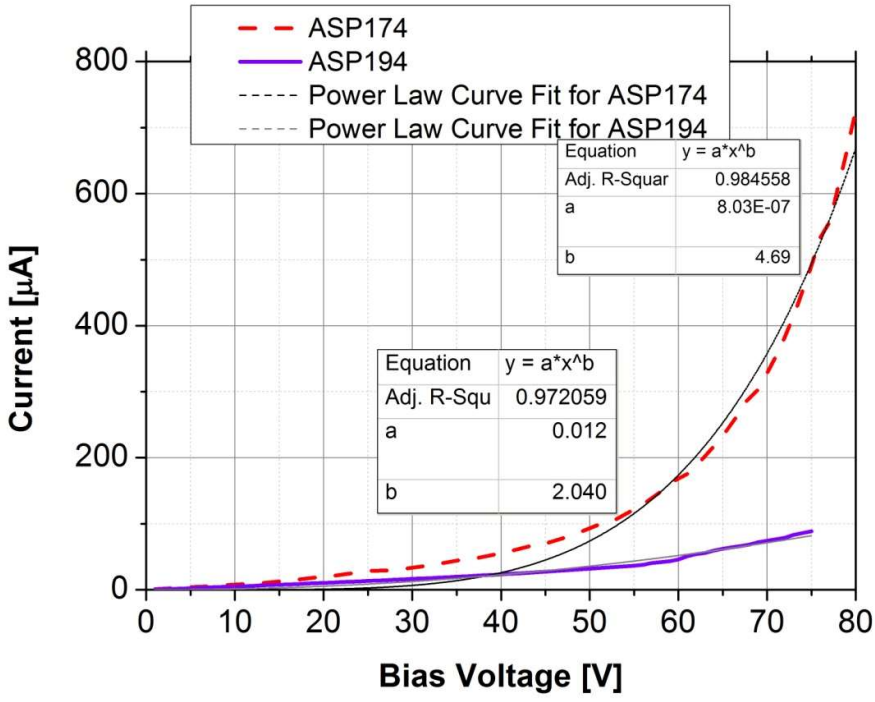

Fig. 5.7 Photocurrents at up to 75V for devices fabricated on ASP174 and ASP194 with design A.

It can be noticed that the current for ASP194 at 75V increases with respect to bias voltage much more slowly compared to that ofASP174. By fitting the two curves to a power law, the exponents are found to be 2.04 and 4.69 for ASP194 and ASP174, respectively. This could be an advantage due to the tendency for quadratic dependence of P_{THz} on photo-current; however, a steep increase of the current for ASP174 will limit the highest bias voltage due to the increased chance of a thermal-runaway breakdown.

Fig. 5.8 shows the comparison of the photo-current between devices with designs A and B fabricated on ASP194. At the lower bias, the photocurrent of design B increases only slightly. The effect of design B can be seen at higher voltages. The current in fact increases with a slower power law. This is advantageous, as it will be shown later, due to the stronger dependence of the THz power on bias voltage compared to that on photo-current.

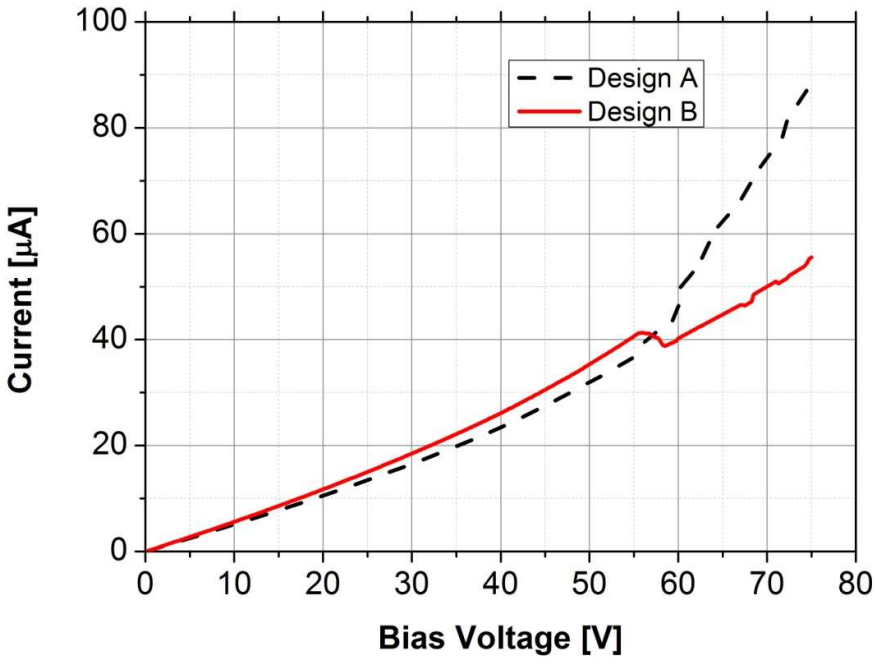

Fig. 5.8 Comparison between the photocurrent generated with the two designs from devices fabricated on ASP194.

Due to lack of ASP174, design B was implemented on sample ASP194. Fig. 5.9 shows the results of the improved device with design B when biased at higher voltages.

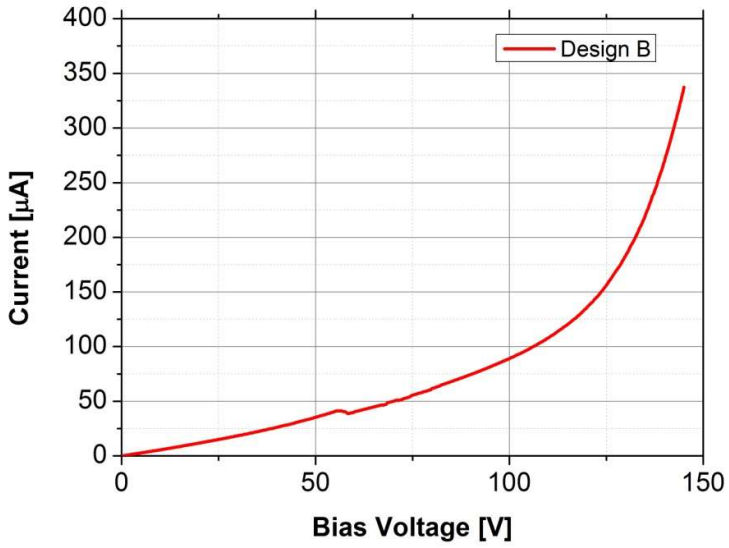

Fig. 5.9 Photo-current for the device fabricated with the design B on ASP194, higher bias voltage.

5.1.3 Responsivity

To quantize the photocurrent generation, the responsivity of the material is calculated. The responsivity is simply calculated as the ratio between the generated photocurrent and the laser power:

$$\Re = \frac{I_{photo}}{P_{optical}} \tag{5.1}$$

Fig. 5.10 shows the responsivities of the different devices at a bias of 50 V and at the maximum bias voltages used for each device. The average optical power from the1550 nm pulsed laser source was approximately 64 mW.

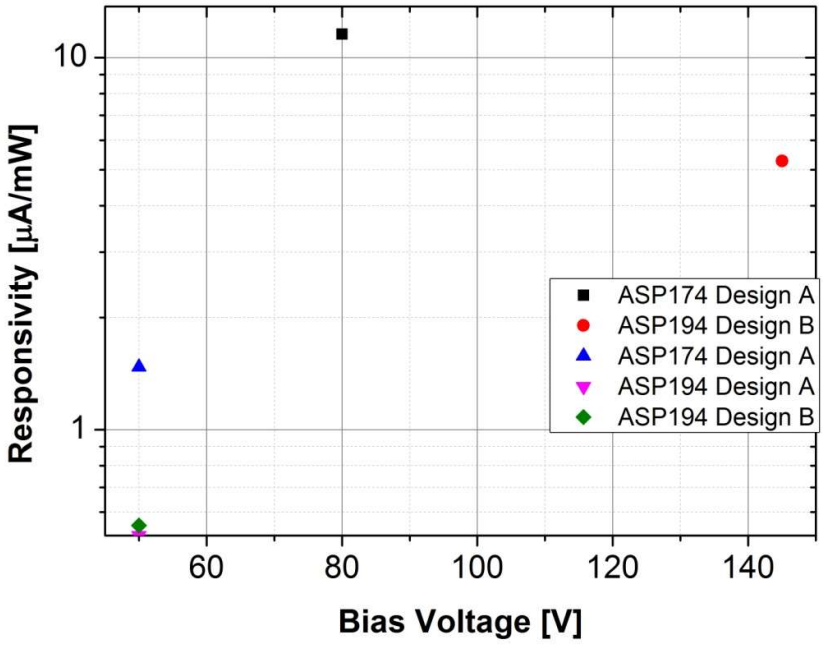

Fig. 5.10 Responsivity vs voltage bias. Design A PCS for ASP174 and designs A and B PCS for ASP194.

From Fig. 5.10, it is clear that ASP174 shows the best responsivity between the two materials. However, ASP174 displays a fast-increasing current to the voltage at low bias (50 V), shown in Fig. 5.7, which prevents a higher operating bias voltage.

The responsivities of these two devices are then compared with the device from Ref. [1], at a bias voltage of 75 V. The values are the following: 7.8 μA/mW, 1.44 μA/mW and 1 μA/mW for ASP174, ASP194 and Ref. [1], respectively. This proves that ASP174 and ASP194 are better samples due to their higher responsivities, which is an important characteristic since THz generation depends also on photo-current, as discussed in Chapter 2.

5.1.4 Infrared filter

The next step was to measure the THz power that the device radiates. Measuring THz power has always been a challenge to researchers, in particular when doing so with ultrafast photoconductive antennas driven by cw or pulsed lasers and characterized with

broadband thermal detectors such as pyroelectrics. With 780-850 nm lasers driving GaAs devices, the problem is usually thermal IR radiation created by the laser-induced heating of the devices, as 780 and 850 nm radiations are readily absorbed by both the GaAs substrate and the silicon lens. With 1550-nm lasers driving InP-, GaAs-, or Si-based devices (the case for this research), an additional problem is the significant leakage of the 1550-nm power through the substrate and the silicon lens. In either case, the THz power is skewed upwards by the 1550-nm radiation that leaks through. To negate this issue, a logical solution is to use better filters that have superior IR blocking capability while allowing excellent THz transmittance.

Black polyethylene (PE) has been used in this way for decades. For example, Blea et. al. [113] showed in detail its performance as a millimeter/THz low-pass filter. Black PE filters are particularly useful for testing 1550-nm-driven ultrafast devices [114]. During the course of this research, a new type of filter based on black polypropylene (black PP) was discovered and shown to provide even better rejection of the 1550 nm than black PE while increasing the THz transmittance. Side by side, two samples were tested: a 1.59 mm thick typical black PE filter (Filter #1) and a new 1.14 mm thick black PP filter (manufactured by Amari Plastics [115]) (Filter #2).

The IR characterization was done using the Cornerstone™ 260 1/4 m VIS-NIR Monochromator, a grating spectrometer, covering from 1.1 μm to 3 μm (Fig. 5.11). Both filters show attenuation greater than 30 dB at 1550 nm, limited only by the noise floor of the pyroelectric detector. To further quantify the attenuation of these two filters at said wavelength, a large area germanium photodiode and a sensitive electrometer (a Keithley Model 6514 System Electrometer) were used. Two laser sources were tested: a 1550-nm continuous source and a 1550-nm mode-locked laser.

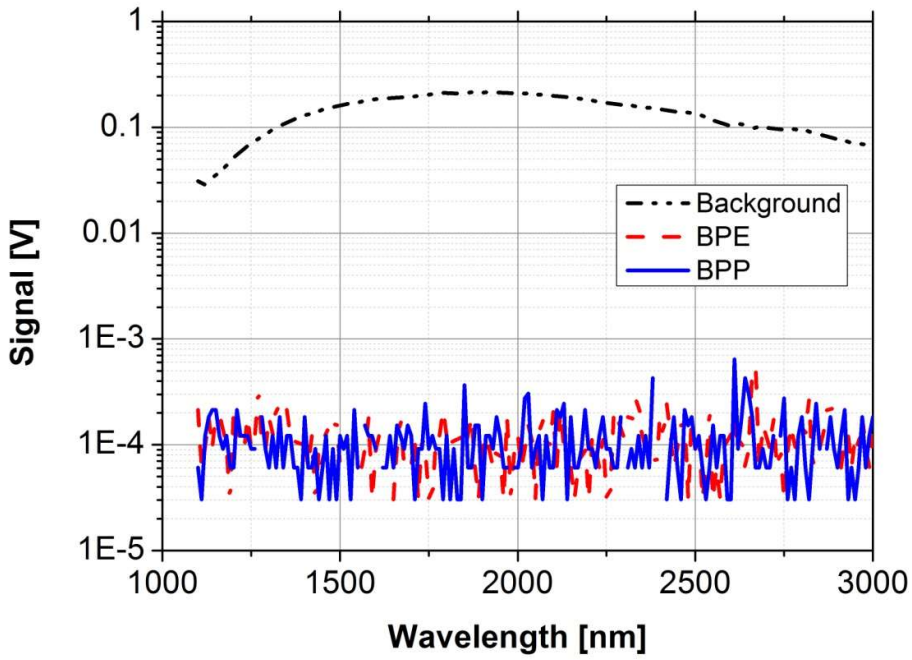

Fig. 5.11 Infrared transmission signals: BPE in red, BPP in blue, background in black.

Both sources were set to generate an average optical power of 30 mW. An attenuation of approximately 75 dB was measured for both filters (limited again by the instrumentation), yielding absorption coefficients of around 107 cm^{-1} for the filter #1 and 150 cm^{-1} for the filter #2. Thus filter #2 has better IR attenuation than filter #1.

The two filters were then measured for transmission in the THz region with an Emcore PB7200 THz frequency-domain spectrometer. The results are shown in Fig. 5.12. In the range of 200 to 600 GHz the transmission (T) for filter #2 is above 80%, while T for #1 is above 60%; in the range from 600 to 1200 GHz, T for #2 is well above 60%, while the T for #1 decreases almost linearly down to approximately 30%. This proves the better performance of the filter #2 for THz transmission.

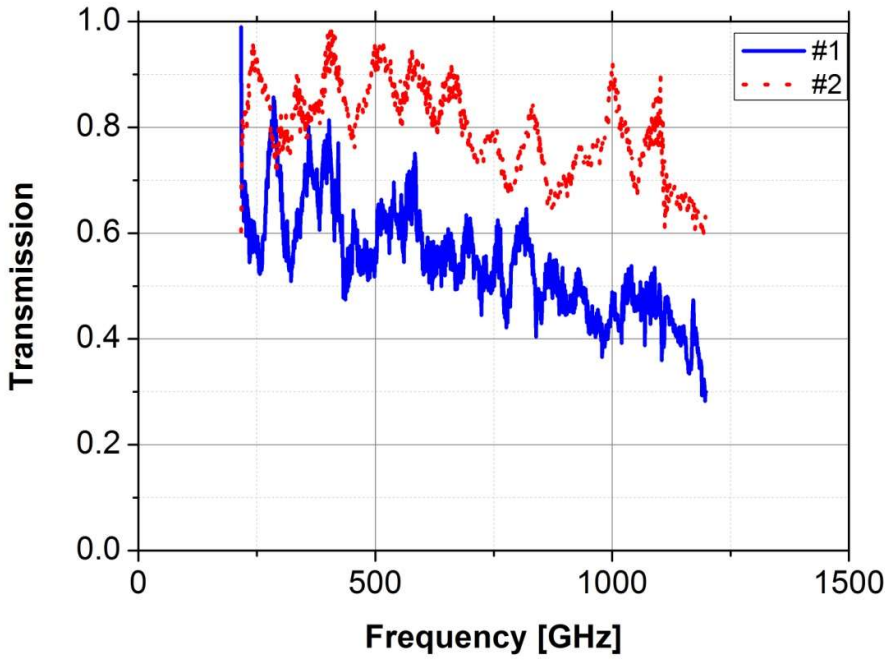

Fig. 5.12 THz transmission of filter #1 and filter #2.

The THz attenuation coefficients α for both samples were calculated from transmission and plotted in Fig. 5.13. Quantitatively, α_2 of filter #2 (PP) is smaller than α_1 of #1 (PE) across the entire 10-40 cm^{-1} range. This demonstrates the superior performance of filter #2 for THz transmission. From the standing-wave interference maxima of Fig. 5.12 the refractive index for filter #2 is estimated to be n_2 roughly 1.48. Interestingly, the experimental data were compared with the empirical formula for Dow black PE obtained previously [113], $\alpha=A^{3/2}/(1+B\nu)$, where ν is the wave number and where $A=2.27\times10^{-2}$ and $B=2.12\times10^{-3}$ are the two parameters that depend on concentration, density and size of the carbon particles. Surprisingly, the curve of filter #2 has better agreement with the empirical curve than the one of filter #1 (Fig. 5.13). A possible explanation is that filter #2 may contain different size and different concentration of carbon particles in a way similar to the Dow black PE while the typical PE filter #1 doesn't.

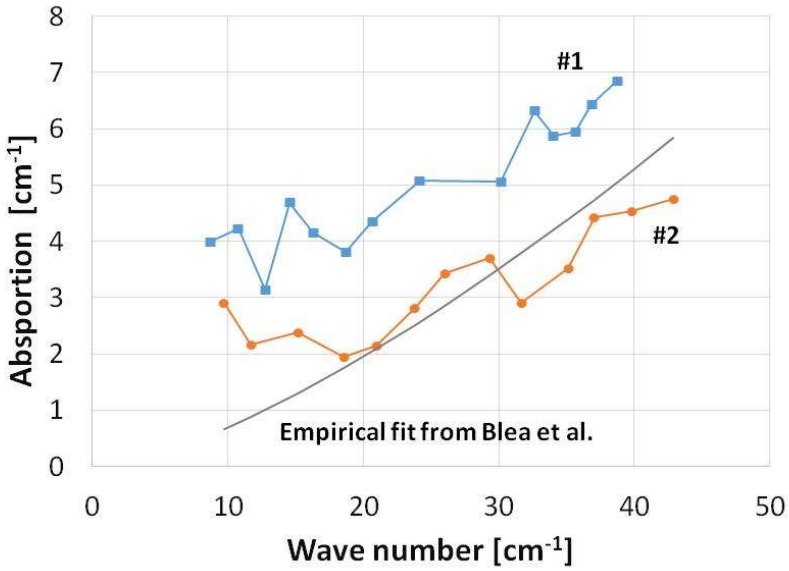

Fig. 5.13 Absorption coefficients of filter #1 and filter #2.

Thus, this new IR-blocking low-pass THz filter has superior performance in transmitting THz power while blocking leaked 1550 radiation. This helps improve the accuracy of the THz power measurements.

5.1.5 THz Power Measurement

The setup used for this experiment is shown in Fig. 5.14 and it is very similar to the one used for photocurrent and photo responsivity shown in Fig. 5.6. A Menlo T-Light 1550-nm mode-locked laser, having ≈90 fs pulses and 100 MHz repetition rate, was used to pump the devices. The maximum available power was P_{1550} = 84 mW and, in order to vary the laser power, a wheel attenuator was added to the setup.

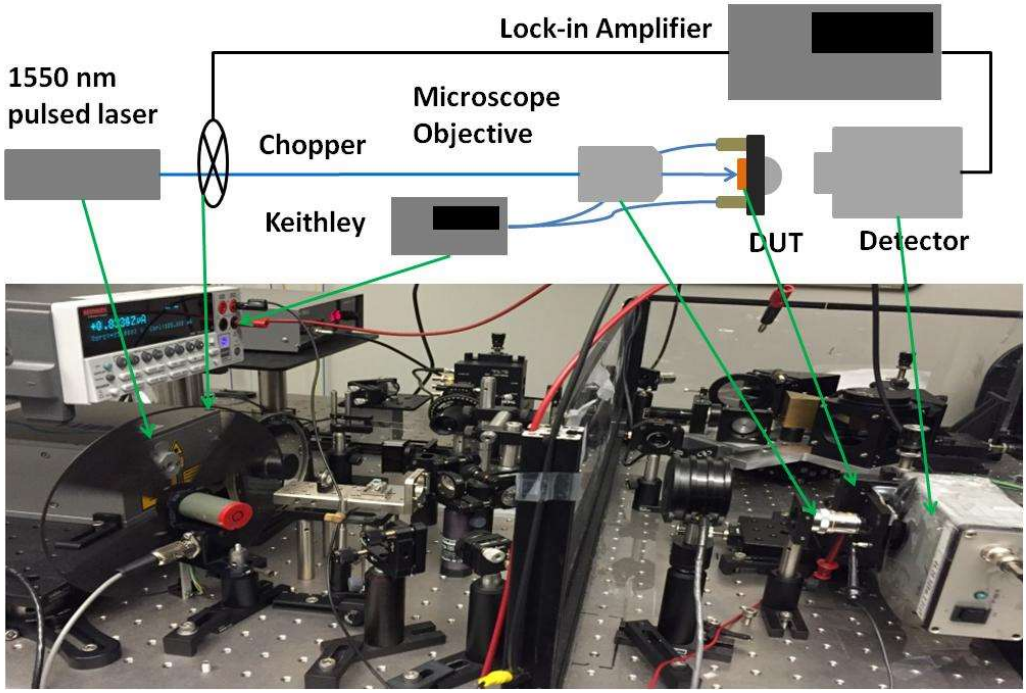

Fig. 5.14 Schematic of the setup for THz power measurements, block diagram on top, picture on the bottom.

The beam was focused with an achromatic standard microscope objective (NA=0.25, EFL=15.2 mm) to be concentrated within the 9 × 9 μm center gap of the spiral antenna. The objective was found to have a transmission, T_{obj}, of around 77% at 1550 nm. The efficiency of the 1550 nm radiation coupled to the device at the air-substrate interface, $T_{substrate}$, is equal to 1-$R_{substrate}$, and $R_{substrate}$ is

$$R_{substrate} = \left(\frac{n_{GaAs} - 1}{n_{GaAs} + 1} \right)^2 \tag{5.2}$$

where is n_{GaAs}= 3.37 is the refractive index of GaAs [116]. $T_{substrate}$ is estimated to be around 0.7. The leaked 1550 nm through the substrate as well as the silicon lens, P_{leak}, was measured to be approximately 2.8 mW when the incident laser power, P_{1550}, was around 84 mW.

The power was first characterized for radiated emission at frequencies above 100 GHz using one of the following detectors connected to an SRS SR810 DSP lock-in

amplifier: a Gentec-EO QS-I-TEST large-area pyroelectric coupled to a 0.34-in-diam brass flared tube, with the flared end placed flush against the Si hyperhemispherical lens [117], or a QMC OAD-7 Golay Cell detector. Both the detectors' responsivities were obtained by cross-calibration against a 104-GHz Gunn oscillator measured with a traceable waveguide thermal power meter, and then attenuated down to microwatt levels. The Gentec-EO QS-I-TEST was determined to have a responsivity of 10000 V/W, and similarly the Golay Cell was tested to have a responsivity of 7000 V/W.

In order to measure photocurrent, the devices were aligned to the focused laser coming out from the microscope objective lens using the same procedure as what was done in 5.1.2. The detector was mounted on a 3-axis stage to position the aperture of the detector so that it intercepted the THz beam and maximized the reading on the lock-in amplifier.

The first sample tested for THz power radiation was ASP174. The antenna design used for this device was design A (9 μm gap width and 9 μm arm width). The detector used was the Gentec-EO QS-I-TEST large-area pyroelectric detector coupled with a brass flared tube. The aperture of the detector was placed 2 millimeters away from the HRFZ silicon lens of the packaged device. The results are shown in Fig. 5.15, where the left axis displays the lock-in signal and on the right axis the correspondent THz broadband power.

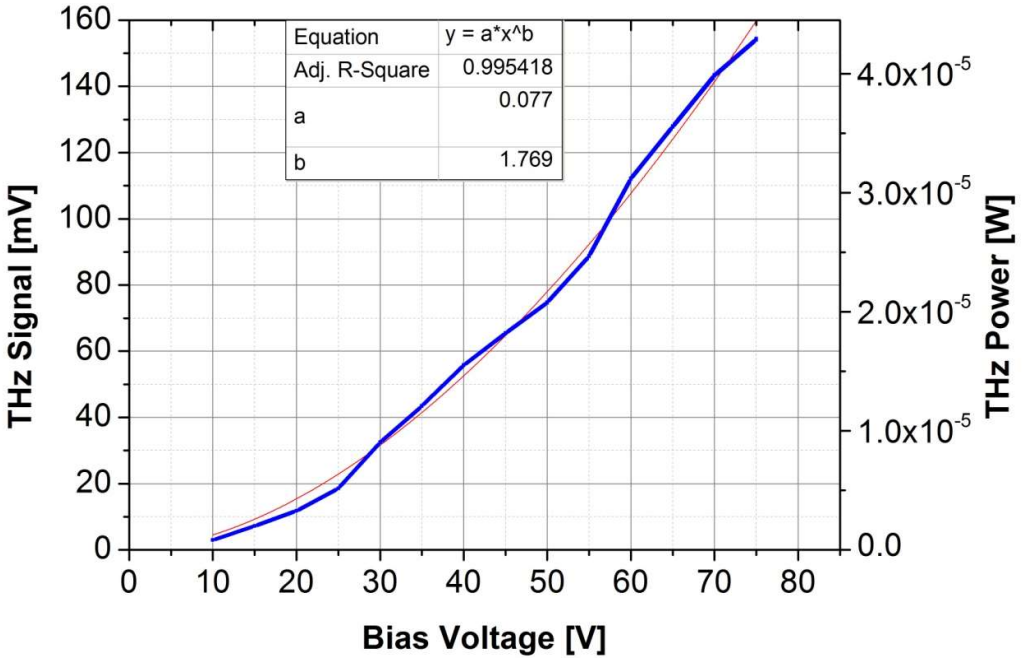

Fig. 5.15 Design A, ASP174, THz power vs bias voltage.

The maximum THz power radiation, when the device was biased at 75 V (across the 9 μm gap of the active region), reached a value of 42 μW, which is enough for imaging applications. Fig. 5.16 shows the THz power dependence to photo-current. As can be seen, the dependence is sub-linear with saturation at high photo-current values.

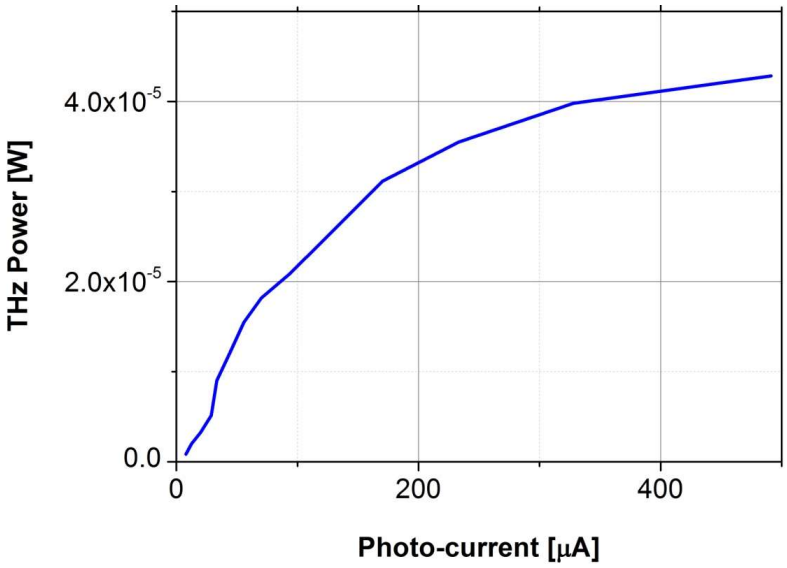

Fig. 5.16 Design A, ASP174, THz power vs photo-current.

The optical-to-THz efficiency was then measured more accurately using the following formula:

$$\eta \approx \frac{P_T}{P_{1550} T_{obj} T_{substrate} - P_{leak}} \tag{5.4}$$

where P_T is the THz generated power, P_{1550} is the maximum available output 1550-nm laser power (approximately 84 mW), T_{obj} is the microscope objective transmission (equal to 77%), $T_{substrate}$ is equal to 1-$R_{substrate}$ as shown in equation (5.2), and P_{leak} is the leaked 1550-nm radiation through the substrate as well as the silicon lens. P_{leak} was measured to be around 2.8 mW when the incident laser power, P_{1550}, was roughly 84 mW, and an optical-to-THz power efficiency of 0.095% was obtained. Noticeably, the dependence of the power on the bias voltage is superlinear with an exponent of 1.76, close to quadratic.

As can be seen, there is still no sign of saturation in the THz power, so more power could be obtained by biasing the device at a higher voltage. However, as described in Fig. 5.7, increasing the bias voltage would most likely drive the device to breakdown due to the very large current already being drawn by the device and the consequent large amount of heat generated. Already at 75 V bias, the rise in temperature of the device in the active region, under the assumption that all the current flows through it, is:

$$\Delta T = R_{thermal} (P_{el} + P_{laser}) \tag{5.3}$$

where P_{el} is simply the electrical power (V·I), P_{laser} is the optical laser power hitting the device, $R_{thermal}$ (806 °C/W) is the thermal resistance of the active region, calculated as $1/(\sqrt{(2)}\, k\pi r)$ where k is the thermal conductivity of GaAs (0.55 W/cm-K), and r is

the equivalent radius of the active region. In this case, with V = 145 V, I ≈ 600 μA and with a P_{laser} = 64 mW, the temperature increases by 120 °C.

Afterwards, the dependence of the THz signal (or power) on the optical laser power was measure. The result is shown in Fig. 5.17. To perform this test, a wheel attenuator was placed on the path of the 1550-nm laser beam in order to obtain the desired amount of laser power to drive the PC switch when biased at the constant voltage of 35 V.

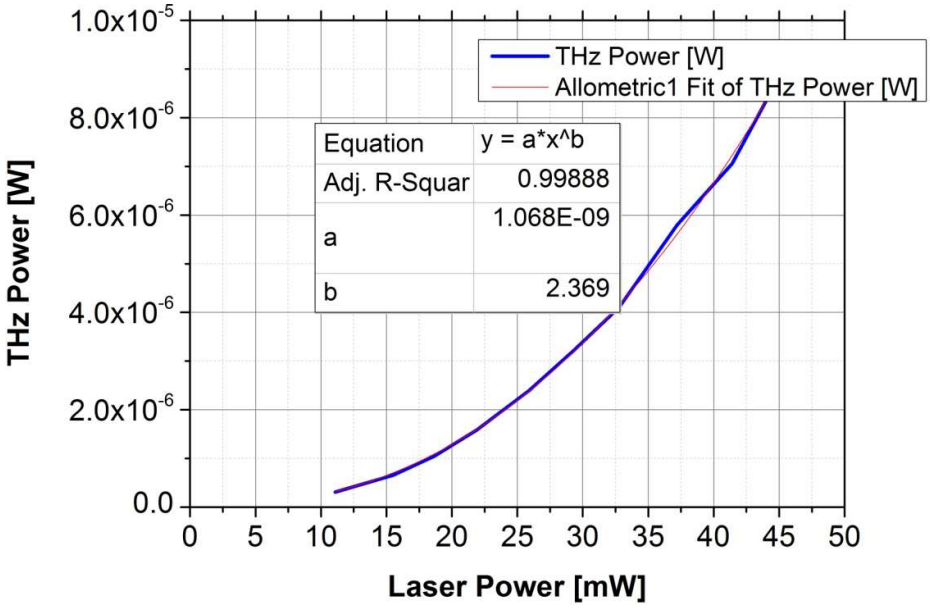

Fig. 5.17 Design A, ASP174, THz power vs laser power under constant bias of 35 V.

Looking at the graph, it can be seen that the dependence follows a power law with an exponent of 2.37, suggesting that the laser power is more important than bias voltage for THz power generation. Interestingly, it is clear that there is still no sign of saturation, and therefore even larger optical power could be used to further increase the generated THz power. However, in this case, increasing the laser power may lead to a thermal breakdown of this particular device as the current is already large (almost 800 μA) under these "safe" operating conditions (75 V of bias and 64 mW of incident laser power). From Fig. 5.16 and Fig. 5.17, it can be noticed that while the THz power increases with both photo-current and bias voltage, the THz power increases faster

based on the latter. As such, it is more important to be able to apply higher bias to the devices than generating a larger photo-current.

ASP194 with the same design A (9 µm gap width and 9 µm arm width) was then tested under the same conditions. The results are plotted in Fig. 5.18. A maximum THz power generation of 22.8 µW was achieved, corresponding to an optical-to-THz efficiency of 0.0518%. Fig. 5.19 shows the dependence of the THz power to photo-current. In this case there is a nearly linear dependence.

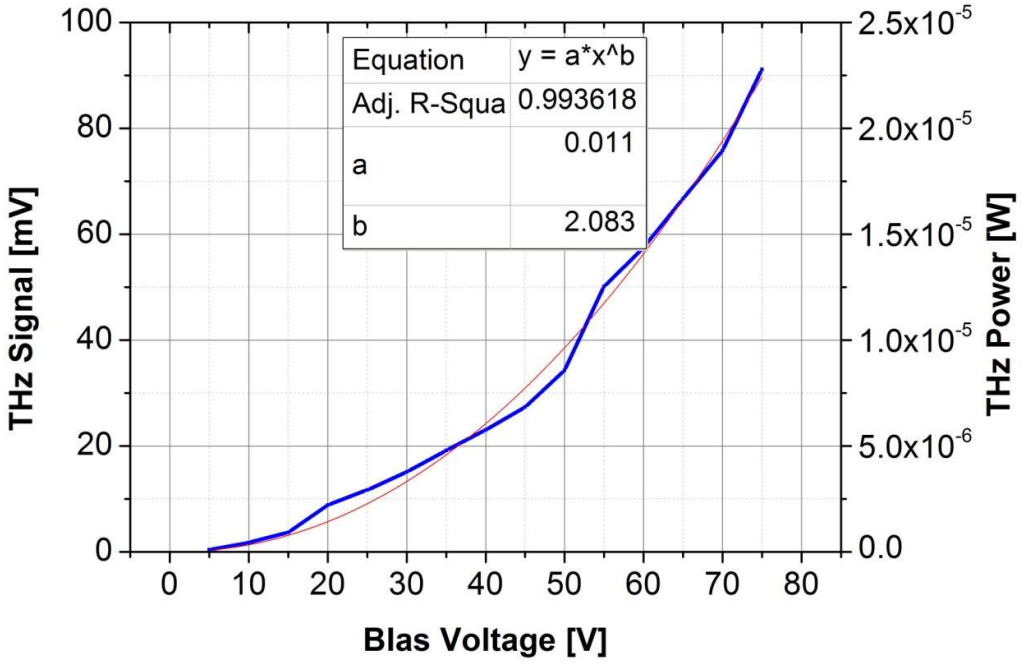

Fig. 5.18 Design A, ASP194, THz power vs bias voltage.

Even in this case, the dependence of the THz power to bias voltage is stronger than to photocurrent. The THz power dependence vs laser power was tested for this material as well, this time when biased at 100 V. Results are shown in Fig. 5.20. An exponent of 2.15 was obtained when performing a power law fitting. From Fig. 5.20 there is still no sign of saturation of the THz power, even at the highest laser powers.

This proves that for THz generation laser power and bias voltage are more important than photo-current.

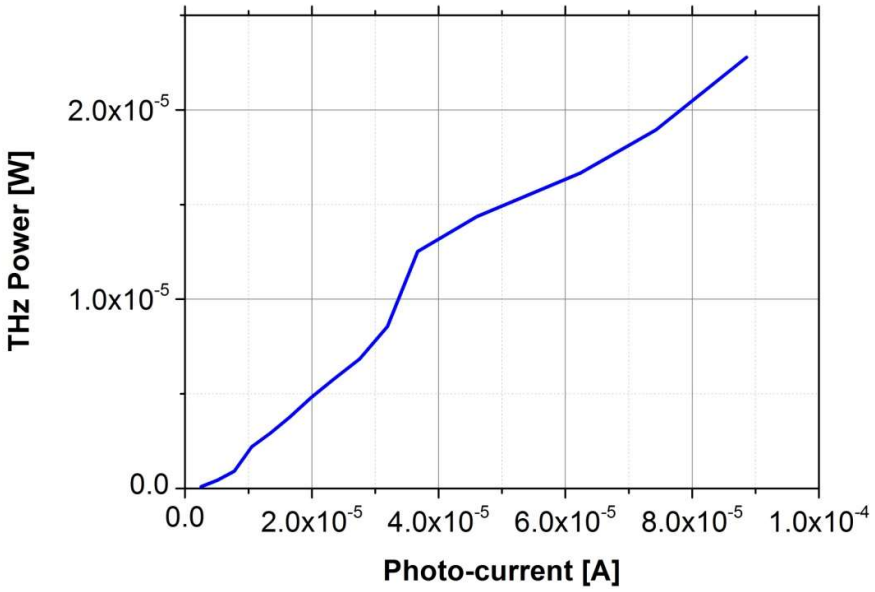

Fig. 5.19 Design A, ASP194, THz power vs photo-current.

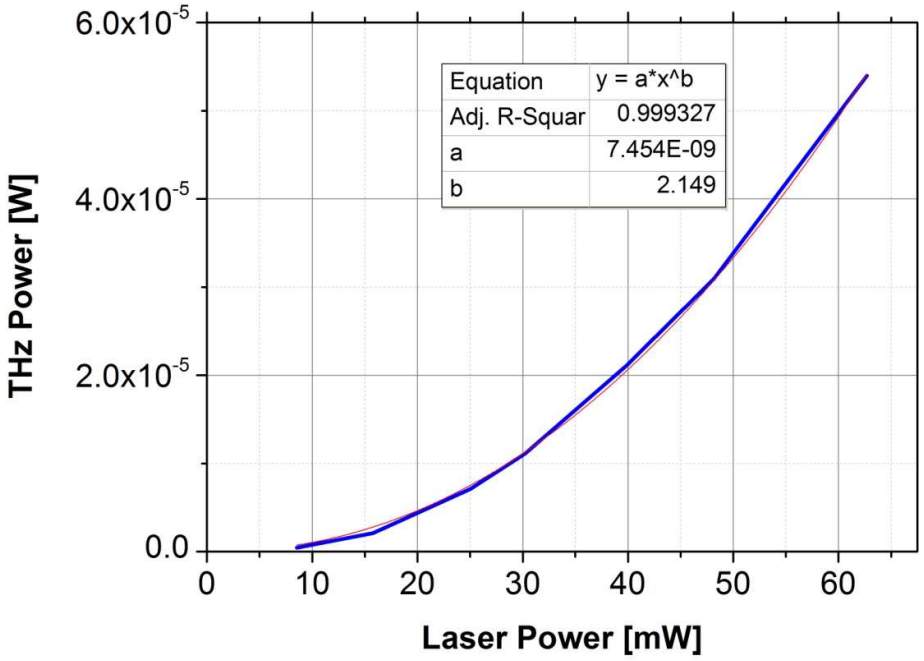

Fig. 5.20 Design A, ASP194, THz power vs laser power under constant bias of 100 V.

The results obtained from ASP174 and ASP194, under the same operating conditions, and using the same design (type A), were then compared. Specifically, the ratio of THz power generated to the photocurrent generated was sought, and the results are shown in Table 5.3.

Table 5.3 THz power, photocurrent and ratio for design A PCSs fabricated on ASP174 and ASP194.

Substrate	THz power [μW]	Photocurrent [μA]	Ratio [μW/μA]
ASP174	42.8	728	0.059
ASP194	22.8	47.5	0.48

The ratio calculated in this Table demonstrates an important characteristic. A material with a higher ratio can be biased at a higher voltage, generating more THz power while keeping the heat generation low, thus reducing the chance of breakdown.

With this in mind, the device fabricated on ASP194 was tested for THz power generation with the design B (14 μm gap width and 4 μm arm's width) under the same operational condition. The results are shown in Fig. 5.21.

As made clear by the figure below, the modification of the design leads to an increase of the THz generated power from the device by a factor of about 50%, from 22.8 to 35.2 μW. This increase resulted in an improved optical-to-THz power efficiency, from 0.0518%, of 0.08%. In addition, the exponent of the power law fit increased from 2.08 to 2.53. Since the dark-current was low, higher bias voltages (up to 145 V) were tested, and the results are shown in Fig. 5.22. Fig. 5.23 shows the THz power dependence to photo-current.

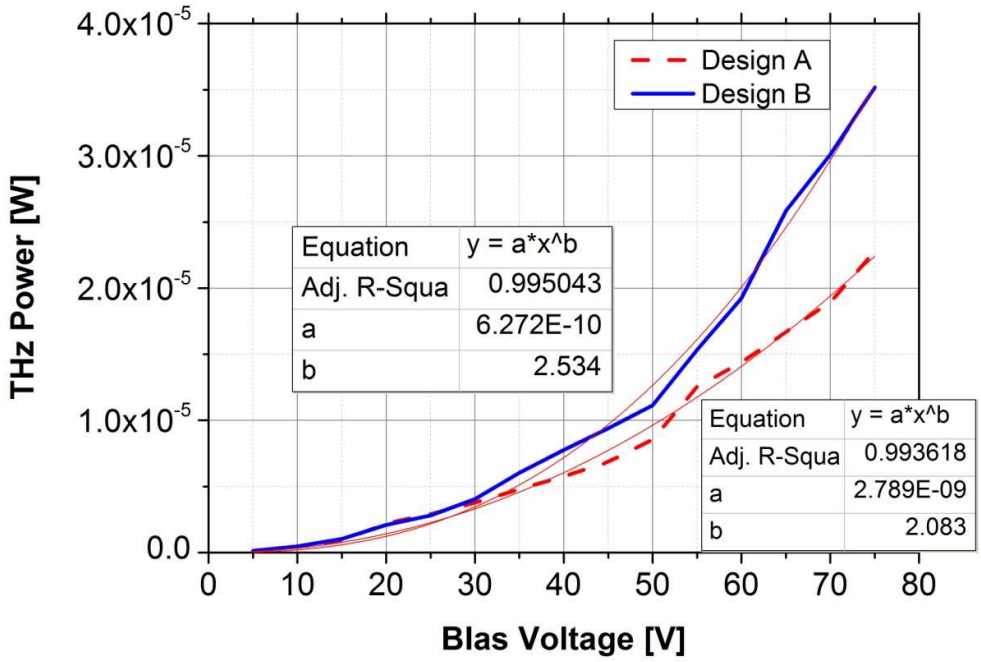

Fig. 5.21 ASP194, THz power vs bias voltage. Comparison between the design A (in red) and B (in blue).

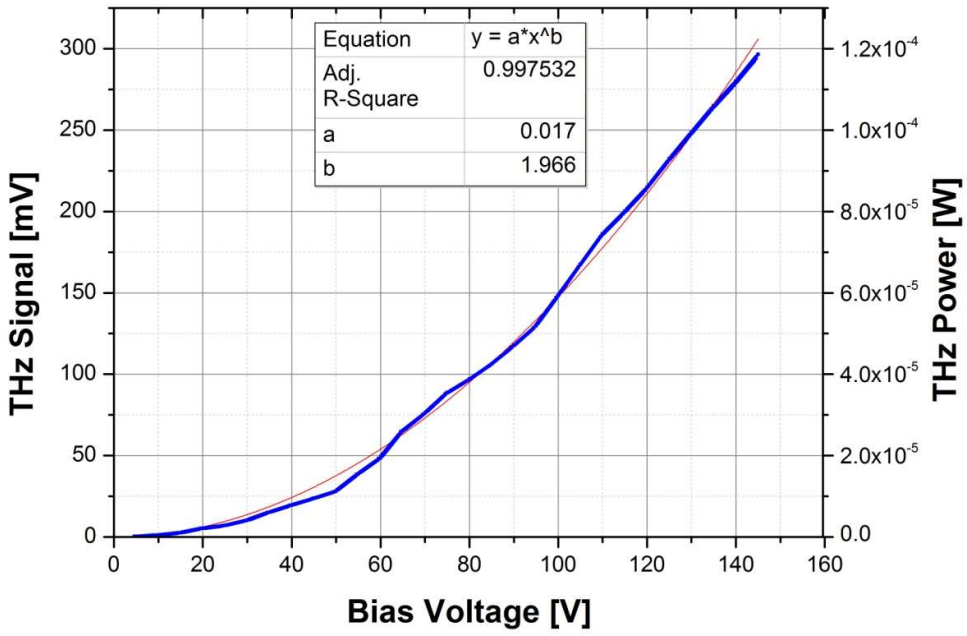

Fig. 5.22 Design B, ASP194, THz power vs bias voltage [118].

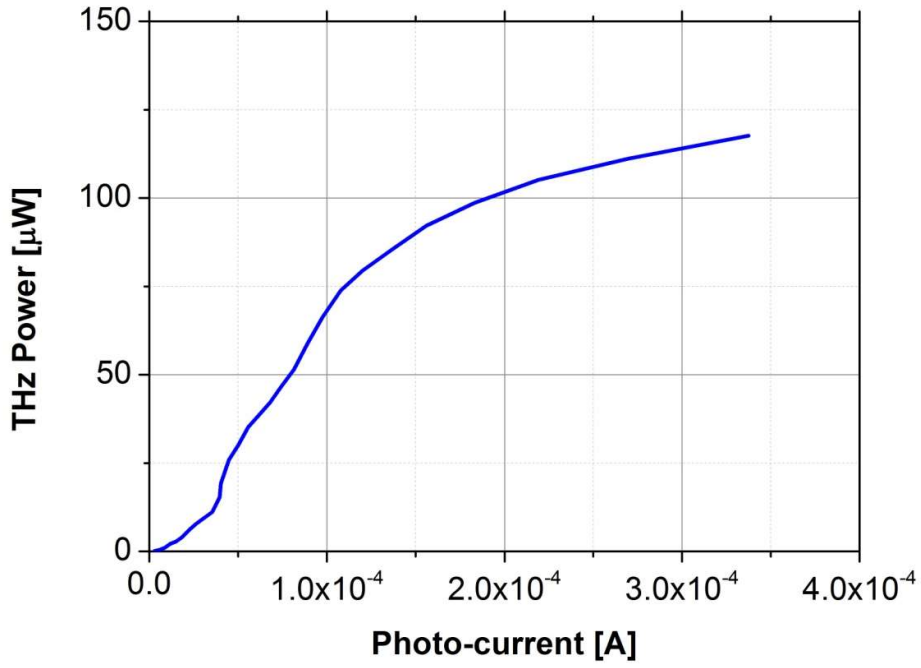

Fig. 5.23 Design B, ASP194, THz power vs photo-current.

The dependence of the THz power on bias voltage closely matches a quadratic curve. At 145 V, this device generated a record broadband THz power of 117 μW [118] amongst devices driven at 1550 nm. The optical-to-THz efficiency of 0.266% renders these devices competitive with the state-of-the-art 1550-nm driven THz PCS based on intrinsic photoconductivity [68], [78] as shown in Fig. 5.24.

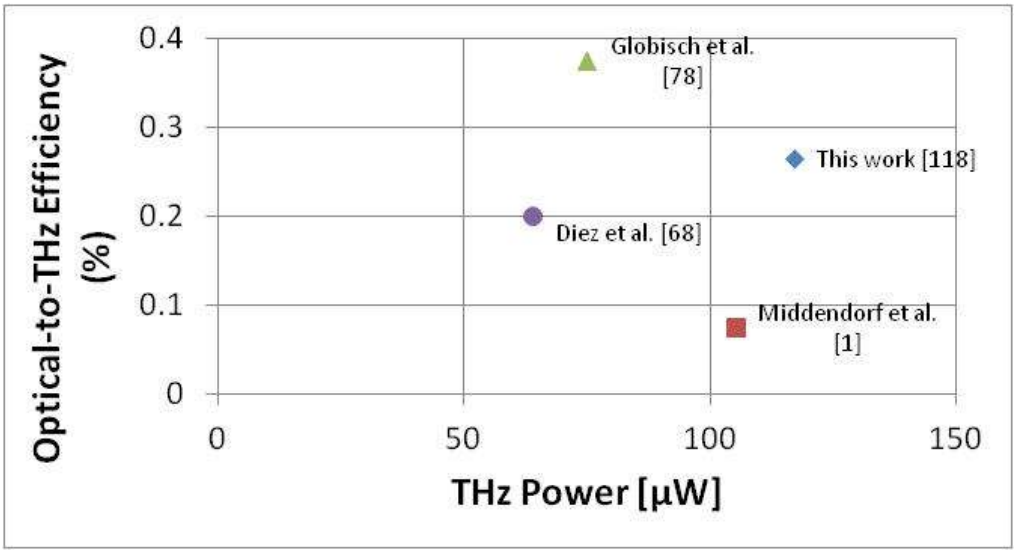

Fig. 5.24 THz power (on x-axis) and efficiency (on y-axis) of THz PCS driven at 1550-nm, state-of-the-art.

In particular, when comparing the result of the devices developed during this research to those from Ref. [1] based on the same material, not only the THz power generation was greater, but the efficiency was increase of about 3 times.

5.1.5.1 THz power polarization radiation

Because of the geometry of the antenna, the polarization was expected to be circular. To confirm this assumption, a test was performed in order to check the type of polarization that this device radiates. Using the same setup used for measuring the broadband THz power, the detector was moved further away from the device in order to insert a wire-grid polarizer (WGP). This type of WGP was developed by Drs. J. Cetnar and J. Middendorf at Wright State University and was proven through experimentation to possess an extinction ratio >35 dB [119]. By rotating the stage over 360 degrees, the polarization can be measured using the WGP. The measurement was taken on a PC antenna with design B fabricated on ASP194. The result of this measurement is shown in Fig. 5.25, where the radial axis is plotted in linear scale.

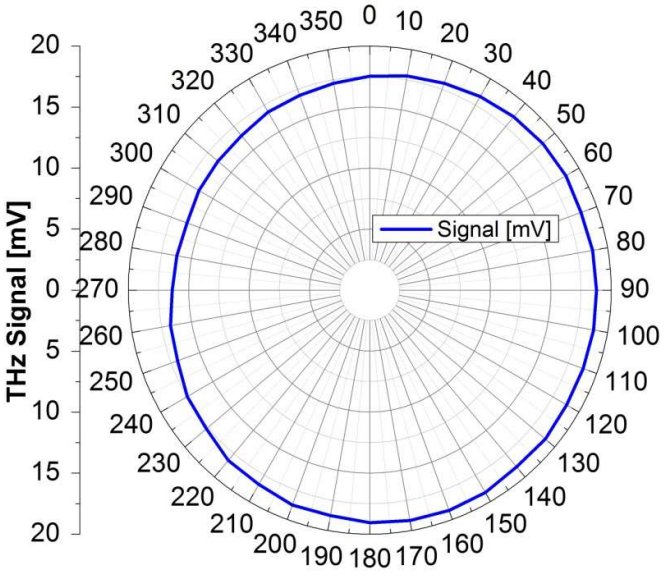

Fig. 5.25 Polarization radiation pattern of a design B PCS fabricated on ASP194.

As it can be seen, the radiation pattern is indeed very close to be perfectly circular.

5.1.6 Toward optimum conversion efficiency, a comparison between gap and finger devices

With the interest of creating a more compact THz source, the attention was turned to the optical efficiency of photonic sources at light-wave frequencies, which is an issued that had largely been overlooked. This is due to the fact that THz sources have struggled to reach useful power levels in system applications. Because THz emission has become more powerful, the goal of reaching an *optimum efficiency* was looked into in order to understand whether such optimum performance could be obtained with a lower average optical power than the approximately 100 mW available from typical fiber mode-locked lasers. The ideal would be down to the roughly 10 mW level that can be provided by semiconductor mode-locked diode lasers.

In order to reach this optimum efficiency, the gap device fabricated on ASP194 with the design A was tested at the bias voltage of 100 V. The resulting conversion efficiency versus laser power is plotted in Fig. 5.26. The conversion efficiency is calculated according to Eqn. 5.3. Even though they are lower than the η values reported for intrinsic (cross-gap) GaAs PC switches, they are amongst the highest for 1550-nm devices.

The performance of a similar PCA to the one shown in Fig. 4.18, but driven at 780-nm, has been studied using a large-signal circuit model [Fig. 5.27 (a)]. In this study, the PC switch's photoconductance G(t) is a strong function of laser instantaneous power and therefore time [120], [121]. The laser power creates the THz pulse across the load resistance R_L, which consists of both the antenna radiation resistance R_A and the internal series resistance R_S. By averaging the THz pulse across R_A, the average power P_{THz} can be obtained. When this quantity is divided by the average laser power $P_{0,}$ it

yields the efficiency curve η versus P_0 in Fig. 5.27 (b) [120], [121]. The curves in Fig. 5.27 (b) depict the characteristic peaked behavior for power delivered from a source to a resistive load in a microwave circuit.

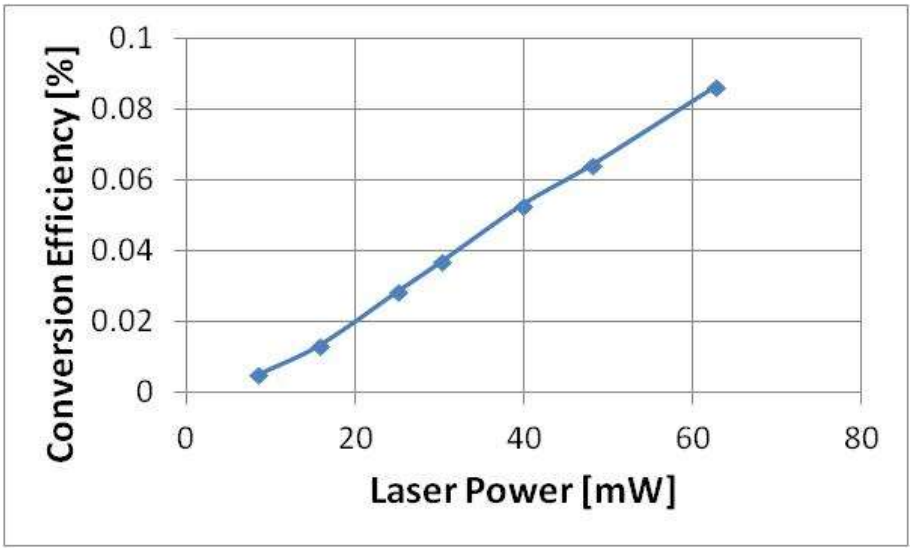

Fig. 5.26 Experimental results of conversion efficiency vs laser power on ASP194 PCS, gap device.

In order to achieve this efficiency at much lower laser power, the interdigital-electrode (IE) PC switch structure shown in Fig. 5.28 was investigated. This structure has been used for a long time for making photomixers, while IE PC switches have been rarely implemented, if ever, because of the added cost of fabricating their deep-submicron features. The advantage is that the IE structure increases the device photoconductance by a factor of around N_{sq} – which is the number of active "squares" as shown in Figure 5.28. This highlighted benefit assumes that the laser illumination intensity is kept the same and that the bias electric field between neighboring electrodes is the same as in a gap device without electrodes.

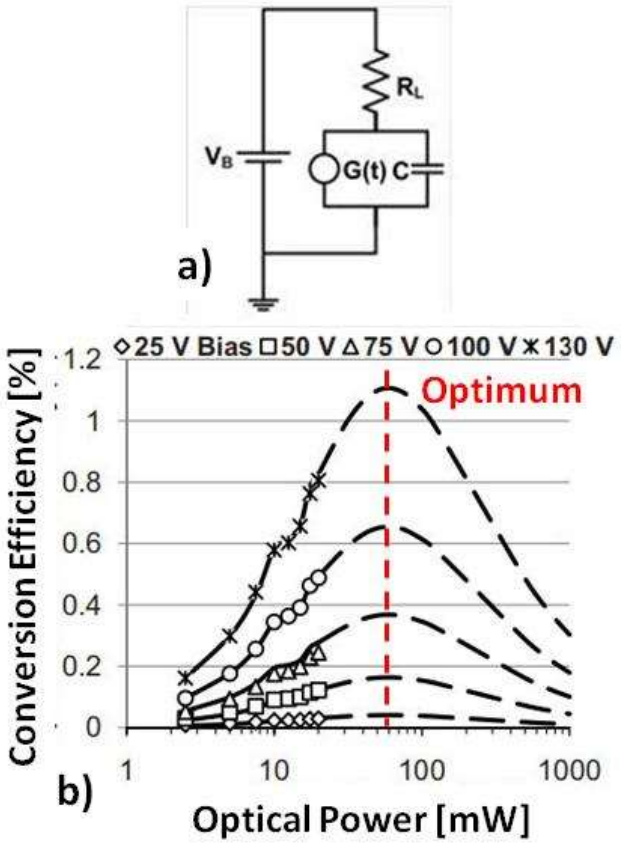

Fig. 5.27 (a) Large signal model of the PCS and (b) conversion efficiency vs optical power when driven at 780 nm.

Additionally, the introduction of the IE structure can cause changes in the capacitance C shown in Fig. 5.27 b), affecting the bandwidth of the device through the $R_L \cdot C$ electrical time constant ($R_L \cdot C = \tau = 1/\omega$). For the IE structure shown in Fig. 5.28, $N_{sq} \approx 25$, so that the optimum laser power in Fig. 5.27 (b) is reduced to ≈10 mW – an average power obtainable from 1550-nm, semiconductor-diode mode-locked lasers. Since such lasers can generally operate with much higher repetition frequency than fiber lasers and can also be embedded in photonic integrated circuits (PICs), it is possible to have THz pulse generators and perhaps THz transceivers on the same chip.

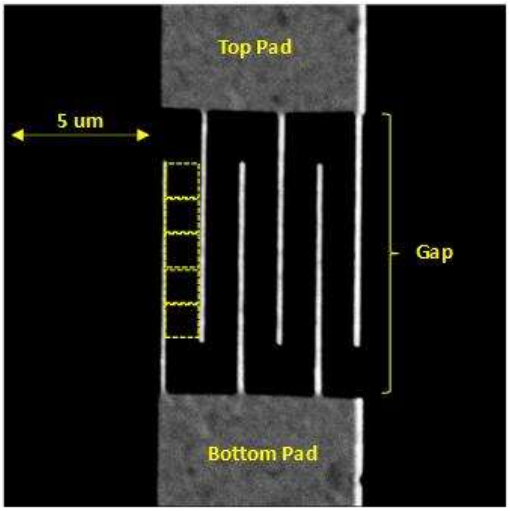

Fig. 5.28 Detail of the photomixing region.

To verify this model at 1550-nm, a comparative study was conducted on a pair of PC switches similar to the one of Ref. [118]. Two devices were tested, both fabricated on ASP194 using the design A for the PCS. One device had the same design with the "gap" that has been tested previously, while the other had the addition of optical fingers in the active region (IE) (Fig. 5.29).

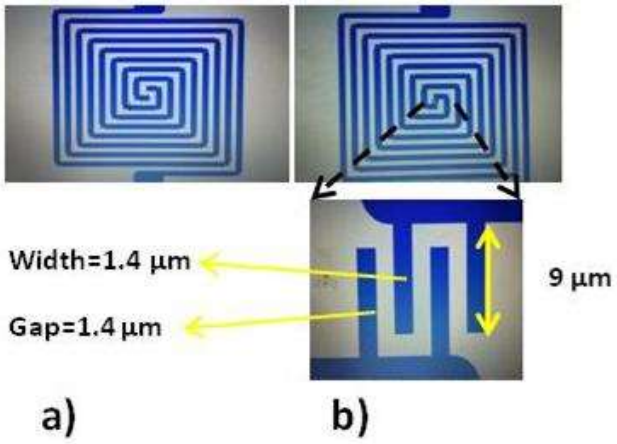

Fig. 5.29 Design a) of the gap device and b) of the finger device.

In these devices, the width and the distance between electrodes was 1.4 µm, and N_{sq} is estimated to be roughly 13.2. Otherwise, the epilayer, fabrication, and test conditions were kept the same. The illumination power at 1550 nm was approximately 43 mW,

and the spot size was about 10 μm. For safe operation, the bias voltage on the gap device was maintained well below the maximum. The results of this study clearly demonstrate that the IE device shows better responsivity (R) (Fig. 5.30) and greater optical-to-THz conversion efficiency (Fig. 5.31) than the gap device, which is consistent with the large-circuit model. To give an example, the performances at 9 V on the IE device and at 50 V on the gap device, such that their bias electric fields are approximately the same, can be compared. In this example, the values for responsivity are approximately 1.41 and 0.70 μA/mW, respectively. Those for efficiency, η, are 0.028% and 0.024, respectively. The design of the current IE device has room for optimization. For one, the use of sub-micron dimensions shown in Fig. 5.28 will reduce the IE optical reflection. This reflection is estimated to be roughly 50% in Fig. 5.29 (b). Clearly, these results are already promising, as they show an increase in both responsivity and efficiency without the use of e-beam IE and with inferior finger electrodes obtained with optical lithography.

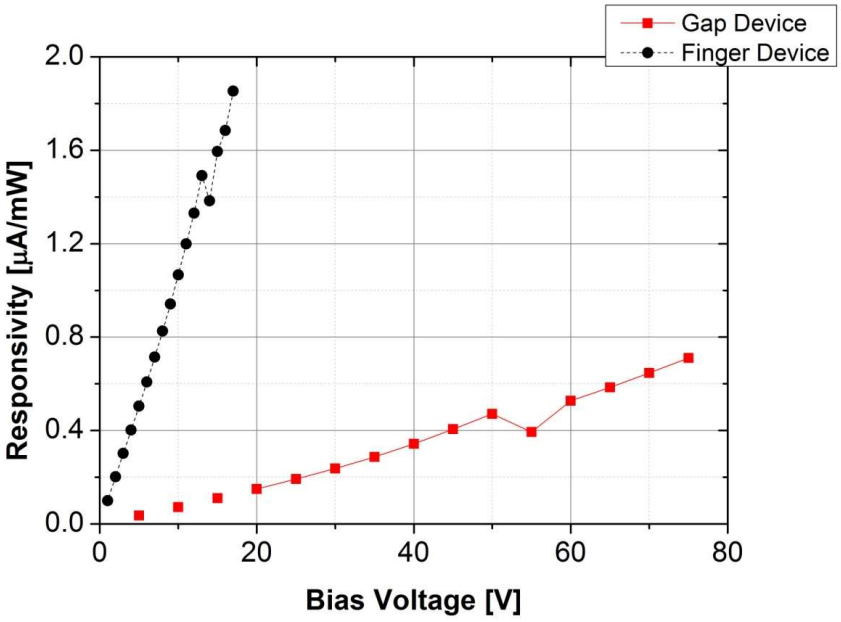

Fig. 5.30 Comparison between the responsivities of the gap device and IE device, ASP194.

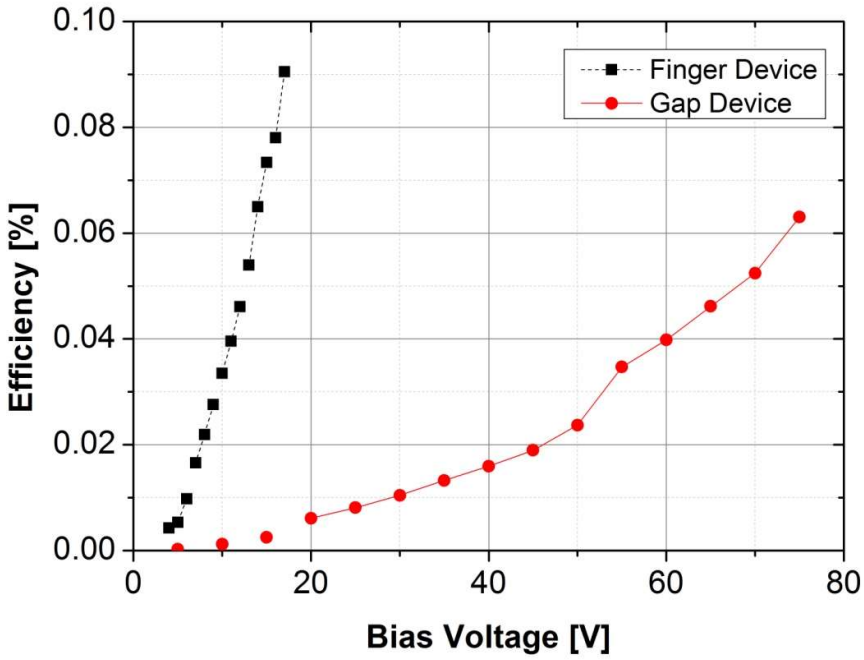

Fig. 5.31 Comparison between the efficiencies of the gap device and the IE device, ASP194.

5.1.7 Summary of spiral antenna photoconductive switches driven at 1550-nm

In summary, the introduction of the design B with the improved arm gap width from 9 μm to 14 μm effectively reduced the dark-current, as was expected. This is due to the increase of the resistance between neighboring arms, which in turn reduces the current flowing between arms and effectively forces the majority of the current to flow between the electrodes at the end of each bias line (across the active region). In addition, design B also slightly increased the photocurrent (when comparing the same material) and the THz power generated. This configuration reached a maximum broadband THz radiation of 117 μW and an optical-to-THz power efficiency of 0.266% using the material ASP194 [118]. This sample proved to be the best material when it comes to THz power over photocurrent generation ratio, a very good metric since being able to produce THz with low current enables an even higher bias voltage (higher bias voltage

leads to higher THz generation as well). Moreover, another significant milestone was the first step towards optimum conversion efficiency in order to increase both responsivity and efficiency of the antenna. This was achieved by introducing optical IE structures in the device, rather than of a simple gap for pulsed laser excitation. Though the early findings are promising, this type of test is still in its early stage and there is therefore room for improvement in the design of the device (i. e. e-beam IE writing instead of optical patterning).

5.2 Slot antenna characterization

Running parallel to the previous tests, the slot antenna device, shown in Fig. 4.19, was also fabricated and tested for responsivity and THz generation. This device was fabricated on ASP194 following the same recipe for the photolithography. Following a similar procedure, this device was diced and packaged like all the other PCS devices. Fig. 5.32 shows the dark- and photo-current of the slot antenna when under 64 mW of 1550-nm pulsed laser power. Fig. 5.33 shows the responsivity.

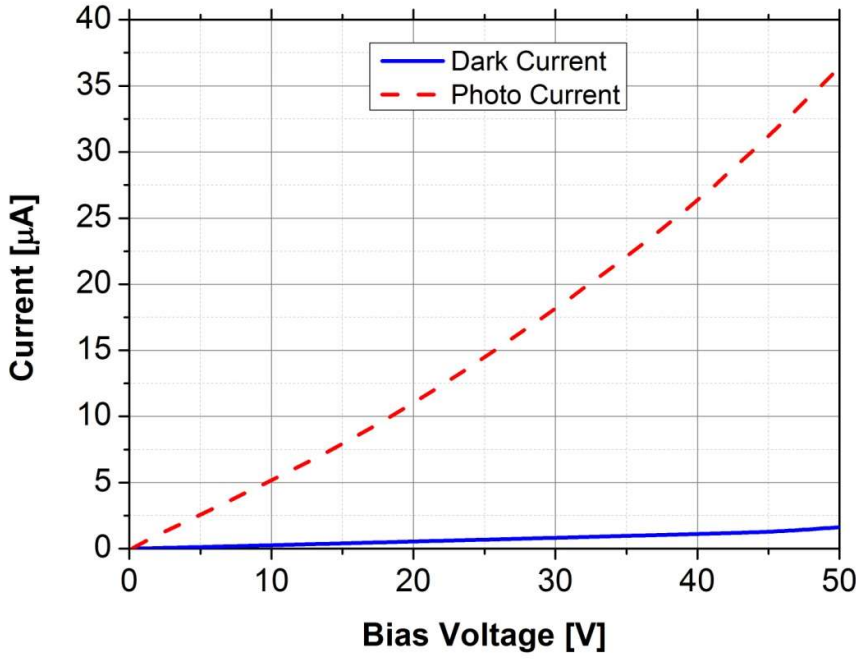

Fig. 5.32 Currents of the slot antenna fabricated on ASP194.

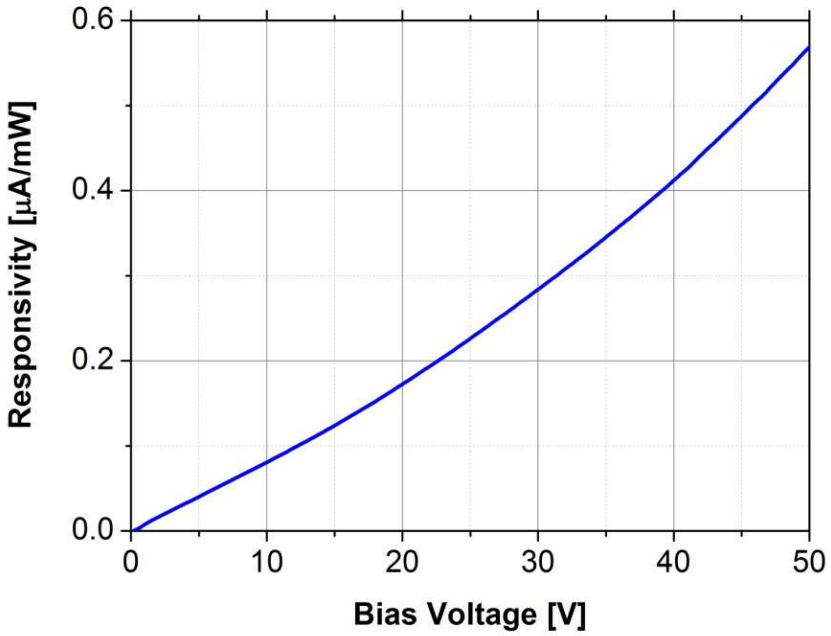

Fig. 5.33 Responsivity of the slot antenna fabricated on ASP194.

The responsivity at 50 V is 0.57 μA/mW, which is very close to the value of the responsivity obtained at the same bias voltage and under the same optical excitation of the spiral antenna PCS fabricated on ASP194.

Finally, the device was then tested for THz broadband radiation (results shown in Fig. 5.34).

As shown in Fig 5.34, the maximum generated power at 50 V is only 3 μW, compared to the 11.15 μW obtained from design B square-spiral PCS fabricated on the same material. This is due to the fact that the slot antenna radiates efficiently only around the full- and half-wave resonant frequencies. The power conversion efficiency is 0.002%.

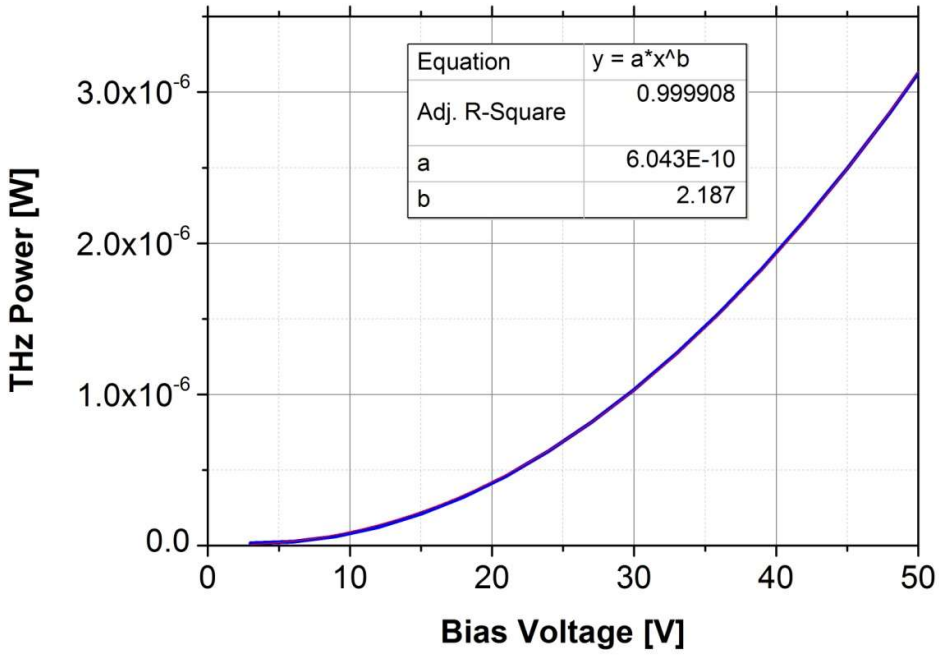

Fig. 5.34 Broadband THz radiated power from the slot antenna fabricated on ASP194.

5.3 Comparison between spiral antennae

Considering the results on the dark-currents of the square-spiral antenna design A, it was clear that the leakage current of the four-turn self-complementary square-spiral antenna was too high. In comparison, with the introduction of design B, the dark-current was effectively reduced, however an additional reduction of this current could be achieved by implementing the Archimedean log spiral antenna presented in Fig. 4.20. The resulting reduction of the dark-current with this new antenna is due to the fact that the gap between the arms increases with radial distance from the center. This increased distance consequentially increases the resistance between neighboring arms, and therefore improving the performance of this antenna in comparison to that of design B.

In order support these assumptions with data, two devices (design B PCS and the Archimedean log spiral antenna), were fabricated on the same substrate (ASP294) using the same fabrication recipe. The two antennae were tested for both dark-current and

photo current under 1550-nm pulsed laser excitation, and THz generation. Fig. 5.35 shows the comparison between the dark-currents of the two antennae. The Archimedean log spiral reduces the dark-current even further compared the design B, reducing the stress on the device.

Fig. 5.36 shows the generated photocurrent, and the difference between the two is not substantial. These results were to be expected, as the photocurrent is mostly from the center 9 x 9 μm center region, which is the same for both designs.

Finally, the THz power was measured with a Golay cell detector. The results are shown in Fig. 5.37.

An increase in the performances can be seen at higher bias voltage, consistent with the small increase in the photocurrent seen in Fig. 5.36. These results led to the possibility of a new type of antenna by merging the two designs: an Archimedean square spiral. The resulting antenna could benefit from the low dark current of the Archimedean log spiral and the higher radiation resistance typical of the square-spiral antenna.

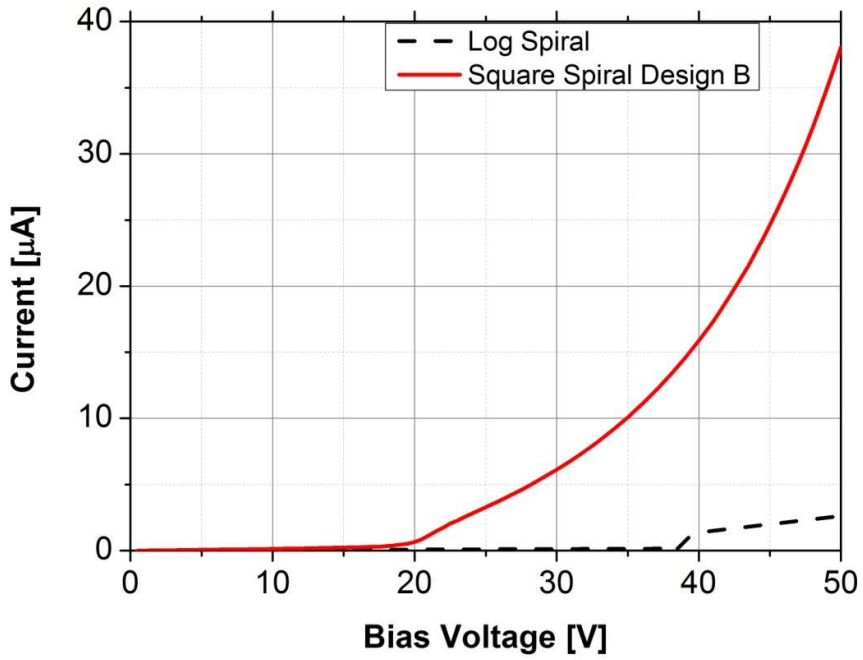

Fig. 5.35 Comparison between the dark-currents of the square spiral antenna and the Archimedean log spiral.

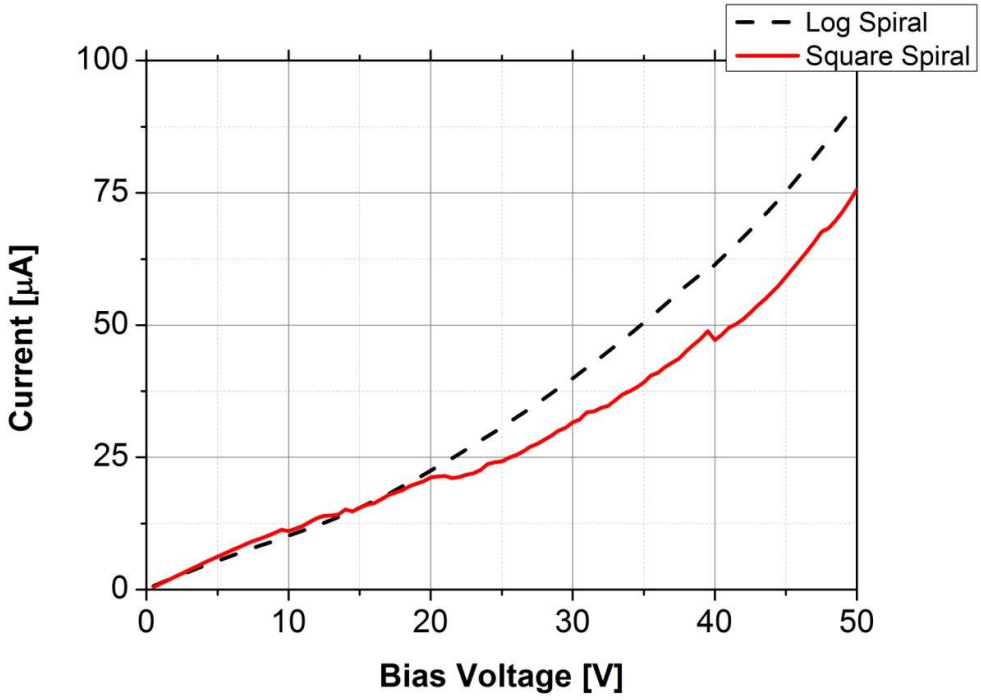

Fig. 5.36 Comparison between the photo currents of the square spiral antenna and the Archimedean log spiral.

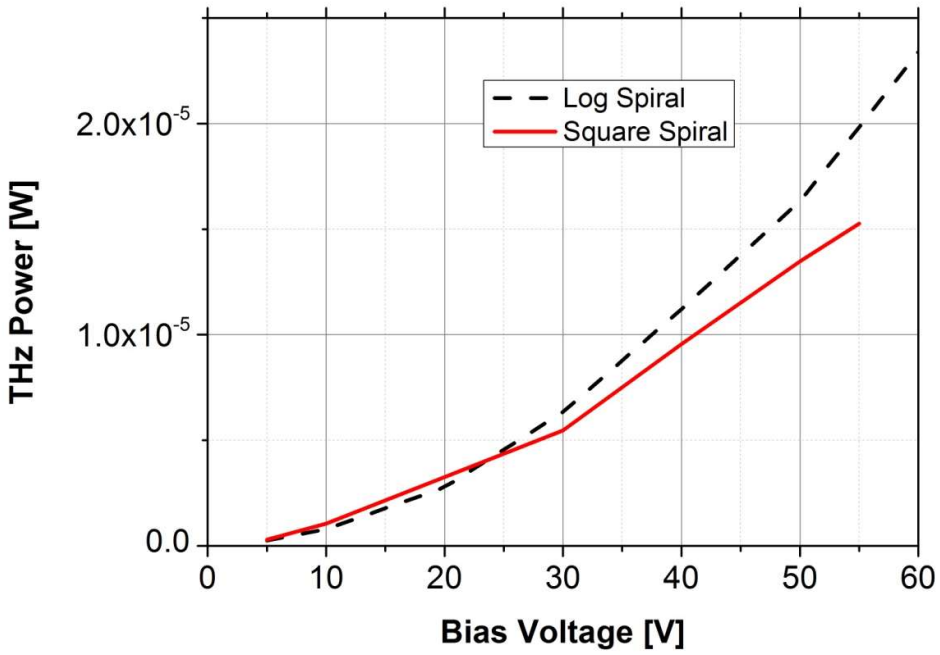

Fig. 5.37 Comparison between the THz powers radiated from the square spiral antenna and the Archimedean log spiral.

5.4 Summary

The results presented in this chapter prove that the excitation of ErAs:GaAs using telecommunication wavelength can produce very high THz power. Additionally, in order to increase the THz generation, more optical power is more important than more bias voltage, with photo-current being the least important factor of the three. In comparing the two samples, sample ASP174 has a much lower value for the conversion of photo-current into THz power (Table 5.2) than ASP194. To date, the power generated by the design B PCS fabricated on ASP194 is the highest THz power generated by this type of material (ErAs:GaAs) and by any source driven at 1550 nm. Another area of progress was the introduction of design B improved the performances of these antennae by lowering the dark-current and making it possible to bias the devices at higher voltages with the possibility of generating more THz power. Furthermore, the use of an Archimedean log spiral antenna decreased even more the

dark-current. Finally, during the characterization of these devices, a new and better IR filter, and with higher THz transmittance compared to the conventional black PE, based on black PP was discovered and characterized.

CHAPTER 6
THz power spectrum

6.1 THz power spectrum data

An important characteristic of the power generated from these devices is not only the total broadband power, but the power spectrum. The spectrum can be obtained with various techniques. The easiest one is to use a spectrum analyzer; however, this type of instrument does not go above 110 GHz. Another option is to first measure the signal at spot frequencies with different narrow-band detectors, and then piece them together to form a power spectrum. A third course of action is to use an interferometer, which was the approach chosen to conduct this experiment. Specifically, a Michelson interferometer was built in order to obtain the autocorrelation function of the THz power generated with the THz photoconductive switch. This approach was used in place of the more precise time-domain measurement due to equipment availability.

The Michelson interferometer employs a division-of-amplitude scheme. The setup, which is displayed in Fig. 6.1, consists of two highly polished plates acting as the mirrors and a thin film beam splitter. Its operation principle is listed as follows: the wave amplitude is divided into two beams with a beam splitter (a thin film that is partially reflective). The splitting occurs when one portion E_1 of the incoming beam is reflected off of the surface of the film, and the rest E_2 is transmitted through it. The two beams obtained by the amplitude division are sent in different directions against the plane mirrors. They are then reflected back along their same respective paths to the

beam splitter, creating a self-interference (interferogram) at the detector (inset in Fig. 6.1). If the detector measures power, then the detector output is given by:

$$P = C_1 E_1(t) E_2(t + \Delta t) \tag{6.1}$$

where C_1 is a constant and Δt is the time-of-flight difference between the two arms. Then by translating one of the arms uniformly using a mechanical stage, Δt becomes variable, leading to:

$$P(\Delta t) = C_1 \int E_1(t) E_2(t + \Delta t) d\Delta t \tag{6.2}$$

Since E_1 and E_2 come from the same source, and assuming that the coherence time is long enough, Eqn. (6.2) becomes the autocorrelation function $R(\Delta t)$. The power spectrum can then be obtained by the famous Wiener-Khintcine theorem of probability [122], [123]:

$$S(\omega) = C_2 \int R(\Delta t) e^{j\omega\Delta t} d\Delta t \tag{6.3}$$

Since Δt is discretized, Eqn. (6.3) can be used in its discrete form

$$S(\omega) = C_2 \sum_k R(k\Delta t) e^{j\omega k\Delta t} \tag{6.4}$$

where Δt is the time difference step determined by the translation stage and the detector sampling rate.

A photograph of the THz Michelson interferometer is shown in Fig. 6.2. An off-axis parabolic mirror was placed between the PC device and the interferometer to collimate the radiation coming out from the silicon lens. The Michelson interferometer was then aligned to the collimated beam at its input, and the output was measured with a QMC OAD-7 Golay Cell power detector. A black polypropylene filter was placed in the aperture of the detector in order to reject the 1550-nm leaked radiation.

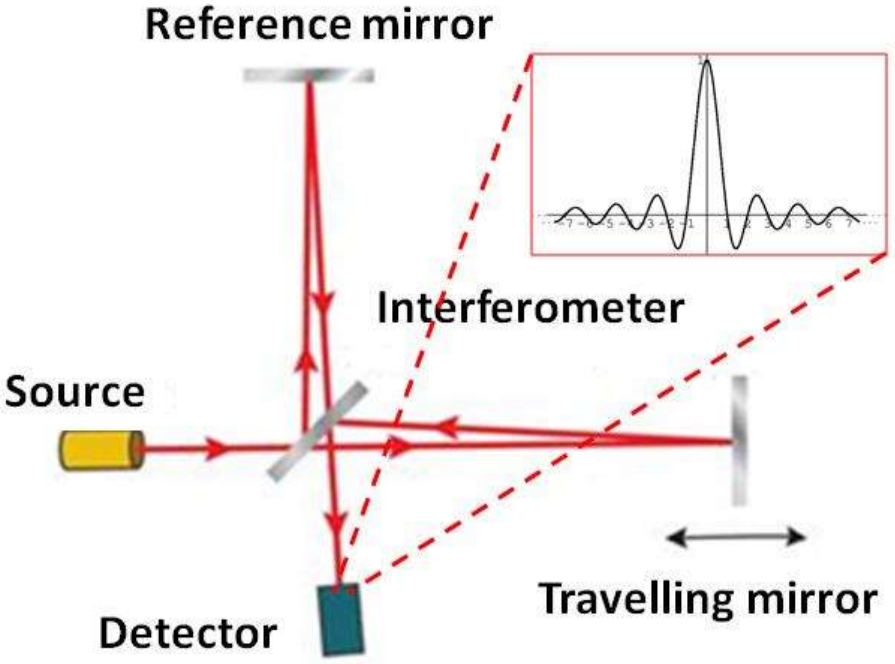

Fig. 6.1 Schematic of the Michelson interferometer.

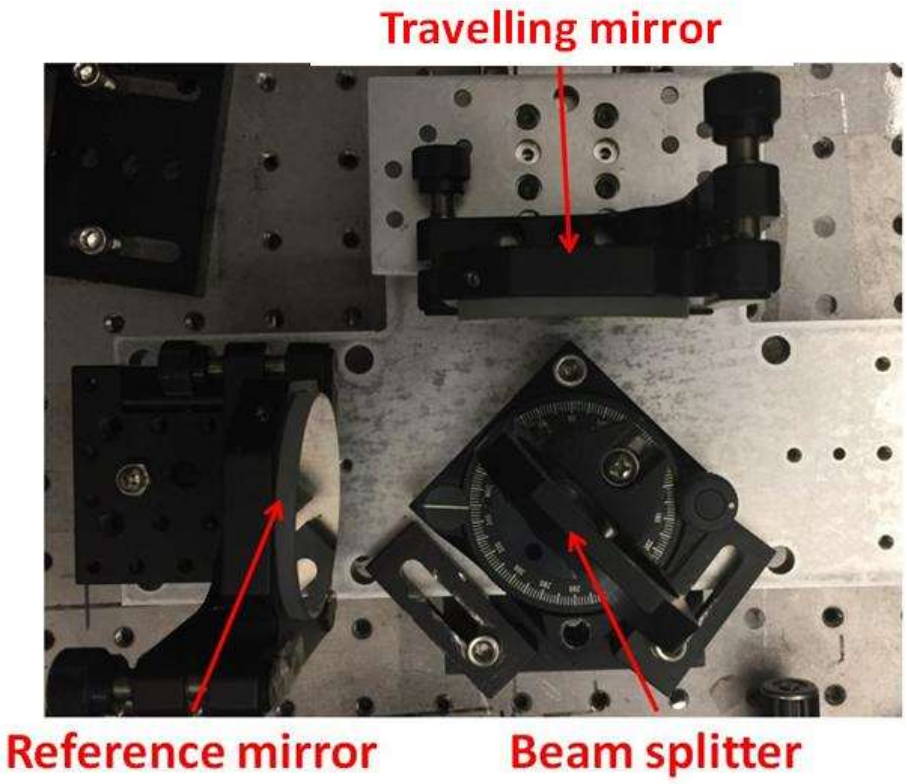

Fig. 6.2 Michelson interferometer.

In order to control the translation stage, a LabView script was used - Newport Motion Controller/Driver SMC100. The THz beam from of the PC switch was chopped and the signal from the Golay Cell detector was demodulated with a lock-in amplifier. This compact linear stage could provide a precision motion over a 25 mm range and 0.1 μm minimum step with excellent stability and stiffness. Unfortunately, for reasons that are not yet understood, this complete interferometer had around 30dB of insertion losses. Because of these reoccurring losses, only the power spectra of a few devices with excellent THz power generation were obtained.

6.1.1 THz power spectrum – ASP174

The first device tested was fabricated on ASP174 with design A, which generated a maximum THz power of approximately 42 μW under 75 V bias with a pump power of 64 mW. A step size of $\Delta x = 0.01$ mm was used, which corresponds to a time difference of 6.67×10^{-14} s according to the equation:

$$\Delta t_0 = \frac{2\Delta x}{c} \tag{6.5}$$

where c is the speed of light in air. The factor of 2 comes from the fact that the beam travels twice the length for each translation Δx of the mirror. The interferogram is shown in Fig. 6.3, measured for a total translation of 3 mm, which corresponds to a total $\Delta t = 2 \times 10^{-11}$ s.

By fast fourier transformation, this signal in the time-domain can be converted to the power spectrum shown in Fig. 6.4. This device produces measurable power up to roughly 3 THz, despite the 30 dB losses of the interferometer.

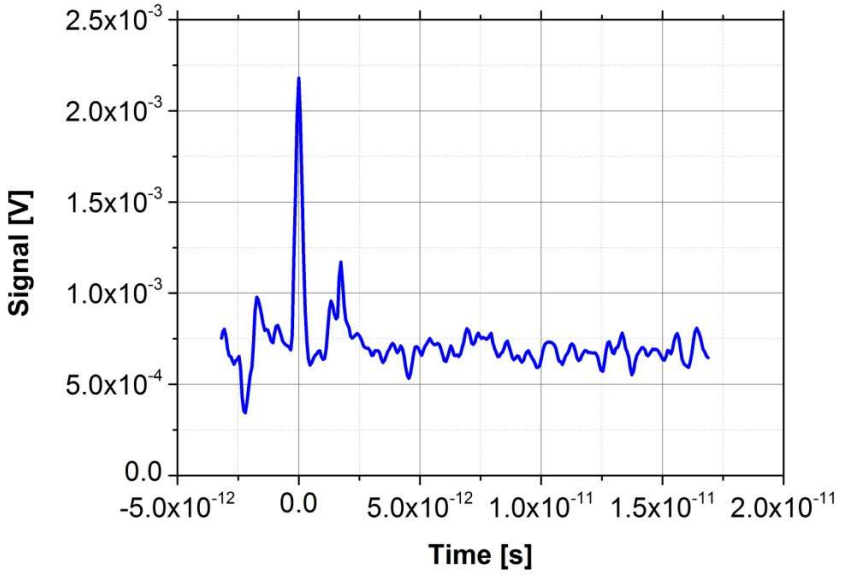

Fig. 6.3 Interferogram of the PCS, design A fabricated on ASP174.

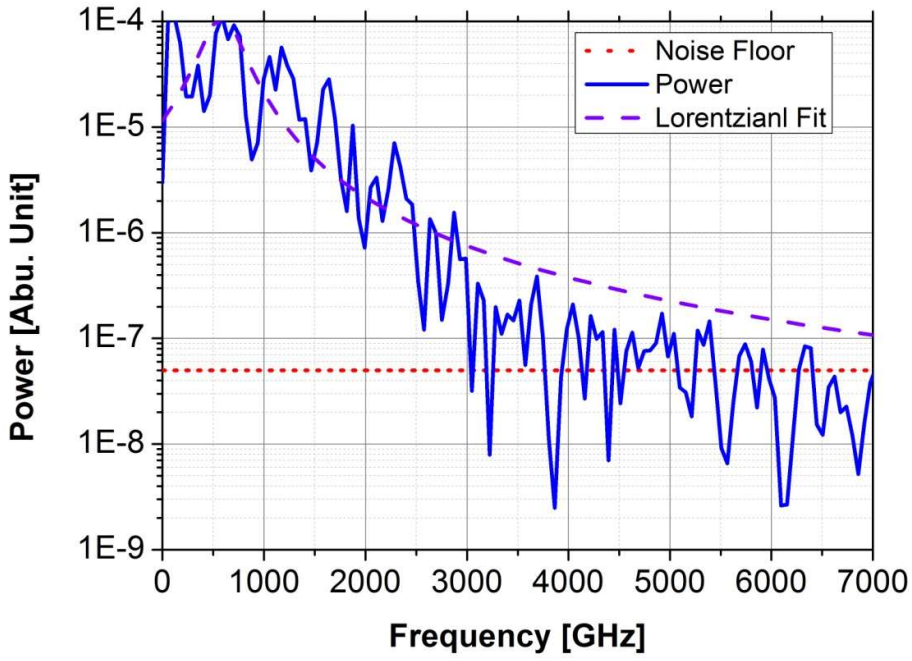

Fig. 6.4 Power spectrum of the PCS, design A fabricated on ASP174, and shifted Lorentzian curve fitting.

The power spectrum can then be fitted with a shifted Lorentzian function

$$x(f) \propto \frac{A_0}{\left\{1+\left[2\pi(f-f_0)(2\tau)\right]^2\right\}} \tag{6.2}$$

where f_0 is the peak frequency and τ is the photocarrier lifetime. This is connected to the principle of uncertainty. According to this principle, the energy, ΔE, is related to the photo-transition (when an excited state decays) and the lifetime (Δt) of the excited state according to the formula:

$$\Delta E \Delta t \geq \hbar \tag{6.3}$$

where $\hbar$ is the reduced Plank constant. As the excited state decays exponentially in time, it produces a line with Lorentzian shape in terms of frequency [124].

The fitting with the equation yields a photocarrier lifetime of ≈0.4 ps, which contrasts with the 1.7 ps obtained through pump probe measurement.

6.1.2 THz power spectrum – ASP194

In the same fashion, the design B device from material ASP194 was tested. The interferogram is shown in Fig. 6.5, and its power spectrum is shown in Fig. 6.6.

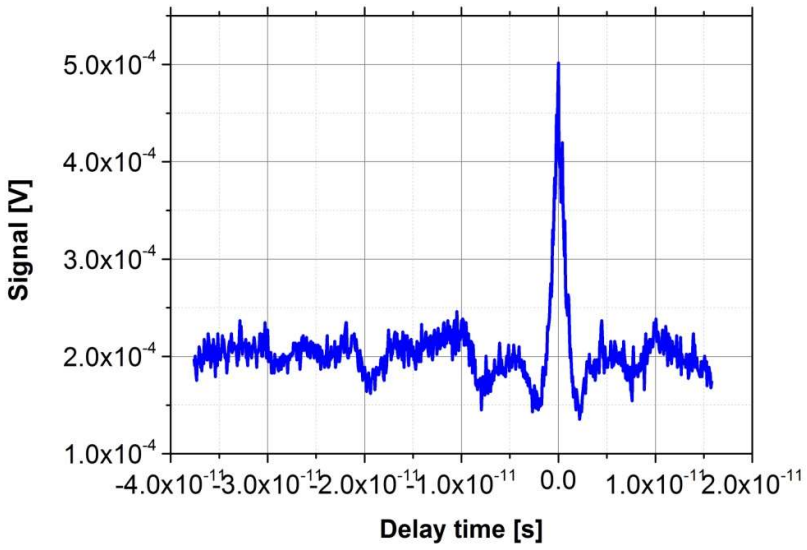

Fig. 6.5 Interferogram of the PCS, design B fabricated on ASP194.

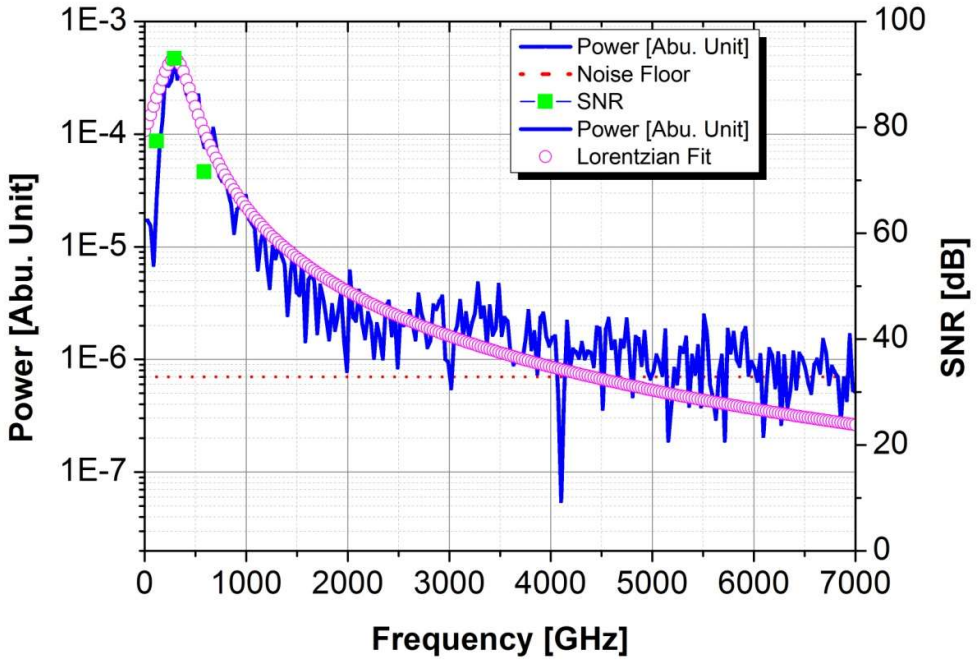

Fig. 6.6 Power spectrum of the PCS, design B fabricated on ASP194, and shifted Lorentzian curve fitting.

The power spectrum was fitted with a shifted Lorenztian function, yielding a photocarrier lifetime of ≈0.5 ps, which is shorter than the 1.7 ps obtained by pump-probe measurement (Section 3.4). The reason remains to be understood, but this kind of discrepancy between the two measurements was observed previously in semi-insulating GaAs-based photoconductors excited at 800 nm [125].

To verify the accuracy of the obtained power spectrum, the radiations around three "spot" frequencies - 100 GHz, 300 GHz and 600 GHz - were measured with three waveguide-mounted, horn-coupled Schottky diode detectors. The signal was self-modulated by the mode-lock frequency of the 1550-nm pulsed laser (i.e. 100 MHz) and then demodulated with an RF lock-in amplifier (SRS model 844). The signal-to-noise ratios (SNR) were obtained using the noise function of the SRS lock-in amplifier. The signal-to-noise-ratios for the three frequencies were determined to be approximately 77 dB, 93 dB and 72 dB respectively. The SNR is plotted on the right vertical axis in Fig.

6.6 and is in good agreement with the power spectrum obtained through autocorrelation measurement, therefore verifying its accuracy.

6.2 Slot antenna – Power Spectrum

The power spectrum for the slot antenna was obtained using the same Michelson interferometer and autocorrelation techniques as used for the spiral-antenna PCS samples. The results are plotted in Fig. 6.7 and 6.8.

Fig. 6.7 shows the interferogram obtain from the slot antenna. In Fig. 6.8, the peak of the power spectrum can be seen at around 290 GHz, in accordance with the half-wavelength resonance calculation (Chapter 4). In order to compare the bandwidths, the power spectrum from design B spiral antenna is plotted against the slot antenna in the same graph (Fig. 6.9). Clearly, the power spectrum of the slot antenna is "narrower", with detectable power up to 1 THz.

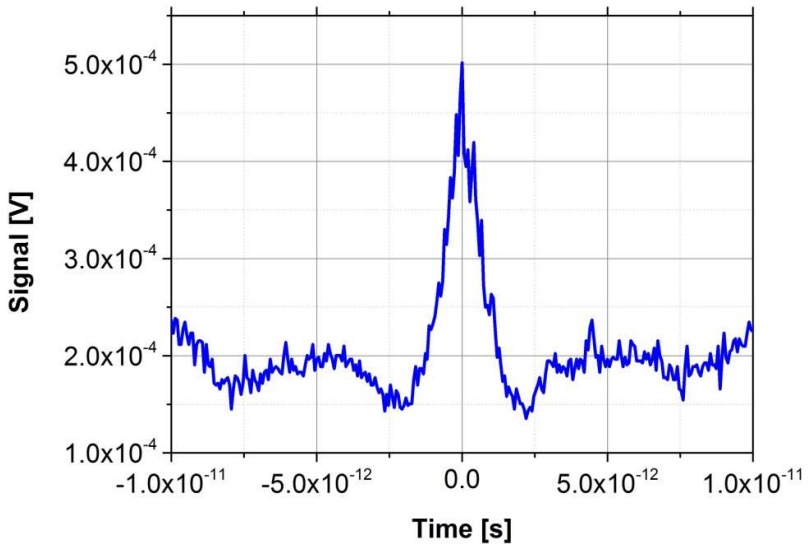

Fig. 6.7 Interferogram of the slot antenna fabricated on ASP194.

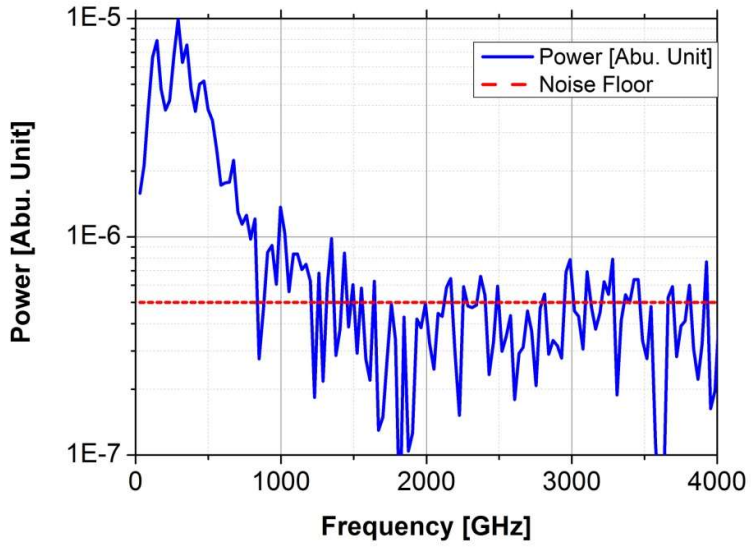

Fig. 6.8 Power spectrum of the slot antenna fabricated on ASP194.

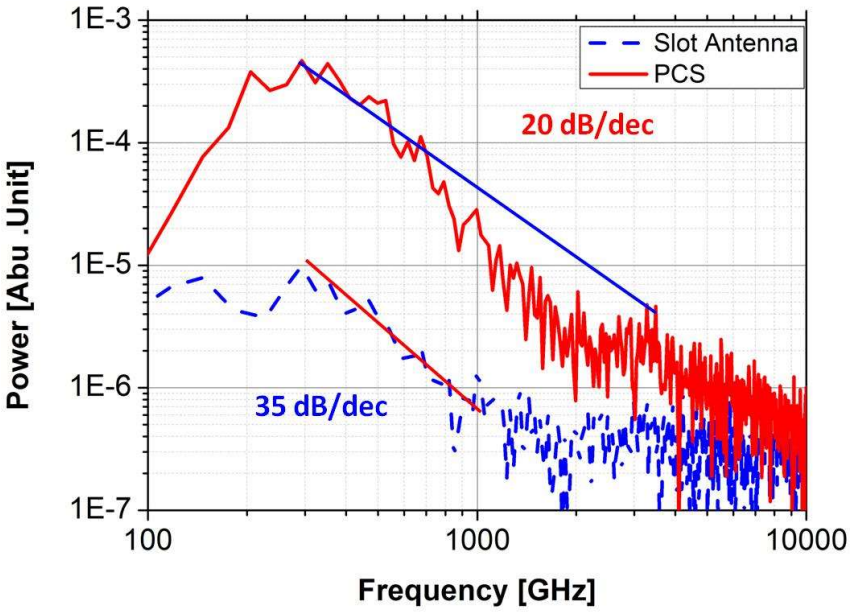

Fig. 6.9 Spectra comparison between a slot antenna (in blue) and a PCS (in red) fabricated on ASP194.

6.3 Summary

The power spectra of the devices were characterized using a custom Michelson interferometer. Lifetimes of ≈0.4 ps and ≈0.5 ps were extrapolated for ASP174 and ASP194, respectively. In square spiral antennas, power up to 3 THz and 4 THz was

detected for ASP174 and ASP194, respectively, despite the 30 dB losses of the interferometer. For the slot antenna, power up to 1 THz was detected.

CHAPTER 7
Dual Band Antenna

This chapter will discuss how the design B antenna allows one PCS to emit simultaneously in two bands. This improved design allows the antenna to radiate in the low-THz region, around 300 GHz, and in the low-frequency region, between roughly 10 and 20 GHz. The low-frequency region was chosen specifically because of its known strong atmospheric transmission, independent of water vapour, rain, etc. – a benefit to wireless communications and radar. Moreover, the 10-to-20 GHz band provides much greater penetration depth into soft tissue than THz radiation – a benefit for biomedical reflective imaging.

7.1 Antenna design

The antenna consists of two concentric planar designs that share a common PCS, as shown in Fig. 7.1. The inner antenna is the same type that was presented in Chapter 5, which is the square spiral design B with four turns. The outer design is a dumb-bell dipole (DBD) with 731 μm arm length and 500 x 500 μm pads that also serve for dc wirebonding. The metal arm width of the square spiral is 4 μm and the gap is 14 μm, creating a total spiral height of 315 μm and a physical length of 2553 μm between the PCS and the dipole arms. Based on past experience, 4-turn square spirals having 4 μm arm-width and the same height tend to be very efficient at frequencies above 150 GHz. However, they then fall off in efficiency at lower frequencies. Therefore, the primary motivation behind this design was to utilize the inherent photocurrent from the PCS at the lower frequencies by coupling to the concentric DBD.

A secondary motivation was to choose a frequency band that propagates under all atmospheric conditions. For that reason, the DBD was designed to radiate strongly below 20 GHz where the atmosphere has tolerably low attenuation, even under rainy conditions [126].

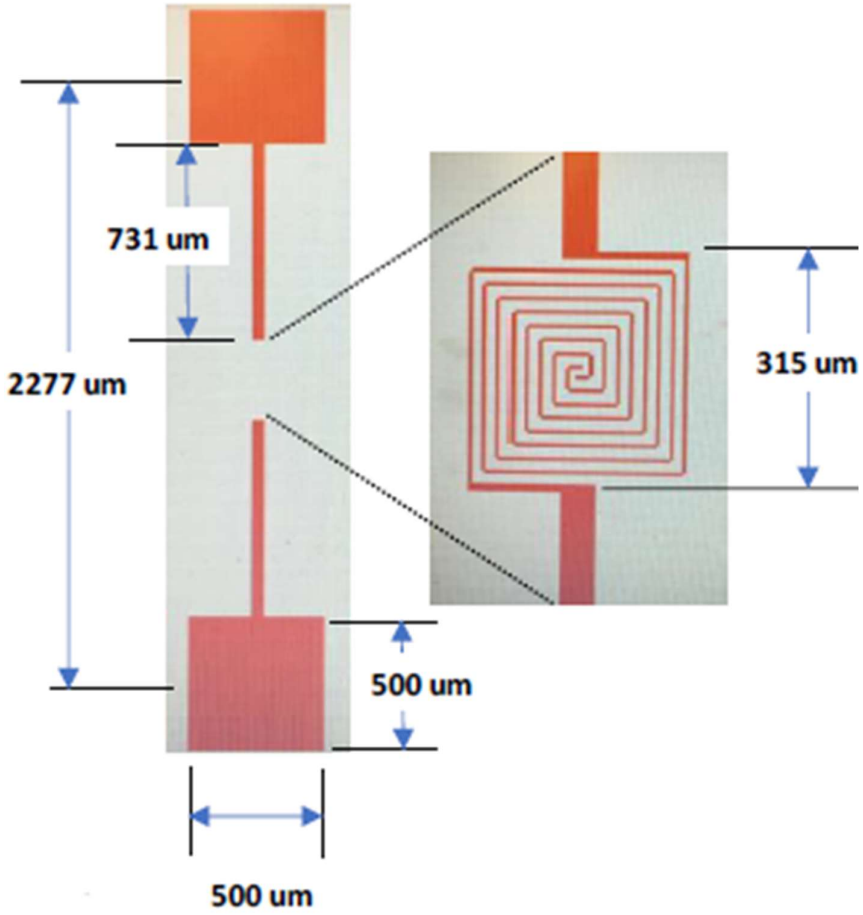

Fig. 7.1 Dual band antenna design, dumb bell dipole (DBD) on the left and PCS on the right.

To predict the performance of the DBD, the full- and half-wave resonant frequencies f_0 and $f_0/2$ were estimated. First, it can be assumed that the propagation velocity of photo-current flowing along the metal layers of the structure is

$$c_{eff} = \frac{c}{\sqrt{\varepsilon_{eff}}} \tag{7.1}$$

where c is the speed of light in vacuum and ε_{eff} is the effective dielectric constant. A reasonable first approximation for ε_{eff} is the arithmetic mean [109],

$$\varepsilon_{eff} = \frac{1 + \varepsilon_{GaAs:Er}}{2} \tag{7.2}$$

where $\varepsilon_{GaAs:Er}$ is dielectric constant of the GaAs:Er substrate. Moreover, due to both the high resistivity (>10^4 Ω·cm) of GaAs:Er and the low (≈1 %) fill factor of the ErAs, the dielectric constant can be approximated as $\varepsilon_{sGaAs:Er} \approx \varepsilon_r = 12.9$, the relative permittivity of GaAs in the microwave-to-THz region [127]. In addition,

$$f_0 = \frac{c_{eff}}{L_A + L_P} \tag{7.3}$$

where L_A is the total physical length of the square-spiral and dipole arms, and L_P is the effective length of the pads. Given the geometry of Fig. 7.1, the total physical length is $L_A = 2 \cdot (2553 + 731) = 6568$ μm. A final assumption is that $L_P \approx 2 \cdot 500$ μm, which is twice the pad width. This leads to an estimation of the full- and half-wave resonance frequencies of 15.1 and 7.54 GHz, respectively, which defines the region of efficient operation for the DBD antenna.

An interesting aspect of the overall antenna design is the effect of the spiral on the dipole. It can be assumed dispersion-free because the square spiral, and self-complementary spirals in general, has no mutual inductance. In fact, the magnetic field created by one spiral arm cancels the field created by the opposite arm. Also, it is assumed to be attenuation-free because each arm of the spiral is much shorter than a

wavelength in the 10-20 GHz region. The metal layers thicknesses lead to a total spiral arm resistance < 170 Ω. Hence, the inner spiral antenna acts primarily as a delay line, which aids significantly in shrinking the overall dimensions of the dual-band antenna structure, especially when compared to typical planar antennas in the 10-20 GHz region.

7.2 Packaging and broadband performances

As for all other devices presented in this work, the antenna used for this testing was fabricated by using the same process presented in Chapter 4. The large lens size is useful because it supports the coupling of the DBD antenna to free space at microwave frequencies with co-alignment to the optical axis of the spiral, without spillover loss or vignetting.

As presented in the previous chapter, the radiated emission at frequencies above 100 GHz was measured using a Golay cell. When driven by a 1550-nm fiber mode-locked laser with an average power of 64 mW, an average THz power above 100 μW was obtained at a bias voltage of 145 V (Chapter 4). The polarization was measured and found to have approximately equal levels of power in all orientations, consistent with circular polarization being emitted from the square spiral.

To understand the radiation at lower frequency, it is possible to note the low-frequency rise in power spectrum in Fig. 7.2 (a) below 100 GHz. Initially, it was thought to be associated with 1/f noise or a similar parasitic effect in the receiver electronics; however, further investigation attributed it to radiation from the DBD structure. Although the Golay Cell detector drops in external responsivity below 100 GHz, there is no sharp cut-off frequency as in a waveguide-mounted device. For this reason, the drop is graceful and not precipitous.

To prove that the DBD antenna was contributing significantly to the total emitted radiation, the power detector in Fig. 5.15 was replaced with a receiver consisting of the combination of a WR-75 waveguide-to-coaxial transition coupled to a calibrated, commercial spectrum analyzer. Although the coupling between the DBD and receiver is inefficient because of mode-mismatch, the power spectrum was easily measured by placing the open end of the WR-75 waveguide section against the Si hyper-hemispherical lens. A typical spectrum analyzer output is shown in Fig. 7.2 (b), consisting of a "comb" of emission spikes separated by the mode-locked repetition frequency of 100 MHz. As was expected, the comb falls into the noise floor at lower frequencies, where it approaches the WR-75 waveguide cut-off frequency near 8.0 GHz. The comb also displays three peaks centered at ≈10.5, 14.6, and 18.2 GHz, proving that the radiation from the DBD at lower frequencies occurs in the 10-to-20 GHz band. In addition, to prove that the radiation was in fact linearly polarized (as expected for dipole antenna), the dipole of the WR-75 waveguide-to-coaxial adapter was connected to a lock-in amplifier. When the dipole of the WR-75 was aligned in parallel to the dipole of the antenna, the measured signal was twice as large as when the dipoles were aligned perpendicularly. This finding confirmed the linear polarized nature of this radiation.

To help understand the performance of the DBD antenna, full-wave simulations of the S_{11} and antenna pattern in both the 10-to-20 GHz and the 300-GHz regions were carried out at the Universidad Carlos III de Madrid [128] using the software CST Microwave Studio [129]. Fig. 7.3 (a) shows the S_{11} relative to the central driving gap over the range 150-350 GHz. Although it is not a great impedance match, the square spiral antenna provides a nearly flat -8 dB return loss over this range. Then, as shown in the directive gain computed at 250 GHz in Fig. 7.3 (b), the E-plane pattern (along

the axis of the dumb-bell) and H-plane have comparable co- and cross-polarization magnitudes. This is consistent with the square spiral emitting approximately circular polarization. It should also be noted that Fig. 7.3 (b) assumes that the GaAs substrate is semi-infinite, so the focusing effect of the Si lens is not accounted for.

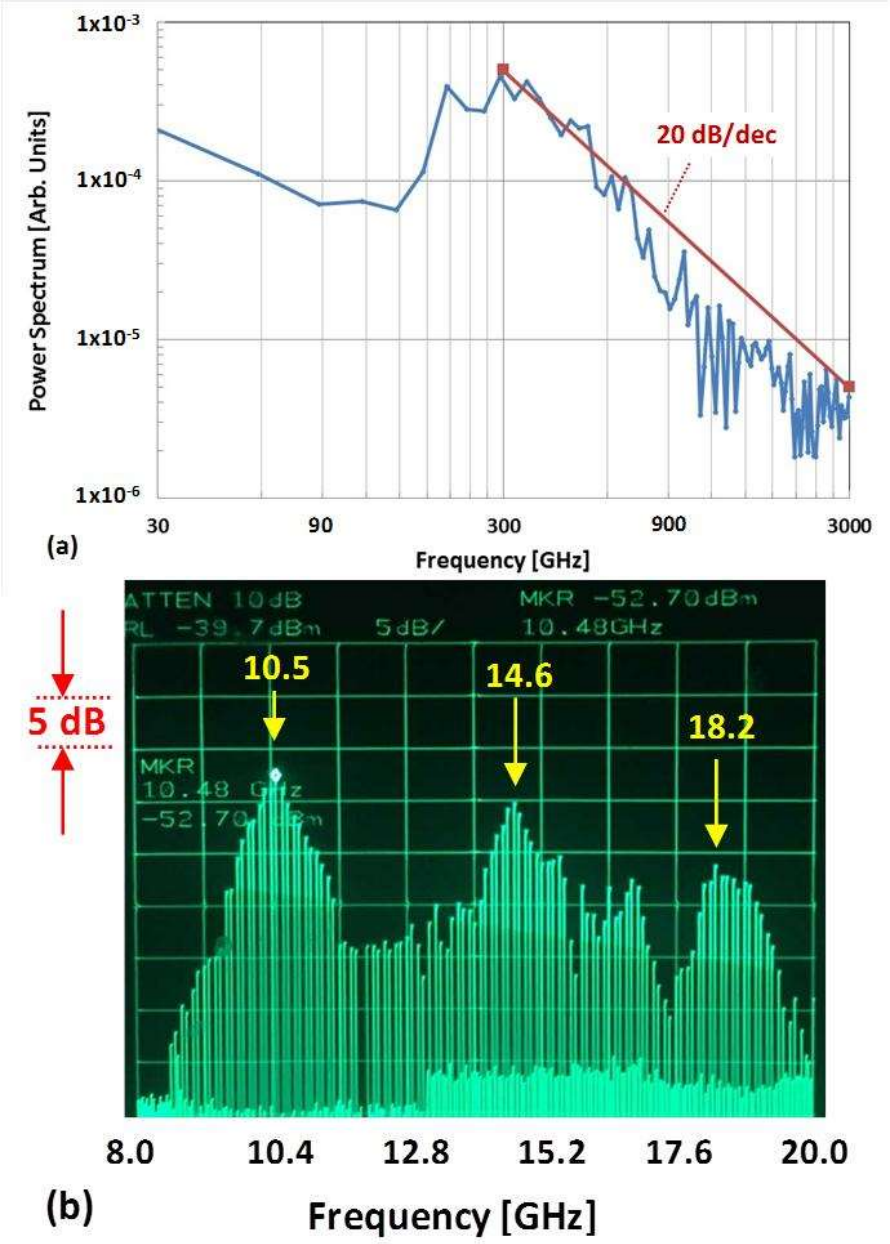

Fig. 7.2 (a) Power spectrum obtained by FFT of the autocorrelation function shown in Fig. 6.5. (b) Power spectrum of radiation emitted from dumb-bell dipole antenna coupled to an open-ended WR-75 waveguide containing a waveguide-to-coax transition.

To further analyze the performance of the antenna, the S_{11} was computed in the range 10-30 GHz and it is shown in Fig. 7.4 (a). Here there is a clear sign of a resonance at ≈17.5 GHz, as was expected for any resonant dipole. The directive gain in Fig. 7.4 (b) is also dipole-like, being scalloped in the E-plane and nearly uniform in the H-plane. In addition, being that the antenna is fabricated on GaAs, most of the radiation propagates into the substrate side, as was also expected. The reason why only one resonance appears in the simulation (Fig. 7.4 (a)) and three in the experimental data (Fig. 7.2 (b)) is not yet understood.

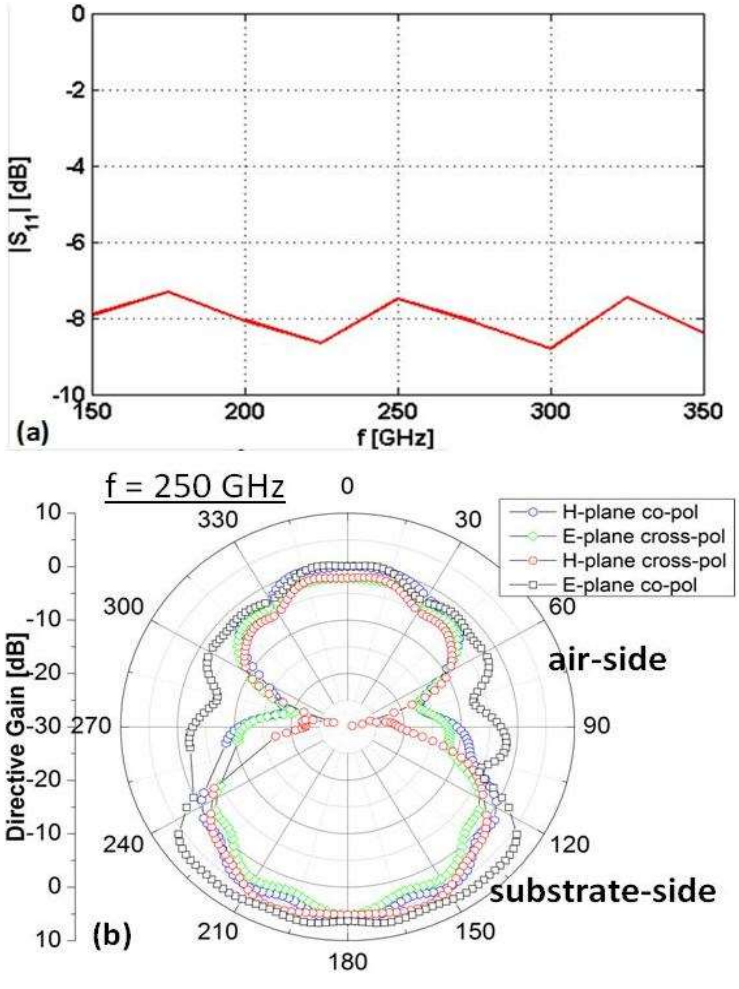

Fig. 7.3 (a) Reflective S parameter vs frequency for the DBD antenna between 150 and 350 GHz. (b) Directive gain at 250 GHz.

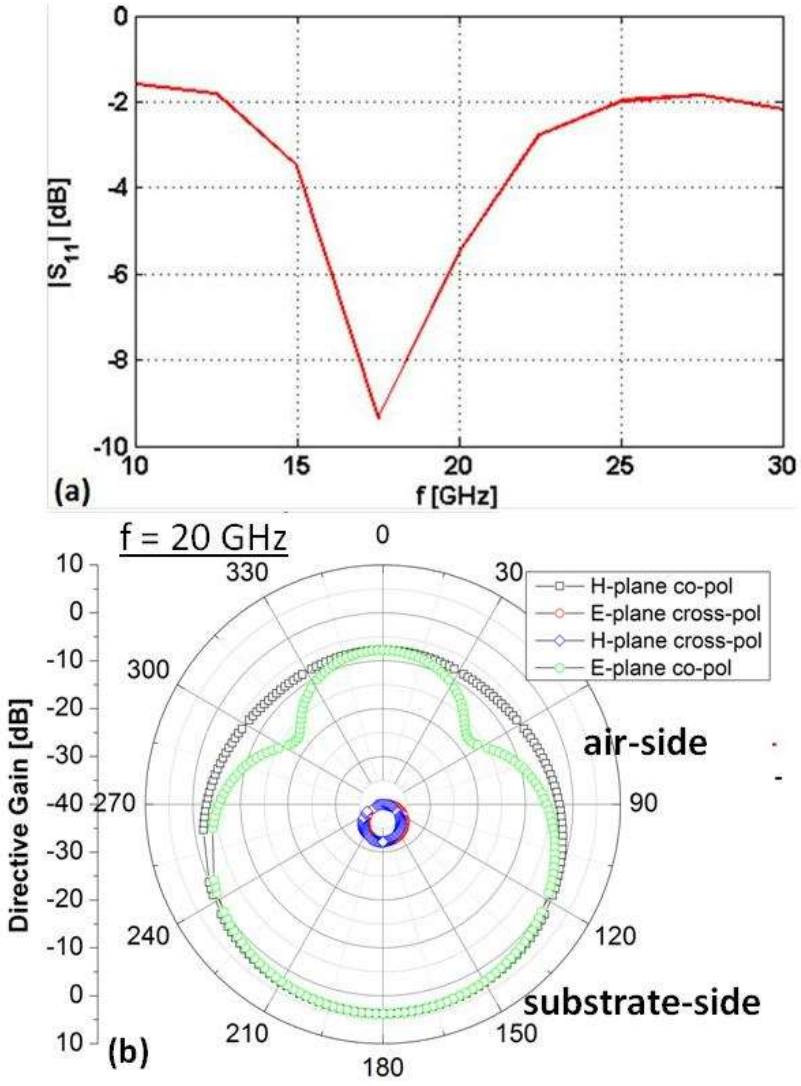

Fig. 7.4 (a) Reflective S parameter vs frequency for the DBD antenna between 10 and 30 GHz. (b) Directive gain at 20 GHz (note: the cross-pol components are very small and are therefore barely visible).

7.3 Metallization and Antenna Gain

To understand whether the metallization for the spiral antennae influenced the antenna performance, a study of the resistance was conducted for both design A and B. From each of the tested designs, the length of the arm was measured in order to numerically calculate their resistances. The length, for both cases, was measured to be 2553 μm from the center of the antenna to the biasing arms. Each of the metal-strip resistance was calculated from:

$$R = \frac{\rho l}{tw} \tag{7.4}$$

where ρ is the metal bulk resistivity, l is the total length of the arm, t its thickness, and w is the width (9 μm for design A and 4 μm for design B). In order to measure R, it was assumed that the conduction happened uniformly throughout the layered stack of metals. For this reason, the total resistance was simply calculated as the parallel combination of the metal layers. When the metallization stack Ni-AuGe-Ni-Au (described in Table 4.2) was used, differential DC arm resistance of 74.2 Ω and 170.3 Ω, respectively for design A and B, were measured.

In addition, for the case of design B, the losses of metal films were investigated using both measurements and computer modeling. These losses are often neglected in THz antenna engineering. The attenuation due to the metallic loss is proportional to the surface resistance Rs,

$$R_s = \sqrt{\frac{2\pi f \mu_0}{2\sigma}} \tag{7.5}$$

where σ is the conductivity of the metallic stack, f is the frequency and μ_0 is the permeability of free-space. Thus, the smaller the conductivity and the greater the frequency, the greater the losses can be.

Unfortunately, the conductivity of a metallic film can be significantly smaller than its bulk value. As the thickness shrinks and becomes comparable to the mean free electron path length, electrons can collide with the surface of the film [104]. Additionally, the surface effect becomes more severe as the thickness decreases. This was confirmed by our experimental results. Two antennas were fabricated and metallized with a stack of Ni/AuGe/Ni/Au, similar to the stack listed in Table 4.2, with total thicknesses of 260 nm and 360 nm. The differential DC arm resistance was then

measured to be 175 Ω and 155 Ω, respectively. Confirming that to enhance the conductivity of the metal stack, an increase of the thickness of the metallization was needed. According to the rule-of-thumb, a good target for the thickness would be 10 times the mean-free-path, as discussed in Chapter 4.

Furthermore, to understand the effect of the decreased conductivity, the antenna gain has been simulated with full wave simulations [129] at the Universidad Carlos III de Madrid [128]. The metallization was assumed to be a single layer of 2000 Å. Two cases were considered: one for a good conductor (mimicking bulk conductivity 2 x 10^5 S/cm, pure gold) and the other for a lossy conductor (mimicking the thin film conductivity 2 x 10^4 S/cm). The results over the ranges of 10-30 GHz and 150-350 GHz are shown in Fig. 7.5 and 7.6, respectively. For the first case, the impedance followed the local resonances of the antenna composed of the square spiral and the DBD. However, the resonances disappeared for the case of a lossy conductor due to its additional losses. At higher frequencies, the discrepancy between the impedances of the two cases is less effective, as was expected, due to the fact that the skin depth is closer to the actual thickness of the simulated conductor.

The difference in the impedance between the two simulated cases proved to affect the gain of the antenna. Fig. 7.7, 8, 9 show the left handed circular polarization (LHCP) and right handed circular polarization (RHCP) directive gains for the design B antenna at the frequencies of 150, 250, and 350 GHz, respectively. As can be seen, a lossy metallization causes a drop of the maximum gain of around 15, 10, and 5 dB, respectively.

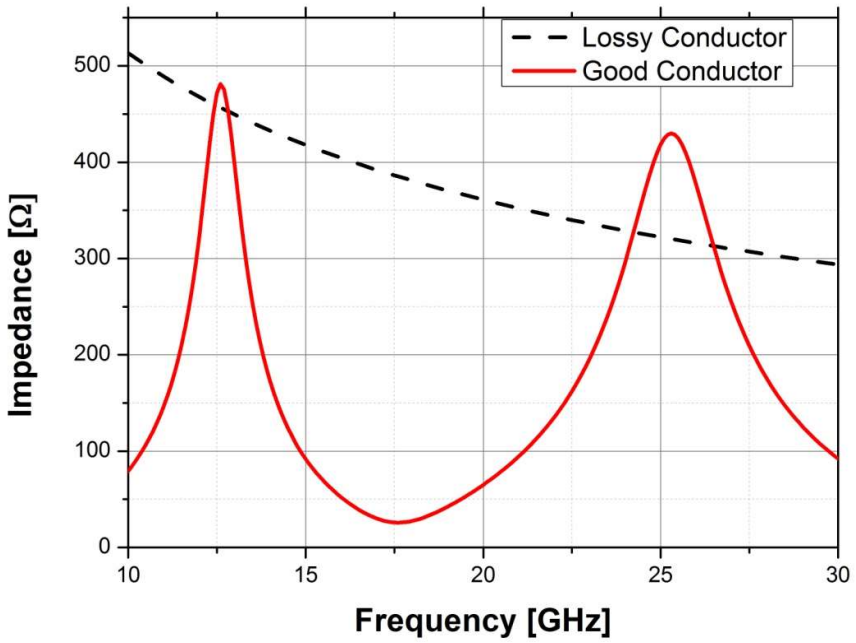

Fig. 7.5 Magnitude of the arm's impedance around 20 GHz.

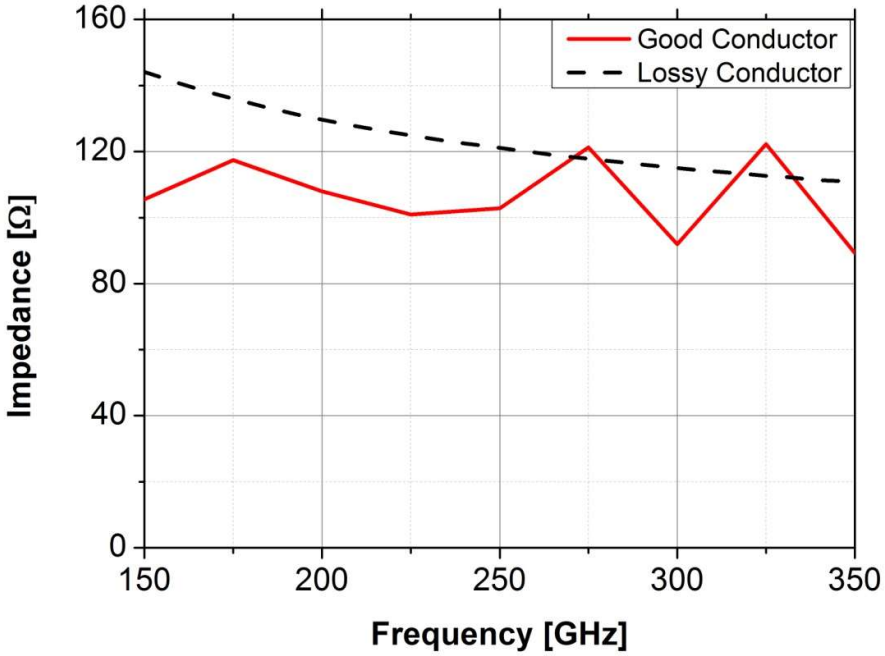

Fig. 7.6 Magnitude of the arm's impedance around 250 GHz.

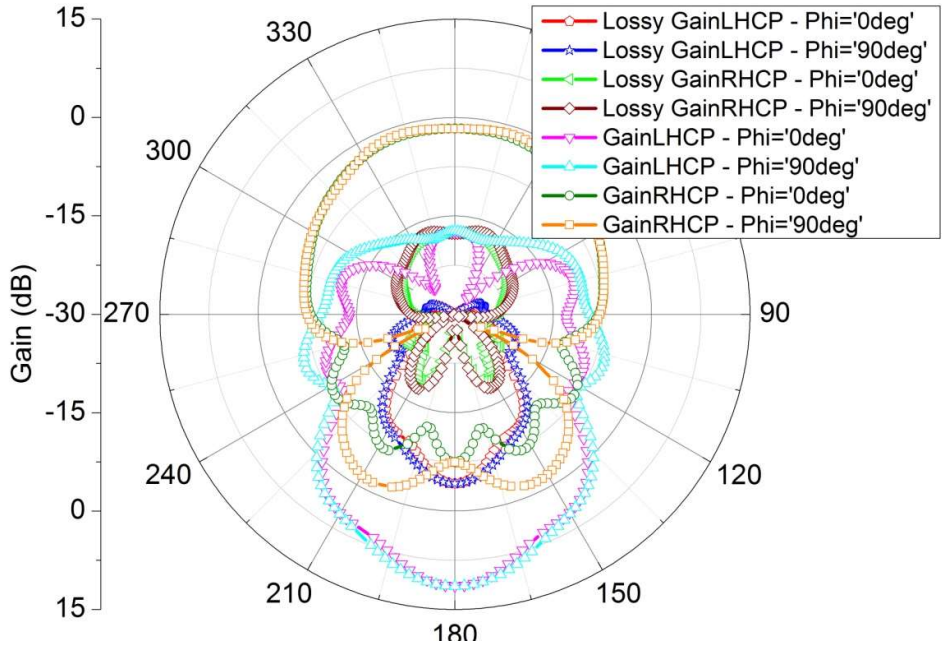

Fig. 7.7 LHCP and RHCP realized gains at 150 GHz with perfect and lossy conductor.

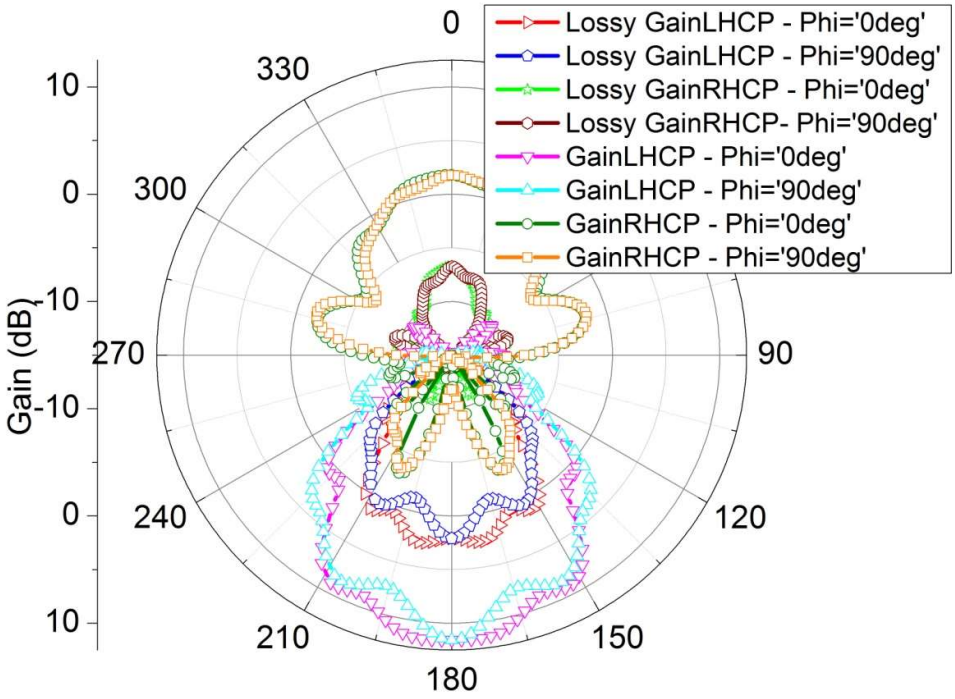

Fig. 7.8 LHCP and RHCP realized gains at 250 GHz with perfect and lossy conductor.

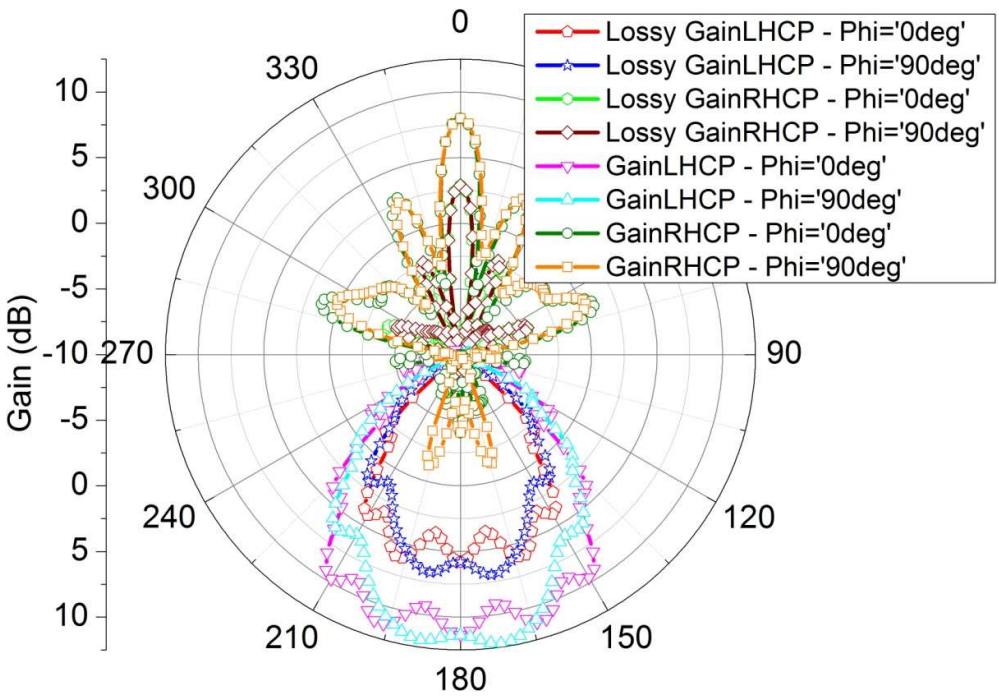

Fig. 7.9 LHCP and RHCP realized gains at 350 GHz with perfect and lossy conductor.

Fig. 7.7-8-9 demonstrates how LHCP is dominant in the substrate and RHCP is dominant through air. This is consistent with the fact that the current flows in the arms of the spiral in a clockwise direction. If looking at the positive z-axis (perpendicular to the plane on which the antenna lies and into the substrate) the copolar component will be left handed. In contrast, when looking at the negative z-axis (into the air), the copolar radiation will be right handed.

CHAPTER 8
Alternative materials and antennae

While the performances of devices fabricated on ASP174 and ASP194 proved to be best, a lot of effort was put towards reproducing these materials with further MBE growths. The results of the test done are presented in this chapter and compared to those of ASP174, 194. The measurements included: dark-current, photocurrent generation, responsivity under pulsed optical excitation at 1550 nm, and THz power generation.

8.1 Dark-current

As in Chapter 5, the results on the design A PCS are shown first. Again, design A is a 4-turn self-complementary square-spiral antenna, with 9 μm widths for the gaps between the arms, 9 μm widths for metallization and a 9 μm x 9 μm area for the active region, as shown in Fig. 5.1.

The materials tested with this design, and summarized in Table 8.1, are the following: ASP174, ASP194, ASP280 (nominally a replica of ASP174) and ASP294.

Table 8.1 List of samples tested and devices fabricated.

	Erbium Concentration [cm^{-3}]	Epilayer Thickness [μm]	Antenna Design
ASP174	4.4×10^{20}	1	A
ASP194	8.8×10^{20}	2	A, B
ASP280	4.4×10^{20}	1	A, B
ASP294	8.8×10^{20}	1	A, B
ASP365	2.2×10^{20}	2	B
ASP372	4.4×10^{20}	2	B

Fig. 8.1 shows the dark-currents.

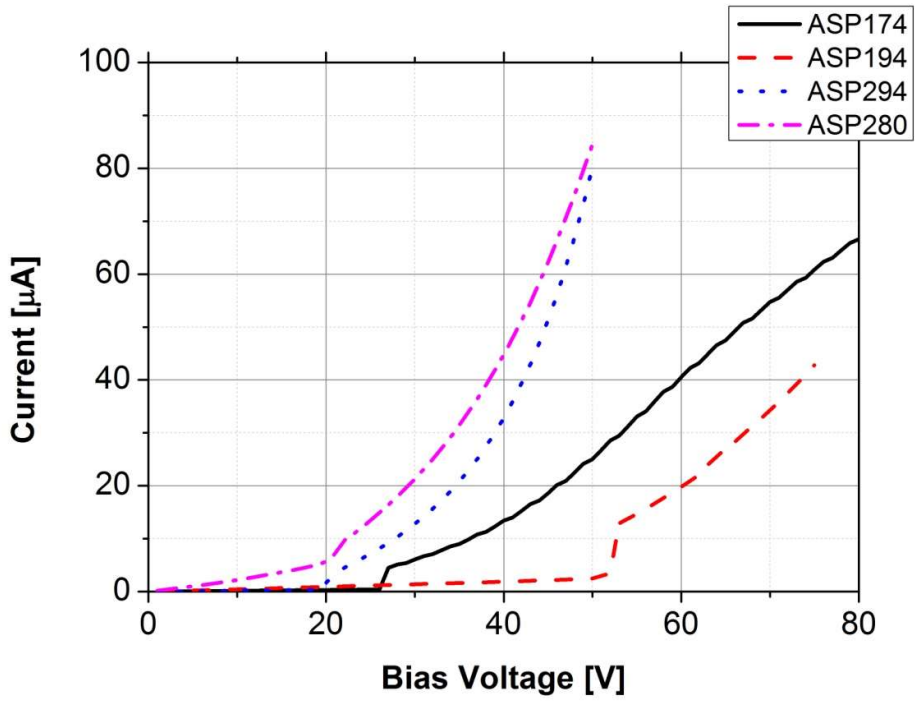

Fig. 8.1 Dark-currents of design A PCS fabricated on ASP174, ASP194, ASP280 and ASP294.

As one can see, the abrupt change in the magnitude of the current and the resistivity of the substrate discovered for ASP174 and ASP194 is also present in these samples.

Compared to that of ASP174, the device from ASP280 (replica of ASP174) shows a larger dark-current over the entire range. In particular, before the voltage discontinuity, the dark-current of ASP280 is 16.5x larger than the one of ASP174 and 3.3x larger after such discontinuity. This difference may be due to different growth conditions that could have impacted the epi-layer quality. Specifically, it could have been cause by either one of the following changes: the As concentration could have varied due to a change in the As effusion cell; or the nanoparticle size or distribution could have varied due to a change of growth temperature by 30 °C [84]. Additionally, when compared to ASP174, ASP294 has a dark-current only 3% larger before the discontinuity and 3.1x larger after it. This proved that ASP174 had the best dark-current

characteristic amongst the materials with an epi-layer 1 μm thick. Table 8.2 lists the dark-currents at 50 V bias voltage and at the highest bias voltage used in the measurements.

Table 8.2 List of dark-currents of Design A devices.

	ASP174	ASP194	ASP280	ASP294
Dark-current [μA] at 50 V	25.4	2.5	84.5	80.3
Dark-current [μA] at max V	66.6 at 80 V	42.8 at 75 V	84.5 at 50 V	80.3 at 50 V

Fig. 8.2 shows the dark-currents of devices fabricated on ASP194 and ASP294 with design A and thicknesses of 2 μm and 1 μm, respectively. Both configurations were doped with a concentration of 8.8 x 10^{20} cm^{-3}. From this I-V curve measurement, it is clear that the discontinuity voltage moves to a higher value as the thickness of the epitaxial layer increases. The obvious advantage of the shift is that the dark-current remains lower for higher bias voltages, reducing the Joule heating that the devices need to withstand. Subsequently, the device can be biased at higher voltages, which is beneficial for responsivity and THz performance.

Next, the design B antenna was tested, as is shown in Fig. 5.2. Fig. 8.3, instead, shows the comparison of the dark-current measurements for the two antenna designs based on the same substrate material with ASP280 (replica of ASP174) having an erbium doping concentration of 8.8 x 10^{20} cm^{-3} and 1-μm thick epitaxial layer. Again, it can be seen how the design B successfully lowered the dark-current.

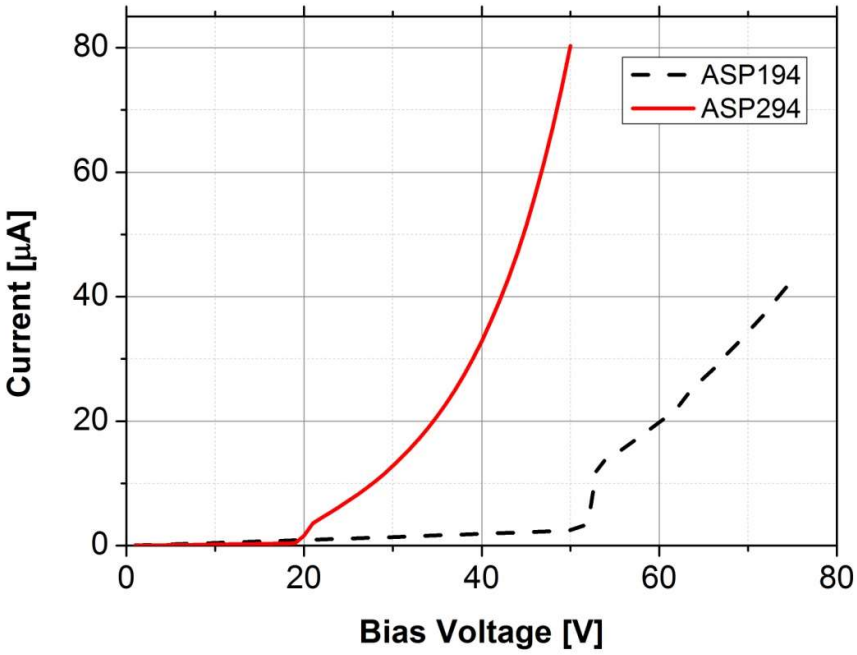

Fig. 8.2 Dark-currents of design A PCS fabricated on ASP194 and ASP294.

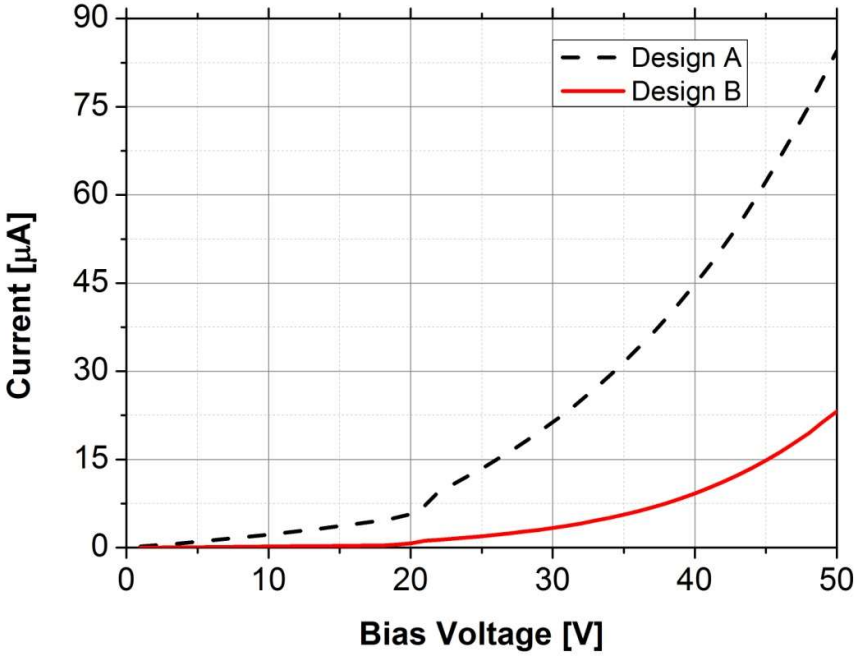

Fig. 8.3 Dark-current comparison between the design A (in black) and B (in red) fabricated on ASP280.

Fig. 8.4 shows the dark-currents of design B devices obtained by testing three samples with 2-µm thick epitaxial layer (ASP194, ASP365 and ASP372), and two with 1-µm thick epi-layer (ASP280 and ASP294). The bias voltage was kept low at a 20 V maximum. It is evident that all of the devices with the design B have very low dark-current before the discontinuity voltage. In particular, ASP294, ASP365 and ASP372 have dark-currents at least 5x lower than those of ASP194 and ASP280.

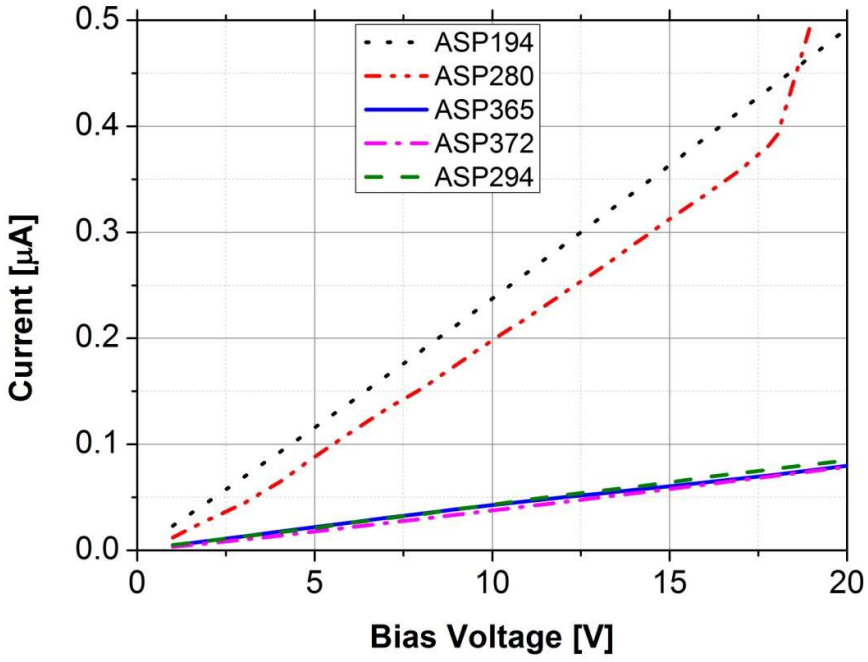

Fig. 8.4 Dark-currents at low voltages of design B devices on the 5 samples of Table 8.1.

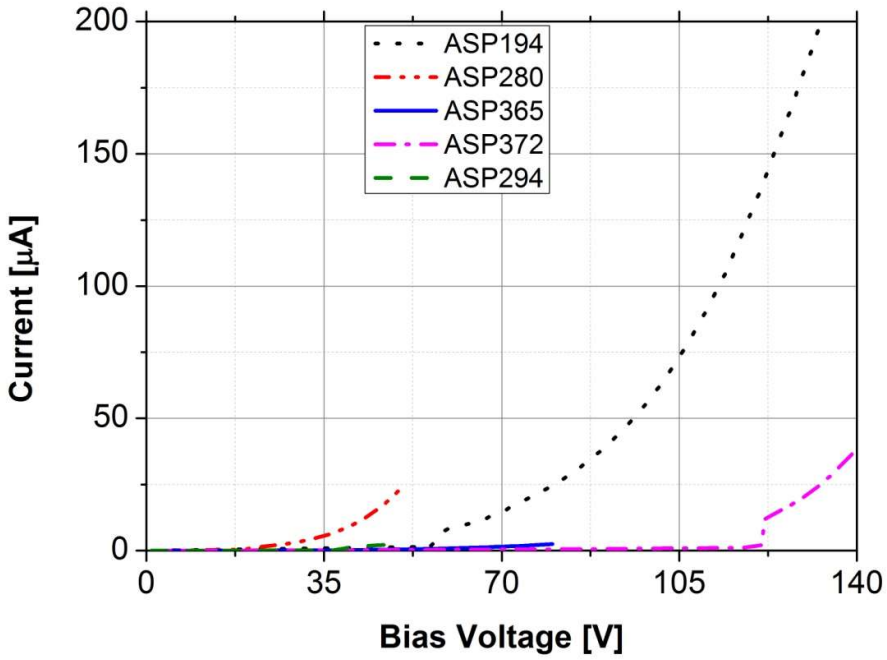

Fig. 8.5 Full dark I-V characteristics of the devices tested with design B.

Subsequently, the bias voltage was increased to the assumed maximum operating value. The resulting curves are plotted in Fig. 8.5, which shows how all three materials with thicker epitaxial layer generates a lower current than ASP280 (1 μm epi-layer). In contrast, ASP294 (1 μm epi-layer) shows slightly higher photo-current compared to samples with a thicker epitaxial layer. This demonstrates the superior performance of the materials with a 2 μm epi-layer, at least for dark resistivity. Moreover, samples ASP365 and ASP372 have superior performance compared to ASP194. Table 8.3 summarizes the dark-currents of these samples at 50 V and at their highest biasing voltage.

In conclusion, based on the I-V measurement in the condition of no optical excitation, it evident that a higher erbium doping concentration leads to a lower dark-current, as previously discussed in Chapter 5. In addition, a thicker epitaxial layer

appears to have the same effect. It also appears that, with respect to the dark-current, samples ASP365 and ASP372 are superior to ASP194.

Table 8.3 List of dark-currents of Design B devices.

	ASP194 (2-µm)	ASP280 (1-µm)	ASP294 (1-µm)	ASP365 (2-µm)	ASP372 (2-µm)
Dark-current [µA] at	1.27	23.2	2.6	0.49	0.25
Dark-current [µA] at	260 at 145	23.2 at 50	2.6 at 50 V	2.48 at 80	38.9 at 140

8.2 I-V curve under 1550-nm pulsed laser excitation

The photocurrents, and consequentially the responsivities, were measured under the optical excitation of the driving 1550 nm pulsed laser. Table 8.4 lists the materials and devices tested.

Table 8.4 List of materials and devices tested for 1550 nm pulsed laser excitation.

	Design A	Design A with optical fingers	Design B	Design B with e-beam fingers
ASP174	Yes			
ASP194	Yes	Yes	Yes	
ASP280	Yes		Yes	Yes
ASP294	Yes		Yes	
ASP365			Yes	
ASP372			Yes	

The setup used is the same as the one shown in Fig. 5.6. Unless stated otherwise, these tests were conducted with a laser output power of 84 mW with an actual power reaching the device of approximately 64 mW. The bias voltage was 50 V and the results are plotted in Fig. 8.6.

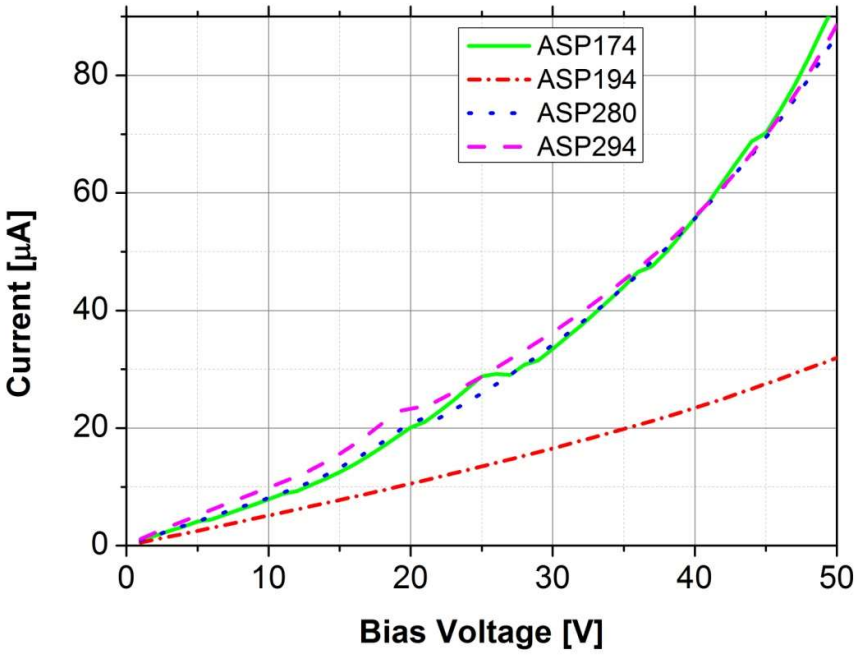

Fig. 8.6 Photocurrents of the PCS devices fabricated with the design A.

The data clearly shows that all the devices fabricated on samples having a 1 μm epi-layer (ASP174, ASP280 and ASP294) generated more photocurrent than the device fabricated on the 2 μm epi-layer material (ASP194). However, the drawback for ASP174, ASP280 and ASP294 is that they all display fast raising I-V curves, making it dangerous to apply higher bias voltage. As previously discussed in Chapter 5, the THz power has a stronger dependency on bias voltage than on photo-current. Interestingly, the fact that ASP194 generates less photocurrent than the other materials appears to be in contrast with the results obtained from IR absorption measurements. For example, in Chapter 3, material ASP194 proved in fact to be one of the best absorbing material for 1550 nm radiation. The reason is still unclear.

The same samples tested for dark I-V measurements with the design B were then tested for photo I-V measurements, and the results are listed in Table 8.4, while Fig. 8.7 shows the measured photocurrents of the five devices.

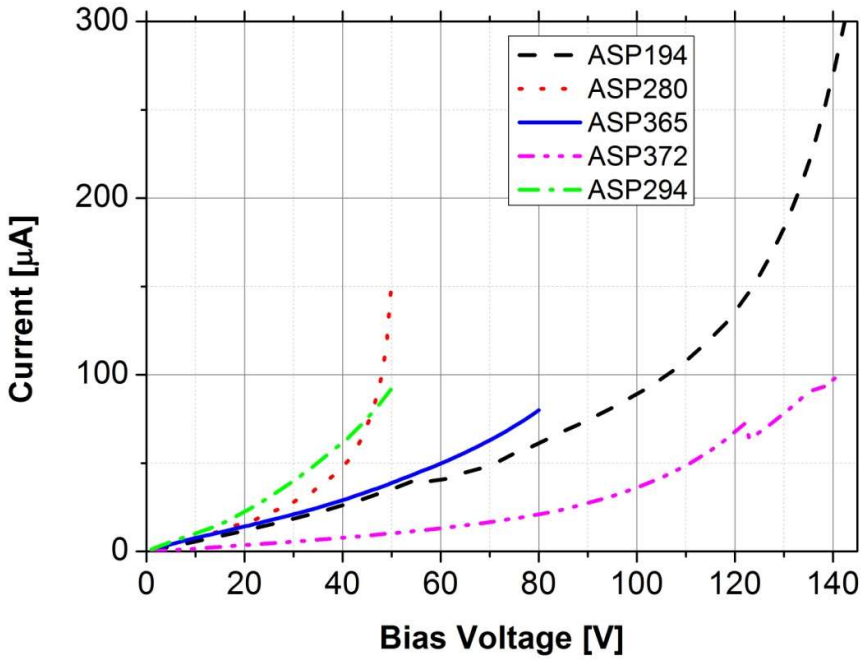

Fig. 8.7 Photocurrents of design B devices fabricated on the 5 substrates.

Between the samples, ASP280 (replica of ASP174) displays a clear power law dependence to the bias voltage already at low values (<50 V). This is possibly a sign of very high responsivity but also of early stage breakdown, due to the steep slope around 50 V. The latter scenario was confirmed by the failure of the device when the bias voltage was increased to 60 V. In comparison, ASP372 shows a very low generation of photocurrent even at high bias voltages, which is not ideal for THz generation. In contrast, samples ASP194, ASP294 and ASP365, generate useful photocurrent at 75 V (55 μA for ASP194 and 70 μA for ASP365) and at 50 V (92 μA for ASP294) without showing signs of early stage breakdown.

8.3 Responsivity

Fig. 8.8 shows the responsivities of the 8 different devices fabricated on different samples. The data points were taken with a bias voltage of 50 V and an optical excitation of 64 mW of 1550 nm pulsed radiation. ASP174, its replica ASP280, and ASP294 are the materials that show the best responsivities amongst all the devices.

However, they display a fast-increasing current to the voltage already at low bias (50 V), rendering it unsafe to apply higher bias voltage. Fig. 8.9 shows the responsivities of all the devices at their highest, bias voltage.

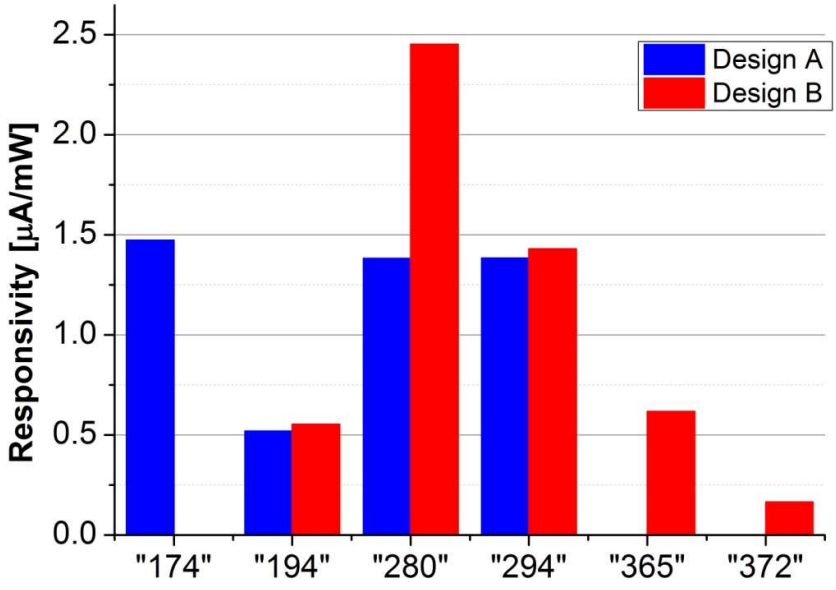

Fig. 8.8 Responsivities calculated at 50 V of voltage bias for the different designs and samples.

ASP174 and ASP194 prove to be the best samples, as they both have high responsivity and allow for biasing up to high voltages.

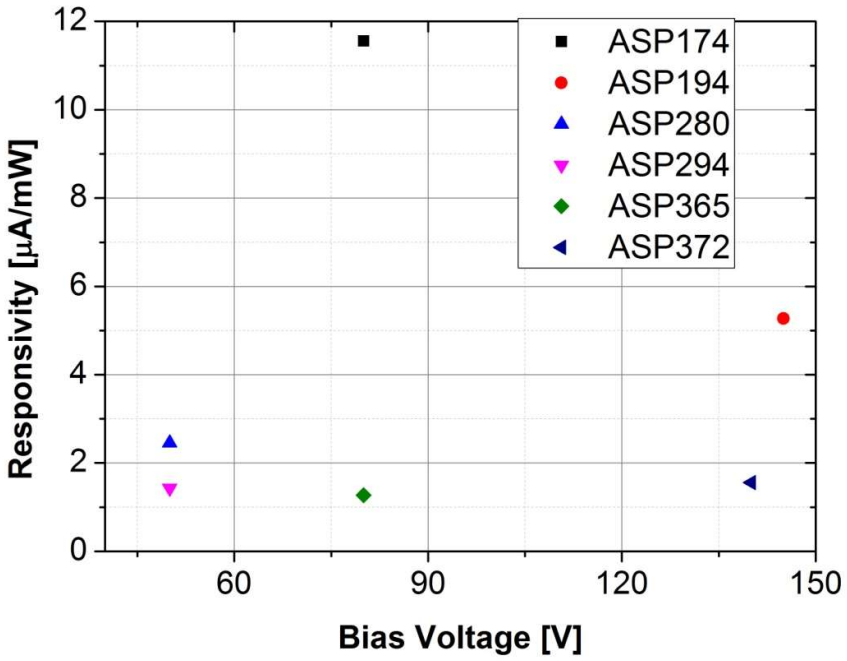

Fig. 8.9 Responsivities vs bias voltage for each substrate under an optical excitation of 64 mW of 1550 nm laser power.

8.4 THz Power Measurement

A device with design A was then fabricated on sample ASP280, nominally a replica of ASP174. The broadband THz power obtained is shown in Fig. 8.10. At 80 V, the maximum generated power was 22.2 μW. The power vs. bias voltage displays a power dependence with an exponent of 1.87.

Sample ASP294 was tested with both designs A (Fig. 5.1) and B (Fig. 5.3), and the results are shown in Fig. 8.11.

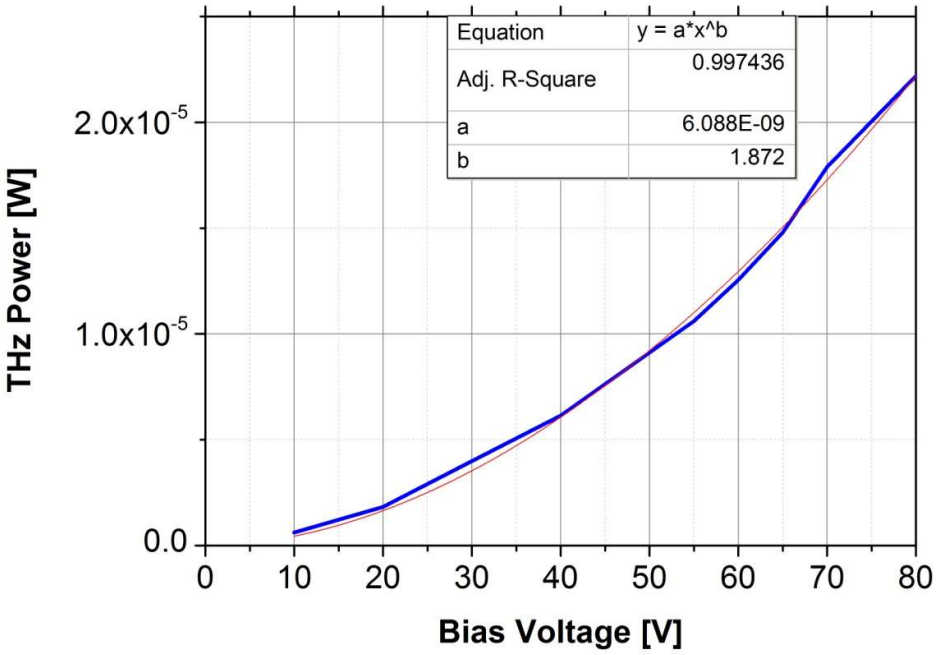

Fig. 8.10 Design A, ASP280, THz power vs bias voltage.

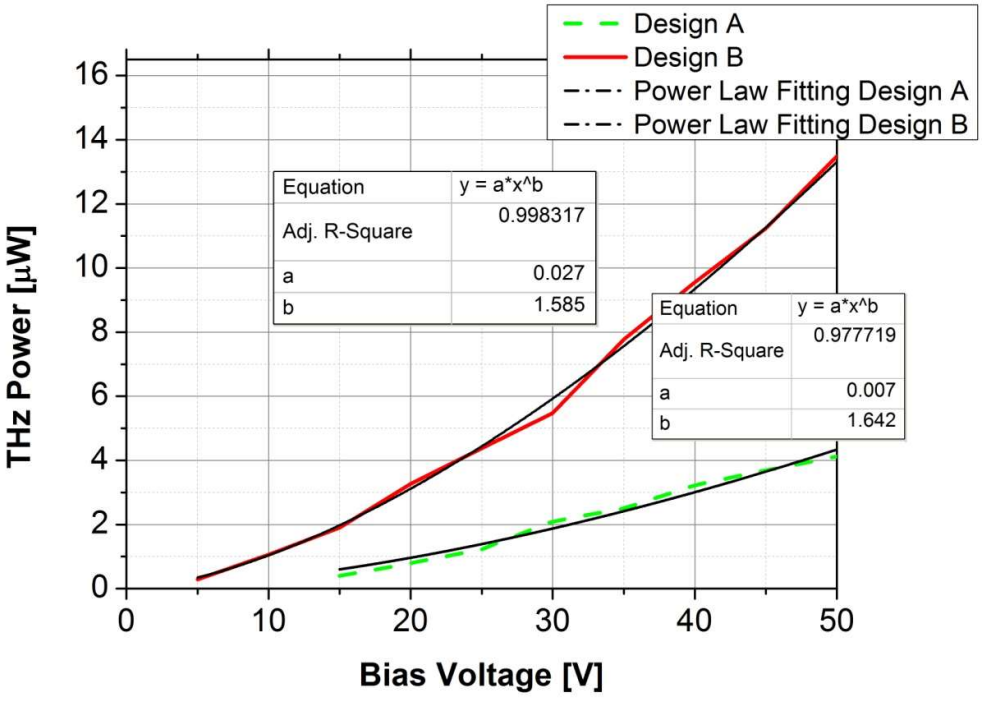

Fig. 8.11 Design A (in blue) and B (in red), ASP294, THz power vs bias voltage.

Design A and B devices based upon ASP294 only generated around 4.1 μW and 13.5 μW, respectively. The optical-to-THz power efficiencies were therefore poor, being 0.0093% and 0.0307%, respectively.

ASP365 was tested only with design B and the results are shown in Fig. 8.12.

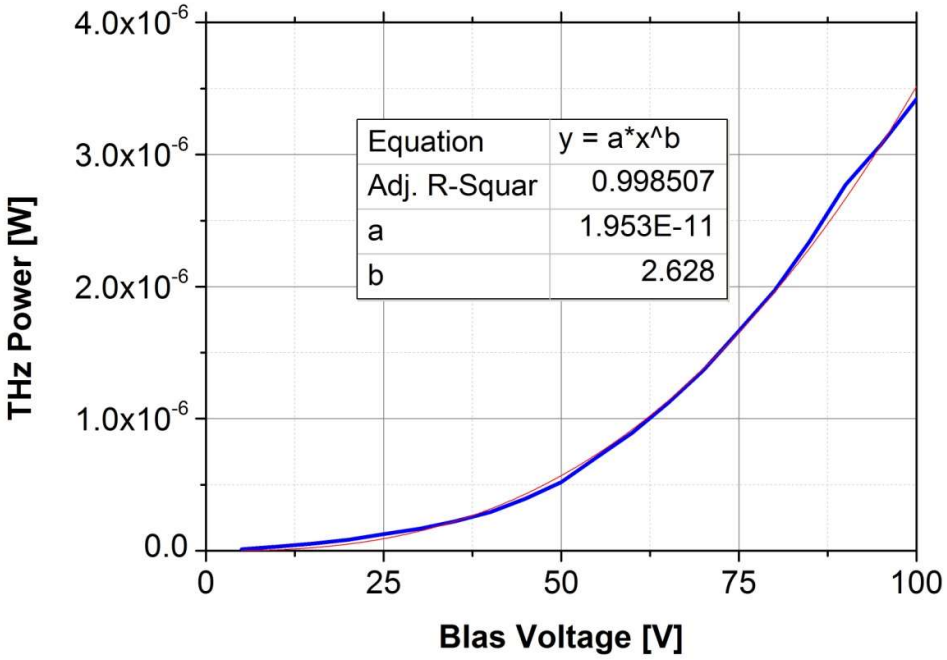

Fig. 8.12 Design B, ASP365, THz power vs bias voltage.

The results did not meet expectations, for only 3.6 μW of THz power was obtained at a bias voltage of 100 V. Similarly, the optical-to-THz power conversion efficiency was only 0.0082%.

8.5 Summary of PCS broadband power

Fig. 8.13 displays a summary of the maximum THz powers obtained from the devices fabricated on different materials (both with design A and B).

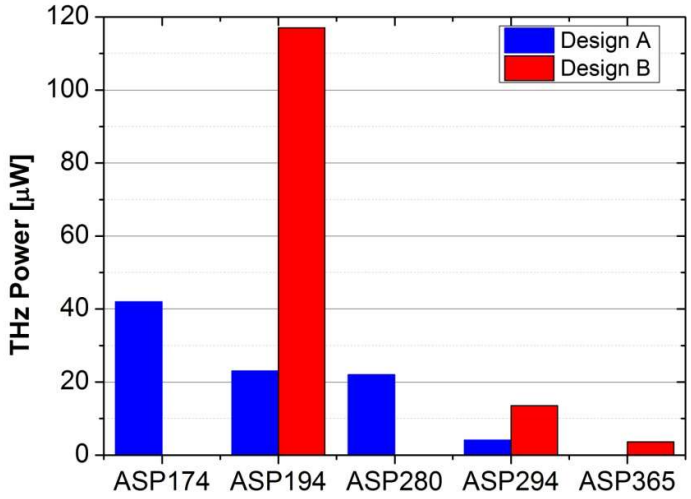

Fig. 8.13 Summary of THz power generated by the different materials at their maximum testing voltages.

As is clear, the device with design B of ASP194 generated the highest THz power by far. One reason for its success can be attributed to the quality of the material, as sample ASP194 is the most optimized material to date.

8.6 Summary of photoconductive switches driven with 1550-nm pulsed laser radiation

The testing of the remaining samples confirmed that ASP174 and ASP194 are capable of generating the highest THz power. This is in agreement with findings discussed in Chapter 3, where IR absorption was found to be consistently smaller after the growth of ASP194. The lower absorption might relate to the MBE growths. Some growth conditions may have been varied, creating limitations on the reproducibility. Further research is ongoing to confirm what actually happened.

CHAPTER 9
Continuous-wave Excitation

9.1 Photocurrent under 1550-nm CW laser excitation

The best performing devices, based upon ASP194, were tested as photomixers under the excitation of 1550-nm CW lasers. The objective was to understand whether or not sample ASP194 could be used for photomixing. The setup used was very similar to the one used for 1550-nm pulsed laser excitation. Fig. 9.1 (a) shows a picture of the setup while Fig. 9.1 (b) shows the schematic.

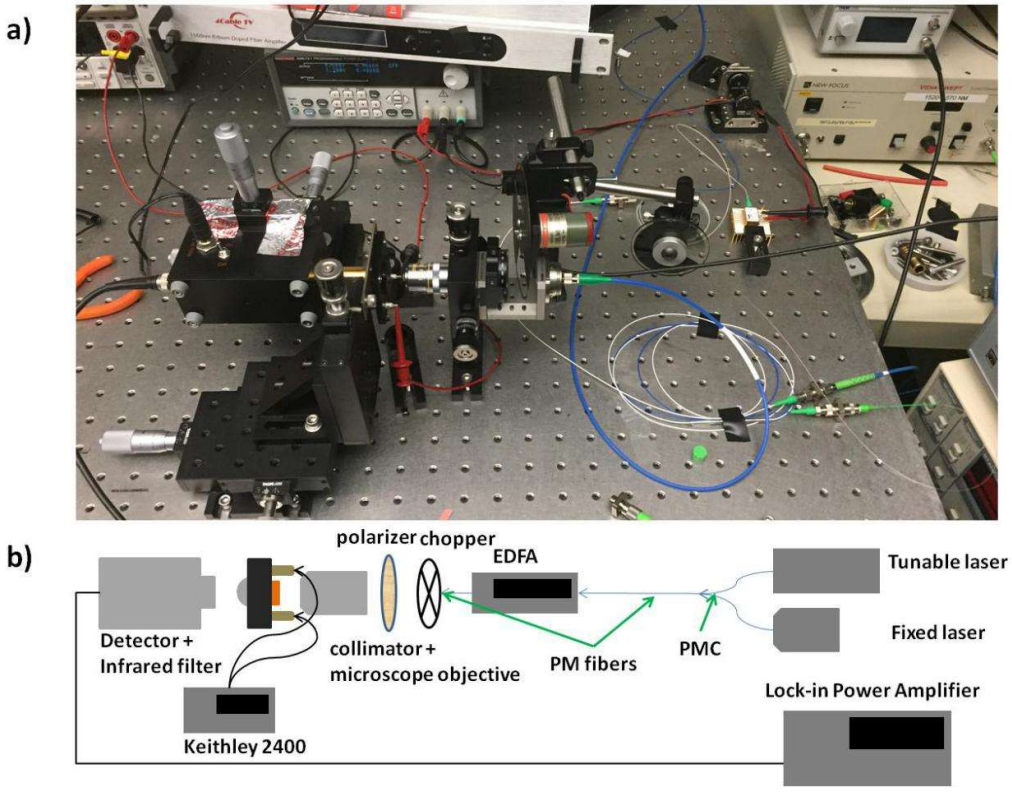

Fig. 9.1 a) picture of the setup and b) block diagram of the photomixing setup.

The setup consists of two continuous wave laser sources: one with a fixed wavelength, namely a Thorlabs SFL1550P; the second with a source capable of varying the wavelength in the range of 1520-1570 nm (New Focus Vidia). A fiber combiner was used to add the two beams, and an Erbium Doped Fiber Amplifier (EDFA) was used to boost the laser power. An NIR polarizer was utilized to increase the extinction ratio of the linear polarized beam. A 10x achromatic standard microscope objective (NA = 0.25, EFL = 15.2 mm) with a focus spot size of 10 μm was used to focus the beam on the active region of the devices. The testing method was the same one presented for 1550-nm pulsed laser excitation.

A polarization maintaining fiber combiner was then used to add the wavelengths from the two linearly polarized lasers. The two-tone output of the combiner was measured with an Anritsu MS9740A Optical Spectrum Analyzer (OSA) to check the purity of the process (i. e. no inter-modulation products) and to make sure the power levels were the same. An example is shown in Fig. 9.2.

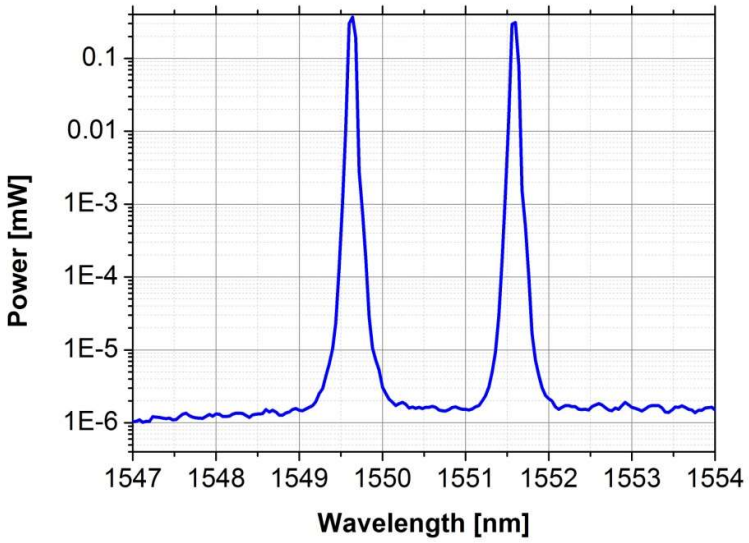

Fig. 9.2 Example of the two-tone beam at the fiber combiner output.

The output of the combiner was amplified by the EDFA from a milliwatt level to tens or hundreds of milliwatts. A U-bench with a collimator and a polarizer was utilized to modify the beam and ensure an even greater degree of common linear polarization between the two tones. Finally, the combined beam was coupled in free space with the microscope objective in order to focus the beam on the device.

A device fabricated on sample ASP194 with the design A pattern was tested for 1550 nm CW responsivity. The laser power was set to 85 mW. Fig. 9.3 shows the currents (dark and photo), while Fig. 9.4 shows the corresponding responsivity.

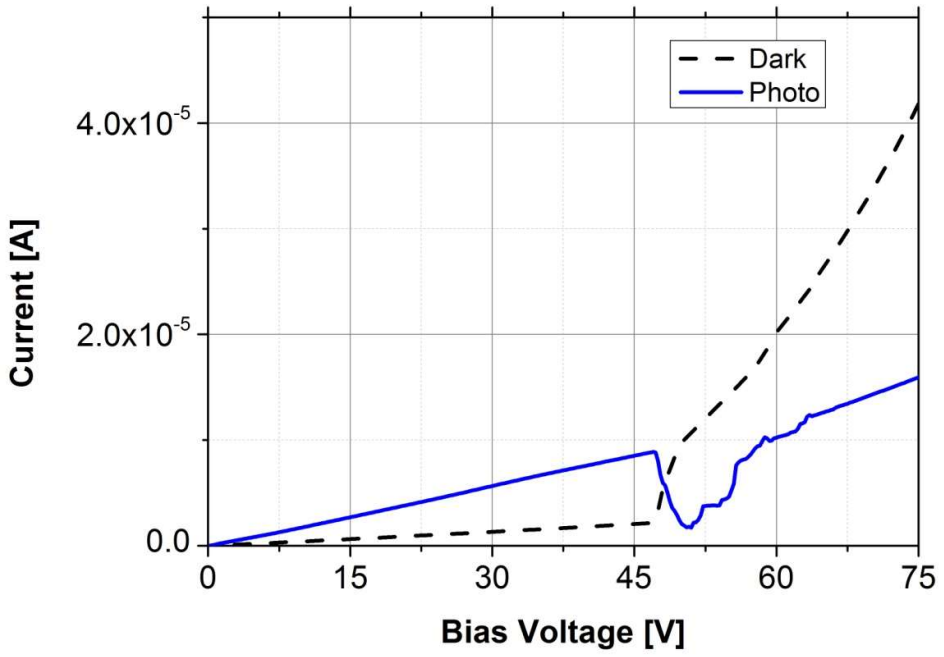

Fig. 9.3 Dark- and photo- current of PCS with design A, fabricated on ASP194, under 1550-nm CW optical excitation.

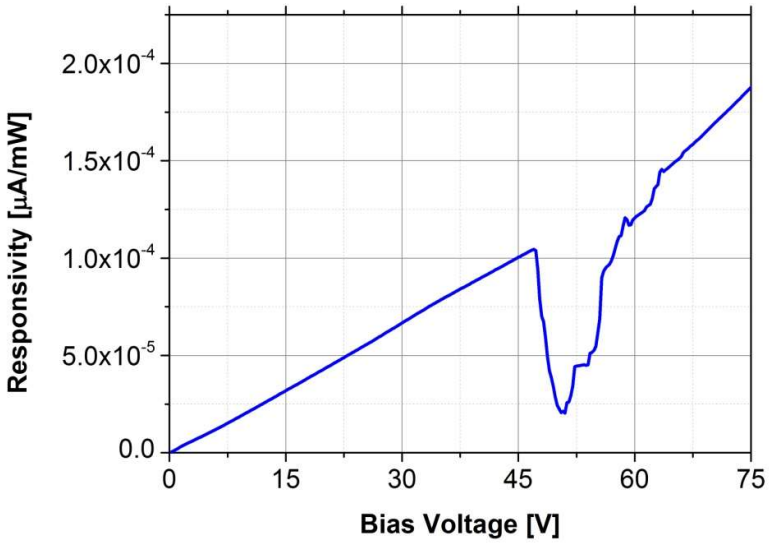

Fig. 9.4 Optical responsivity of a design A PCS, fabricated on ASP194, under 1550-nm CW optical excitation.

For reasons that are still unclear, there was a drop in the photocurrent and responsivity at the discontinuity voltage. Due to this drop, the value of the responsivity was measured at the bias just before the discontinuity (45 V), and at the highest bias voltage (75 V). The measured values are 0.1 μA/mW and 0.18 μA/mW, respectively. These values were lower than those obtained with the same device under pulsed laser excitation with values of 0.33 μA/mW and 0.57 μA/mW, respectively, a factor of almost 3 of difference between the two types of excitation. Additionally, the comparison between the two responsivity curves is shown in Fig. 9.5.

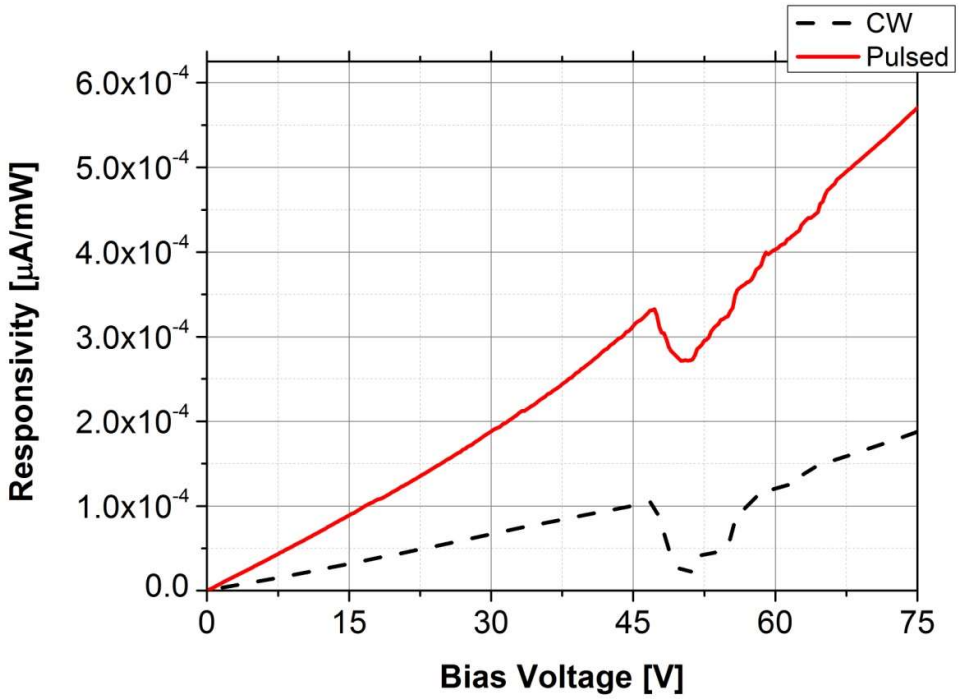

Fig. 9.5 Comparison between pulsed and CW laser excitation responsivity on a design A PCS, fabricated on ASP194.

In the next step, the PCS with design B fabricated on ASP194 was tested in the same fashion. The laser power was set to be 140 mW of 1550-nm CW excitation with a wavelength offset of 3 nm. The results for the currents and responsivity are shown in Fig. 9.6 and 9.7. As the data shows, the responsivity is still low, even at 100 V bias (approximately 0.5 μA/mW), compared to the values obtained for pulsed laser excitation (approximately 1.5 μA/mW), while the maximum photocurrent generated was only 70 μA.

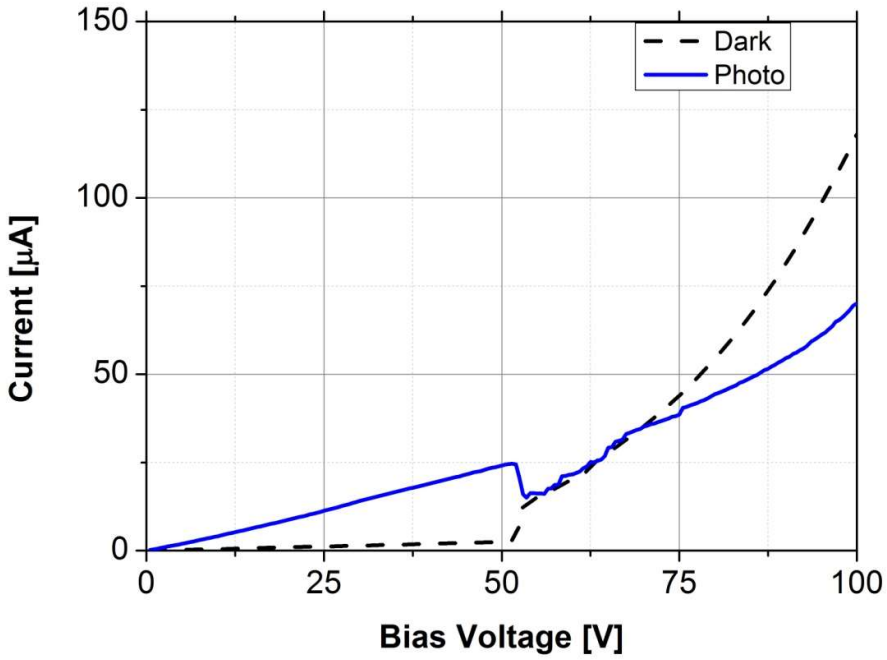

Fig. 9.6 Currents of a design B PCS fabricated on ASP194 under 1550-nm CW excitation.

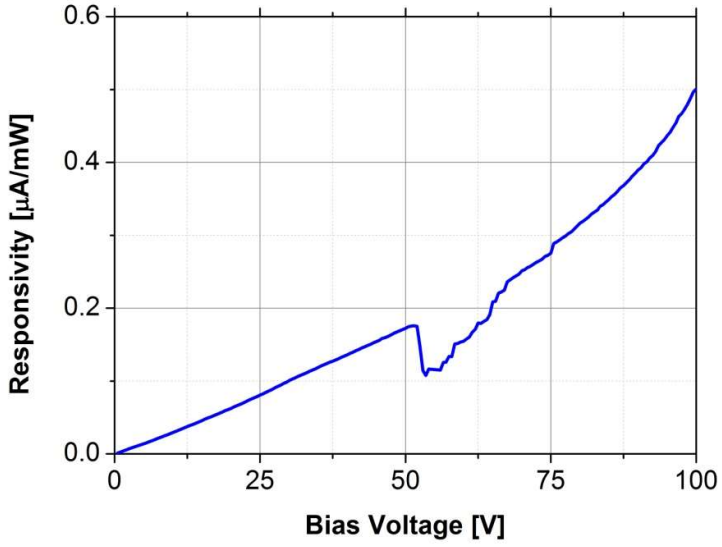

Fig. 9.7 Responsivity of a design B PCS fabricated on ASP194 under 1550-nm CW excitation.

In an attempt to improve their performances, devices with deep-sub-micron fingers dimensions were used for their enhanced responsivity, as previously mentioned in Chapter 5. The IE device structure shown in Fig. 5.28 was implemented and fabricated

on ASP280 due to a lack of both ASP174 and ASP194. The IE fabrication was executed at the NanoTech West laboratories at Ohio State University via electron beam lithography and e-beam metal deposition. The interdigital electrodes, shown in Fig. 5.28, have an electrode length of 8 µm and a width of 100 nm, separated by 1.4 µm. For the IE structure, a metallization consisting of 10 nm of Ti and 50 nm of Au was used. After this step, the rest of the fabrication (second optical mask and evaporation) was completed internally. This required a re-alignment step using the MJB3 mask-aligner, making this the first multi-level optical lithography process done in the THz lab at Wright State University.

The device was then tested in the same setup used previously with a 1550-nm laser power of 150 mW. The results for the currents are shown in Fig. 9.8, while the data for responsivity is provided in Fig. 9.9. These results prove that the use of IE structures can significantly improve the performances of these devices.

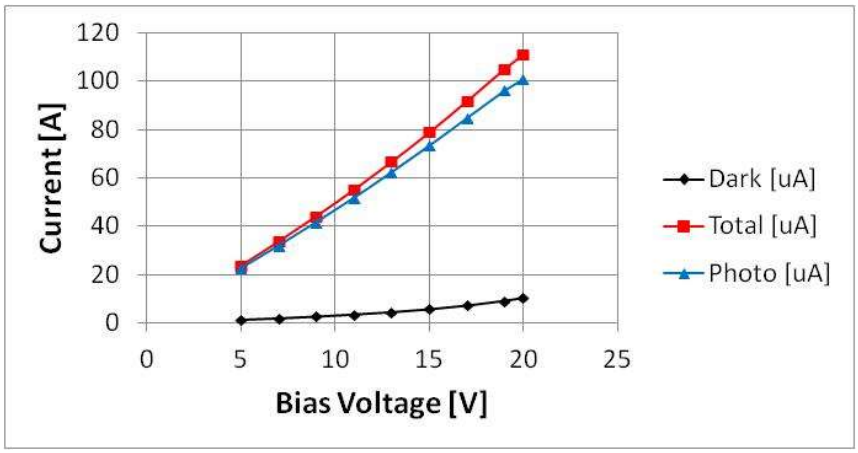

Fig. 9.8 Currents for the IE PCS fabricated on ASP280.

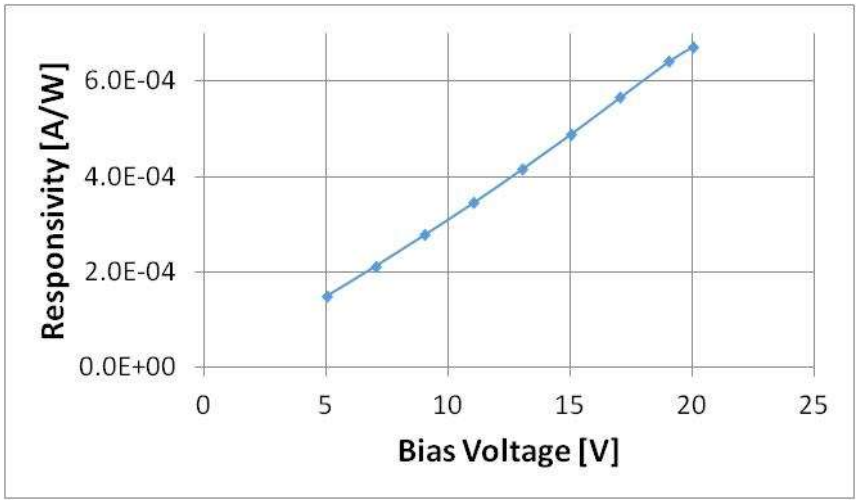

Fig. 9.9 Responsivity of IE PCS fabricated on ASP280.

9.2 Photomixing power spectrum

In order to obtain photomixing excitation, and therefore THz generation, the photoconductive antenna needs to be excited by two frequency-offset lasers. The offset between the wavelengths of the drive lasers determines the frequency at which the device radiates. Fig. 9.10 depicts the difference in frequency generation for 780 nm and 1550 nm wavelengths. For example, in order to generate 1 THz light, an offset of 8 nm between the two frequencies around 1500 nm is required.

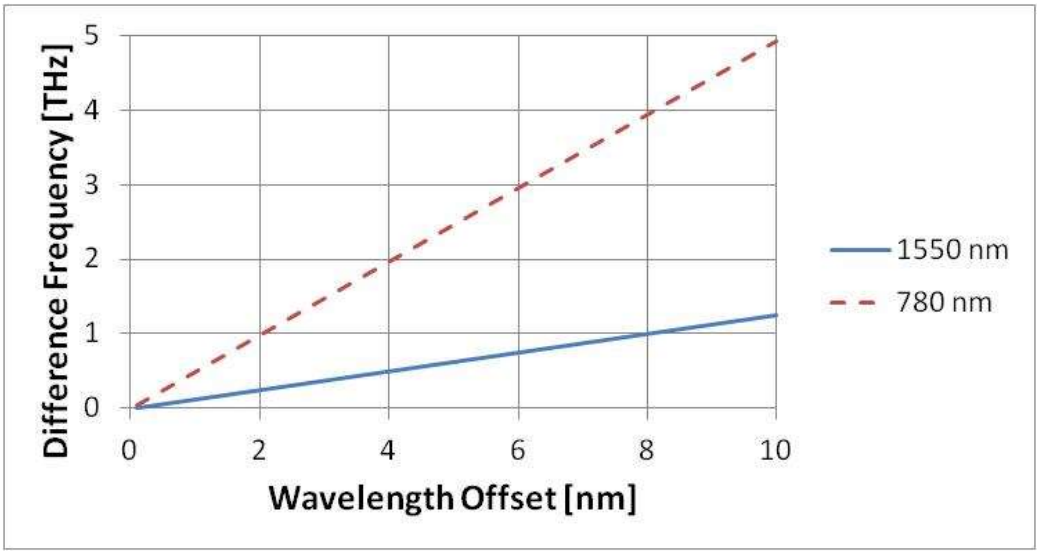

Fig. 9.10 Difference frequency as function of wavelength offset for 780 nm and 1550 nm wavelengths.

For this experiment, various devices have been tested. However, only the device fabricated on sample ASP194 with design B proved to generate measurable THz radiation. Using the QMC OAD-7 Golay Cell as detector and the New Focus Vidia to adjust the wavelength offset, a frequency sweep from 200 GHz to 1300 GHz was performed. The resulting data is provided in Fig. 9.11. The results show that the levels of the signals were weak. These power results are lower in magnitude compared to those obtained by Zhang et al. [2] on a sample of ErAs:GaAs, which had a lower erbium doping and unknown nanoparticle size, shape and concentration.

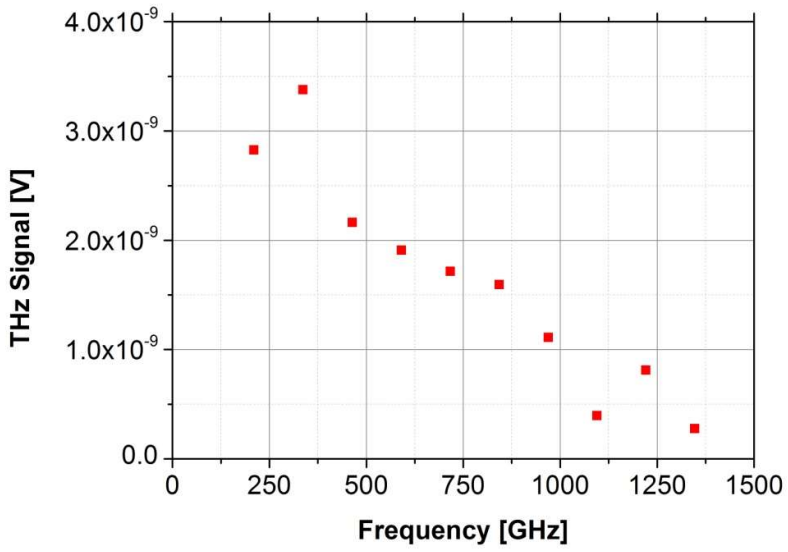

Fig. 9.11 Power spectrum for 1550-nm CW laser excitation obtained through difference frequency generation.

Fig. 9.12 compares this CW power spectrum curve with the one obtained from pulsed laser excitation, showing that the two curves are in strong agreement with one another. Note that the CW power spectrum was obtained by tuning the lasers, whereas the pulsed PC switch spectrum was obtained by the autocorrelation method.

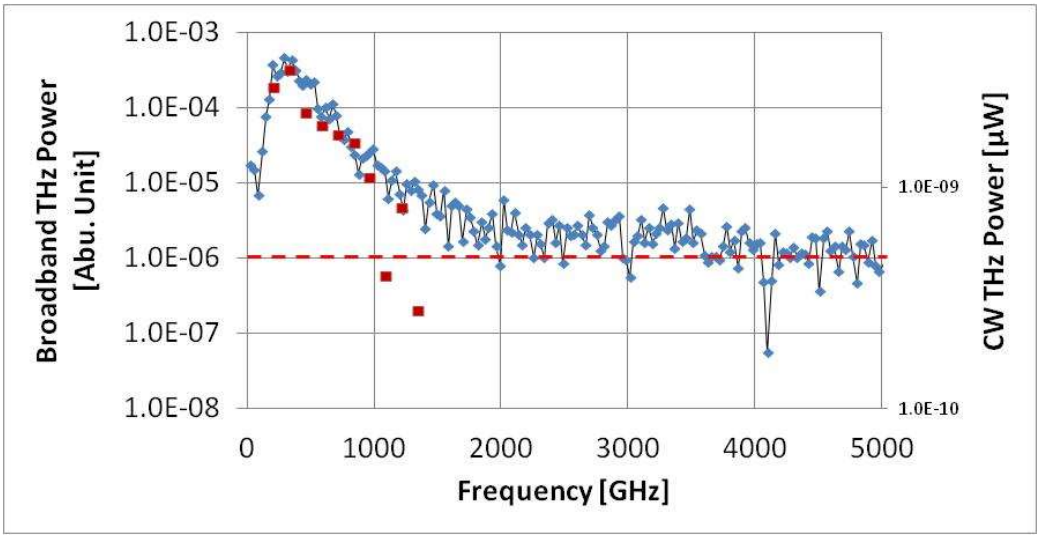

Fig. 9.12 Comparison between the power spectra obtained with pulsed laser excitation (in blue) and CW laser excitation (in red).

9.3 780 nm CW Responsivity

These results turned the attention to the photoconductive mechanism. To better understand this mechanism, an additional experiment was conducted in order to compare the extrinsic photoconduction mechanism to the intrinsic mechanism. A PCS with design B fabricated on ASP194 was tested for responsivity under three different regimes: 1550 nm pulsed, 1550 nm cw and 780 nm cw excitations. The setups for 1550 pulsed and cw excitation are the same as those previously discussed in this dissertation. The setup for 780 nm cw excitation is shown in Fig. 9.13. The source was a Cheetah laser system and the microscope objective lens is used to focus the laser beam on the active region of the antenna. The alignment procedure was the same one used throughout this research.

In Fig. 9.14 are shown the resulting responsivities. According to the plot, under a bias voltage of 50 V, the cw responsivity at 1550 nm (1.4×10^{-4} A/W) is 10 times lower than the 780 cw responsivity (1.5×10^{-3} A/W). Fig. 9.14 also highlights the comparison between the responsivity at 1550-nm under pulsed and cw excitation. More research

and testing on the exact photo-carrier generation and transport mechanism would be necessary in order to understand this difference.

Fig. 9.13 Setup for 780 cw optical excitation.

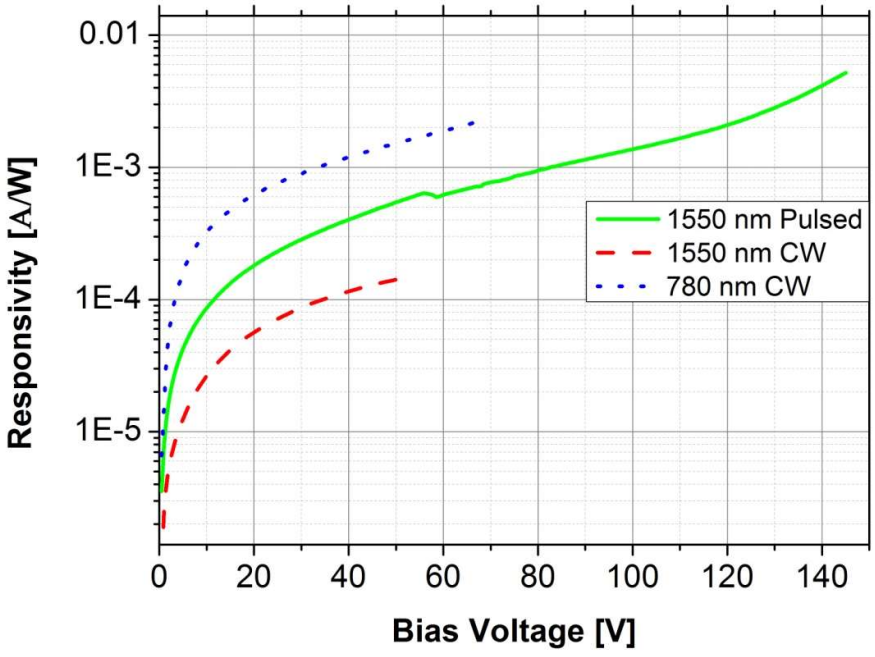

Fig. 9.14 Responsivities of design B square spiral antenna, with CW 780 nm, pulsed 1550 nm and CW 1550 nm excitations.

9.4 Summary

The experimentation of THz generation through photomixing led to the realization that the excitation mechanism strongly affects the responsivity and THz power generation. 780 nm (cross-gap) excitation creates much higher responsivity than 1550 nm. At 1550 nm, pulsed excitation is much more effective than CW. To explain this, further investigation into the excitation and transport mechanisms would be required. One main question to answer is, how are the photo-carriers being generated? The differences noted between 1550 nm pulsed and cw excitation could be due to either the fact that peak power may play a crucial role in generating photo-carriers or to a different recombination mechanism between the two. This can be deduced by the fact that the responsivity under cw excitation is only one third of the responsivity under pulsed regime. An additional explanation could be that the weaker cw responsivity and photomixing power could be caused by a long photo-carrier lifetime. A possible explanation of this phenomena is reported in Ref. [130]. In fact, as stated in Chapter 1, the lifetime of the photo-carrier is crucial for photo-mixing generation but not for generating THz power under a pulsed regime.

CHAPTER 10
Reliability studies

During the course of this research, several devices failed. This brought forth an important question: how robust are these devices? To date, to the best knowledge of the author, there has been no study on the failure mechanisms of THz photoconductive devices. To gain more insight, an investigation of failure mechanisms and the stability of the devices were conducted. This study was limited to only tens of devices.

9.1 Electrical based stress

In order to test the stability over time under simple electric stress, 2 types of experiments were run. The first was a long-term electrical bias. It was carried out by running successive I-V curve scan with step size of 1 V and with 3 seconds of delay between each step. The voltage range was from 0 to 120 V, and the data was saved for each scan. This test was performed non-stop for 75 days on a PCS with design B fabricated on ASP365. Throughout this period, no significant sign of change in the shape of the curve or peak values were recorded. The only notable differences were small fluctuations likely due to changes in room temperature, light and humidity. Fig. 10.1 shows the curve taken on the first day of testing and the curve taken on the last day.

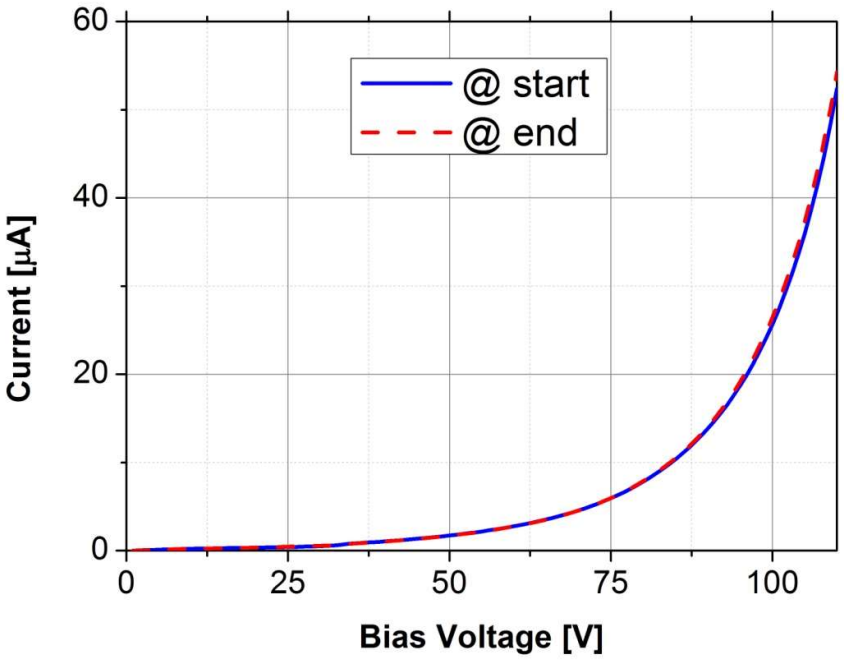

Fig. 10.1 Dark-currents on design B ASP365, at the beginning (in blue) and at the end (in red) of the experiment.

The second test was performed by biasing the device at a constant high bias 100 V. This test has been running for 126 days straight and is still ongoing (>3000 hours). The current has been stable around a value of 26.8 ± 0.6 μA, with the fluctuation attributed to the ambient light level, air humidity and room temperature. Both devices are still functional, proving the robustness of the materials and fabrication with respect to electrical stress alone.

10.2 Stress by optical excitation and electrical bias

A third test was conducted in order to check for the stability under optical 1550-nm pulsed excitation. Among all the gap devices tested under safe operating conditions, only one device has failed to date. Safe operation consisting of 64 mW of laser power and a bias voltage low enough to not draw currents in the milliampere range. This single failing device was a PCS with the design A fabricated on ASP174, and it was tested for over 6 months. It was fully characterized for 1550-nm CW and pulsed responsivity as

well as for THz radiation. The maximum bias voltage at which this device was tested was 80 V, under a 1550-nm pulsed laser excitation of 64 mW, driving a current of 800 μA. Until its failure, no sign of a change in the photocurrent or THz power radiation was recorded. The failed device was imaged, but there was no clear sign of the type failure, neither on the semiconductor material nor on the metallization.

Other devices were tested over several days under the same operating condition but none of them failed. One device in particular was heavily tested (especially under 1550-nm pulsed laser excitation) for over a year at the highest bias voltage of 145 V. It was fabricated on ASP194, and to date it is still operational. The drained current at this bias voltage reached a value of 600 μA, while the radiated power reached 117 μW. As was the case in the previous device, there has been no notable sign of a change in the photocurrent or THz power to date.

In addition to pulsed laser excitation, all of the gap devices were also tested under CW laser excitation. In this case, a variable laser power, ranging from 4 mW up to 300 mW, was used to drive the devices. A maximum bias voltage of 110 V was used. Similar to the previous tests, only a few of the many tested gap PCS devices failed during the experiments. However, none of them showed any clear sign of the cause of failure, neither on the semiconductor nor on the metal. It appears that a thermal breakdown may be the reason behind the failures. Using Eqn. 5.3 under the condition of 300 mW of laser power, a voltage of 100 V and a current of 100 μA, the increase in the temperature reaches 250 °C. Looking at the ASP194, design B gap PCS device (with an optical pulsed laser power of 64 mW, a voltage of 145 V and a current of 0.6 mA), the increase in the temperature was only 121 °C. With these findings, it is conceivable that the main cause of the breakdown of the devices is thermal rather than electrical.

All of these tests lead to the conclusion that the gap PCS devices are very robust to electrical breakdown and can sustain heating of the active region up to at least 133°C for long periods of time.

Things change with the IE devices, both with large (made by optical lithography) and small (e-beam lithography) fingers. Many devices were tested from different samples (listed in Table 10.1). Design A IE PCSs with optical fingers were fabricated on ASP194 and ASP294 with a metallization stack of Ni/AuGe/Ni/Au, and design B devices with e-beam IE PCS based upon ASP280. The e-beam fingers were metalized with Ti/Au while the PCS with Ni/AuGe/Ni/Au.

Table 10.1 List of device characteristics for reliability tests. All devices have IE structures. Details on the epitaxial layer and fingers fabrication.

	ASP194	**ASP280**	**ASP294**
Erbium concentration [cm^{-3}]	8.8×10^{20}	4.4×10^{20}	8.8×10^{20}
Epilayer thickness [µm]	2	1	1
Optical fingers	No	Yes	No
E-beam fingers	Yes	No	Yes

Of the many devices tested, a large portion failed while being operated under what were initially thought to be safe operating conditions: bias voltage of only 5 V and under at most 64 mW of pulsed laser excitation power and 40 mW CW.

Fig. 10.2 and Fig. 10.3 show the active region area of the optically fabricated fingers on ASP294 and e-beam fingers fabricated on ASP280, respectively. These images were taken after device failure.

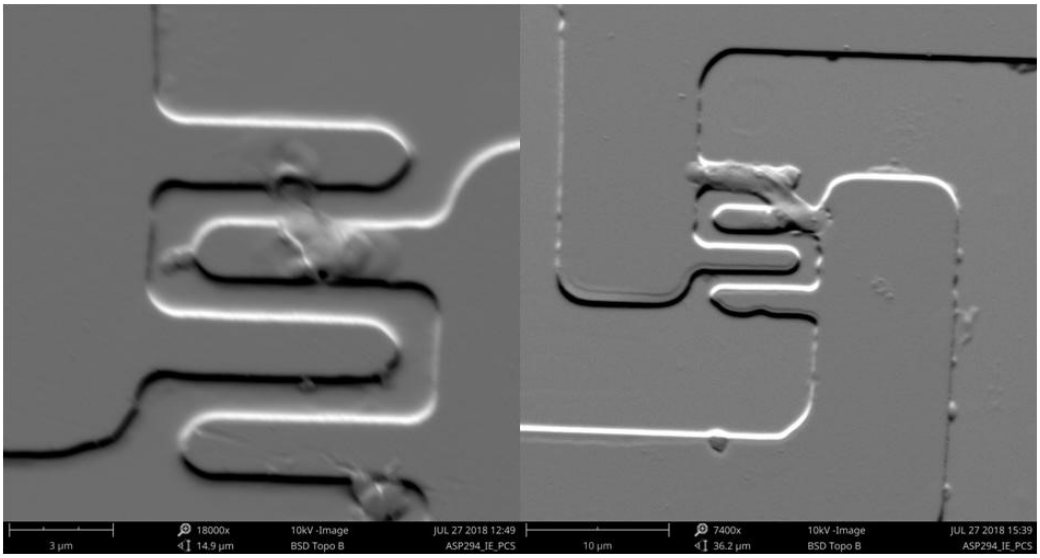

Fig. 10.2 Detail of the active region areas with optical fingers, ASP294.

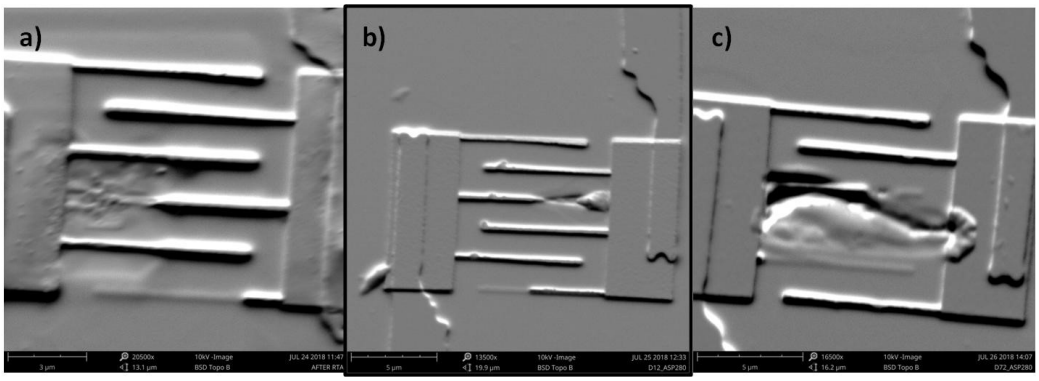

Fig. 10.3 Detail of the active region areas with e-beam fingers, ASP280.

During these experiments, the way these devices failed was the same: after testing the devices for dark-current, they were put under optical excitation (either pulsed and CW) and they all failed during the alignment procedure. Looking at the images, it appears that the two failing mechanisms are similar (involving the metallization), but they are in fact different. Considering ASP294, it appears that the metal simply melted and created a short circuit between neighboring fingers. In contrast failure of the e-beam fingers of ASP280 seems to relate to electro-migration [131], [132]. The electric field between the fingers was only 4.1 x 10^4 V/cm. Evidence for this failing mechanism can

be seen in Fig. 10.3 (a) and (b). The metal from one of the fingers migrated onto the opposite electrode leaving grooves in the semiconductor surface between them. This detail could be a result of the presence of ErAs quantum-dots (metallic) close to the surface of the substrate. In contrast, the device fabricated on ASP194 with optical IEs did not show any sign of instability or change in performance, despite the fact that it was tested under the same conditions for over 90 hours.

More tests (most likely destructive) on multiple devices and from different samples would be necessary to draw a more definitive conclusion. However, one key factor from Table 10.1 is that the ASP194 material had a 2-μm thick epitaxial layer of GaAs:Er compared to 1-μm thick for the other two.

10.3 Summary

The reliability tests are at an early stage and final conclusions cannot be drawn yet. However, some observations can be made from the recorded failures and stability tests. For one, the PCSs (with no fingers in the active region) based upon ErAs:GaAs material are very stable, both electrically and thermally. Secondly, it appears that the introduction of the fingers in IE PCSs, whether they are fabricated through optical or e-beam lithography, de-stabilize the materials and render them less thermally stable. The failing mechanism is most likely either thermal runaway (CW devices) or electro-migration (pulsed devices). Finally, there appears to be a strong correlation between the thickness of the epitaxial layer and the stability of the samples. In order to confirm or deny these observations, additional testing under different operating conditions would be necessary.

CHAPTER 11
Conclusions and Future Work

11.1 Conclusions

To reiterate, the objectives shown in Fig. 0.1 were to obtain superior devices and a better physical understanding, as well as to discover new physical phenomena of ErAs:GaAs. With these objectives the following results shown in Fig. 11.1 were obtained (Fig. 11.1).

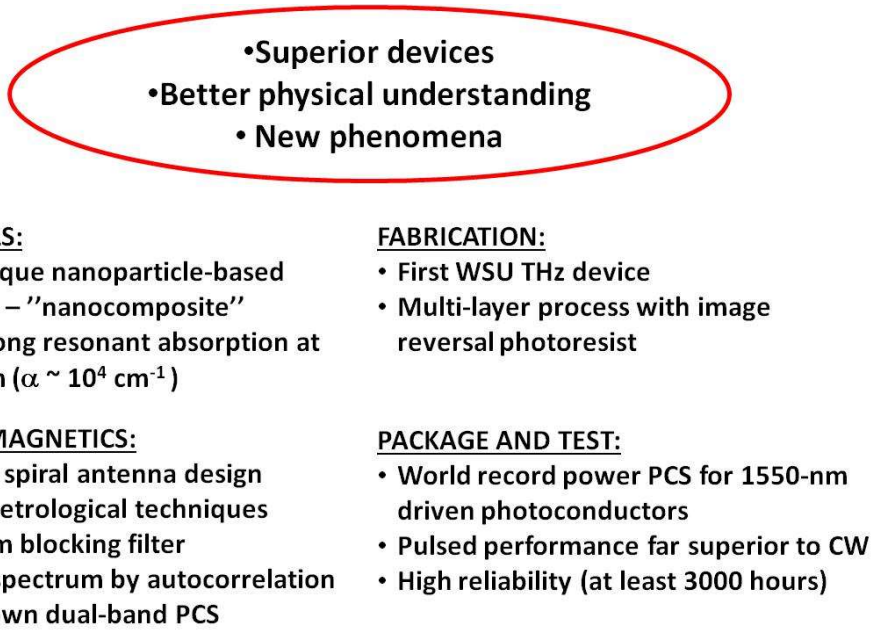

Fig. 11.1 Summary of thesis objectives and results.

The nanoparticle diameter and concentration of the unique nanocomposite ErAs:GaAs material have been optimized through erbium concentration and epitaxial layer thickness in order to increase the resonant absorption of 1550-nm light through the extrinsic photoconductivity mechanism. Strong 1550-nm resonant absorption was obtained (roughly 10^4 cm^{-1}), comparable to that of 850-nm (cross-gap) for GaAs (around 1.5-2 x 10^4 cm^{-1}). The material was characterized and proved to provide very desirable characteristics for a THz PCS: short lifetime (approximately 1 ps), high mobility (>0.65

x 10^3 cm^2/Vs), high dark resistivity (>6.8 x 10^4 Ohm-cm), and strong resonant absorption at 1550-nm (as high as 10^4 cm^{-1}).

A satisfactory multi-layer photo-lithography process was designed with high yield on the substrate (95% of working devices) and low dimensional mismatch between the patterned device and the optical mask. The metallization of the THz antennae has been studied both through experimentation and simulation. A metal stack consisting of Ni/AuGe/Ni/Au was found to better compare to the traditional TiAu. This metal stack proved to have lower resistivity and a more uniform surface morphology, reducing both resistive and radiative losses. Additionally, the simulations proved that in order to further reduce the losses and increase the antenna performance, a metallization thicker than the one used during this research should be sought.

A new design (B) for the 4-turn self-complementary square spiral antenna was developed. This design reduces electrical stress on the devices and improves the THz power generation. In addition, with the implementation of design B, the device proved to be able to radiate simultaneously in two bands: around 300 GHz from the spiral antenna, and between 10 and 20 GHz from the dumbbell dipole. Both are inherently possible because of the broadband nature of ultrafast photoconductivity. In Chapter 5, a new IR-filter based on black polypropylene was introduced with the same 1550-nm radiation blocking capability of the commonly used black polyethylene, but with a better THz transmission. Additional study on this material could help to further improve the metrology of THz power detection. Finally, the power spectrum was obtained through an autocorrelation technique using a Michelson interferometer.

From this unique material, PCS devices were fabricated that can generate a world-record THz power of approximately 117 μW of THz. This THz power is the highest among all the 1550-nm based PCS, with an optical-to-THz conversion efficiency of

0.266%. The pulse performances were found to be far superior to those of cw pumping regime, suggesting that different electrical transport mechanisms are happening. Finally, the devices were tested for reliability and stability under electrical and optical excitation. The PC devices proved to be very stable with no apparent degradation in photo-current generation and THz radiation over time.

11.2 Future Work

The results obtained during this work also brought to light several more experiment that could help to better understand this material and lead to even more efficient THz sources.

Since the material was found to absorb 1550-nm light poorly after the growth of ASP294, a more in-depth study of the material science of the different growths could help in understanding why the absorption behavior changed. In addition, it could provide more insight into whether it could be possible to further improve the 1550-nm resonant absorption.

In addition, the responsivity under cw 1550-nm excitation was found to be 3 times lower than that under pulsed excitation. Moreover, the cw 780-nm responsivity was 10 times larger than the CW 1550-nm one with a difference of a factor of 5 between the CW 780 responsivity and its theoretical prediction. More study on the two different types of optical transport mechanisms between cw and pulsed regime could clarify this difference. Preliminary results on this can be found in Ref. [130].

Considering the simulation results obtained on the effect of the resistance of the arms of the antenna on the gain, it would be interesting to obtain additional experimental results. In particular, interesting insights could be gained by comparing the THz performance of antennae fabricated on the same sample but with different metallization thicknesses.

Finally, due to the results obtained on the dual band antenna, this device should be used in real systems.

Appendix A

Discontinuity voltage

As mentioned previously, the theory behind this phenomenon is beyond the scope of this thesis, however the results gathered on it through the research done for this dissertation are here shown.

Fig. A.1 presents the data point of each substrate, first and second design (per availability) of the transition voltage.

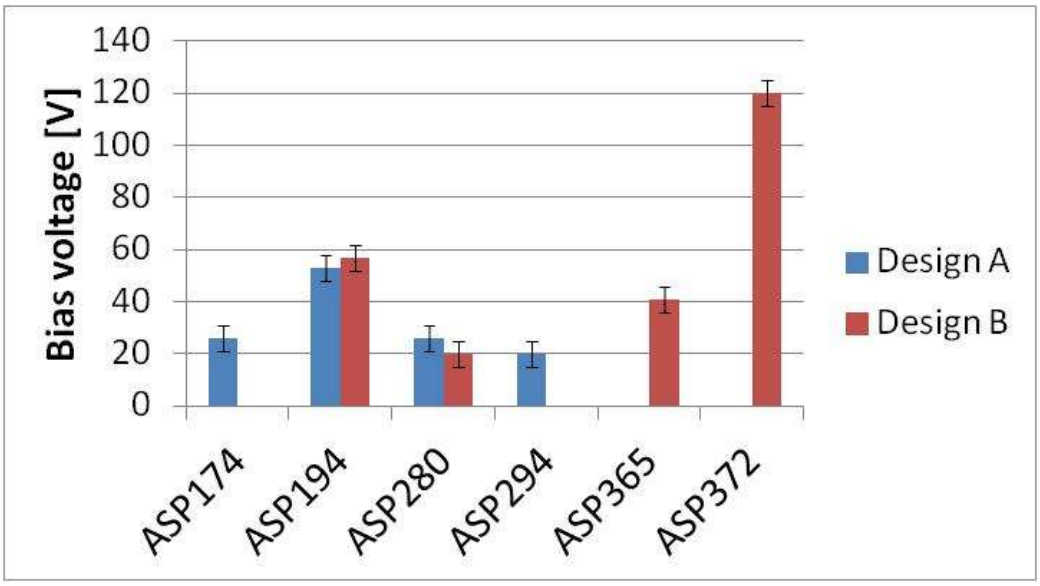

Fig. A.1 Discontinuity voltages for the different substrates and different antenna designs.

From Fig. A.1 it is clear how the change of the antenna design (with the same active region), does not affect the transition voltage which remain in within the error boundaries. However, the change in epitaxial layer thickness (from 1 µm to 2 µm) increases the voltage at which this discontinuity happens. The doping concentration

also affects this voltage; however, it is not clear how it is related to the doping concentration, as depicted in Fig. A.2.

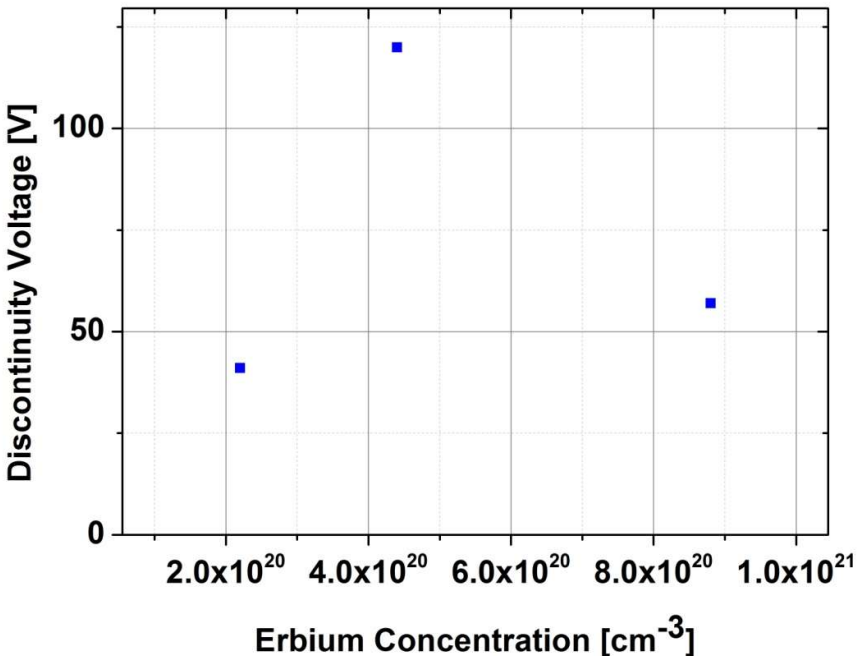

Fig. A.2 Discontinuity voltage vs erbium doping concentration.

Appendix B

1550-nm pulsed responsivity versus laser power

A test was conducted on the dependence of the generated photocurrent on the optical excitation. For this experiment, a device fabricated on ASP194 with design A was used and biased at the constant voltage of 75 V. The setup was identical to the one shown in Fig. 5.6 with the only addition of an optical wheel attenuator to adjust the laser optical power. As stated previously, the maximum optical power available from the laser source was 85 mW which, after the microscope objective lens, was reduced to 64 mW. For this reason, this is the maximum optical power used for this experiment.

Fig. A.3 shows the results of the generated photocurrent versus laser power. It is noticeable that at low laser powers there is negative photoconductivity at voltages right after the transition. Fig. A.4 shows the details of the photocurrent dependence versus laser power at the constant bias voltage of 75 V. It is interesting to notice how, while at lower laser power values the dependence is linear, at the highest optical excitation there is a deviation from linearity to a super-linear dependence.

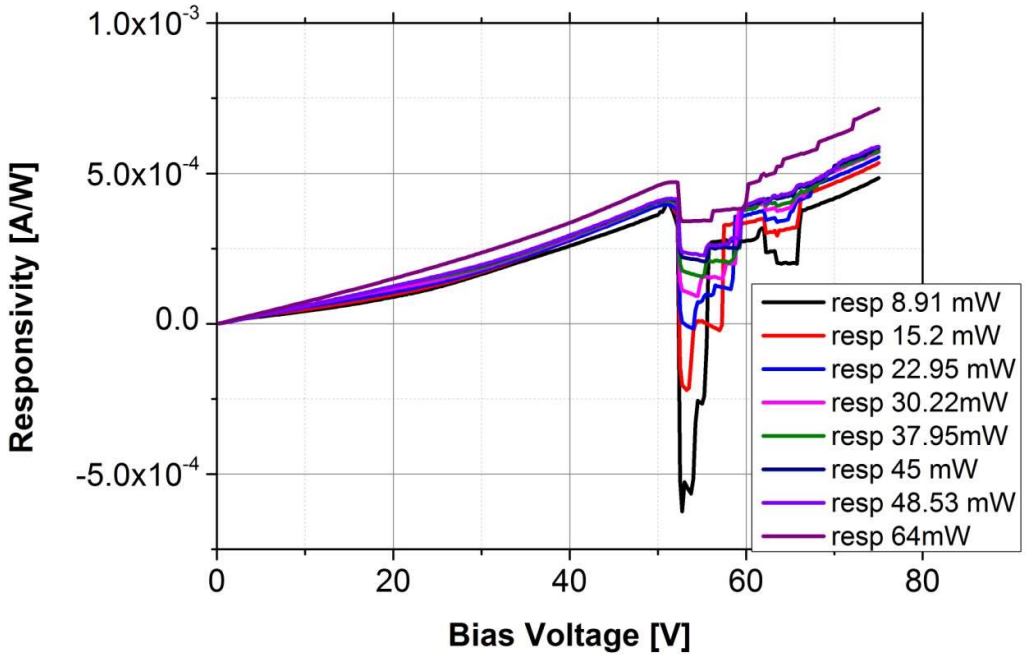

Fig. A.3 Photocurrent dependence to the optical excitation of a design A PCS fabricated on ASP194.

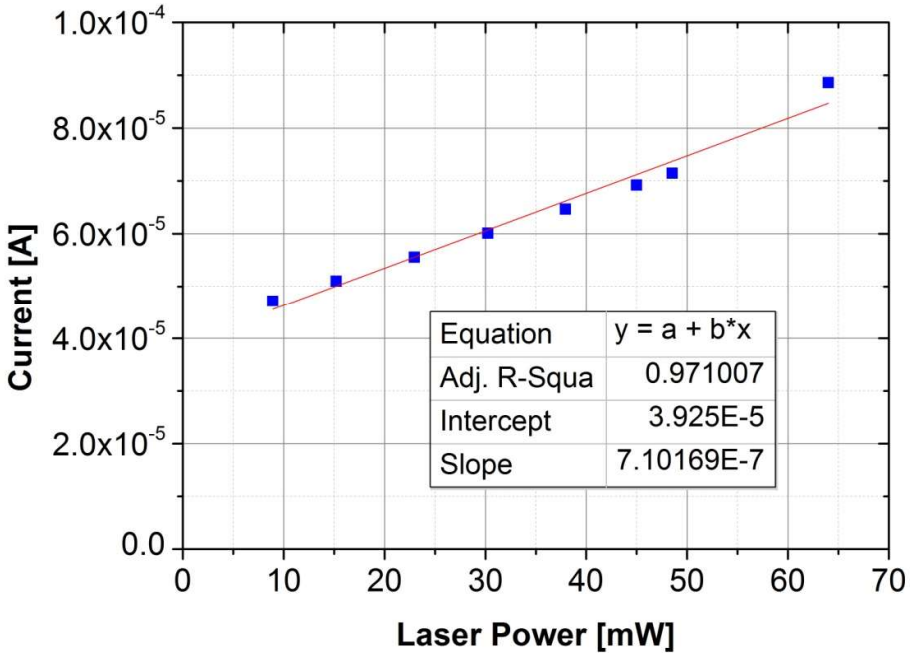

Fig. A.4 Photocurrent dependence to the optical excitation under 75 V of bias voltage for a design a PCS fabricated on ASP194.

For the same reason, a change in the responsivity of the device as a function of the laser power can be seen in Fig. A.5.

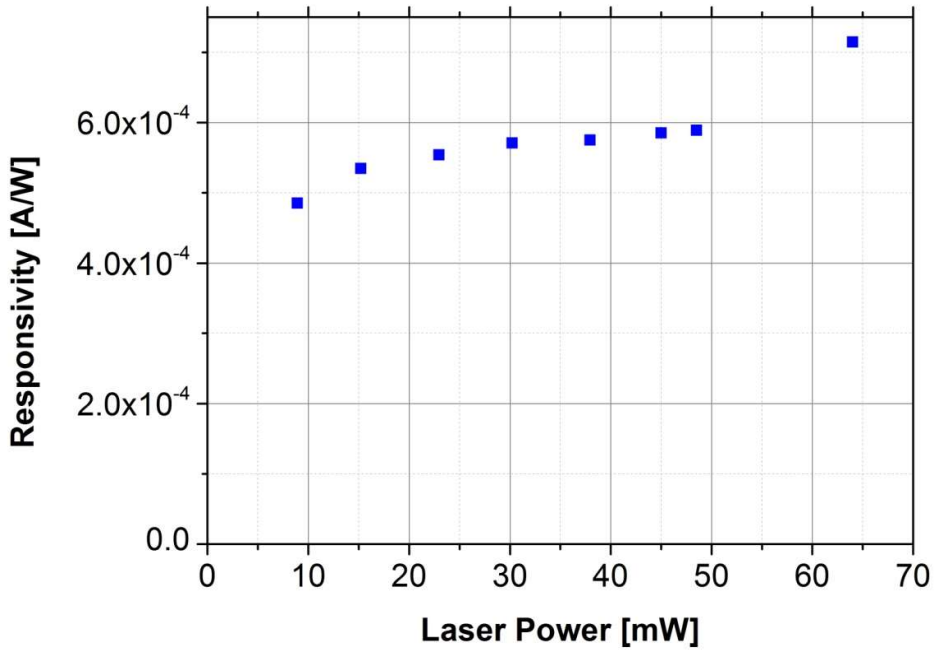

Fig. A.5 Responsivity of the device as a function of laser power at the constant bias voltage of 75 V for a design A PCS fabricated on ASP194.

While up to around 50 mW of laser power the responsivity stays roughly constant around 0.55 µA/mW, at 62 mW of optical excitation the responsivity jumps at a value of 0.75 µA/mW.

In addition, when looking at the total current shown in Fig. A.6 it can be seen that there is a shift in the main jump of the current as the laser power changes (Fig. A.7).

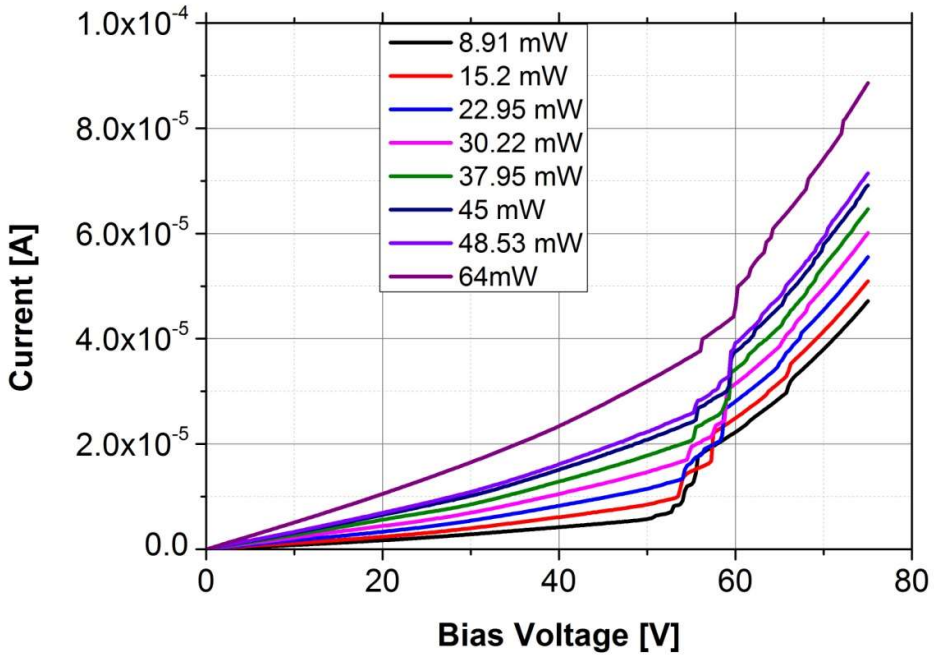

Fig. A.6 Total current versus 1550-nm pulsed laser power of a design A PCS fabricated on ASP194.

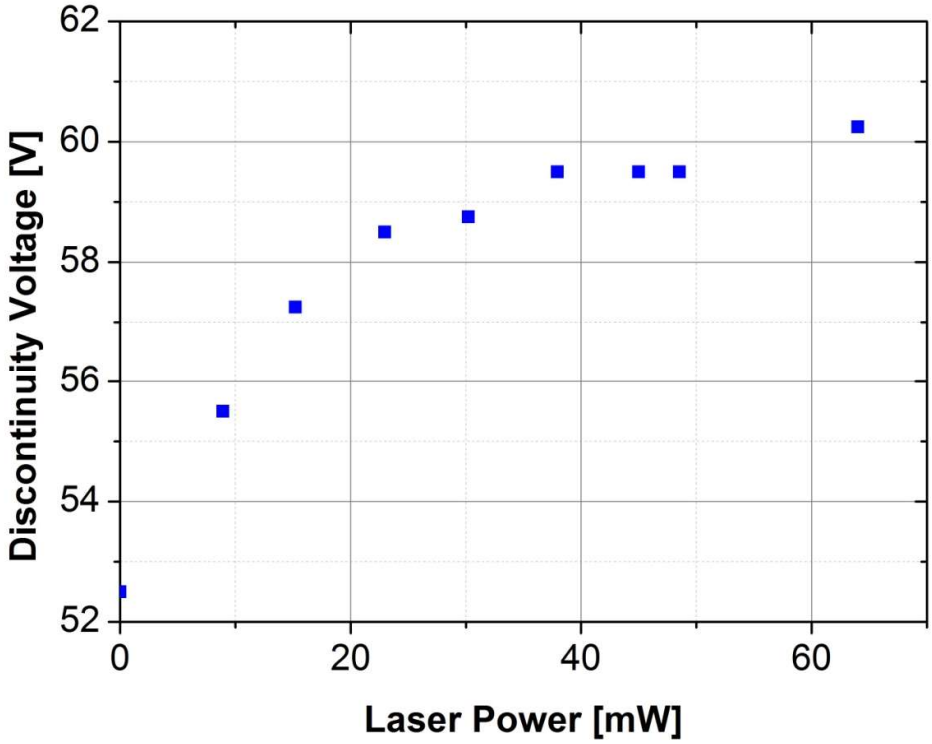

Fig. A.7 Transition voltage as a function of 1550-nm pulsed laser power.

Appendix C

CW responsivity versus laser power

As done for the case of pulsed laser excitation, a study of the responsivity as a function of the laser power was carried out. The device used in this case was design A PCS fabricated on ASP194.

An optical power from a minimum of 4.7 mW and a maximum of 94.5 mW was used in this experiment and the resulting total current and responsivities are shown in Fig. A.8 and A.9.

To be noted as even in this case with CW excitation, negative photoconductivity can be seen when the laser power is low, with this phenomenon appearing in the region right after the transition voltage. Again, the voltage at which the discontinuity voltage was monitored and checked for dependency with respect of the laser power. The results are shown in Fig. A.9.

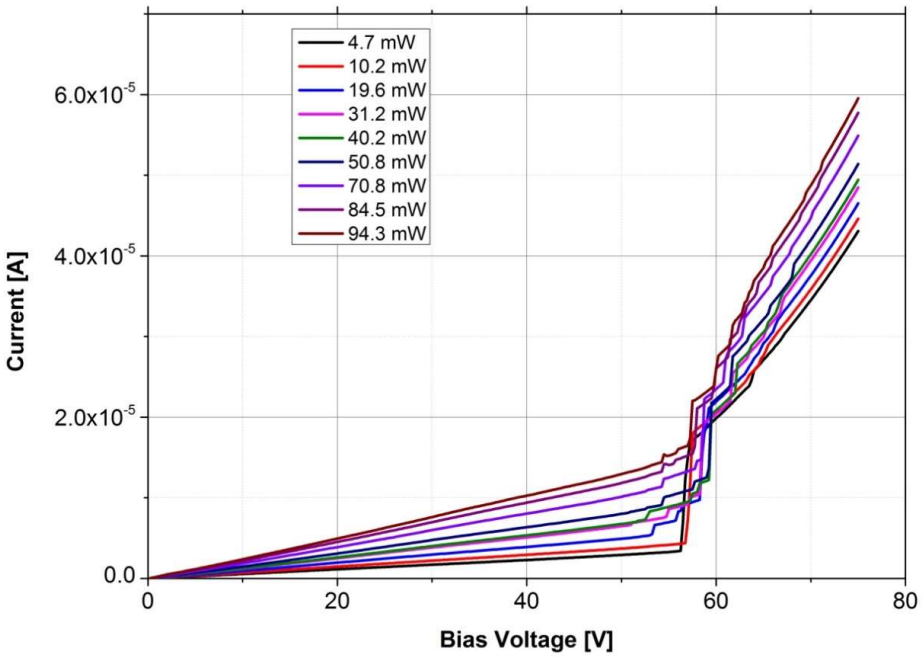

Fig. A.8 Photocurrent on PCS design A fabricated on ASP194 at different 1550-nm CW laser powers.

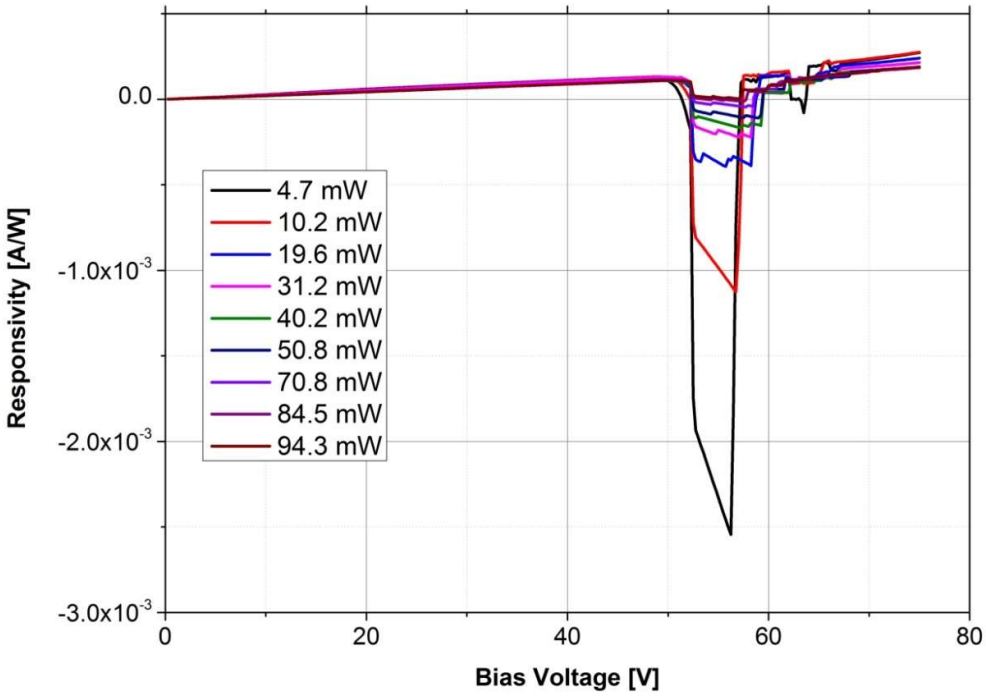

Fig. A.9 Responsivity on PCS design A fabricated on ASP194 at different 1550-nm CW laser powers.

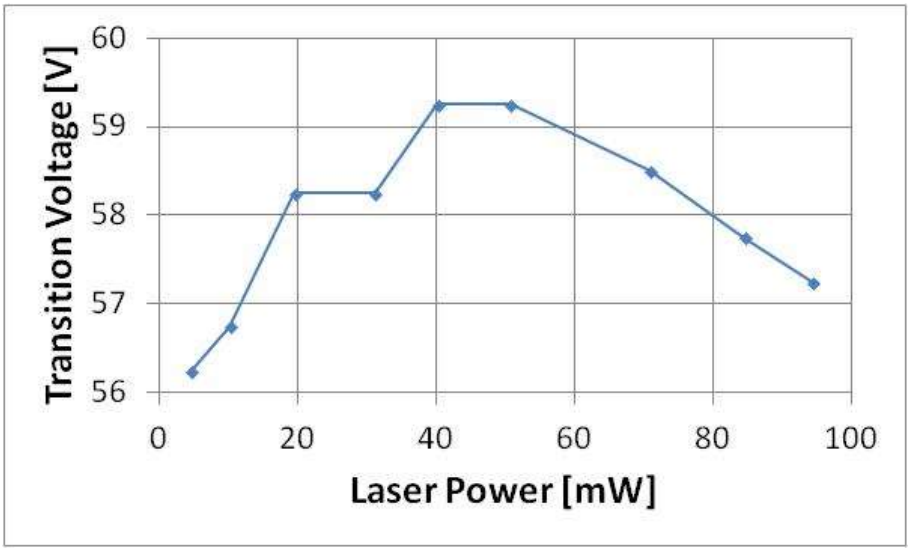

Fig. A.10 Discontinuity voltage as a function of the 1550-nm CW laser power.

No clear dependence exists between the insulator-to-metal transition voltage and the laser power.

Appendix D

Fabrication

D.1 Pre-process

To begin, a standard cleaning process was performed in order to ensure an extremely clean surface, free of any contaminants or water vapor, both of which can cause processing problems. The cleaning consists of spraying acetone, isopropyl alcohol (IPA) and de-ionized (DI) water, followed by a drying step using compressed air. The acetone is the primary chemical used to remove organic contaminants from the surfaces of the wafers. It is a good polar solvent that dissolves most organic contaminants, although its high evaporation rate may result in some residual contaminants on the surface. For this reason, the surface is subsequently rinsed with isopropanol (IPA) which is widely used as a secondary chemical to remove the contaminants after acetone is applied. IPA evaporates more slowly than acetone and dissolves non-polar contaminants that are left on the wafer. DI water is then used to rinse off the isopropyl alcohol, and compressed air is used to dry the wafers. The final step in the pre-processing is to eliminate any moisture adsorbed by the surface of the substrate. To do so, a dehydration baking is performed for 5 minutes at a temperature of 140 °C. This step helps avoid adhesion failures of the samples caused by residual

hydration. After these cleaning steps are completed, the substrate is ready for processing.

D.2 Photolithography

The first step in the fabrication involves the photolithography process. For this step, two types of photoresists have been tested: positive resist and image reversal positive photoresist. Positive photoresists were chosen because the exposed areas in negative ones swell when the unexposed areas are dissolved by the developer. This swelling, which is simply a volume increase due to the penetration of the developer solution into the resist material, results in distortions in the pattern features, and therefore limits the resolution. In contrast, when positive resist is applied, the unexposed regions do not exhibit any swelling or distortions to the same extent. As result, positive resist allows to obtain better image resolution.

Fig. A.11 shows the flow chart for the photolithography process for the two types of resists: positive and image reversal resists.

As illustrated in Fig. A.11, there are two major differences between the photoresists: the first one is the pattern, with dark and clear fields being switched between the two (i. e., with the developer dissolving the area exposed for positive resist and the unexposed area for image reversal positive resist); the second one is the slope of the sidewalls of the patterned photoresist (the slopes in Fig. A.12 are accentuated for clarity).

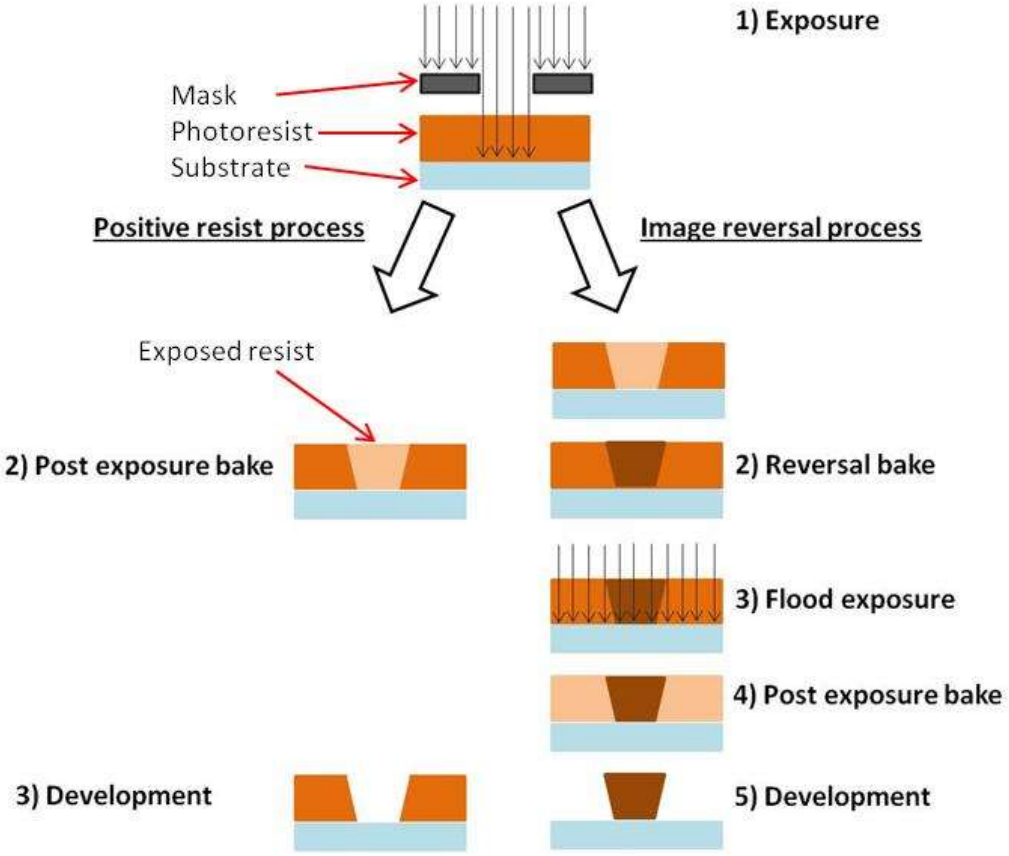

Fig. A.11 Flow chart of the photolithography processes.

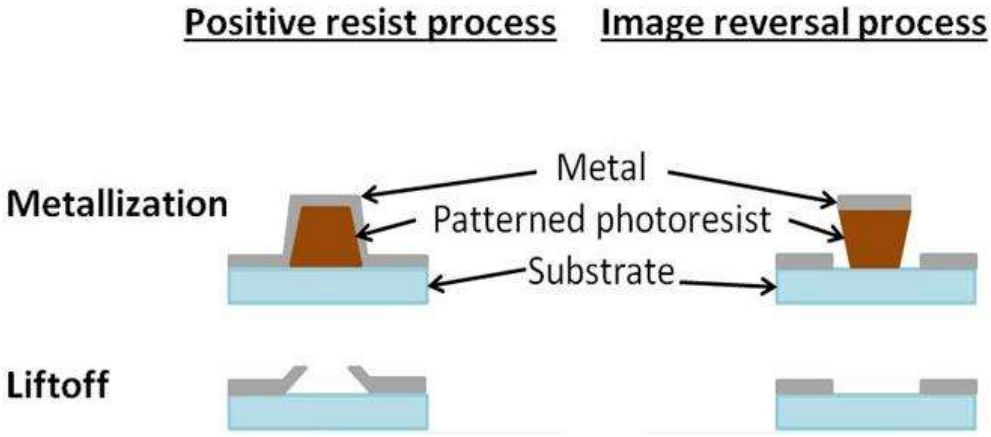

Fig. A.12 Metallization and liftoff for the two types of photoresist.

The latter difference is of great importance when the process requires only a single photoresist layer. As depicted in Fig. A.12, a metallic film is first evaporated on the patterned positive photoresist, and the liftoff process is then performed. Because of the

deposition of metal on the side wall, the metal could either come off partially or not at all during the lift-off. When using image reversal positive photoresist, the undercut helps prevent this problem by physically separating the metal on top of the resist and the one bound to the substrate. For this reason, a process involving image reversal photoresist and the AZ-5214-IR resist was used.

In the next step of the fabrication, a programmable SCS G3P-8 spin coater was used to spin the image reversal positive photoresist and to perform spin development. A Karl Suss MJB3 contact mask-aligner, capable of resolving features as small as ≈0.8 μm, was used to pattern the photoresist. The complete recipe is as follows:

- Spin photoresist at 5000 RPM with 5000 RPM/sec acceleration ramp
- Soft bake at 95 °C for 60 seconds
- Expose for 2.5 seconds with a light intensity of ≈12 mW/cm^2
- Post exposure bake at 115 °C for 60 seconds
- Flood exposure for 20 seconds with a light intensity of ≈12 mW/cm^2
- Spin develop for 60 seconds with successive steps:
    - 35 seconds of developing using MIF-319
    - 15 seconds of DI water
    - 10 seconds of drying at room temperature

A yield of around 95% of devices was achieved with this recipe, with minimum feature size = 1.4 μm and little dimensional mismatch (5% for the smallest features) between the devices and the optical mask.

D.3 Metallization and lift-off

After the photoresist is patterned, a metal stack can be evaporated. The metal stack needs to have a low resistivity, as low resistivity reduces the Joule heating and RF loss.

Prior to depositing the metal stack, the surface of the sample must be treated. The first step for surface preparation is to use a plasma oxygen treatment to remove mono-layers of organic materials that may remain after the photoresist is developed. A March CS-1701 Anisotropic Reactive-Ion Etching (RIE) Plasma System was used to carry out this step. This Asher uses an RF input at 13.56 MHz to create plasma, but first vacuum is achieved by reaching a base pressure of 80 mTorr. Oxygen is then introduced under a controlled flow so that the pressure reaches 700 mTorr. When the pressure is stable, the cleaning is initiated by generating the plasma and keeping it at a constant forward power of 400 W for 30 seconds. The pressure inside the chamber vs time for this process is shown in Figure A.13.

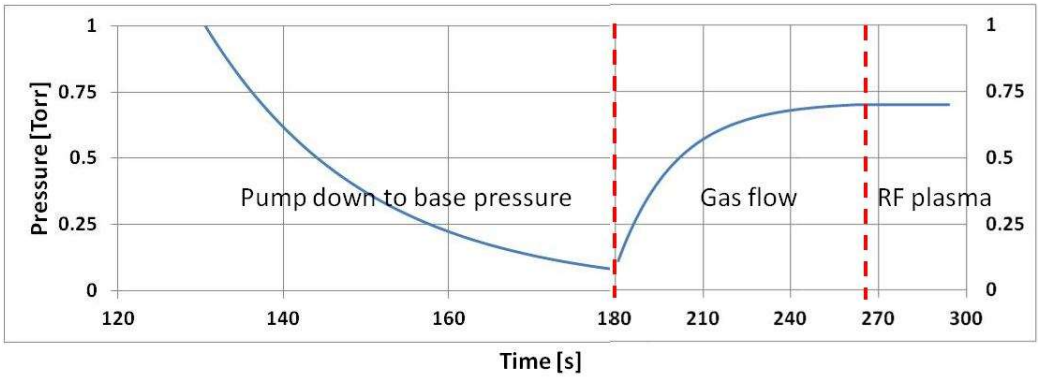

Fig. A.13 Pressure vs time of the cleaning process in the March system.

After cleaning of the exposed surface, an HCl dip is necessary to improve the adhesion of the metal to the substrate by removing the native oxide that naturally grows on GaAs when exposed to air. For this step, the patterned substrate was dipped into a solution of HCl/water at 50%/50% for 5 seconds, rinse with DI water and dried with compressed air. This step to prepare the surface was done immediately prior the evaporation in order to reduce the amount of time the sample is exposed to air.

D.4 Re-alignment technique

An important step during the fabrication of the devices with e-beam finger (Fig. 5.28) and presented in Chapter 8, was the alignment of the second-level mask with the patterned obtain through e-beam photolithography. Being able to successfully align the second layer with the first one is of great important in order to achieve high yield.

For this reason, alignment marks, like the one shown in Fig. A.14, were added to both layers. These marks were placed around each device chip at the four corners (Fig. A.15), in order to make the alignment of the second mask easier and to have references for the dicing step.

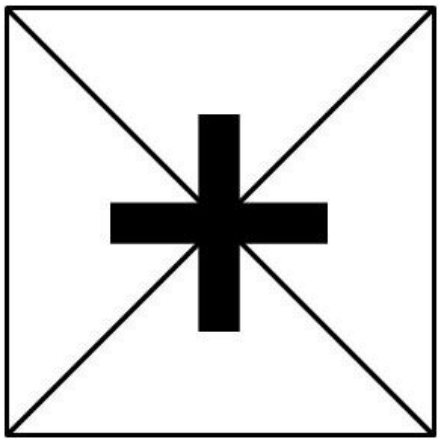

Fig. A.14 Alignment mark.

After the fabrication at OSU through e-beam lithography, the patterned sample was brought back to WSU's cleanroom in order to use optical lithography to pattern the second layer (i. e. to pattern the antenna).

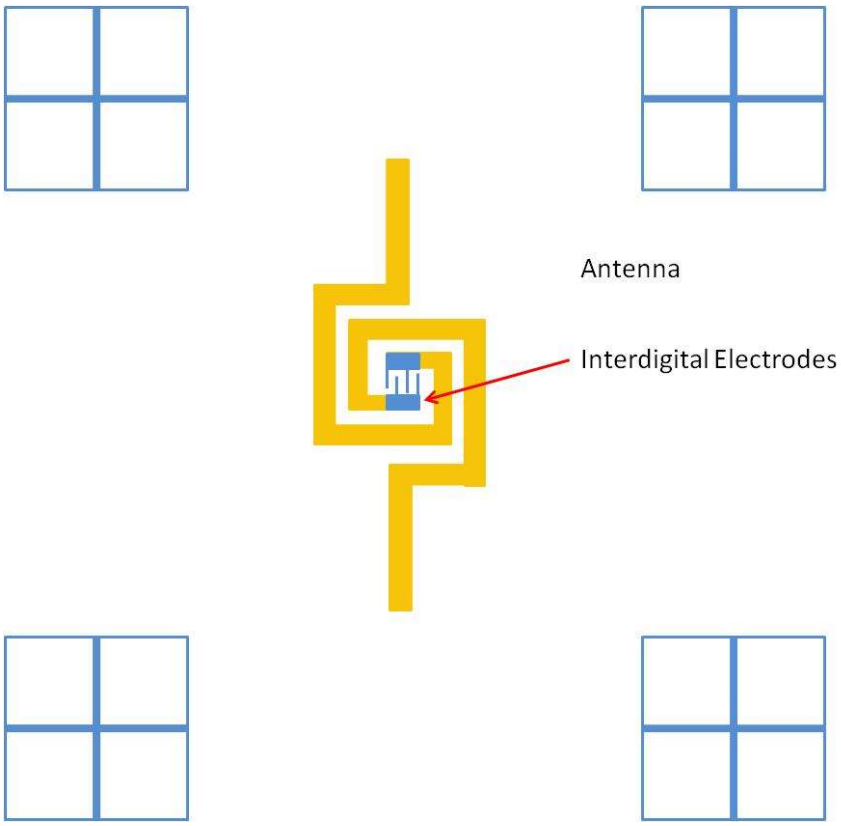

Fig. A.15 Single chip with the four alignment marks.

The MJB3 mask-aligner used to align the second mask with the sample patterned at OSU. This was possible thanks the 4- axis stage of the mask-aligner (x, y, z and θ). To start the sample was place at the exact center of the stage, as shown in Fig. A.16.

The microscope head of the MJB3 was then placed above the center of the stage as well. The x and y- axis were then carefully adjusted using through micrometers connected to the stage in order to align one of the marks (closest to the center) from the sample to the mark (closest to the center) of the mask. By moving the microscope head the edge of the sample along the x and y-axis, small adjustments on the θ were made. The full procedure consists of a repetition of these two steps. By making sure that the adjustments on the x-y plane were done only when looking at the center-most alignment mark, and the adjustments on θ only when looking at alignment marks on the edge of the sample, an optimal alignment was obtained.

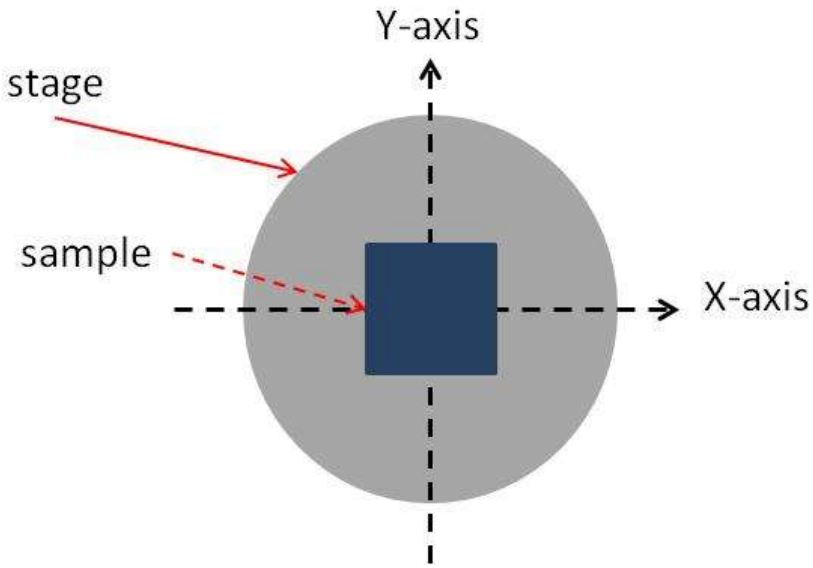

Fig. A.16 top-view of the substrate mounted on the MJB3 stage.

Appendix E

Gating circuit

In Chapter 6, signal-to-noise ratios (SNR) as high as 93 dB (at 300 GHz) were measured at spot frequencies using Schottky diode detectors. During this research, effort was put into increasing these numbers thanks to an improved detection system.

As a direct consequence of the pulsed excitation of the device, the signal collected with the Schottky detector is pulsed as well (Fig. A.17). The pulses are generated with the same frequency of the mode-lock laser source (i. e. 100 MHz), causing two consecutive pulses to be 10 ns apart in the time domain, with most of the signal generated in a time-window of around 1 ns.

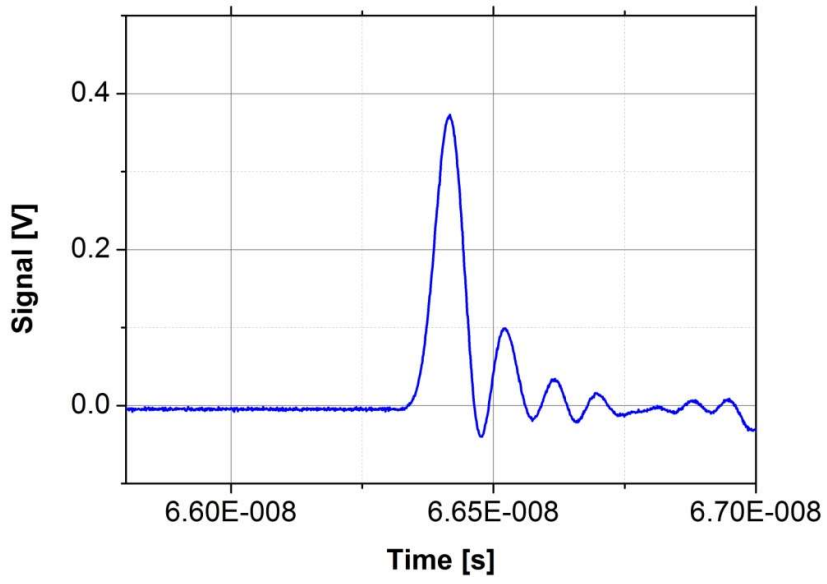

Fig. A.17 300 GHz pulsed signal from Schottky detector.

The drawback of the detection technique used in Chapter 6 is that the detector continuously collects both the signal and noise and averages these values over a set integration time. For this reason, in order to improve the SNR, a gating circuit was designed, with the intent of rejecting part of the noise (around 9 ns over the 10 ns period). Fig. A.18 shows the schematic of the circuit.

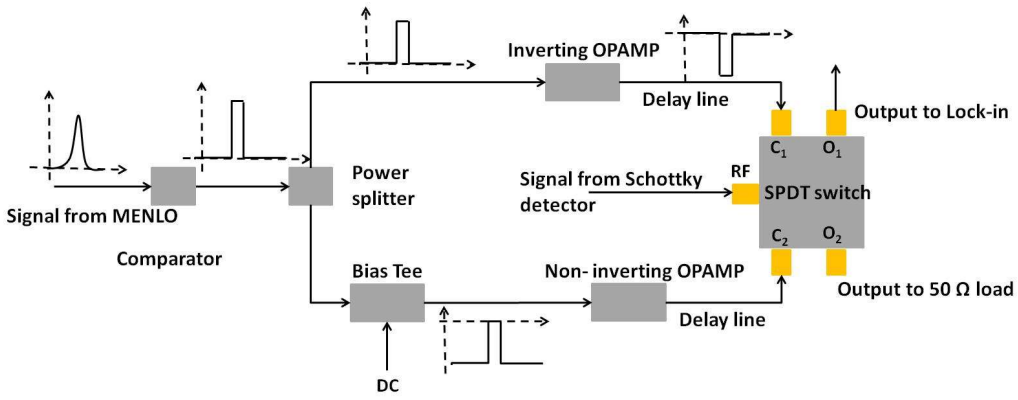

Fig. A.18 Schematic of the gating circuit.

The core part of this circuit is the SPDST switch (i. e. ZFSW-2-46) capable of switching between O_1 and O_2 in approximately 2 ns. The switch is driven by two control signals as shown in Fig. A.19. The control logic is shown in Table A.1.

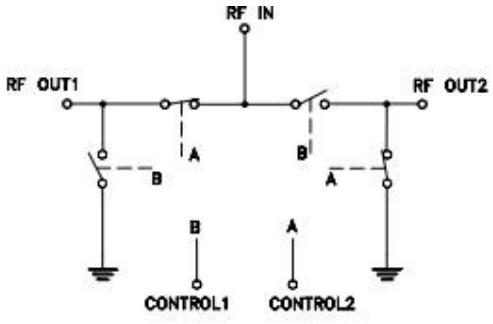

Fig. A.19 Electrical schematic of the SPDT switch.

Table A.1 Control logic for SDPT switch.

Control Ports		RF Outputs	
1	2	1	2
-V	0	On	Off
0	-V	Off	On

To drive the circuit, the RF output reference from the MENLO mode-lock laser (FWHM ≈ 1 ns, peak-to-peak voltage ≈ 200 mV) was used. This ensures that the switching frequency of the SPDT switch is the same as the signal of the Schottky diode. To better drive the SPDT switch, the two reference signals need to be as close to square wave signals as possible (with peak voltage of -8 V) in order to avoid having both control ports at 0 (or 1) logic values. To obtain the two control signals, the reference pulse from the MENLO laser is placed at the input of a comparator. The output square wave signal is then split into two: the first signal is then inverted using an inverting op-amp and use to control port $C_{1,}$ to the second one is added DC voltage (through a bias-tee) in order to render the signal negative, and then it is amplified with a non-inverting op-amp. Finally, delay lines are places before the ports C_1 and C_2 of the SPDT switch in order to correctly time the switching event. Fig. A.20 shows the ideal control voltages as a function of time.

This system is still under development, for this reason results on the improved SNR are still not available.

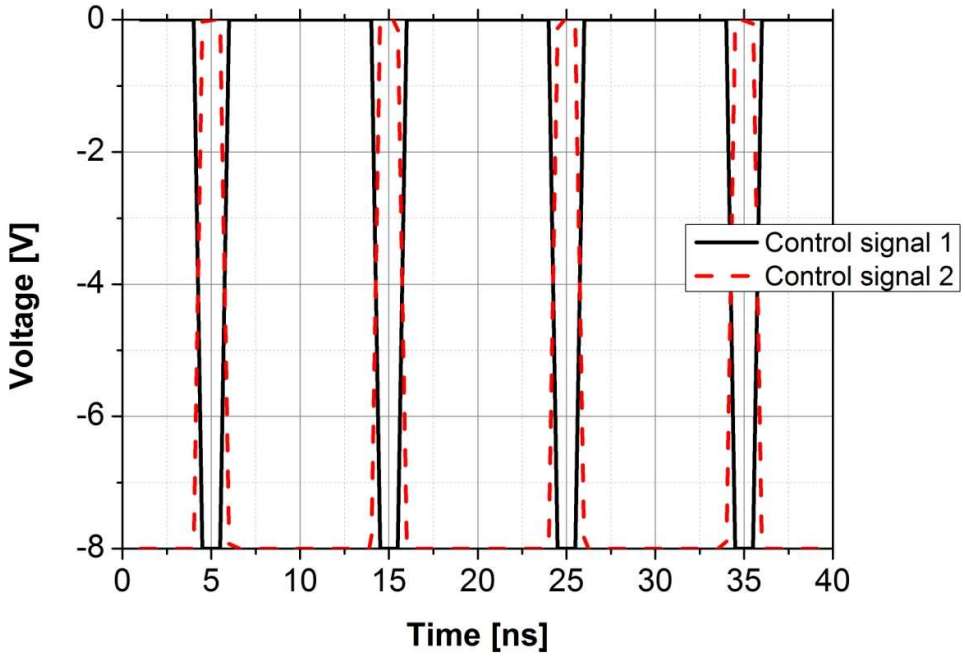

Fig. A.20 Ideal control voltage vs time.

Appendix F

Publications

Journal Articles:

A. Mingardi, W-D. Zhang and E. R. Brown "Characterization of an IR-Blocking, THz Low-Pass Filter for Improved THz Power Metrology "– in preparation

W-D. Zhang, E. R. Brown, A. Mingardi, R. P. Mirin, R. A. Annable and D. Saeedkia "THz Superradiance from a GaAs: ErAs Quantum Dot Array at Room Temperature" – under review at Optica (2018)

A. Mingardi, W–D. Zhang, E. R. Brown, A. D. Feldman, T. E. Harvey and R. P. Mirin "High power generation of THz from 1550-nm photoconductive emitters," Opt. Express 26, 14472-14478 (2018). https://doi.org/10.1364/OE.26.014472

E. R. Brown, A. Mingardi, W–D. Zhang, A. D. Feldman, T. E. Harvey and R. P. Mirin, "Abrupt Dependence of Ultrafast Extrinsic Photoconductivity on Er Fraction in GaAs:Er," Applied Physics Letters 111, 031104 (2017). https://doi.org/10.1063/1.4991876

Conference Proceedings:

A. Mingardi, W–D. Zhang, E. R. Brown, L.E. García-Muñoz, G. Carpintero del Barrio, and D. Segovia-Vargas "THz and Microwave Dual-Band Ultrafast Photoconductive Antenna" at EuMW 2018. https://doi.org/10.23919/EuMC.2018.8541500

A. Mingardi, W-D. Zhang, E. R. Brown "Advances in 1550-nm Driven THz, GaAs Photoconductive Switches" at IRMMW 2017. https://doi.org/ 10.1109/IRMMW-THz.2017.8067209

W-D. Zhang, A. Mingardi, E. R. Brown, A. Feldman, T. Harvey, R. P. Mirin "Ultrafast Photoconductive Devices Based upon GaAs:ErAs Nanoparticle Composite Driven at 1550 nm" at SPIE Defense + Security 2017. https://doi.org/10.1117/12.2262647

A. Mingardi, W-D. Zhang, E. R. Brown "THz Performance of 1550-nm Driven Photoconductive Switches Made from GaAs:Er with ErAs Quantum Dots" at NAECON 2017. https://doi.org/10.1109/NAECON.2017.8268796

W. Zhang, A. Mingardi and E. R. Brown, "New high-extinction wire-grid polarizers for polarimetric W-band radar," 2017 IEEE National Aerospace and Electronics Conference (NAECON), Dayton, OH, 2017, pp. 335-337. https://doi.org/10.1109/NAECON.2017.8268797

A. Mingardi, W-D. Zhang, E. R. Brown “Non-Contact, Antenna-Free Probe for Characterization of THz Devices and Components” at NAECON-IOS 2016. https://doi.org/10.1109/NAECON.2016.7856845

References

[1]. J. R. Middendorf and E. R. Brown, "THz generation using extrinsic photoconductivity at 1550 nm," Opt. Express 20, 16504–16509 (2012).

[2]. W-D. Zhang, J. R. Middendorf, and E. R. Brown, "Demonstration of a GaAs-based 1550-nm continuous wave photomixer," Appl. Phys. Lett. 106, 021119 (2015).

[3]. J. R. Middendorf, "Novel Devices and Components for THz Systems," Ph.D. Dissertation, Wright State University, 2014.

[4]. L. A. Samoska, "An overview of solid-state integrated circuit amplifiers in the submillimeter-wave and THz regime," IEEE Trans. Terahertz Sci. Technol. 1, 9–24 (2011).

[5]. P. Dean et al., "Terahertz imaging using quantum cascade lasers—a review of systems and applications," J. Phys. D. Appl. Phys. 47, 374008 (2014).

[6]. http://lts.fzu.cz/en/intro.php

[7]. H.-T. Chen, R. Kersting and G. C. Cho (2003) "Terahertz imaging with nanometer resolution" Appl. Phys. Lett. 83 3009–11

[8]. W. L. Chan, J. Deibel, and D. M. Mittleman, "Imaging with terahertz radiation," Reports Prog. Phys., 70 (8), 1325–1379, (2007).

[9]. R. G. Mathew, J. R. Middendorf, E. R. Brown, C. Koneka, J. Wilkinson, O. Esenturkb, E. Heilweilb, and M. Kemp, "Database of all THz Signatures measured on Solids and Liquids in the range 100 GHz to 10 THz," IRMMW 2011

[10]. S. Sung et al., "Optical system design for non-contact, normal incidence, THz imaging of in vivo human cornea," IEEE Trans. THz Sci. Technol., 2017

[11]. S. Jae Oh, S.-H. Kim, Y. B. Ji, K. Jeong, Y. Park, J. Yang, D. W. Park, S. K. Noh, S.-G. Kang, Y.-M. Huh, J.-H. Son, and J.-S. Sue, "Study of freshly excised brain tissues using terahertz imaging," Biomed. Opt. Express 5, 2837–2842 (2014).

[12]. Z. D. Taylor et al., "THz and mm-wave sensing of corneal tissue water content: In vivo sensing and imaging results," IEEE Trans. THz Sci. Technol., 5 (2), 184–196, (2015).

[13]. D. Bennett, "Hydration Sensing in Biological Tissues with the Terahertz Band," University of California, Santa Barbara, 2011.

[14]. Y. Yang, A. Shutler, and D. Grischkowsky, "Measurement of the transmission of the atmosphere from 0.2 to 2 THz," Opt. Express, vol. 19, pp. 8830–8838, 2011

[15]. A. Dobroiu, C. Otani, and K. Kawase, "Terahertz-wave sources and imaging applications" *Measurement Science and Technology*, **17**(11): R161–R174, 2006.

[16]. W. Ryu, Y. Won, and M. Lee, "Compact and portable terahertz imaging system using single-mode Fabry-Perot laser diode photomixer". 52. 10.1117/12.2289500, (2018).

[17]. S. Fan, E. P. J. Parrott, B. S. Y. Ung, and E. Pickwell-MacPherson, "Calibration method to improve the accuracy of THz imaging and spectroscopy in reflection geometry," Photon. Res. 4(3), A29–A35 (2016).

[18]. S. Sung, S. Selvin, N. Bajwa, S. Chantra, B. Nowroozi, J. Garritano, J. Goell, A. D. Li, S. Deng, E. R. Brown, W. Grundfest, and Z. D. Taylor, "THz Imaging System for in vivo Human Cornea". IEEE Transactions on Terahertz Science and Technology. PP. 1-11. 10.1109/TTHZ.2017.2775445, (2017).

[19]. P. H. Siegel, "Terahertz Technology in Biology and Medicine," IEEE Trans. Microwave Theory Tech., 52 (10), 2438–2447, (2004).

[20]. T. W. Crowe, T. Globus, D. L. Woolard, and J. L. Hesler, "Terahertz sources and detectors and their application to biological sensing," Phil. Trans. R. Soc. Lond. A, **362** (1815), 365–377, (2004).

[21]. P. H. Bolivar, M. Nagel, F. Richter, M. Brucherseifer, H. Kurz, A. Bosserhoff, and R. Buttner, "Label-free THz sensing of genetic sequences: towards THz biochips," Phil. Trans. R. Soc. Lond. A, **362** (1815) 323–335, (2004).

[22]. T. Globus, D. Woolard, M. Bykhovskaia, B. Gelmont, L. Werbos, and A. Samuels, "THz-frequency spectroscopic sensing of DNA and related biological materials," International Journal of High Speed Electronics and Systems, **13** (4) 903–936, (2003).

[23]. M. R. Scarfi, M. Romano, R. Dipietro, O. Zeni, A. Doria, G. P. Gallerano, E. Giovenale, G. Messina, A. Lai, G. Campurra, D. Coniglio, and M. D'Arienzo, "THz Exposure of Whole Blood for the Study of Biological Effects on Human Lymphocytes," J. Biol. Phys., **29** 171–175, 2003.

[24]. M. Naftaly, A. P. Foulds, R. E. Miles, and A. G. Davies, "Terahertz Transmission Spectroscopy of Nonpolar Materials and Relationship with Composition and Properties," Int. J. Infrared Millim. Waves, **26 (**1), 55–64, (2005).

[25]. Y. Watanabe, K. Kawase, T. Ikari, H. Ito, Y. Ishikawa, and H. Minamide, "Component analysis of chemical mixtures using terahertz spectroscopic imaging," Opt. Commun., **234** (1-6), 125–129, (2004).

[26]. E. R. Brown, J. Bjarnason, T. L. J. Chan, D. C. Driscoll, M. Hanson, and A. C. Gossard, "Room temperature, THz photomixing sweep oscillator and its application to spectroscopic transmission through organic materials," Rev. Sci. Instrum., **75** (12)5333–5342, (2004).

[27]. T. L. J. Chan, J. E. Bjarnason, A. W. M. Lee, M. A. Celis, and E. R. Brown, "Attenuation contrast between biomolecular and inorganic materials at terahertz frequencies," Appl. Phys. Lett., **85** (13) 2523–2525, (2004).

[28]. C. Zhang and K. Mu, "Applications of Terahertz spectroscopy and imaging," SPIE Proc., **7385** (10) 738504–738504–8, (2009).

[29]. A. G. Davies, A. D. Burnett, W. Fan, E. H. Linfield, and J. E. Cunningham "Terahertz spectroscopy of explosives and drugs" Mater. Today, 11 18-26 (2008).

[30]. J. Sibik, J.A. Zeitler "Direct measurement of molecular mobility and crystallization of amorphous pharmaceuticals using terahertz spectroscopy" Adv. Drug Deliv. Rev., 100 147-157, (2016).

[31]. N. Karpowicz, H. Zhong, C. Zhang, K.-I. Lin, J.-S. Hwang, J. Xu, and X.-C. Zhang, "Compact continuous-wave subterahertz system for inspection applications," Appl. Phys. Lett., **86** (5) 54 105–3, (2005).

[32]. M. K. Choi, A. Bettermann, and D. W. Van Der Weide, "Potential for detection of explosive and biological hazards with electronic terahertz systems," Phil. Trans. R. Soc. Lond. A, **362** (1815), 337–349, (2004).

[33]. S. Wang, B. Ferguson, D. Abbott, and X.-C. Zhang, “T-ray imaging and tomography,” J. Biol. Phys., **29** (2-3), 247–256, (2003).
[34]. D. M. Mittleman, R. H. Jacobsen, and M. C. Nuss, “T-Ray Imaging,” IEEE J. Sel. Top. Quantum Electron., **2** (3), 679–692, (1996).
[35]. B. B. Hu and M. C. Nuss, “Imaging with terahertz waves,” Opt. Lett., **20** (16), 1716–1718, (1995).
[36]. J. E. Bjarnason, T. L. J. Chan, a. W. M. Lee, M. a. Celis, and E. R. Brown, “Millimeter-wave, terahertz, and mid-infrared transmission through common clothing,” *Appl. Phys. Lett.*, **85** (4), 519, (2004).
[37]. J. Grajal et al., “3-D high-resolution imaging radar at 300 GHz with enhanced FoV,” IEEE Trans. Microw. Theory Techn., **63** (3), 1097–1107, (2015).
[38]. Li Ding, Xi Ding, Yangyang Ye, Sixuan Wu, and Yiming Zhu “High-Resolution Grid-Independent Imaging for Terahertz 2-D Synthetic Aperture Radar with Spatial Under-Sampling” Progress in Electromagnetics Research, 160, 29–39, (2017)
[39]. J. Yang, W. Su, H. Gu, ‘High-resolution multiple-input–multiple-output–inverse synthetic aperture radar imaging based on sparse representation’, IET Radar Sonar Navig., 2016, **10**, (7), 1277–1285.
[40]. N. Khalid, N. A. Abbasi, and O. Akan, “300 GHz Broadband Transceiver Design for Low-THz Band Wireless Communications in Indoor Internet of Things”. 770-775. 10.1109/iThings-GreenCom-CPSCom-SmartData.2017.118. (2017).
[41]. G. Ducournau, P. Szriftgiser, A. Beck, D. Bacquet, F. Pavanello, E. Peytavit, M. Zaknoune, T. Akalin, and J.-F. Lampin, “Ultrawide-bandwidth single-channel 0.4-THz wireless link combining roadband quasi-optic photomixer and coherent detection,” IEEE Trans. Terahertz Sci. Technol., vol. 4, no. 3 pp. 328–337, May, 2014
[42]. Nagatsuma T., Ducournau G., Renaud C.C. “Advances in terahertz communications accelerated by photonics” Nat. Photonics, **10** (6), 371-379, (2016).
[43]. S. Koenig, D. Lopez-Diaz, J. Antes, F. Boes, R. Henneberger, A. Leuther, A. Tessmann, R. Schmogrow, D. Hillerkuss, R. Palmer, T. Zwick, C. Koos, W. Freude, O. Ambacher, J. Leuthold, and I. Kallfass, “Wireless sub-THz communication system with high data rate enabled by RF photonics and active MMIC technology,” in Proc. IEEE Photonics Conf, 414-415, (2014).
[44]. K. Nallappan, H. Guerboukha, C. Nerguizian and M. Skorobogatiy, "Live Streaming of Uncompressed 4K Video Using Terahertz Wireless Links," IEEE ICC 2018 Wireless Communications Symposium, I-WCS.01, USA (2018)
[45]. D. H. Auston, “Picosecond optoelectronic switching and gating in silicon,” Appl. Phys. Lett. **26**, 101-103 (1975).
[46]. D. Auston, K. Cheung, J. Valdmanis, and D. Kleinman, “Cherenkov Radiation from Femtosecond Optical Pulses in Electro-Optic Media,” Phys. Rev. Lett., **53 (**16), 1555–1558, (1984).
[47]. A. Johnson and D. Auston, “Microwave switching by picoseconds photoconductivity,” IEEE J. Quantum Electron., **11** (6), 283–287, (1975).
[48]. D. B. Bennett, Z. D. Taylor, P. Tewari, R. S. Singh, M. O. Culjat, W. S. Grundfest, D. J. Sassoon, R. D. Johnson, J.-P. Hubschman, and E. R. Brown, “Terahertz sensing in corneal tissues.,” J. Biomed. Opt., **16** (5), 057003, (2011).

[49]. E. R. Brown, F. W. Smith, and K. a. McIntosh, "Coherent millimeter-wave generation by heterodyne conversion in low-temperature-grown GaAs photoconductors," J. Appl. Phys., **73** (3), 1480, (1993).
[50]. S. I. Lepeshov, A. Gorodetsky, A. E. Krasnok, E. U. Rafailov and P. A. Belov "Enhancement of Terahertz Photoconductive Antennas and Photomixers Operation by Optical Nanoantennas", Laser Photonics Reviews, **11** (1), (2017).
[51]. D. H. Auston, "Subpicosecond electro-optic shock waves," Appl. Phys. Lett. 43, 713–715 (1983).
[52]. D. H. Auston, K. P. Cheung, and P. R. Smith, "Picosecond photoconducting Hertzian dipoles," Appl. Phys. Lett. **45**, 284–286 (1984).
[53]. P. R. Smith, D. H. Auston, and M. C. Nuss, "Subpicosecond photoconducting dipole antennas," IEEE J. Quantum Electron. **24**, 255–260 (1988).
[54]. P. U. Jepsen, R. H. Jacobsen, and S. R. Keiding, "Generation and detection of terahertz pulses from biased semiconductor antennas," J. Opt. Soc. Am. B **13**, 2424 (1996).
[55]. Y. S. Lee, "Princ. Terahertz Sci. Technol." Springer US, Boston, MA,1-340, (2009).
[56]. F. P. Kapron D. B. Keck and R. D. Maurer "Radiation losses in glass optical waveguides". Appl. Phys. Lett. **17**, 423–425, (1970).
[57]. https://networkel.com/network-fiber-optic-cable-fundamentals/
[58]. http://www.laser-femto.com/products/laserfemto_price_list_2016.pdf
[59]. https://www.ozoptics.com/ALLNEW_PDF/DTS0079.pdf
[60]. https://www.rp-photonics.com/spotlight_2007_09_01.html
[61]. http://photonicswiki.org/index.php?title=Dispersion_and_Attenuation_Phenomena
[62]. J. L. Hudgins, G. S. Simin, E. Santi, and M. S. Khan, "An assessment of wide bandgap semiconductors for power devices". IEEE Transactions on Power Electronics, **18**, 907, (2003).
[63]. O. Hatem, J. R. Freeman, J. E. Cunningham, et al. J Infrared Milli Terahz Waves **37,** 415, (2016).
[64]. J. Mangeney, "THz photoconductive antennas made from ion-bombarded semiconductors", J. Infrared Millim. Terahertz Waves **33** 455-473, (2012).
[65]. D. Kostakis, Saeedkia, and M. Missous, "Terahertz Generation and Detection Using Low Temperature Grown InGaAs-InAlAs Photoconductive Antennas at 1.55," IEEE Trans. THz. Sci. Technol. 2(6), 617–622 (2012).
[66]. I. Kostakis, D. Saeedkia, and M. Missous, J. Appl. Phys. 111 (2012).
[67]. B. Sartorius, H. Roehle, H. Künzel, et al. "All-fiber terahertz time-domain spectrometer operating at 1.5 μm telecom wavelengths". Optics Express, **16**, 9565, (2008).
[68]. R. J. B. Dietz, B. Globisch, M. Gerhard, et al. "64 μW pulsed terahertz emission from growth optimized InGaAs/InAlAs heterostructures with separated photoconductive and trapping regions". Applied Physics Letters **103**, 061103, (2013).
[69]. M. A. Scarpulla, J. M. O. Zide, J. M. LeBeau, et al. "Near-infrared absorption and semimetal-semiconductor transition in 2 nm ErAs nanoparticles embedded in GaAs and AlAs". Applied Physics Letters, **92** 173116, (2008).

[70]. J. E. Bjarnason, T. L. J. Chan, A. W. M. Lee, et al. “ErAs:GaAs photomixer with two-decade tenability and 12W peak output power”. Applied Physics Letters, 85, 3983, (2004).
[71]. C. Kadow, A. W. Jackson, A. C. Gossard, et al. “Self-assembled ErAs islands in GaAs for optical heterodyne THz generation”. Applied Physics Letters, **76**, 3510, (2000).
[72]. https://www.photonics.com/Articles/Germanium_Quantum_Wells_for_High-Performance/a30705
[73]. H Ennen, J. Wagner, H. D. Muller, and R. S. Smith, J. Appl. Phy: 61, 4877 (1987).
[74]. I. Poole, K.E. Singer, A.R. Peaker, Journal of Crystal Growth121 (1992) 121.
[75]. S. Sethi, and P. K. Bhattacharya, JEM (1996) 25: 467. https://doi.org/10.1007/BF02666622
[76]. S. Gupta. S. Sethi, and P. K. Bhattacharya, “Picosecond carrier lifetime in erbium-doped GaAs,” Appl. Phys. kit., vol. 62, p. 1128, 1993
[77]. Z. D. Taylor, E. R. Brown, and J. E. Bjarnason, “Resonant-optical-cavity photoconductive switch with 0.5% conversion efficiency and 1.0W peak power”. Opt. Lett. 31, 1729–1731 (2006)
[78]. B. Globisch et al. “Iron doped InGaAs: Competitive THz emitters and detectors fabricated from the same photoconductor,” J. Appl. Phys. 121, 053102 (2017).
[79]. J. K. Kawasaki, R. Timm, K. T. Delaney, E. Lundgren, A. Mikkelsen, and C. J. Palmstrøm, Phys. Rev. Lett. 107, 036806 (2011).
[80]. E. R. Brown, W. Zhang, A. Feldman, T. Harvey and R. P. Mirin, "Model for ultrafast extrinsic photoconductivity in Er-doped GaAs," 2016 41st International Conference on Infrared, Millimeter, and Terahertz waves (IRMMW-THz), Copenhagen, 2016, pp. 1-2.
[81]. http://icy.bioimageanalysis.org
[82]. Assuming all Er atoms incorporate as ErAs, and the nanoparticles ware perfect spheres having diameter equal to the "most likely" value
[83]. https://www.nanoscience.com/products/scanning-electron-microscopes/phenom-pro/
[84]. Private conversation with Dr. Richard Mirin
[85]. https://www.stellarnet.us/spectrometers/dwarf-star-miniature-nir-spectrometer/
[86]. https://www.newport.com/f/cs260-vis-nir-monochromators
[87]. E. R. Brown, A. Mingardi, W.-D. Zhang, A. D. Feldman, T. E. Harvey, and R. P. Mirin, “Abrupt dependence of ultrafast extrinsic photoconductivity on Er fraction in GaAs:Er,” Appl. Phys. Lett. 111(3), 031104 (2017).
[88]. E. R. Brown, A. Bacher, D. Driscoll, M. Hanson, C. Kadow, and A. C. Gossard, “Evidence for a strong surface plasmon resonance on ErAs nanoparticles in GaAs,” Phys. Rev. Lett. 90(7), 077403 (2003)
[89]. L. J. van der Pauw, “A Method of Measuring Specific Resistivity and Hall Effect of Discs of Arbitrary Shape,” Philips Research Reports, Vol. 13, February 1958, pp. 1-9.
[90]. D. L. Rode, R. K. Willardson, and A. C. Beer, Semiconductors and Semimetals, Vol. 10, Academic Press, New York (1975), p. 1.
[91]. M. De Laurentis and A. Irace, “Optical Measurement Techniques of Recombination Lifetime Based on the Free Carriers Absorption Effect,” Journal

of Solid State Physics, vol. 2014, Article ID 291469, 19 pages, 2014. https://doi.org/10.1155/2014/291469.
[92]. M. Martin and E. R. Brown, "Photoconductive materials for THz generation at 1550 nm: ErAs:GaAs vs InGaAs based materials," Proc. SPIE 9362, 936207 (2015).
[93]. S. Matsuura, M. Tani, and K. Sakai, "Generation of coherent terahertz radiation by photomixing in dipole photoconductive antennas," Appl. Phys. Lett. 70, 559-561 (1997).
[94]. M. Tonouchi, M. Yamashita, and M. Hangyo, "Terahertz radiation imaging of supercurrent distribution in vortex-penetrated YBa2Cu3O7-d thin film strips," J. Appl. Phys. 87, 7366-7375, (2000).
[95]. S. M. Duffy, S. Verghese, K. A. McIntosh, A. Jackson, A. C. Gossard, and S. Matsuura, "Accurate Modeling of Dual Dipole and Slot Elements Used with Photomixers for Coherent Terahertz Output Power," IEEE Trans. Microwave Theory Tech. 49, 1032-1038 (2001).
[96]. J. D. Speight and K. Cooper, "Interlayer diffusion phenomena in Ti-Au metallization on n-type GaAs at 250°-450°C," Thin Solid Films 25, S31-S37 (1975).
[97]. R. V. Ghita, C. Logofatu, C. Negrila, A. S. Manea, M. Cernea, and M. F. Lazarescu, "Studies of Ohmic Contact and Schottky Barriers on Au-Ge/GaAs and Au-Ti/GaAs," J. Optoelectronics Adv. Mat. 7, 3033- 3037 (2005).
[98]. M. Ogawa, "Alloying of Ni/Au-Ge films on GaAs," J. Appl. Phys. 51, 406-412 (1980).
[99]. N. Braslau, J. B. Gunn, and J. L. Staples, Solid-State Electron. 10, 381 (1967)
[100]. G.Y. Robinson, Solid-State Electron. 18 (1975) 331.
[101]. M. Heilblum, M. I. Nathan and C. A. Chang, Solid-State Electron. 25 (1982) 185.
[102]. E. Relling, and A. P. Botha 1988 Appl. Surf. Sci. 35 380
[103]. https://www.pveducation.org/pvcdrom/characterisation/four-point-probe-resistivity-measurements
[104]. K. Fuchs (1938). "The conductivity of thin metallic films according to the electron theory of metals". Mathematical Proceedings of the Cambridge Philosophical Society, 34(1), 100-108. doi:10.1017/S0305004100019952
[105]. D. B. Barker, and W. C. Caldwell, "Electrical properties of thin metallic films" (1952). Ames Laboratory ISC Technical Reports. 35.
[106]. X. W. Han, L. Hou, L. Yang et al. (2016) Chin. Phys. Lett. 33 120701
[107]. D. Rutledge, D. Neikirk, and D. Kasilingam "Integrated Circuit Antennas", in Infrared and Millimeter Waves, vol. 10, pp. 1-90 (Academic Press, 1983).
[108]. https://patentimages.storage.googleapis.com/c1/0c/7b/dc29c53fac436b/US2863145.pdf
[109]. https://www.microwaves101.com/encyclopedias/permittivity
[110]. E. R. Brown, A. W. M. Lee, B. S. Navi, and J. E. Bjarnason, "Characterization of a Planar Self-Complimentary Square-Spiral Antenna in the THz Region," Microw. Opt. Technol. Lett., 48 (3), 524–529 (2006).
[111]. J. D. Dyson, "The Equiangular Spiral Antenna,". IRE Trans. Antennas Propagat., 1959, 7, pp. 181-188

[112]. W-D. Zhang, E. R. Brown, A. D. Feldman, T. E. Harvey, R. P. Mirin "Kondo-Resonance Mediated Metal-Insulator Transition in GaAs Embedded with Erbium Arsenide Quantum Dots" arXiv:1711.01188
[113]. J. M. Blea, W. F. Parks, P. A. R. Ade and R. J. Bell (1970), J. Opt. Soc. Am. 60, 603.
[114]. S. Preu, G. H. Dohler, S. Malzer, L. J. Wang and A. C. Gossard "Tunable, continuous-wave Terahertz photomixer sources and applications, "J. Appl. Phys. 109, 061301(2011).
[115]. www.amariplastics.com
[116]. J. B. Theeten, D. E. Aspnes, and R. P. H. Chang, J. Appl. Phys. 49, 6097 (1978)
[117]. E.R. Brown, H. Bagherzadeh, and W-D. Zhang, "Sub-THz Power Measurements with Room-Temp Pyroelectric Detectors", IRMMW-THz 2016 Conference, Copenhagen, Denmark, Sept 2016.
[118]. A. Mingardi, W-D. Zhang, E. R. Brown, A. D. Feldman, T. E. Harvey, and R. P. Mirin, "High power generation of THz from 1550-nm photoconductive emitters," Opt. Express 26, 14472-14478 (2018)
[119]. J. S. Cetnar, J. R. Middendorf, and E. R. Brown, Appl. Phys. Lett. 100, 231912 (2012).
[120]. "Towards 1-mW THz Photoconductive Sources with Low-Cost Laser Drivers" in Special Session on Optics Sensors, Optical Society of America Advanced Photonics Congress, June 12-16, 2011 at the Westin Harbour Castle, Toronto, Canada.
[121]. J. Y. Suen, W. Li, Z. D. Taylor, and E.R. Brown, "Characterization and Modeling of a THz Photoconductive Switch," Appl. Phys. Lett. vol. 96,141103 (2010).
[122]. N. Wiener, Acta Mathematica 55, 117 (1930).
[123]. A. Khintchine, Mathematische Annalen 109, 604 (1934).
[124]. http://www4.ncsu.edu/~franzen/public_html/CH431/math/lineshape/lineshape.html
[125]. M. Beck, H. Schäfer, G. Klatt, J. Demsar, S. Winnerl, M. Helm, and T. Dekorsy, "Impulsive terahertz radiation with high electric fields from an amplifier-driven large-area photoconductive antenna," Opt. Express 18(9), 9251–9257 (2010).
[126]. S. Das and A. Maitra, "Rain attenuation modeling in the 10-100 GHz frequency using drop size distributions for different climatic zones in tropical India," Prog. In Electromagnetics Research B, 25, 211-224 (2010).
[127]. http://www.ioffe.ru/SVA/NSM/Semicond/GaAs/basic.htm
[128]. Prof. L. E. García-Muñoz, Prof. G. Carpintero del Barrio, and Prof. D. Segovia-Vargas performed the simulations.
[129]. https://www.cst.com/products/cstmws
[130]. W-D. Zhang, E. R. Brown, A. Mingardi, R. P. Mirin, R. A. Annable and D. Saeedkia "THz Superradiance from a GaAs: ErAs Quantum Dot Array at Room Temperature" – under review at Optica (2018).
[131]. Kilgore, S., "Electromigration Reliability of Passivated Gold Interconnects for GaAs Devices," ECS Transactions, vol. 61, pp. 57–63, September 22, 2014 (2014)
[132]. P. F. Tang, A.G Milnes, C.L. Bauer, S. Mahajan, "Electromigration in thin films of Au on GaAs", Proc. Mater. Res. Soc., vol. 167, pp. 341, 1989.